Probing solid-earth, ocean, and structural dynamics with distributed fiber-optic sensing

Thesis by
Ethan Francis Williams

In Partial Fulfillment of the Requirements for the
Degree of
Doctor of Philosophy

CALIFORNIA INSTITUTE OF TECHNOLOGY
Pasadena, California

2023
Defended November 2, 2022

Ethan Francis Williams
ORCID: 0000-0002-6471-4497

ACKNOWLEDGEMENTS

Ad maiorem Dei gloriam

First, I thank my advisor, Zhongwen. With an infectious enthusiasm for geophysics, Zhongwen encouraged and guided my development as a scientist. More than just a supervisor, he gave me the freedom to explore my own interests and follow the data, leading to many unexpected projects. I am immeasurably grateful.

I thank the members of my committee: Tom, Rob, Jörn, Monica, and Mark. Tom has shared many unique perspectives on earthquakes and mechanics, on which I will surely ruminate for many years to come. Rob has been a bottomless font of practical advice on seismology, and I enjoyed many dusty seismic surveys in his geophysical field course. Jörn has supplied several oceanography interventions over the past few years, as I am continually perplexed by fluid mechanics. Monica is perhaps the only other person on the planet whose research interests spans seafloor sensing to earthquake engineering, and her suggestions have always been insightful. Mark supervised my start at Caltech in June 2017 and shared many intuitions on inverse theory which I have found foundational. I am deeply indebted to Miguel, Hugo, Sonia, and Rosario at UAH and Arantza at ICM who provided much of the data for this thesis, and who, with regular discussions over the past four years, taught me a lot about fiber-optic sensing. Thank you to the Seismolab staff for their continual help, especially Priscilla, Donna, and Kim.

My graduate career would not have occurred were it not for the formative tutelage of my undergraduate research mentors at Stanford: Simon, Chris, Eileen, Kate, and Biondo. In particular, Simon taught me how to write a scientific paper through many painstaking word-by-word revisions of my undergraduate thesis. Thank you to Chris for taking me to sea in 2015, and to Eileen for introducing me to DAS.

For creating a supportive environment, abounding in puns and debates, I thank the inhabitants of South Mudd 358, my office mates: Celeste, Tobi, Jimmy, Rachel, Chris, and our many short-term visitors. Thank you to the community of GPS grad students and postdocs: Valere, Ollie, Voon, Jack, other Jack, Ben, other Ben, Erin, Olivia, Will, Emma, Yan, Ettore, and many other peers (who tragically can't all be listed here) for numerous stimulating conversations, both social and scientific. Thank you also to Nico, Carolyn, Sarah, Albert, and other non-work friends.

Since moving to Southern California, I have made so many friends in music, and I thank them for keeping me sane. Thank you to Lindsey, Joan, and the Los Angeles Baroque community for much music making over the years; to Nicole and the St. Philip the Apostle choir for challenging me and providing me with a musical and spiritual home; to Steven for teaching me so much; and to many, many others.

Finally and most importantly, I thank my family, especially my parents Colin and Ginger. From the vacations that were more like geologic field trips to the scientific posters hanging on the walls of our home, my parents' passion for the geological sciences led directly to my interest in seismology and my chosen career path. Some fond memories include tagging along as a child while my father logged a well, explaining heat flow and boreholes; a trip to Newberry Volcano, where we inadvisably attempted to form obsidian into arrow heads; and many walks along the cliffs in Half Moon Bay watching coastal erosion in real time. Without the unending support and encouragement of my parents, none of this would have been possible.

ABSTRACT

Observational geophysics conventionally relies on point sensors to document and monitor Earth's dynamic processes, from locating earthquakes and imaging subsurface structure with seismometers to forecasting coastal wave heights and detecting tsunamis with buoys. Distributed acoustic sensing (DAS) offers a fundamentally different paradigm: distributed instead of point sensing. DAS converts fiber-optic cables into dense arrays of broadband, linear strainmeters, with spatial resolution as fine as one meter and temporal resolution up to several thousand samples per second. The first four chapters of this thesis concern ocean-bottom DAS, repurposing pre-existing telecommunications and power cables as distributed seafloor sensing networks for seismology and physical oceanography. In Chapter 2, we analyze one of the first ocean-bottom DAS datasets, demonstrating that seismic and ocean waves observed on the same array are related by a classic theory of double-frequency microseism generation. We also extract the principal body-wave phases of a M8.2 deep earthquake, demonstrating the earthquake detection capabilities of DAS even in a shallow water environment. In Chapter 3, we apply ambient noise interferometry to a one-hour of ocean-bottom DAS data and derive a shallow shear-wave velocity model. We also isolate spurious arrivals in noise cross-correlations associated with nearby offshore wind turbines, suggesting potential for remote monitoring. In Chapter 4, we adapt ambient noise interferometry to the ocean surface gravity wavefield, and estimate the tidal current velocity along a short cable segment in the Strait of Gibraltar with a waveform stretching method. In Chapter 5, we explore the application of DAS as a temperature sensor at long periods, documenting temperature signals up to 4 K associated with internal wave and boundary layer dynamics. We demonstrate that while ocean-bottom DAS exhibits sufficient strain sensitivity to record seafloor geodetic processes, oceanic temperature transients may overprint such signals. The last part of this thesis concerns a different frontier in geophysical instrumentation: long time-series. With a 20-year continuous record of ambient vibrations from a single accelerometer located on the ninth floor of a concrete building, we document long-term, passive changes in the building's natural frequencies as well as complex, time-dependent nonlinear elasticity during earthquakes.

PUBLISHED CONTENT AND CONTRIBUTIONS

Williams, E. F., A. Ugalde, H. F. Martins, C. E. Becerril, J. Callies, M. Claret, M. R. Fernandez-Ruiz, M. Gonzalez-Herraez, S. Martin-Lopez, J. Pellegri, K. B. Winters, and Z. Zhan (in preparation). “Fiber-optic observations of internal waves and tides”. In:
E.F.W. analyzed the data, designed the figures, and wrote the manuscript. A.U., H.F.M., and C.E.B. collected the data and edited the manuscript. J.C., M.C., M.R.F.-R., M.G.-H., S.M.-L., J.P., K.B.W., and Z.Z. variously edited the manuscript, participated in formative scientific discussions, and supervised the project.

Williams, E. F., T. H. Heaton, Z. Zhan, and V. R. Lambert (2022). “Variability in the natural frequencies of a nine-story concrete building from seconds to decades”. In: *The Seismic Record* in press.
E.F.W. collected and analyzed the data, designed the figures, and wrote the manuscript. T.H.H. and Z.Z. supervised the project and edited the manuscript. V.R.L. assisted in data collection and reviewed the manuscript.

Williams, E. F., Z. Zhan, H. F. Martins, M. R. Fernandez-Ruiz, S. Martin-Lopez, M. Gonzalez-Herraez, and J. Callies (2022). “Surface Gravity Wave Interferometry and Ocean Current Monitoring With Ocean-Bottom DAS”. In: *Journal of Geophysical Research: Oceans* 127.e2021JC018375.
E.F.W. analyzed the data, designed the figures, and wrote the manuscript. H.F.M., M.R.F.-R., S.M.-L. and M.G.-H. collected the data and edited the manuscript. Z.Z. and J.C. supervised the project and edited the manuscript.

Williams, E. F., M. R. Fernandez-Ruiz, R. Magalhaes, R. Vanthillo, Z. Zhan, M. Gonzalez-Herraez, and H. F. Martins (2021). “Scholte wave inversion and passive source imaging with ocean-bottom DAS”. In: *The Leading Edge* 40.8, pp. 576–583.
E.F.W. analyzed the data, designed the figures, and wrote the manuscript. R.M. and R.V. collected the data. M.R.F.-R. and H.F.M. assisted with data analysis and edited the manuscript. Z.Z. and M.G.-H. supervised the project and edited the manuscript.

– (2019). “Distributed sensing of microseisms and teleseisms with submarine dark fibers”. In: *Nature Communications* 10.5778.
E.F.W. analyzed the data, designed the figures, and wrote the manuscript. R.M. and R.V. collected the data. M.R.F.-R. and H.F.M. assisted with data analysis and edited the manuscript. Z.Z. and M.G.-H. supervised the project and edited the manuscript.

TABLE OF CONTENTS

LIST OF ILLUSTRATIONS

LIST OF TABLES

Chapter 1

INTRODUCTION

Solid-earth and ocean dynamics are inherently multi-scale in both space and time, which poses a significant challenge for observational instrumentation. In general, permanent observatories offer high-fidelity, temporally continuous measurements spanning seconds to decades, but are costly to install and consequently spatially sparse. By contrast, temporary networks of low-cost sensors can be deployed in large numbers and with arbitrary spatial density, but are limited by factors like battery life and data telemetry to a duration of days to months. The tension between these two paradigms is particularly acute in the study of extreme events, which are both spatially and temporally localized. For example, integration of seismometers or pressure gauges into successful earthquake and tsunami early warning systems requires observing networks to both record continuously with real-time data telemetry and include dense spatial coverage in earthquake-prone regions. The trade-off between spatial and temporal coverage also forces dramatic simplifications in hazard models. For example, the ergodic assumption in engineering seismology considers that parameters like ground motion intensity and recurrence interval measured at an ensemble of locations over a short time period are representative of the long-term statistics at a single site. The validity of the ergodic assumption in ground motion prediction is impossible to test because the seismic wavefield is highly spatially aliased by contemporary seismic networks and instrumental records of damaging earthquakes are few. The same assumption is also found in stochastic ocean wave modeling and used to inform the design and operation of ships and maritime structures. Similarly, the only long-term records of wave height statistics come from sparse wave buoys and records of extreme seas are rare. Development of geophysical sensing solutions with multi-scale spatio-temporal resolution is therefore a grand challenge in contemporary seismology and oceanography.

To date, only two paradigms have been proposed for truly multi-scale geophysical monitoring: satellite remote sensing and distributed fiber-optic sensing (DFOS). Active remote sensing platforms, such as synthetic aperture radars and laser altimeters, can resolve topography and sea surface height with meter-scale horizontal resolution and near-global coverage, but have coarse time resolution with typical repeat times on the order of days. Consequently, satellite remote sensing has revolutionized our understanding of slow tectonic processes like fault creep or interseismic loading and large-scale ocean dynamics like tides or surface currents. However, both ocean and seismic waves are temporally aliased by all contemporary remote sensing methods, and observations are limited to the earth and ocean surfaces. Compared to remote sensing, DFOS only has one dimension of spatial coverage (along a fiber) and a maximum sensing range of about 100-km for a single instrument, but offers flexible spatial and temporal sampling rates as fine as 1 1/m and 1 kHz that render an unaliased image of seismic and ocean wave fields. Data telemetry occurs at the speed of light, so DFOS is possible to integrate with earthquake and tsunami early warning systems. Further, DFOS can be deployed in boreholes or at the seafloor to resolve earth structure and ocean dynamics beneath the surface; and, where existing fiber-optic infrastructure exists, DFOS deployment is logistically simple and cost-effective compared to deploying an equivalent number of point sensors.

Optical fibers are thin threads of glass, consisting of a core with a higher refractive index (as narrow as 8 microns in diameter for single-mode fiber) surrounded by a cladding with a lower refractive index. Light propagating through an optical fiber at shallow angles undergoes total internal reflection at the core-cladding interface, and so the fiber acts as a waveguide, permitting transmission of light over long distances with relatively low loss for applications like communication. DFOS refers to a class of methods that utilizes optical fibers as sensing elements. Physical processes affecting optical fibers, like changes in temperature or elastic vibrations, perturb the light traveling within, encoding valuable information about the fiber's environment. The goal of DFOS is to recover this information.

Whereas many DFOS methods exist, this thesis is concerned only with distributed acoustic sensing, or DAS, which relies on scattered light to measure elastic strain. A DAS system, often called an interrogator unit, is an opto-electronic instrument that includes a laser and a photodetector, which are connected to an optical fiber. Optical fibers contain inherent density fluctuations that locally perturb the index of refraction, causing Rayleigh scattering of transmitted light. As the DAS interrogator repeatedly probes the fiber with laser pulses, an infinitesimal amount of backscattered light propagates back down the fiber, where it is recorded at the photodetector. The accumulation of light from numerous scattering points constitutes a measurable backscatter trace, where the two-way propagation time of light permits a direct mapping to the scattering location in the fiber. Using the intensity of backscattered light in this manner to measure transmission loss with distance along the fiber is termed optical time-domain reflectometry (OTDR) and is commonly employed in fiber-optic networking. DAS, by contrast, relies on the phase of backscattered light from one pulse to the next to reconstruct changes in the optical path length, and is sometimes called phase-sensitive or coherent OTDR. Because the distribution of scattering imperfections in the cable is predetermined by the fiber manufacture, changes in the phase of backscattered light can only result from physical elongation of the fiber (strain) or changes in the refractive index. Consequently, DAS is sensitive to both elastic strain and temperature changes, which contribute both thermal expansion and a thermo-optic change in refractive index. However, at short periods (<50-100 s) temperature effects can generally be neglected, and DAS can be considered purely a dynamic strain sensor. The minimum spatial resolution of DAS is termed the gauge length, representing a finite distance along the fiber over which strain is measured, analogous to the rod length in the strain seismograph of Benioff (1935) or the arm length in a long-baseline laser strainmeter (Agnew, 1986). At present, the maximum sensing range of DAS is around 100 km, owing to transmission losses and the weak amplitude of backscatter signals. For a more comprehensive review of DAS and other DFOS methods and applications, see Masoudi and Newson (2016), Hartog (2017), Fernandez-Ruiz et al. (2020), Zhan (2020), and N. J. Lindsey and E. R. Martin (2021).

The modern development of commercial DAS systems was largely driven by oilfield applications, beginning about 15 years ago. In particular, replacing conventional wireline geophones with DAS in boreholes has permitted low-cost, time-lapse vertical seismic profiling without the need to interrupt production (Mestayer et al., 2011; Daley et al., 2013; Mateeva, Mestayer, et al., 2012; Mateeva, Lopez, et al., 2013) as well as high-resolution microseismic event detection and low-frequency strain measurements during hydraulic fracturing (Jin and Roy, 2017; Karrenbach et al., 2019). More recently, significant interest has developed in leveraging "dark" fiber–that is, unused fibers in pre-existing telecommunications infrastructure– as horizontal DAS arrays. Horizontal DAS arrays have been demonstrated for earthquake detection (Jousset et al., 2018; N. Lindsey, E. Martin, et al., 2017; H. Wang et al., 2018; Li and Zhan, 2018; Yu et al., 2019), subsurface imaging and surface wave inversion (Dou et al., 2017; J. Ajo-Franklin et al., 2019; Cheng et al., 2021; Yang et al., 2022), site characterization and ground motion studies (Spica et al., 2020; Lior et al., 2021; Yang et al., 2022), infrastructure monitoring (X. Wang, Williams, et al., 2020; Yuan et al., 2020; N. J. Lindsey, Yuan, et al., 2020; X. Wang, Zhan, et al., 2021), icequake detection (Walter et al., 2020; Hudson et al., 2021), and more. Although the instrument response of DAS as a seismic instrument has rarely been calibrated in these diverse field environments (N. J. Lindsey, Rademacher, and J. B. Ajo-Franklin, 2020; Paitz et al., 2021), the wide-ranging success of recent field experiments has demonstrated that DAS offers similar value to large nodal seismic arrays, with the significant advantage of unlimited deployment duration. Although DAS is only a single-component sensor, measuring longitudinal strain along the fiber axis, the spatio-temporal resolution of DAS yields an unaliased slice of the seismic wavefield, which motivates an image-based approach to DAS data processing. Image- and array-based filters and transforms have been applied to denoise DAS data, separate wavefield components, and detect earthquakes below the instrumental noise floor (Li and Zhan, 2018; E. R. Martin et al., 2018; Atterholt et al., 2022; van den Ende et al., 2021).

Multi-scale and permanent geophysical instrumentation is especially challenging in the oceans, owing to the added cost of marine deployments and the remote location away from power and communication networks. In particular, much less than 1% of the global network of permanent broadband seismic stations is installed at the seafloor, despite about 70% of the Earth's surface being covered by water, which greatly limits seismic raypath coverage for deep-Earth imaging and early warning implementation for offshore fault zones and tsunamis (Kohler et al., 2020). With over 1 million km of fiber-optic cables deployed across the oceans for global telecommunications, applying DAS at the seafloor is a promising solution. In 2019, three concurrent studies deployed DAS on seafloor fiber-optic cables for the first time (N. Lindsey, Rademacher, et al., 2019; Sladen et al., 2019; Williams et al., 2019), finding a complex superposition of diverse signals from ocean waves and seismic ambient noise and demonstrating the earthquake detection capabilities of seafloor DAS arrays as comparable to conventional ocean-bottom seismometers. The development of ocean-bottom DAS for seismology and oceanography applications is the principal subject of this thesis.

With the success of the DFOS concept in seismology, several alternative fiber-optic sensing methods have emerged in the past few years, specifically tailored to address the problem of limited range, which presently restricts ocean-bottom DAS to about 100-km from shore. Ultra-stable laser interferometry utilizes femtosecond precision to measure perturbations in the integrated travel-time along an entire fiber, such as from earthquakes (Marra, Clivati, et al., 2018; Marra, Fairweather, et al., 2022). Another approach, polarization-based sensing, exploits the state-of-polarization of ordinary optical communications signals, which is sensitive to stretching and bending of the fiber (Zhan et al., 2021; Mecozzi et al., 2021). Because these methods rely on transmitted light instead of backscatter, the sensing range can span thousands of kilometers across entire ocean basins. However, the minimum resolvable resolution is the distance between optical repeaters on a given cable, which is typically 50-100 km. While these methods are promising for earthquake and tsunami monitoring across the global oceans, they are not multi-scale solutions and their measurements are not yet well understood.

Overview

The first four chapters of this thesis explore the applications of fiber-optic sensing at the seafloor, for seismology and oceanography. We begin in Chapter 2 with one of the first ocean-bottom DAS datasets, recorded on a buried power cable in the Belgian North Sea in 2018. Faced with a complex superposition of seismic and ocean waves, we apply a frequency-wavenumber transform to isolate each phase based on its characteristic velocity. We demonstrate that the double-frequency relationship between seismic Scholte waves and ocean surface gravity waves requires microseism generation in-situ, consistent with the classic theory of Longuet-Higgins (1950). This dataset also includes teleseismic phases from a M8.2 deep earthquake from the Fiji region. Applying a frequency-wavenumber filter to remove the strong overprint of ocean waves and ambient noise, we isolate the principal P and S phases, demonstrating the detection capabilities of ocean-bottom DAS for global seismic monitoring even in shallow-water environments where conventional ocean-bottom seismometers struggle.

In Chapter 3, we revisit the 2018 Belgium dataset with an eye towards applications of ocean-bottom DAS in offshore engineering and hazard analysis. The small-strain shear modulus of shallow marine sediments is an essential parameter for site selection and foundation design of offshore wind turbines and platforms; yet, because the water column is opaque to shear waves, offshore shear-wave velocity profiling is challenging. Cross-correlating just over 1 hr of data, we apply a local wavefield transformation to measure multi-modal Scholte wave dispersion along the cable, and then invert for a shallow shear-wave velocity model along the cable path, demonstrating a non-invasive alternative for site characterization in coastal regions where cable networks are already present. We also identify spurious arrivals in noise cross-correlation functions originating from individual wind turbines along the cable path. With an imaging approach, we localize these arrivals to their wind turbine sources, suggesting potential for remote operational and structural health monitoring.

In Chapter 4, we turn back to ocean surface gravity waves observed by ocean-bottom DAS in shallow water. First, we demonstrate that amplitude and bandwidth of ocean wave signals in DAS data scales proportionally to seafloor pressure, though the observed amplitude differs from theoretical predictions by 1-3 orders of magnitude. We then apply ambient noise interferometry to ocean surface gravity waves recorded on a power cable in the Strait of Gibraltar, south of Spain, extracting an empirical estimate of the Green's function between any two channels in a manner analogous to seismic ambient noise. With subarray beamforming and waveform stretching, we measure time-dependent changes in the ocean wave dispersion relation along the cable, and combined with a simple model of wave-current interaction, recover an estimate of depth-averaged ocean current velocity in the along-cable direction. The 2D matrix of current velocity measurements with resolution <1 hr in time and <100 m includes a tidal flow component which agrees favorably with existing models, as well as sharp spikes in flow velocity every 12 hrs likely related to tidal bores or internal waves.

In Chapter 5, we investigate the long-period sensitivity of ocean-bottom DAS with two datasets: the dataset from a power cable in the Strait of Gibraltar previously discussed in Chapter 4, and a 30-day dataset from a telecommunications cable that runs between Gran Canaria and Tenerife in the Canary Islands, with depths in excess of 3 km. Between 75 and 200 m water depth in the Strait of Gibraltar dataset, where the cable is exposed at the seafloor, we observe transients up to 40 $\mu\varepsilon$ every 12 to 24 hours, which we interpret as temperature signals (with an equivalent amplitude of 4 K) associated with groups of internal solitary waves propagating eastward through the strait. The generation of internal waves at Camarinal Sill in the Strait of Gibraltar is a well-known phenomenon, and a synthetic aperture radar image acquired hours after the end of the 4.5-day dataset confirms that internal waves passed the cable during the experiment. On the Gran Canaria cable, we observe temperature signals up to 2 K (20 $\mu\varepsilon$), associated with internal tide dynamics on the steep submarine slope. Non-linear bore-like fronts drive cold water up the slope, dissipate, and then reform as weaker warm fronts propagating back down the slope, such that the semidiurnal variation in temperature at 2–3-km depth is as large as 0.2 K. We also isolate a signal which is proportional to the barotropic tidal pressure, including the variation of the fortnightly tide, but is an order of magnitude smaller than temperature signals at the same location. This last observation suggests sufficient sensitivity of DAS for long-period seismology, tsunami monitoring, and possibly even geodesy at the seafloor, but highlights that oceanic temperature transients may dominate solid-earth strains in fiber-optic data along slopes.

The final chapter addresses another problem of multi-scale geophysical instrumentation: temporally continuous recordings in engineering seismology. While the seismology community has largely moved towards continuous waveform recordings, many strong motion networks, such as Japan's K-net and KiK-net and including most structural health monitoring arrays in buildings, still only record triggered waveforms. In Chapter 6, we examine a 20-year record of continuous waveform data from a single accelerometer installed on the ninth floor of Caltech Hall, a reinforced concrete building on the Caltech campus which has been studied extensively since its construction in 1967. Applying a simple spectral analysis to track the temporal evolution of the building's first six natural frequencies, we find that the building has increased in apparent stiffness by as much as 10% since 2001, with greater seasonal and interannual variability up to 20%. While some of this variability is correlated with seasonal rainfall and other environmental trends, the majority is challenging to explain and suggests long-term healing of the soil-structure system, which is not the expected lifetime behavior of concrete buildings. We also document the response of Caltech Hall to almost 700 local and regional earthquakes with peak accelerations ranging over three orders of magnitude, revealing that the building softens significantly at the onset of strong motion, after which it regains stiffness over the scale of minutes following an approximately log-linear trend. These findings challenge several norms in earthquake engineering, such as the assumption of linear, time-invariant elasticity at small strains, and suggest that structural health monitoring approaches using only triggered records may be insufficient for damage detection.

A conclusion and two short appendices follow. Appendix A showcases additional DAS datasets acquired on seafloor power cables offshore, which principally confirm the interpretations of high-frequency seismic noise generation by wind turbine structural vibration in Chapter 4. Appendix B is a short, informal discussion of the challenges to DAS posed by small-scale heterogeneity, which can distort the solid-earth strain field and introduce a scale-dependent bias.

References

Agnew, D. C. (1986). “Strainmeters and tiltmeters”. In: *Rev. Geophys.* 24.3, pp. 579–624.

Ajo-Franklin, J.B. et al. (2019). “Using Dark Fiber and Distributed Acoustic Sensing for Near-Surface Characterization and Broadband Seismic Event Detection”. In: *Scientific Reports* 9.1, p. 1328.

Atterholt, J. et al. (2022). “A unified wavefield-partitioning approach for distributed acoustic sensing”. In: *Geophys. J. Int.* 228.2, pp. 1410–1418.

Benioff, H. (1935). “A linear strain seismograph”. In: *Bull. Seis. Soc. Am.* 25.4, pp. 283–309.

Cheng, F. et al. (2021). “Utilizing distributed acoustic sensing and ocean bottom fiber optic cables for submarine structural characterization”. In: *Sci. Rep.* 11.1, pp. 1–14.

Daley, T. M. et al. (2013). “Field testing of fiber-optic distributed acoustic sensing (DAS) for subsurface seismic monitoring”. In: *The Leading Edge* 32.6.

Dou, S. et al. (2017). “Distributed acoustic sensing for seismic monitoring of the near surface: A traffic-noise interferometry case study”. In: *Sci. Rep.* 7, p. 11620.

Fernandez-Ruiz, M. R. et al. (2020). “Distributed acoustic sensing for seismic activity monitoring”. In: *APL Photonics* 5.3, p. 030901.

Hartog, A. H. (2017). *An introduction to distributed optical fibre sensors*. CRC Press.

Hudson, T. S. et al. (2021). “Distributed acoustic sensing (DAS) for natural microseismicity studies: a case study from Antarctica”. In: *J. Geophys. Res.: Solid Earth* 126.7, e2020JB021493.

Jin, G. and B. Roy (2017). “Hydraulic-fracture geometry characterization using low-frequency DAS signal”. In: *The Leading Edge* 36.12.

Jousset, P. et al. (2018). “Dynamic strain determination using fiber-optic cables allows imaging of seismological and structural features”. In: *Nat. Comm.* 9.1, p. 2509.

Karrenbach, M. et al. (2019). “Fiber-optic distributed acoustic sensing of microseismicity, strain and temperature during hydraulic fracturing”. In: *Geophysics* 84.1, pp. D11–D23.

Kohler, M. D. et al. (2020). “A plan for a long-term, automated, broadband seismic monitoring network on the global seafloor”. In: *Seis. Res. Lett.* 91.3, pp. 1343–1355.

Li, Z. and Z. Zhan (2018). “Pushing the limit of earthquake detection with distributed acoustic sensing and template matching: a case study at the Brady geothermal field”. In: *Geophys. J. Int* 215.3, pp. 1583–1593.

Lindsey, N. J. and E. R. Martin (2021). “Fiber-optic seismology”. In: *Ann. Rev. Earth Planet. Sci.* 49, pp. 309–336.

Lindsey, N. J., H. Rademacher, and J. B. Ajo-Franklin (2020). “On the broadband instrument response of fiber-optic DAS arrays”. In: *J. Geophys. Res.: Solid Earth* 125, e2019JB018145.

Lindsey, N. J., S. Yuan, et al. (2020). “City-Scale Dark Fiber DAS Measurements of Infrastructure Use During the COVID-19 Pandemic”. In: *Geophys. Res. Lett.* 47.16, e2020GL089931.

Lindsey, N.J., E.R. Martin, et al. (2017). “Fiber-optic network observations of earthquake wavefields”. In: *Geophys. Res. Lett.* 44.23, pp. 11792–11799.

Lindsey, N.J., H. Rademacher, et al. (2019). “How Broadband is DAS? Two Empirical Evaluations of Instrument Response”. In: *Seismological Society of America Annual Meeting 2019 Technical Sessions*.

Lior, I. et al. (2021). “Strain to ground motion conversion of distributed acoustic sensing data for earthquake magnitude and stress drop determination”. In: *Solid Earth* 12, pp. 1421–1442.

Longuet-Higgins, M. S. (1950). “A theory of the origin of microseisms”. In: *Philos. Trans. R. Soc. A* 243.857, pp. 1–35.

Marra, G., C. Clivati, et al. (2018). “Ultrastable laser interferometry for earthquake detection with terrestrial and submarine cables”. In: *Science* 361, pp. 486–490.

Marra, G., D. M. Fairweather, et al. (2022). “Optical interferometry–based array of seafloor environmental sensors using a transoceanic submarine cable”. In: *Science* 376.6595, pp. 874–879.

Martin, E. R. et al. (2018). “A Seismic Shift in Scalable Acquisition Demands New Processing: Fiber-Optic Seismic Signal Retrieval in Urban Areas with Unsupervised Learning for Coherent Noise Removal”. In: *IEEE Signal Processing Magazine* 35.2, pp. 31–40.

Masoudi, A. and T. P. Newson (2016). “Contributed Review: Distributed optical fibre dynamic strain sensing”. In: *Rev. Sci. Instr.* 87, p. 011501.

Mateeva, A., J. Lopez, et al. (2013). “Distributed acoustic sensing for reservoir monitoring with VSP”. In: *The Leading Edge* 32.10, pp. 1278–1283.

Mateeva, A., J. Mestayer, et al. (2012). “Advances in distributed acoustic sensing (DAS) for VSP”. In: *SEG Technical Program Expanded Abstracts 2012*, pp. 1–5.

Mecozzi, A. et al. (2021). “Polarization sensing using submarine optical cables”. In: *Optica* 8.6, pp. 788–795.

Mestayer, J. et al. (2011). “Field trials of distributed acoustic sensing for geophysical monitoring”. In: *SEG Technical Program Expanded Abstracts 2011*, pp. 4253–4257.

Paitz, P. et al. (2021). “Empirical investigations of the instrument response of distributed acoustic sensing (DAS) across 17 octaves”. In: *Bull. Seis. Soc. Am.* 111.1, pp. 1–10.

Sladen, A. et al. (2019). “Distributed sensing of earthquakes and ocean-solid Earth interactions on seafloor telecom cables”. In: *Nature Communications* 10.1, p. 5777.

Spica, Z. J. et al. (2020). “Marine sediment characterized by ocean-bottom fiber-optic seismology”. In: *Geophys. Res. Lett.* 47.16.

van den Ende, M. et al. (2021). “A Self-Supervised Deep Learning Approach for Blind Denoising and Waveform Coherence Enhancement in Distributed Acoustic Sensing Data”. In: *IEEE Transactions on Neural Networks and Learning Systems*, pp. 1–14.

Walter, F. et al. (2020). “Distributed acoustic sensing of microseismic sources and wave propagation in glaciated terrain”. In: *Nat. Commun.* 11.2436.

Wang, H.F. et al. (2018). “Ground motion response to an ML 4.3 earthquake using co-located distributed acoustic sensing and seismometer arrays”. In: *Geophys. J. Int.* 213.3, pp. 2020–2036.

Wang, X., E. F. Williams, et al. (2020). “Rose parade seismology: Signatures of floats and bands on optical fiber”. In: *Seis. Res. Lett.* 91.4, pp. 2395–2398.

Wang, X., Z. Zhan, et al. (2021). “Ground vibrations recorded by fiber-optic cables reveal traffic response to COVID-19 lockdown measures in Pasadena, California”. In: *Comms. Earth Env.* 2.160.

Williams, E. F. et al. (2019). “Distributed sensing of microseisms and teleseisms with submarine dark fibers”. In: *Nature Communications* 10.1, p. 5778.

Yang, Y. et al. (2022). “Sub-Kilometer Correlation Between Near-Surface Structure and Ground Motion Measured With Distributed Acoustic Sensing”. In: *Geophys. Res. Lett.* 49.1, e2021GL096503.

Yu, C. et al. (2019). “The potential of DAS in teleseismic studies: Insights from the Goldstone Experiment”. In: *Geophys. Res. Lett.* 46.

Yuan, S. et al. (2020). “Near-surface characterization using a roadside distributed acoustic sensing array”. In: *The Leading Edge* 39.9, pp. 646–653.

Zhan, Z. (2020). “Distributed acoustic sensing turns fiber-optic cables into sensitive seismic antennas”. In: *Seis. Res. Lett.* 91.1, pp. 1–15.

Zhan, Z. et al. (2021). “Optical polarization-based seismic and water wave sensing on transoceanic cables”. In: *Science* 371.6532, pp. 931–936.

Chapter 2

DISTRIBUTED SENSING OF MICROSEISMS AND TELESEISMS WITH SUBMARINE DARK FIBERS

Williams, E. F. et al. (2019). “Distributed sensing of microseisms and teleseisms with submarine dark fibers”. In: *Nature Communications* 10.1, p. 5778.

Abstract

Sparse seismic instrumentation in the oceans limits our understanding of deep Earth dynamics and submarine earthquakes. Distributed acoustic sensing (DAS), an emerging technology that converts optical fiber to seismic sensors, allows us to leverage pre-existing submarine telecommunication cables for seismic monitoring. Here we report observations of microseism, local surface gravity waves, and a teleseismic earthquake along a 4192-sensor ocean-bottom DAS array offshore Belgium. We observe in-situ how opposing groups of ocean surface gravity waves generate double-frequency seismic Scholte waves, as described by the Longuet-Higgins theory of microseism generation. We also extract P- and S-wave phases from the 2018-08-19 M_w8.2 Fiji deep earthquake in the 0.01-1 Hz frequency band, though waveform fidelity is low at high frequencies. These results suggest significant potential of DAS in next-generation submarine seismic networks.

2.1 Introduction

One of the greatest outstanding challenges in seismology is the sparsity of instrumentation across Earth’s oceans (Lay, 2009; McGuire, Plank, and al., 2017). Poor spatial coverage results in biases and low-resolution regions in global tomography models as well as significant location uncertainty for offshore seismicity. Modern ocean-bottom seismometers (OBS) generally fall into two categories: short-period instruments (~1-5 Hz), which can record for up to a month or more, and long-period or broadband instruments (BBOBS), which often employ the same sensors as terrestrial broadband seismic stations and can operate for as long as two years (Suetsugu and Shiobara, 2014). Whereas short-period instruments are primarily used in active-source experiments, BBOBS are ideal for passive-source experiments and have been used for tomographic studies, earthquake location, and ocean wave monitoring among numerous other applications (Forsyth et al., 1998; Toomey et al., 1998; Webb, Deaton, and Lemire, 2001; Dolenc et al., 2005; Suetsugu, Shinohara, et al., 2005; Shinohara et al., 2011; Ito et al., 2012; Sugioka et al., 2012; Tan et al., 2016). However, BBOBS are expensive and limited by data telemetry and battery life except in near-shore environments (Suetsugu and Shiobara, 2014). Recent work has explored several alternatives to conventional BBOBS for offshore seismic monitoring, including free-floating robots equipped with hydrophones (Hello et al., 2011), moored surface buoys or autonomous surface vehicles for satellite telemetry acoustically linked to BBOBS (Frye et al., 2005; Berger et al., 2016), and cabled arrays of broadband sensors (Goertz and Wuestefeld, 2018). Recently, Marra et al. (2018) applied laser interferometry to convert long ocean-bottom telecommunications optical fiber links into seismic strainmeters. This work is particularly promising because repurposing the >1 million km of pre-existing trans-oceanic telecommunications cables as seismic sensors would permit rapid detection and location of earthquakes throughout the world's ocean basins. Unfortunately, the particular technique in Marra et al. (2018) is limited to measuring propagation delays integrated across an entire cable length, resulting in a single seismograph with equivalent station location uncertainty on the order of 1 km and complicated instrument response.

Distributed acoustic sensing (DAS) is an emerging technology with strong potential to form the core of next-generation submarine seismic monitoring infrastructure. A DAS interrogator unit probes a fiber-optic cable with a coherent laser pulse and measures changes in the phase of the returning optical backscatter time-series. Optical phase shifts between pulses are proportional to longitudinal strain in the fiber and can be mapped into the finite, distributed strain across a fiber segment (termed gauge length) by integration. Applying DAS technology to a fiber-optic cable effectively converts the cable into a seismic recording array with thousands of single-component channels, real-time data telemetry, and unlimited deployment duration as long as the DAS unit is powered. For about a decade, DAS has been successfully utilized in boreholes for active-source seismic profiling (Mestayer et al., 2011; Mateeva et al., 2012; Parker, Shatalin, and Farhadiroushan, 2014). Recent work with onshore trenched or conduit-installed horizontal fibers has demonstrated the ability of DAS arrays to record earthquakes and other seismic signals at local to teleseismic distances with high waveform fidelity (Jousset, Reinsch, Henninges, et al., 2017; Martin et al., 2017; Lindsey, Martin, et al., 2017; Jousset, Reinsch, Ryberg, et al., 2018; Li and Zhan, 2018; H. Wang et al., 2018; Ajo-Franklin et al., 2019; Yu et al., 2019).

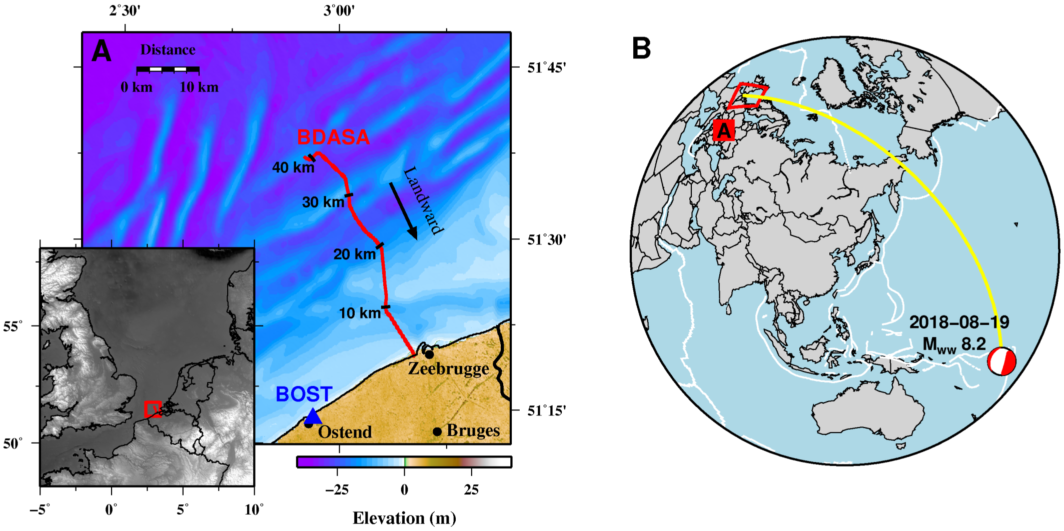

Figure 2.1: Array location. (A) Local map showing the location Belgium Distributed Acoustic Sensing Array (BDASA, red line) and nearby broadband station BOST (blue triangle), with a regional map inset. (B) World map showing the location of the array (red box), the GCMT solution for the 2018-08-19 M8.2 Fiji deep earthquake, and great circle path between the earthquake epicenter and the array (yellow).

In this paper, we demonstrate that submarine horizontal DAS arrays utilizing pre-existing ocean-bottom fiber-optic cables are similarly effective for seismological studies and can also record pressure perturbations from ocean wave phenomena. We first examine ocean surface gravity waves and associated seismic modes directly observed on an ocean-bottom DAS array offshore Zeebrugge, Belgium, which we interpret as evidence of in-situ microseism generation. We then report our observation of body waves from the 2018-08-19 M_w8.2 Fiji deep earthquake. Finally, we discuss implications for future DAS deployments in marine settings.

2.2 Results

2.2.1 Experiment Overview

The Belgium DAS array (BDASA) occupied a pre-existing ocean-bottom fiber-optic cable in the Southern Bight of the North Sea offshore Zeebrugge, Belgium (Figure 2.1). During August of 2018, the BDASA recorded continuously for nearly a month. Here, we analyze the 1-hr record containing the principal body wave phases from the 2018-08-19 M_w8.2 Fiji deep earthquake, along with ocean wave signals and microseism noise. The fiber-optic cable was originally installed to monitor a power cable for the Belwind Offshore Wind Farm (cable and fiber specifications are given in the Supplementary Material, Figure 2.S1). Cable geometry is approximately

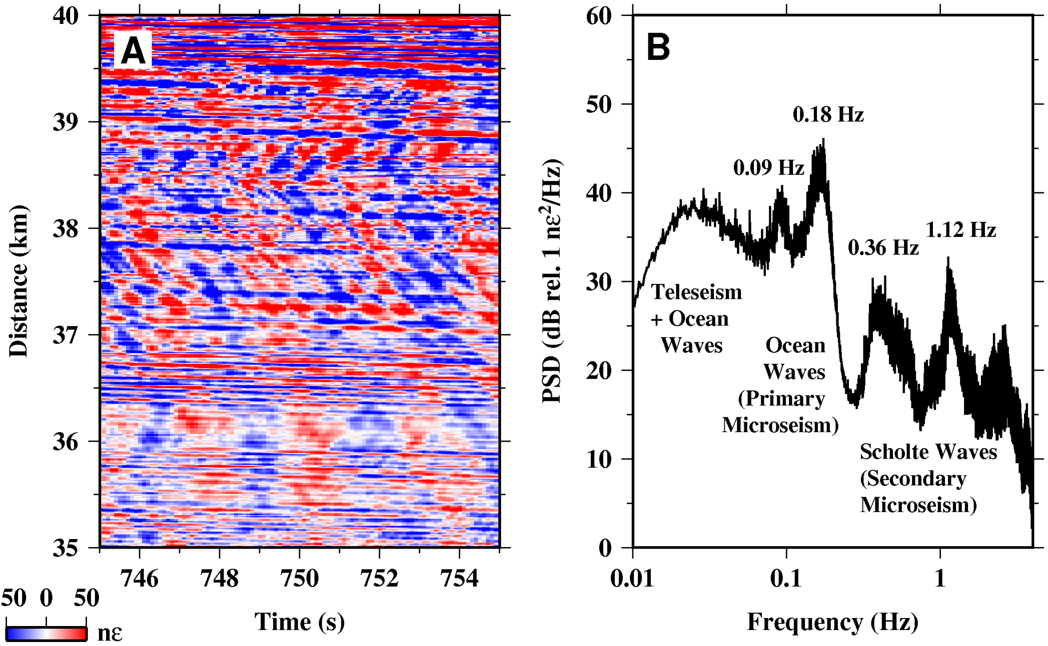

Figure 2.2: Raw DAS data. (A) Ten seconds of raw distributed acoustic sensing (DAS) data along the last five kilometers of the array illustrating the superposition of coherent signals from ocean and seismic waves propagating both landward and seaward across the array. (B) Mean power spectral density (PSD) of raw DAS strain data over the complete 1 hr record between 35–40 km (same position as (A)).

straight over four 10-km segments and is flat or shallowly dipping, except for a steep channel around 10 km and two ~15 m bathymetric ridges at ~30 and 40 km from the coast (Figure 2.1A). The cable is buried between 0.5 and 3.5 m below the seafloor in water depths shallower than 40 m. A chirped-pulse DAS system built and installed by the University of Alcala (Pastor-Graells, Martins, et al., 2016) continuously interrogated a 42-km near-shore segment of the fiber with channel spacing of 10 m, creating 4192 simultaneously recording seismic sensors (see Methods).

In Separation of Coherent Signals, we first decompose the raw BDASA data in the frequency-wavenumber domain, separating and identifying oceanic and seismic signals. In Microseism Generation, we compare our observations of ocean surface gravity and Scholte waves to the Longuet-Higgins (Longuet-Higgins, 1950) theory of double-frequency microseism generation. In Ocean Waves and Ocean Currents, we describe sea state and ocean currents across the BDASA, evident from variations in the symmetry of ocean surface gravity wave dispersion. Finally, we discuss the quality of teleseismic body waves from 2018-08-19 M_w8.2 Fiji deep earthquake, recovered from the BDASA after filtering out ocean wave and microseism signals.

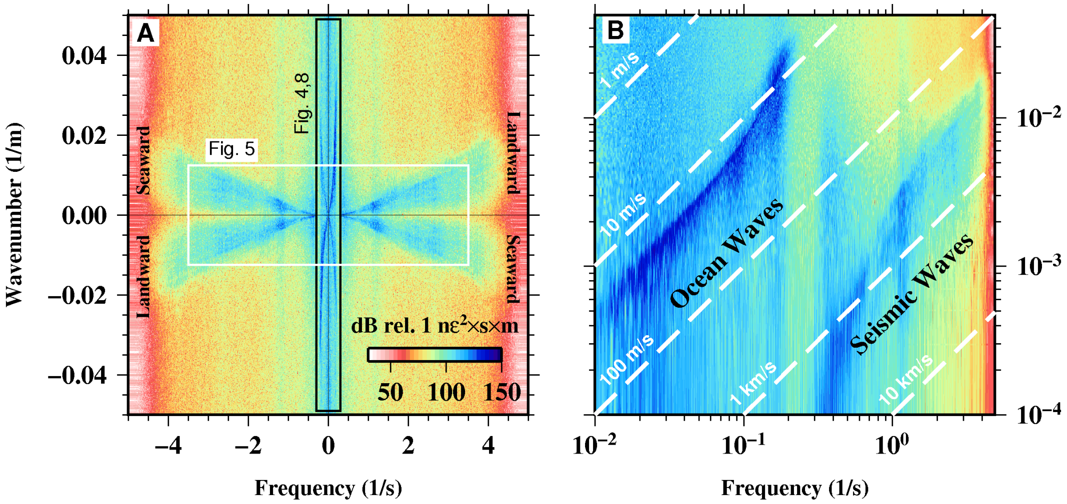

Figure 2.3: Separation of ocean and seismic waves. (A) Raw frequency-wavenumber power spectrum of 1 hr of strain data across the full 42-km array. (B) Quadrant 1 (landward-propagating waves) plotted in logarithmic space, showing coherent ocean wave energy at low frequencies and coherent seismic wave energy at high frequencies. Dashed white lines are plotted along contours of constant phase velocity ($c = f/k$).

2.2.2 Separation of Coherent Signals

In the time-domain, raw strain records from the BDASA are complicated by the superposition of several coherent signals with incoherent noise from sources such as temperature drift (Figure 2.2A). In the frequency-domain, the power spectral density (PSD) of each channel exhibits five distinct peaks, corresponding to different wave modes propagating across the array (Figure 2.2B). In order to identify and interpret the wave types comprising each peak, we apply a 2D Fast Fourier Transform from the raw strain records into the frequency-wavenumber (f-k) domain (Figure 2.3). F-k domain analysis of the raw BDASA data is possible here because the chirped-pulse DAS system exhibits negligible fading of sensitivity along the fiber, as is common in conventional DAS and which would require pre-processing at the expense of bandwidth (see Supplementary Material). Given the quasi-linear geometry of the fiber cable, no corrective algorithms or fiber sectioning methods were applied to compensate cable turns, resulting in slight smearing of energy along the wavenumber axis.

Visualization of BDASA data in the f-k domain allows identification and separation of coherent seismic and oceanic signals in each frequency band based on their characteristic phase velocities ($c = f/k$). Figure 3A shows the complete 4192-

channel, 1-hr dataset transformed into a single f-k spectrum. Energy in quadrants 1 and 3 corresponds to waves with positive phase velocities. In the coordinate system we adopted, this represents waves propagating landward across the array. Similarly, energy in quadrants 2 and 4 corresponds to waves with negative phase velocities, propagating seaward across the array. There are two distinct groups of energy in the f-k spectrum, which are easily visualized in log-log space (Figure 2.3B). Ocean waves appear at low frequencies (<0.3 Hz) with apparent phase velocity slower than ~17 m/s. Seismic waves appear at high frequencies (>0.3 Hz) with apparent phase velocity faster than ~300 m/s. Teleseismic body waves from the $M_w 8.2$ Fiji deep earthquake are not directly visible in the f-k spectrum.

2.2.2.1 Ocean Surface Gravity Waves

Surface gravity and infragravity waves are excited in oceanic waters by wind-sea interaction. Ocean surface gravity waves follow the dispersion relation $\omega^2 = gk\tanh(kH)$, where ω is angular frequency, g is gravitational acceleration, k is angular wavenumber, and H is water depth (e.g. Holthuijsen (2007)). F-k analysis of BDASA data shows strong, coherent energy packets in all four quadrants between <0.01 and 0.3 Hz (Fig 4A) with peaks at 0.09 and 0.18 Hz (Figure 2.2B). The upper edge of these packets follows the ocean surface gravity wave dispersion relation, corresponding to energy propagating axially along the cable both landward and seaward. Energy appearing below this edge represents surface gravity waves with faster apparent phase velocity that obey the same dispersion relation but are obliquely incident to the cable. For the 20-30 km cable segment shown in Figure 4A, landward-propagating ocean surface gravity waves are stronger than seaward-propagating waves.

We project the f-k spectrum into frequency-phase velocity space (f-c) using the coordinate transformation $c = f/k$, permitting better visualization of phase velocity dispersion (Figure 2.4B). In f-c space, ocean surface gravity waves exhibit coherent dispersion from faster phase velocity (~ 17 m/s) at low frequencies (~ 0.01 Hz) to slower phase velocity (~ 6 m/s) at 0.3 Hz. Ocean wave energy tapers off quickly above 0.3 Hz.

2.2.2.2 Scholte (Seismic) Waves

Seismic waves propagating faster than 300 m/s are represented in the f-k domain by symmetric fans of energy at frequencies >0.3 Hz (Figure 2.5A) with peaks at 0.36

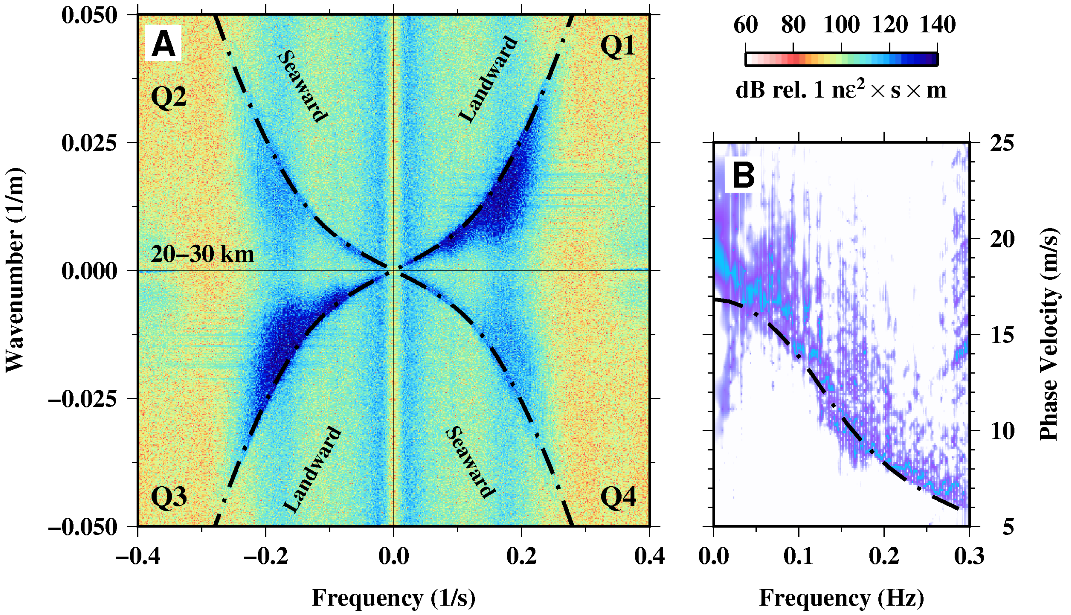

Figure 2.4: Ocean surface gravity waves. (A) Raw distributed acoustic sensing frequency-wavenumber (f-k) spectrum calculated over 10 min between 20–30 km, showing strong landward-propagating and weak seaward-propagating ocean surface gravity waves. (B) The f-k spectrum from quadrant 1 of (A) projected into phase velocity space showing coherent dispersion from ~ 17 m/s at small wavenumbers to ~ 6 m/s at 0.3 Hz (each frequency bin is normalized). Both (A) and (B) are overlaid with the theoretical dispersion curve for ocean surface gravity waves, evaluated at a water depth of 25 m (black).

and 1.12 Hz (Figure 2.2B). When projected from the f-k domain into f-c space, the high-frequency energy packet exhibits strong dispersion from phase velocities close to the compressional velocity of water (~1500 m/s) at 0.36 Hz to an asymptotic velocity of ~300 m/s above 1 Hz (Figure 2.5B). This is consistent with the expected dispersion relation of Scholte waves along the sediment-water interface, which follows the compressional velocity of water at low frequencies and the shear-wave velocity of the shallow sediment layer at high frequencies (Rauch, 1980). As for ocean waves, the low-velocity edge of the f-k energy packets in each quadrant represents Scholte waves propagating axially along the cable. Energy appearing at faster apparent phase velocities represents Scholte waves obliquely incident to the cable. We note that the 0.3-3.5 Hz Scholte waves are observed in the 550 s of data preceding the arrival of the first P-wave phases from the Fiji earthquake and therefore must be an independent, local phenomenon.

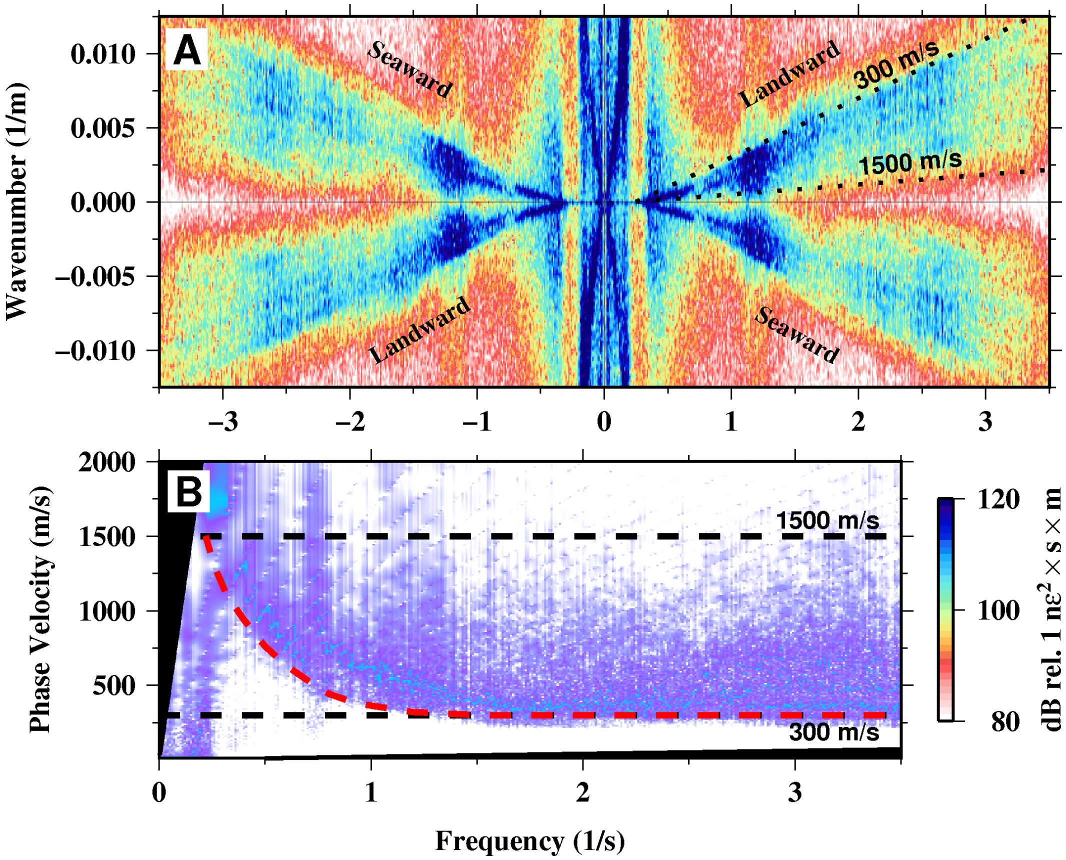

Figure 2.5: Scholte (seismic) waves. (A) Raw distributed acoustic sensing frequency-wavenumber (f-k) spectrum calculated over 1 hr between 35-40 km, showing symmetric landward- and seaward-propagating Scholte waves between 0.3-3.5 Hz. (B) The f-k spectrum from quadrant 1 of (A) projected into phase velocity space showing coherent dispersion from ∼ 1500 m/s at 0.36 Hz to ∼ 300 m/s above 1 Hz (each frequency bin is normalized). Both (A) and (B) are overlaid with contours of constant velocity at 1500 and 300 m/s (black), and an approximate dispersion curve is hand-drawn in (B) (red).

2.2.3 Microseism Generation

Globally, seismograms record broadband seismic noise with peaks around 14 and 7 s period, termed microseisms, which have long been attributed to ocean wave sources (e.g. Kedar et al. (2008)). The longer period (lower frequency) peak is commonly referred to as primary microseism, while the shorter period (higher frequency) peak is called secondary microseism. Source locations of primary microseism appear to be restricted to coastal areas, with seismic noise excited by direct loading of the seafloor where gravity waves impinge on shallow coastal waters (Haubrich and McCamy, 1969; Cessaro, 1994). Source locations of secondary microseism, however, include both near-shore and deep-water environments (Cessaro, 1994; Bromirski, Duennebier, and Stephen, 2005), and the amplitude of the secondary microseism peak has not been tied directly to coastal ocean wave conditions (e.g. Bromirski (2001)). While the relative amplitude and central frequencies of the microseism peaks vary by region and sea state, the double-frequency relationship between primary and secondary microseism is universal and a subject of continued research. Here, we argue that ocean surface gravity waves and Scholte waves observed on the BDASA at double-frequency (0.18 and 0.36 Hz respectively) together represent in-situ microseism generation following the theory of Longuet-Higgins (1950).

2.2.3.1 Primary Microseism and its Depth Dependence

Based on our f-k analysis above, the 0.18 Hz peak in Figure 2.2B corresponds to ocean surface gravity waves propagating across the BDASA. Because the cable is buried at a depth of 0.5-3.5 m, the BDASA is only mechanically coupled to the water body above through the intermediary shallow sediment layer, so ocean waves cannot be observed directly. Instead, ocean waves signals observed on the BDASA are poroelastic strains in the solid earth induced by the pressure field of ocean waves propagating above, hence primary microseism generated in-situ by ocean wave loading. Common observations of primary microseism on terrestrial seismic networks (e.g. Cessaro (1994)) constitute diffuse seismic energy radiated into the far-field, whereas here we observe the primary microseim source directly.

To test this interpretation, we compare the variation in amplitude of the 0.18 Hz peak to the expected seafloor pressure under ocean surface gravity waves along the cable depth profile. The strength of ocean surface gravity waves decays rapidly with depth, which is why source regions of primary microseism are constrained to the coast. Invoking linear wave theory, the magnitude of the pressure perturbations at the seafloor beneath a surface gravity wave scales with angular wavenumber k and water depth H as $p_d \propto \text{sech}(kH)$ (e.g. Holthuijsen (2007)). To evaluate p_d, we iteratively solve the implicit dispersion relation for ocean surface gravity waves, $\omega^2 = gk\tanh(kH)$, to obtain $\omega(k)$, and then calculate a theoretical p_d as a function of distance and depth using the cable profile. In order to determine a scaling factor between seafloor pressure and fiber strain, we fit the Fourier amplitude observed on the BDASA at 0.18 Hz as a linear function of theoretical p_d (see Supplementary Material), to produce the model plotted in Figure 6. We observe a good correspondence between the observed and modeled Fourier amplitude at 0.18 Hz with both water depth and distance along the cable (Figure 2.6). To leading

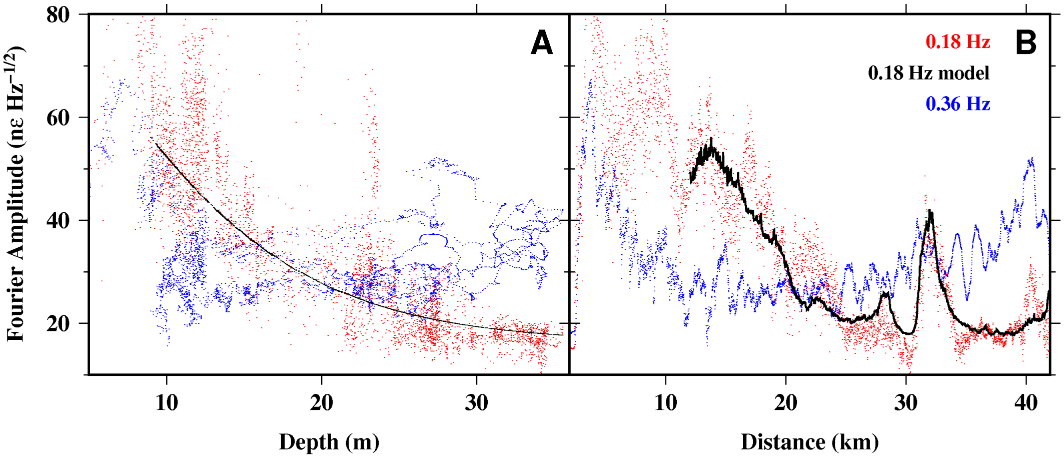

Figure 2.6: Depth and distance scaling. (A) Fourier components of the raw distributed acoustic sensing strain spectrum at 0.18 (primary microseism, red) and 0.36 Hz (secondary microseism, blue) calculated at each channel plotted versus water depth. Also shown is the model of 0.18 Hz noise as a function of theoretical seafloor pressure described in the text (black). (B) Same as (A) but plotted with distance along the fiber.

order, then, 0.18 Hz energy observed on the BDASA is proportional to pressure applied by ocean surface gravity waves at the seafloor, confirming our interpretation of primary microseism generation.

2.2.3.2 Secondary Microseism by Ocean Wave Interaction

Longuet-Higgins (1950) first proposed a mechanism for the double-frequency nature of microseisms, whereby nonlinear interaction of opposing groups of surface gravity waves at one frequency generates a depth-invariant pressure term of second-order magnitude which oscillates at twice the frequency of the surface waves. Hasselmann (1963) expanded this theory to demonstrate that appreciable microseisms are excited only by components of the ocean pressure field that match the phase velocities of the seismic modes of the coupled water-seabed system. In the simplest case, the phase velocity of Longuet-Higgins's second-order pressure term scales as $c = 2\omega/||\vec{k}_1+\vec{k}_2||$ for two plane surface gravity waves with phase $\vec{k}_1 \cdot \vec{x} - \omega t$ and $\vec{k}_2 \cdot \vec{x} - \omega t$. Hence, for opposing waves (when $\vec{k}_1$ is close to $-\vec{k}_2$), c approaches seismic velocities.

Based on these theories, we assert that the 0.36 Hz Scholte waves discussed above represent secondary microseism associated with the 0.18 Hz opposing surface gravity wave groups. Unlike the 0.18 Hz energy peak, the 0.36 Hz peak observed in the BDASA PSD is almost invariant with depth and is not adequately described by the pressure-depth scaling of ocean surface gravity waves (Figure 2.6A). Instead, the Fourier amplitude at 0.36 Hz decreases over the first 12-15 km of the array and then increases gradually with distance out to 40 km (Figure 2.6B). Therefore, Scholte waves at 0.36 Hz cannot be the product of direct loading by ocean surface gravity waves.

Longuet-Higgins (1950) predicts that the amplitude of the secondary pressure term generated by non-linear wave interaction is proportional to the product of the amplitudes of the two opposing ocean wavefield components. Hence, we expect to observe the strongest Scholte waves where seaward- and landward-propagating ocean surface gravity waves are of similar strength and the weakest Scholte waves where seaward- and landward-propagating ocean waves are of significantly different strengths. To test this property, we plot directional spectra for both ocean surface gravity waves and Scholte waves (Figure 2.7). For each wave type, theoretical dispersion curves are constructed for waves with different incident azimuths. For each of four 10-km quasi-linear segments along the fiber, we then take the mean f-k spectral amplitude interpolated along each dispersion curve to form the polar plots in Figure 7 (see Supplementary Material). The cable segment in water depths $<$ 10 m is neglected in this analysis, as the PSD of this region is saturated by incoherent energy across a broad band, likely associated with shoaling of ocean waves.

The relative strength of seaward- and landward-propagating ocean surface gravity wavefield components is most similar for the 30-40 km segment, slightly less equal for the 10-20 km segment, and most disparate for the 20-30 km segment (Figure 2.7A). As predicted by this scaling, the absolute strength of the Scholte wavefield components (in both quadrants) is greatest for the 30-40 km segment, less for the 10-20 km segment, and smallest for the 20-30 km segment (Figure 2.7B). Note that because Longuet-Higgins's second-order pressure term does not decay with depth, this result is dependent only on the relative strengths of ocean wavefield components shown in Figure 7A, and not their absolute strength.

For Scholte (similar to Rayleigh) waves, the theoretical azimuthal sensitivity of DAS is approximately $cos^2(\theta)$, where $\theta = 0$ is along the axis of the fiber, in the limit that the wavelength is much longer than the gauge length used by the DAS system (Martin, 2018). The directional spectra shown in Figure 8B all approximately follow a cos^2 shape, suggesting that the azimuthal distribution of Scholte wave energy is relatively diffuse (or isotropically propagating) along most of the fiber. The diffuse nature of the secondary microseism wavefield is further evidence that these waves

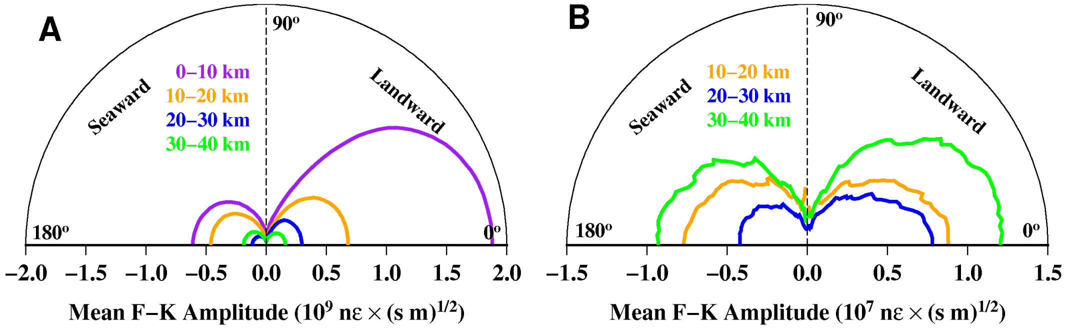

Figure 2.7: Directional spectra. (A) Mean frequency-wavenumber (f-k) amplitude of ocean waves (primary microseism) as a function of azimuth calculated between 0.05-0.25 Hz using the ocean surface gravity wave dispersion relation for each of four 10-km array segments. (B) Mean f-k amplitude of Scholte waves (secondary microseism) as a function of azimuth calculated between 1.5-3.5 Hz assuming a true phase velocity of 300 m/s and no dispersion across this frequency band.

must be generated in-situ and also offers a direct observation of the radiation pattern of secondary microseism at its source.

Within this framework, we are unable to describe the 1.12 Hz peak (Figure 2.2B) and associated high-frequency Scholte wave energy observed up to 3.5 Hz (Figure 2.5A). The 1.12 Hz peak likely does not represent secondary microseism associated with a pair of opposing surface gravity wave groups with dominant frequency of 0.55 Hz, as no 0.55 Hz peak is observed in our data. However, the strength of ocean waves observed at the seafloor attenuates strongly with decreasing wavelength, so it is possible that 0.55 Hz ocean waves do exist. The 1.12 Hz peak could also correspond to external environmental noise from an unknown (potentially anthropogenic) source. Alternatively, it could represent a resonant mode of the coupled sediment-water system.

2.2.4 Ocean Waves and Ocean Currents

Beyond their implications for microseism generation, ocean surface gravity waves observed on the BDASA demonstrate the potential of ocean-bottom DAS for investigations in physical oceanography. Computing f-k spectra across different segments of the cable, we can distinguish spatial variations in the intensity of landward-propagating versus seaward-propagating ocean surface gravity waves in order to interpret sea state. For example, on the 20-30 km segment (Figure 2.4A) landward-propagating waves are stronger than seaward-propagating waves, while on the 30-40 km segment (Figure 2.8A) landward-propagating and seaward-propagating waves are of similar strength (see also Figure 2.7A). Because the strength of seaward-propagating waves is greater on the outermost segment of the cable than on the next segment closer to shore, we infer that some of the seaward-propagating waves must be local reflections from the bathymetric ridge at 30 km. Inboard of the 30-km ridge, we observe the ratio of seaward-propagating to landward-propagating wave energy decrease systematically, which is consistent with the expectation that all seaward-propagating ocean waves observed on the BDASA are generated by reflection from the sloping seabed approaching the coast. While the extent of our interpretation is limited by the 1-hr record length of BDASA data, the framework for ocean wave analysis demonstrated here would be easily applicable to monitor temporal variations in sea state over tidal to annual scales.

Because of the large number of channels and high-sample rate on the BDASA, f-k domain resolution is sufficiently fine to distinguish small perturbations in surface gravity wave dispersion associated with ocean currents. For example, the f-k spectrum of the last 10 km segment (30-40 km) is asymmetrical and evolves over the 1-hr record (only the last 10-minute window is shown in Figure 2.8). On this segment, landward-propagating waves appear faster than sea-ward propagating waves, as the result of an ocean current with a component of flow in the landward direction along the array (Figure 2.8B,C). We fit the dispersion asymmetry with a mean-flow correction to the dispersion relation $(\omega - Uk)^2 = gk\tanh(kH)$, which describes the first-order effect of surface gravity waves propagating in a current, where U is the apparent velocity of the current along the cable (as above, ω is angular frequency, k is angular wavenumber, g is gravitational acceleration, and H is water depth). Over the 1-hr record, the strength of the observed current increases gradually from 0.1 to 0.5 m/s apparent velocity in the landward direction. Contemporary methods of ocean current measurement are largely limited to either high-frequency radio observation of surface currents (Chapron, Collard, and Ardhuin, 2005; Paduan and Washburn, 2013) or in-situ observation of current-depth profiles using spatially-sparse moorings, drifters, or ship-board instruments (MODE Group, 1978; Lumpkin and Pezos, 2007; Wunsch, 2015). Our observation of spatio-temporal variations in current speed is significant because it suggests potential application of ocean-bottom DAS to in-situ measurement and monitoring of ocean currents by exploiting models of wave interaction with heterogeneous currents (e.g. Huang et al. (1972)) to recover high-resolution spatial variations in current speed along an array.

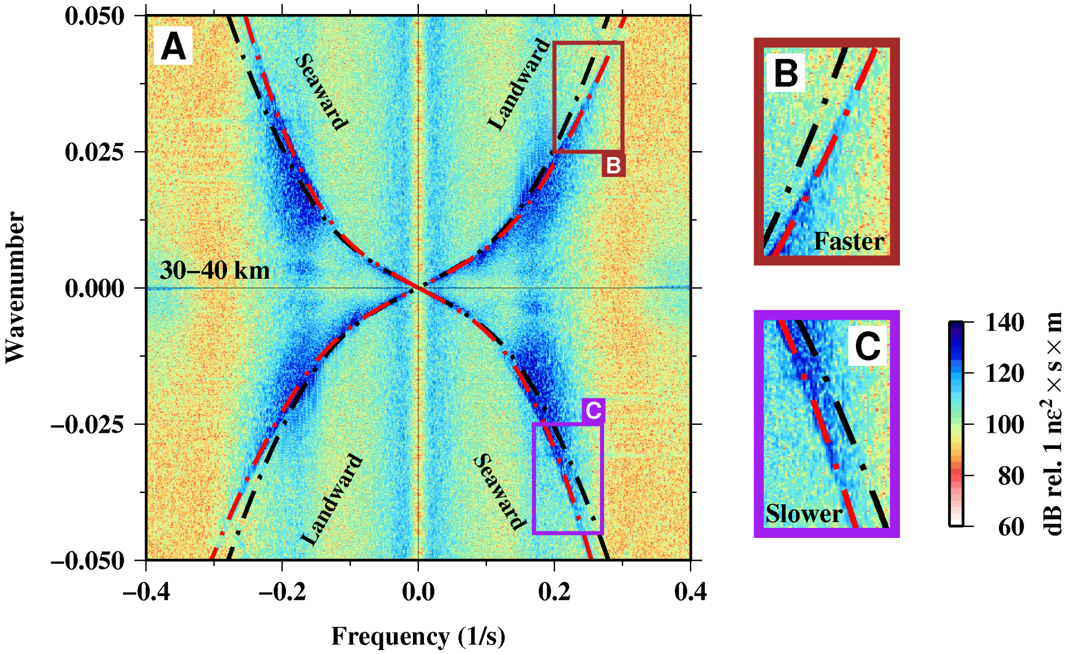

Figure 2.8: Ocean currents. (A) Raw distributed acoustic sensing frequency-wavenumber spectrum calculated over 10 min between 30-40 km, showing asymmetrical dispersion due to an ocean current. (B),(C) Insets to (A) illustrating how landward-propagating ocean waves exhibit faster velocities than seaward-propagating ocean waves. The theoretical dispersion curves for ocean surface gravity waves are plotted with (red) and without (black) the effect of a mean-flow current.

2.2.5 2018-08-19 $M_w 8.2$ Fiji Deep Earthquake

Rapid, accurate measurement of body wave travel-times is an essential goal of next-generation broadband marine seismology (Lay, 2009) and has motivated many recent advances in ocean-bottom seismic instrumentation (e.g. Hello et al. (2011)). Ocean-bottom DAS arrays are an ideal technological solution because they offer real-time telemetry and are intrinsically synchronized (all channels are interrogated with the same unit, thus avoiding any differential clock drift across the array), neither of which are easily achievable features of OBS networks. Northern Europe is a seismically quiescent area, so no local or regional seismic events were recorded. However, the BDASA captured teleseismic body waves from a $M_w 8.2$ deep earthquake in the Fiji-Tonga area on August 19, 2018 (Figure 2.1B). Teleseisms arrived from an epicentral distance of 146.7^o (>16,300 km), at a back azimuth of 358.5^o (27.6^o oblique to the mean fiber azimuth of 330.9^o). Because the 2018-08-19 Fiji event occurred at a depth of 600 km, only weak surface waves were excited and hence could not be analyzed.

Teleseismic body waves from the Fiji earthquake are close to vertically incident and expected to arrive almost simultaneously along the array, hence appearing at wavenumbers lower than can be resolved across a few kilometers aperture. In order to isolate teleseisms from ocean surface gravity and Scholte waves, we apply a 2D band-pass filter in the f-k domain between 0.001-1 Hz and 0-0.002 m^{-1} in the first and third quadrants (corresponding to energy propagating landward across the array from the north/west; Figure 2.S2), stack waveforms across a 5-km array segment to form a beam trace, and finally apply a range of bandpass filters to the beam trace to produce the BDASA waveforms shown in Figure 9 (see Supplementary Material). We compare the BDASA beam trace to nearby broadband seismometer BOST (30-50 km south of BDASA), after rotating the horizontal channels into the mean azimuth of the BDASA and bandpass filtering.

At high frequencies (>0.1 Hz), we recover the PKP phase (~550 s) and its associated pPKP + sPKP depth phases (~690 s), the travel times of which correspond well to those recorded on BOST (Figure 2.9). The envelopes of the recovered P phases (not shown) are similar to those from BOST, although the they show low-to-moderate waveform fidelity (mean correlation coefficient of 0.25; Figure 2.S4). Hence, the polarity of the first P-wave arrival recovered from the BDASA is not reliable across parts of the array. Spatially variable P waveforms may be physical, however, as high frequency waves can be strongly affected by near-surface structures and the water layer. At low frequencies (<0.15 Hz), the background noise is substantially stronger, but we still recover a complex S wavetrain, which exhibits moderate-to-high waveform fidelity when compared with BOST (mean correlation coefficient of 0.6; Figure 2.S5). Recovered P and S waveforms are both coherent along the length of the array (Figure 2.S3).

Because the BDASA measures strain across a 10-m gauge length whereas BOST measures particle velocity at a single point, theoretical amplitudes are approximately proportional by a factor of the apparent horizontal slowness for wavelengths longer than twice the gauge length (H. Wang et al., 2018). For the Fiji earthquake, the ratio of BDASA strain amplitude to BOST particle velocity amplitude does not yield reasonable apparent velocities for the observed phases across any band. Hence, we infer that strain-transfer coupling between the solid earth and the BDASA fiber, a consequence of the fiber casing and installation, is complex (Figure 2.S1).

While a $M_w 8.2$ deep earthquake is a rare and particularly large event, body wave energy observed in Belgium at 146.7^o epicentral distance is lower in spectral am-

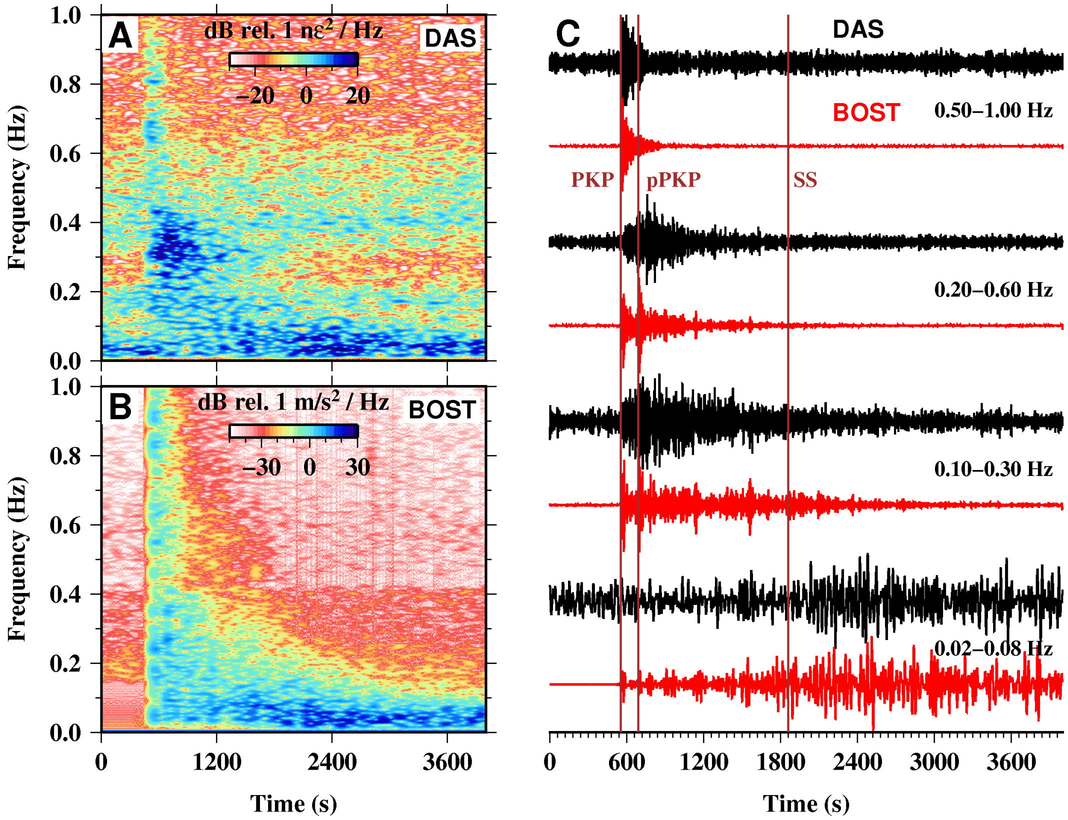

Figure 2.9: Teleseismic waveforms. (A) Spectrogram of power spectral density (PSD) over time for the f-k filtered and stacked distributed acoustic sensing (DAS) beam trace (black in (C)), showing strong energy between 0-1 Hz around the arrival of the PKP phase around 550 s and below 0.1 Hz following the arrival of the SS phase around 1860 s. (B) Spectrogram for the rotated BOST channel (red in (C)), showing the same major features. (C) Stacked DAS beam trace (black) filtered to various bands between 0.02 and 1 Hz compared with amplitude-normalized particle velocity from broadband station BOST rotated into the mean azimuth of the DAS array (red).

plitude than would be expected for regional earthquakes ($< 1^o$ epicentral distance) greater than $\sim M3.5$ (Figure 2.S6). Hence, BDASA clearly exhibits teleseismic and regional seismic monitoring capability, as both P-wave and S-wave travel-times can be recovered across a broad band, and S-wave polarity is robust over the frequencies of interest to global seismology.

2.3 Discussion

We have presented and analyzed our observations of seismic and ocean waves on an ocean-bottom DAS array offshore Belgium, demonstrating that DAS arrays utilizing existing ocean-bottom fiber optic installations can offer high value seismographic and oceanographic data products. In particular, we recovered both P- and S-phases from the 2018-08-19 Fiji deep earthquake, though only S-waves exhibited moderate-to-high waveform fidelity. While we were unable to recover robust polarity of high-frequency P-phases, we can expect that ocean-bottom DAS arrays in deep water would have much lower detection thresholds for seismic signals than observed here, as has been demonstrated for OBS (e.g. Webb and Crawford (2010)). For an ocean-bottom DAS array, the noise floor can be considered as the superposition of instrumental noise from the DAS interrogator unit and fiber, temperature noise from variations in pore fluid temperature, pressure noise from ocean waves, and seismic noise. The aggressive filtering procedure we applied to recover teleseismic waveforms was necessitated to remove environmental signal, not instrument noise, as coherent signals of physical origin were observed across the full band of interest (0.01-5 Hz). Onshore studies with DAS arrays have found that instrument noise is approximately inversely proportional to frequency with a noise floor no higher than 1 $\mu\varepsilon/\mathrm{Hz}^{1/2}$ at 1 Hz (Williams et al., 2018). Laboratory experiments show that in a stable temperature environment, DAS systems can exhibit a noise floor below 100 p$\varepsilon/\mathrm{Hz}^{1/2}$ at 1 Hz (Costa et al., 2018). On a DAS array, a temperature perturbation of 1 mK is indistinguishable from a 10 nε strain, so high-frequency temperature fluctuations along the fiber can contribute spurious signals. Water-bottom temperatures may vary on the order of 1 K at tidal periods in the near-shore environment; however, such variability attenuates strongly with depth and is inversely correlated to frequency (e.g. Kaplan et al. (2003) and MacDonald et al. (2005)). Consequently, instrumental and temperature noise are not limiting factors for most seismological applications, as seen here. In deep water settings, the magnitude of pressure oscillations beneath ocean surface gravity waves, the primary environmental noise which dominates BDASA data between 0.01 and 0.26 Hz, decays exponentially with depth. Therefore, the shallow-water setting of the BDASA actually represents a ‘worst case’ environment for recording teleseismic events (Webb, 1998; Webb and Crawford, 2010), and thus our ability to recover both P- and S-phases is particularly significant.

Compared to traditional OBS deployments, another advantage of DAS is the number and density of stations. Utilizing hundreds of stations from any segment of the array we were able to apply array-based processing in order to distinguish seismic and ocean signals based on their phase information. So-called “large N” deployments permit low detection thresholds for small earthquakes, precise location of earthquakes, low uncertainty in travel-time measurements, and high-resolution imaging studies (Rost and Thomas, 2002; Nakata et al., 2015; Li and Zhan, 2018). Further, we have demonstrated that large-N ocean-bottom networks open up new possibilities in studying ocean wave phenomena and microseism generation. The vast majority of studies examining the physics of ocean microseism generation have been limited to remote observation of radiated energy on terrestrial broadband networks (Friedrich, Krueger, and Klinge, 1998; Bromirski, 2001; Kedar et al., 2008; Traer et al., 2012). The few studies utilizing ocean-bottom instrumentation to correlate ocean-wave phenomena with microseism in-situ have been restricted by small network size, effectively resulting in measurements of microseism direction and intensity at a single point with or without simultaneous ocean wave information, and have had mixed success in validating theoretical models (Bradner, Doods, and Foulks, 1965; D. Goodman et al., 1989; Dorman et al., 1993; Kibblewhite and Wu, 1993; Nye and Yamamoto, 1994; Bromirski, Duennebier, and Stephen, 2005). Simultaneous observation of ocean pressure variations and seismic noise across several thousand channels on ocean-bottom DAS arrays of arbitrary geometry permits reconstruction of the full surface gravity wave and Scholte wave fields, as shown here, and, with the addition of a time-lapse component to future surveys, offers a leap forward in our ability to study microseism and its source processes.

However, several technological challenges still remain before DAS systems can complement or even replace BBOBS on a global scale. Foremost is the axial (single-component) directional sensitivity of DAS. Though work with helically wound optical fibers offering multi-component DAS sensitivity is underway (Hornman et al., 2013), modern BBOBS already provide four-component (three-component + pressure) recording capability with the same state-of-the-art instruments used in terrestrial networks. We noted that teleseismic waveforms recovered from the BDASA did not exhibit coherent strain amplitude when compared with particle velocity at BOST, suggesting that the mechanics of strain transfer from the solid earth across the cable housing and into the optical fiber are complex and deserve further study (Mellors et al., 2018). In the laboratory, DAS exhibits a linear frequency response, resulting in correct amplitude and distortion free waves (Jousset, Reinsch, Ryberg, et al., 2018; Lindsey, Rademacher, et al., 2019; Yu et al., 2019), hence amplitude preservation may be currently limited by installation conditions and not by the DAS technology itself. Finally, ocean-bottom DAS deployments are not presently possible in remote oceanic locations. Most commercial DAS systems and laboratory measurements claim operation across up to 50 km of fiber, with sensitivity decreasing along the fiber due to optical attenuation. With the use of more complex pulse formats or distributed amplification, the sensing range can be extended to 70-100 km (Fernandez-Ruiz, Martins, Pastor-Graells, et al., 2016; Martins et al., 2015; Pastor-Graells, Nuño, et al., 2017) with a more even distribution of sensitivity along the fiber, while still using a standard telecom fiber installation. In principle, longer distances can be achieved with complex dedicated fiber installations and power supply along the fiber link (via use of optical repeaters (Kim et al., 2001; Gyger et al., 2014) and/or multiple stage distributed amplification (Z. N. Wang et al., 2014; Martins et al., 2015)), but the impact on the cost and DAS sensitivity means that such systems are not currently practical.

Supplementary Material

Chirped-pulse Distributed Acoustic Sensing

A chirped-pulse DAS (Pastor-Graells, Martins, et al., 2016) was used for the interrogator system, assisted by first order co-propagating Raman amplification (Pastor-Graells, Nuño, et al., 2017). In comparison with conventional DAS systems, chirped-pulse DAS offers high signal-to-noise ratio (SNR) and low variations in sensitivity along the fiber (Pastor-Graells, Nuño, et al., 2017; Costa et al., 2018; Fernandez-Ruiz, Martins, Costa, et al., 2018). The key of its performance lies in the use of a linearly chirped probe pulse for the time-domain interrogation. Temperature or strain perturbations around the fiber affect its refractive index, which in turn slightly alters the central wavelength of the propagating light. An appropriately high linear chirp in the probe pulse (i.e., that inducing a spectral content much higher than the spectral content of the transform limited pulse) induces a local wavelength-to-time mapping arising from the temporal far-field condition (J. Goodman, 1994). Hence, variations in the central wavelength of the propagating light translate into temporal shifts in the trace at the particular location of the perturbation. The perturbation is then quantified by a time-delay estimation process via local trace-to-trace correlations over temporal windows similar to the probe pulse width.

The principle of operation of chirped-pulse DAS substantially improves the performance of the sensor over conventional DAS schemes. First, strain perturbations can be properly quantified by simply using direct detection. This contrasts with the conventional case, in which it is necessary to detect the trace optical phase for that purpose. Avoiding phase detection brings important advantages. Coherent detection imposes stringent requirement in the coherence length of the laser source, as it limits the DAS operation range due to the need for beating with a local oscillator. In chirped-pulse DAS, the coherence length of the probe laser can be relaxed, in principle simply requiring it to be substantially higher than the pulse width, with almost no detrimental effect on the acoustic SNR (Fernandez-Ruiz, Pastor-Graells, et al., 2018). Polarization fading is not observed in chirped-pulse DAS (due to use of direct detection). More importantly, sensitivity of conventional DAS completely fades in certain points along the fiber (acoustic SNR <1 in up to 6% of fiber locations considering a healthy-SNR optical trace) due to the impossibility of maintaining the phase reference in low intensity trace regions caused by its interferometric nature (Gabai and Avishay, 2016). Those blind spots need to be corrected using complex post-processing techniques or multi-wavelength measurements (Chen, Lui, and He, 2017), typically at the expense of sensing bandwidth and higher measurements times. Chirped-pulse DAS, however, shows no fading sensitivity, enabling the raw strain signal as measured by the DAS to be directly processed without using any denoising/smoothing algorithm. This steady sensitivity is particularly beneficial for the subsequent 2D processing applied to isolate seismic events from other sources, since all points are captured with similar noise/sensitivity along the whole fiber length (>40 km) (Fernandez-Ruiz, Martins, Costa, et al., 2018).

In addition, signal attenuation due to fibre loss is greatly mitigated in our scheme with the use of distributed Raman amplification. Note that in Pastor-Graells, Nuño, et al. (2017), the fiber trace optical power fluctuation along a 75-km link is kept below 7 dB, as opposed to the ~28.5 dB attenuation expected without distributed amplification (28.5 dB =75km×2×0.19 dB, using 0.19 dB/km as typical standard single mode fiber loss; note that roundtrip DAS attenuation is twice that of the fiber transmission losses). In this study, we observed DAS trace power fluctuations lower than 3 dB along the 42-km fiber. This is in contrast with the optical signal attenuation of ~16 dB (= 42km×2×0.19dB/km) expected without distributed amplification.

The optical resolution (or gauge length) and channel spacing of the employed sensor were both 10 m (equivalent to one seismometer placed very 10 m, measuring distributed strain over a length of 10 m), totaling 4192 channels over 42 km. Each channel was sampled at 1 kHz and later downsampled to 10 Hz in order to reduce the dataset size.

Fiber-optic cable

The BDASA occupied an optical fiber deployed within a power cable to the Belwind Offshore Wind Farm, offshore Belgium. The fiber is internally coupled with fillers to the cable's armor bedding (Figure 2.S1A). The cable consists of 3 core cables, an

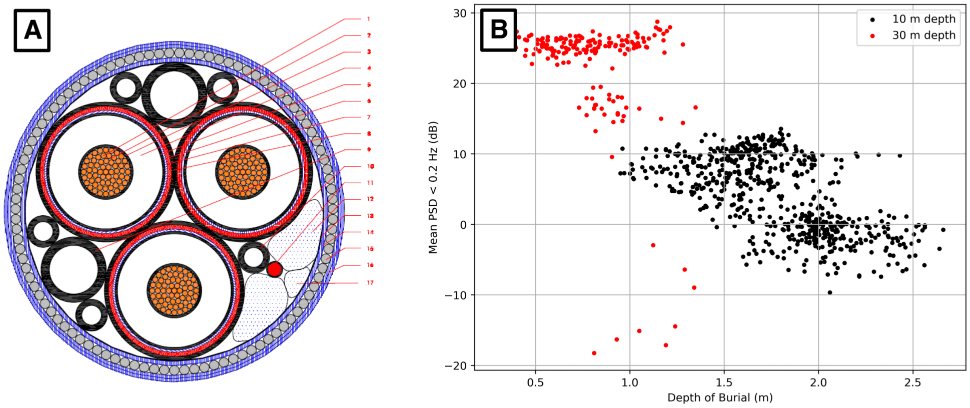

Figure 2.S1: Cable coupling. (A) Schematic cable cross-section. Number 11 (red) indicates the position of the fiber. (B) Scaling of observed ocean wave energy with depth of burial for each of two water depths (10 m in black, 30 m in red).

optical fiber, and a filler in polypropelene (PP) yarn. The outer serving in PP wraps the layer of round galvanized steel wires and is the layer that has direct contact with subsea sediments. Hence, vibrations that are passed from sediment into the fiber propagate through a frictional contact between adjacent components. The fiber and core cables are helically inserted into the cable.

Burial of the cable further attenuates vibrations generated by ocean gravity waves, as described in Godfrey, WO2018154275A1, 2018-02-09. This is clearly shown in Figure 2.S1B, where the strength of observed ocean wave energy in the 0.01-0.2 Hz band decreases as a function of increasing burial depth. Figure 2.S1B plots channels at constant water depth, as the change in ocean-bottom pressure associated with increasing water depth is a much stronger signal across the array.

Increasing depth of burial also attenuates temperature variations from the ocean water above. However, temperature variations within the cable due to changing electric load can exceed 1 K. We do not analyze the effect of temperature in-situ.

0.18-Hz model

In order to fit depth-dependence of noise at the primary microseism peak (0.18 Hz), we first calculate a theoretical curve for the pressure at the seafloor under an ocean surface gravity wave as a function of seafloor depth. Here, we consider only p_d, the dynamic pressure due to wave propagation. The pressure profile with water depth for ocean surface gravity waves over a flat bed is given as

$$p_d(t,x) = \rho g \eta(t,x) \frac{\cosh(k(H+z))}{\cosh(kH)}$$

where ρg is the specific weight of water, $\eta(t,x)$ represents the sea-surface height along the propagating surface gravity wave, H is depth to the seafloor, and k is angular wavenumber (Holthuijsen, 2007). Evaluated at the seafloor ($z = -H$), we find: $p_d(x) \propto \mathrm{sech}(k(x)H(x))$. In order to evaluate this expression, we solve the implicit dispersion relation for surface gravity waves ($\omega^2 = gk\tanh(kH)$) to find angular wavenumber $k = k(x)$ using an iterative scheme given the depth profile of the seabed $H(x)$ and frequency $\frac{\omega}{2\pi} = 0.18$ Hz. Finally, we perform a linear regression to find a single constant of proportionality between the Fourier amplitude at 0.18 Hz and our theoretical $p_d(x)$ as a function of depth/distance (i.e. $\mathrm{FFT}_t[\varepsilon](f = 0.18\mathrm{Hz}, x) = Ap_d(x) + B$). The resulting pressure-depth model is plotted against BDASA data in Fig. 2.3. We only perform this fit further than 12 km from shore where water depth is >10 m, as shoaling waves in shallow water do not adhere to linear wave theory. We neglect any effects of variable burial depth of the fiber.

Directional spectra

The directional spectra plotted in Fig. 2.7 (polar diagrams) are calculated from the frequency-wavenumber spectrum of raw BDASA strain records. For each wave type, we first assume a dispersion relation $\omega = \omega(k)$ and then evaluate ω for a range of apparent wavenumbers $k_a = k/\cos(\theta)$, corresponding to waves propagating across the array from oblique azimuths. For ocean surface gravity waves (Fig. 2.7A), we use the relation $\omega^2 = gk\tanh(kH)$. For Scholte waves (Fig. 2.7B), we use only 1.5-3.5 Hz, where the observed f-k spectrum appears non-dispersive, and assume constant phase velocity ($\omega \propto k$). The mean f-k amplitude is then obtained for each incident azimuth θ by interpolating the f-k spectral amplitudes along each calculated dispersion curve and averaging them. To separate the incoming and outgoing energy, we perform this calculation independently for f-k quadrants 1 and 2. We plot only 0180^o because quadrants 1 and 3 (similarly, 2 and 4) are symmetrical by nature of the 2D FFT, so we cannot distinguish the direction of energy propagating perpendicular to the array (whether SW-NE or NE-SW).

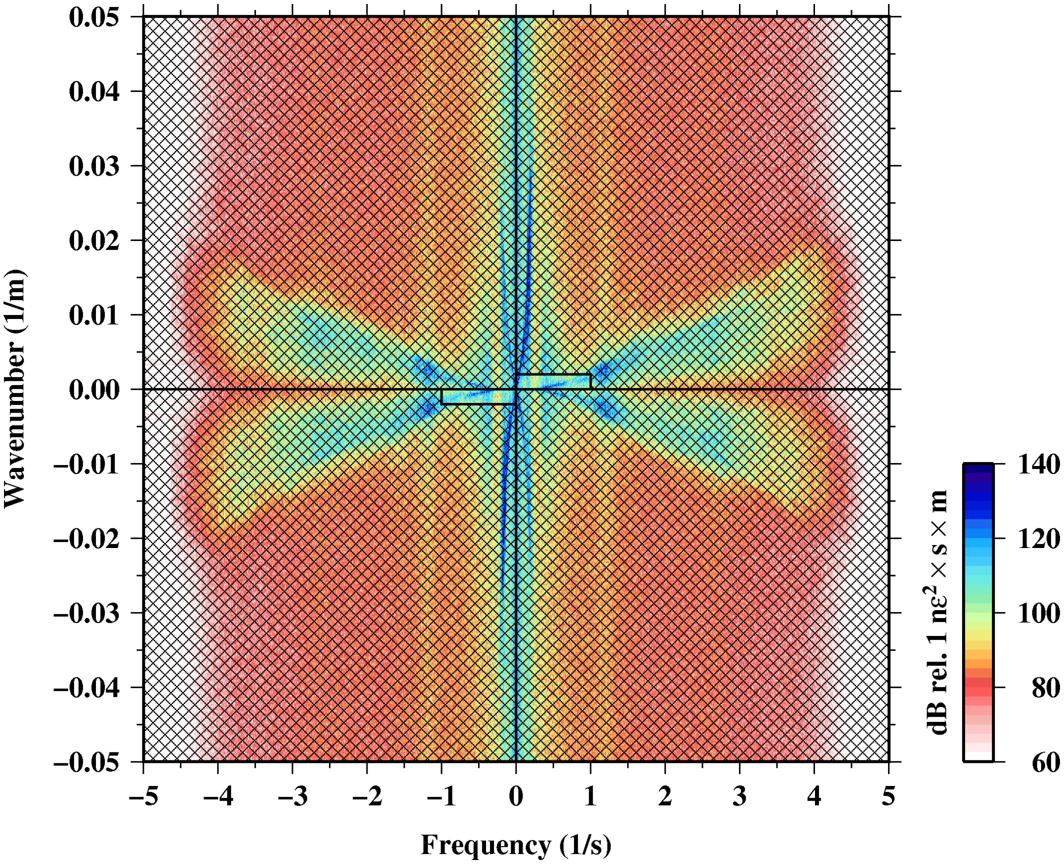

Figure 2.S2: Frequency-wavenumber filter. The rectangular frequency-wavenumber filter applied to preserve only seismic waves in quadrants 1 and 3, indicating propagation from the north/west. Shaded regions are zero, unshaded regions are 1. The inverse 2D Fast Fourier Transform was computed, time-series from each channel between 35 and 40 km were stacked, and finally a bandpass filter was applied to produce the waveforms shown in Fig. 2.9, Supp. Fig. 2.S3, and Supp. Fig. 2.S4.

Teleseism extraction by filtering

The superposition of coherent signals from ocean waves, Scholte waves, and teleseism in BDASA data makes interpretation of raw strain records challenging (Fig. 2.2A). Because these signals also inhabit overlapping frequency bands, simple time-domain or time-frequency filtering is insufficient to isolate individual signals. Instead, we employ a frequency-wavenumber filtering approach that exploits the dense spatial sampling and wide aperture of the BDASA. We first apply a 2D Hamming (cosine-sum) taper $W_H[n,m]$ to the raw t-x domain strain data $\varepsilon(t,x)$ and then compute the 2D Fast Fourier Transform (FFT) to obtain the f-k spectrum $\hat{\varepsilon}(f,k)$.

$$W_H[n,m] = \left(\frac{25}{46} - \frac{21}{46}\cos(\frac{2\pi n}{N_t})\right)\left(\frac{25}{46} - \frac{21}{46}\cos(\frac{2\pi m}{N_x})\right)$$

$$\hat{\varepsilon}(f,k) = \mathrm{FFT}_{2D}[W_H \times \varepsilon(t,x)](f,k)$$

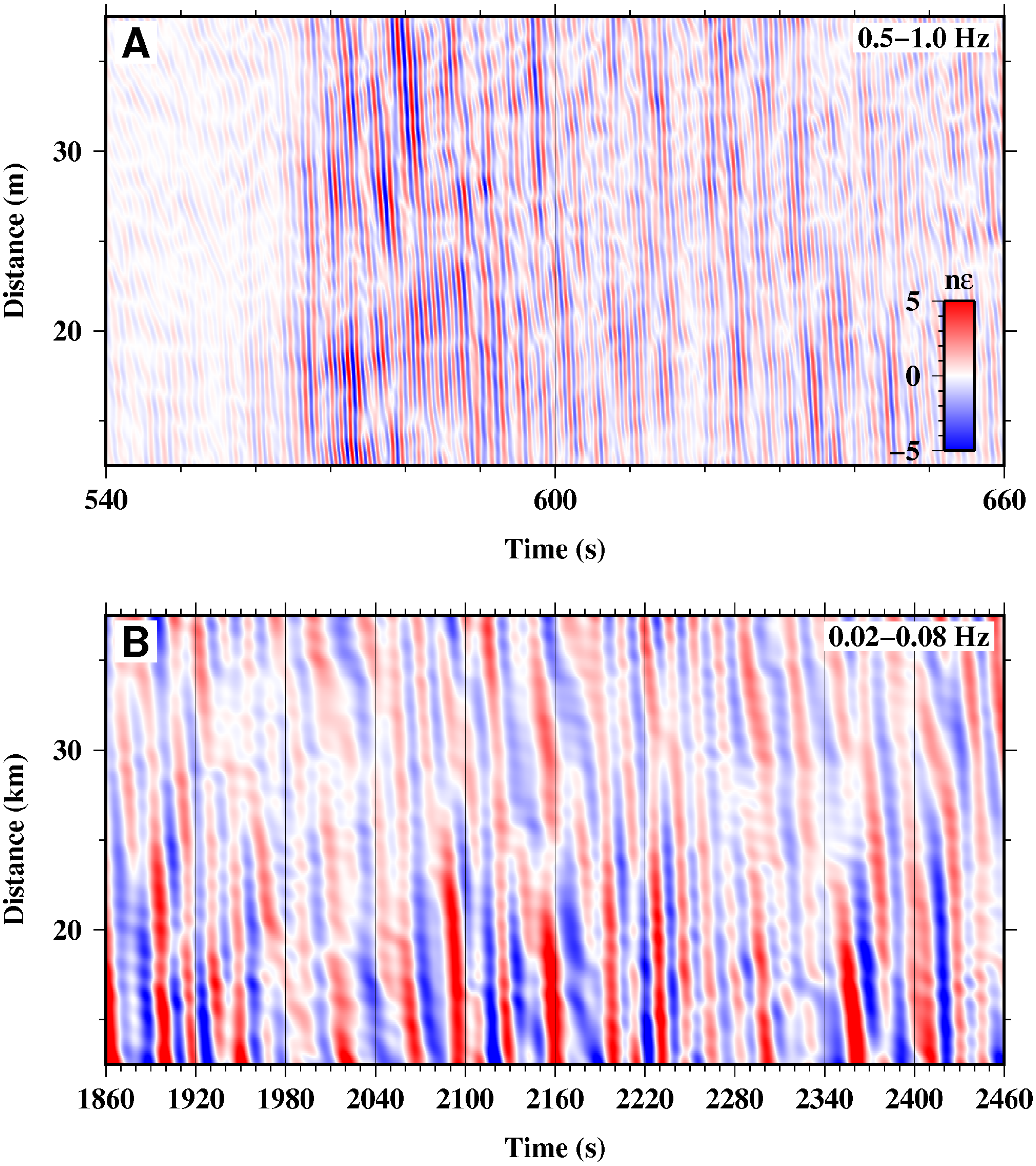

Figure 2.S3: P-wave fidelity. (A) BDASA beam trace filtered 0.5-1 Hz (same as shown in Figure 2.9c). (B) Correlation coefficient (C.C.) between the DAS and BOST waveforms filtered 0.5-1 Hz calculated over a 120 s moving window. (C) Blow-up of 1860-2320 s for the waveforms filtered 0.5-1 Hz around the arrival of the PKP phase just after 550 s, showing low-to-moderate waveform coherence between BOST (red) and BDASA (black) (C.C. = 0.2650). The time-shift between BOST and BDASA (~50 km apart) has not been removed.

In the f-k domain, the spectrum is organized according to apparent phase velocity along the array. We only transform data from quasi-linear array segments because this simplifies interpretation of the f-k spectrum relative to a single reference direction (the axis of the fiber). Teleseismic phases from the Fiji deep earthquake, which is nearly antipodal to the BDASA, arrive with apparent horizontal velocity >10 km/s, and for non-dispersive body waves the energy should appear in the f-k domain along a line of constant f/k. However, the aperture of the BDASA determines wavenumber domain sampling, relegating energy from teleseismic phases to the zero-wavenumber bin across most of the frequency range of interest. For example, a 5-km transformed segment with 500 channels at 10-m spacing has 0.0002 m^{-1}-wide wavenumber bins, and the wavenumber of a 1 Hz teleseismic P-wave arriving at apparent horizontal velocity $c = f/k \approx 10000$ m/s is ~0.0001 m^{-1}. The f-k domain also contains directional information: for the BDASA, energy that appears in f-k quadrants 1 and 3 corresponds to waves propagating land-ward (from the north/west) across the array, and energy that appears in quadrants 2 and 4 corresponds to waves propagating sea-ward (from the south/east). Hence, teleseismic phases from the Fiji earthquake only appear in f-k quadrants 1 and 3.

In conventional f-k processing, we would apply a dip filter to isolate a non-dispersive signal, which passes a sector between two lines of constant f/k. However, we found that this approach is not numerically stable for low frequencies where the pass sector is only a few bins wide. Consequently we reverted to a simple approach, using a 2D rectangular bandpass filter between 0.001-1 Hz and 0-0.002 m^{-1}, without any tapering (Fig. 2.S2). We apply this filter only in f-k quadrants 1 and 3 to attenuate all energy propagating across the BDASA from the south/east. With $f_1 = 0.001$ Hz, $f_2 = 1$ Hz, $k_1 = 0\ \mathrm{m}^{-1}$, $k_2 = 0.002\ \mathrm{m}^{-1}$, $f_m = (f_1 + f_2)/2$, and $k_m = (k_1 + k_2)/2$, the filter $H(f, k)$ can be expressed as

$$H(f,k) = \Pi\left(\frac{f - f_m}{f_2 - f_1}\right)\Pi\left(\frac{k - k_m}{k_2 - k_1}\right) + \Pi\left(\frac{f + f_m}{f_2 - f_1}\right)\Pi\left(\frac{k + k_m}{k_2 - k_1}\right)$$

where Π denotes a rectangular boxcar of unit amplitude. This filter is non-causal ($h(t,x) = \mathrm{FFT}_{2D}[H(f,k)]$is even) and exhibits some Gibbs ringing because of its finite implementation, so a more careful approach may need to be considered for accurate seismic travel-time picking in future studies. After filtering, some residual energy from Scholte waves remains, so we stack across a 5-km segment to improve SNR and isolate teleseismic body waves. When the stack is applied across many sub-sections of the array, relatively high spatial coherence is observed for both P- and S-wave phases (Fig. 2.S3).

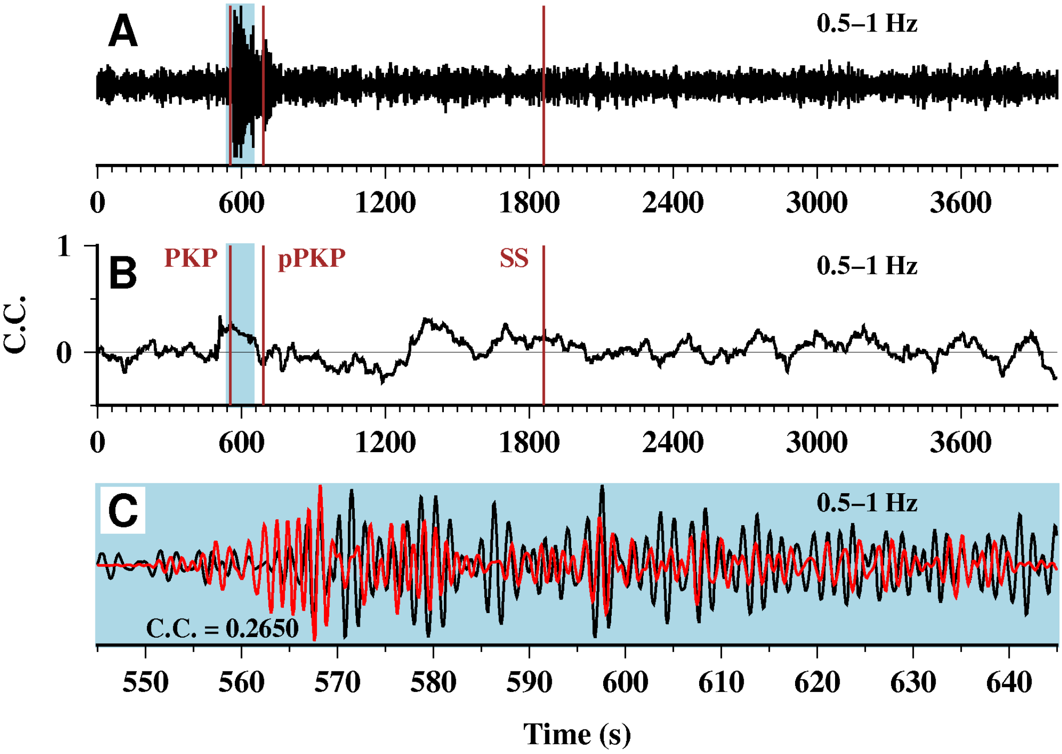

Figure 2.S4: S-wave fidelity. (A) BDASA beam trace filtered 0.02-0.08 Hz (same as shown in Figure 2.9c). (B) Correlation coefficient (C.C.) between the DAS and BOST waveforms filtered 0.02-0.08 Hz calculated over a 240 s moving window. (C) Blow-up of 1860-2320 s for the waveforms filtered 0.02-0.08 Hz around the arrival of the SS phase just after 1860 s, showing moderate-to-high waveform coherence between BOST (red) and BDASA (black) (C.C. = 0.6009).

Teleseism waveform fidelity

As discussed in the main text, recovered P-waves exhibit low-to-moderate waveform fidelity at high frequencies and recovered S-waves exhibit moderate-to-high waveform fidelity at low frequencies. Figure 2.S5A shows the evolution of P waveforms along the array, showing that some coherent energy arrives before the first arrival because of our acausal filter. Overall, P-wave fidelity is low, with a maximum correlation coefficient of 0.26 in the 0.5-1 Hz frequency band calculated in a window centered between the PKP and pPKP arrivals (Fig. 2.S3). However, a high spike in correlation coefficient up to 0.39 is observed when the first PKP motions enter the correlation window (Fig. 2.S3B), suggesting that the BDASA beam trace contains sufficient phase information at high frequencies to permit correlation-based detection algorithms such as template matching. Overall, S-wave fidelity is moderate to high, with a maximum correlation coefficient of 0.60 in a window centered around the SS phase, and average correlation coefficient greater than 0.40 throughout the

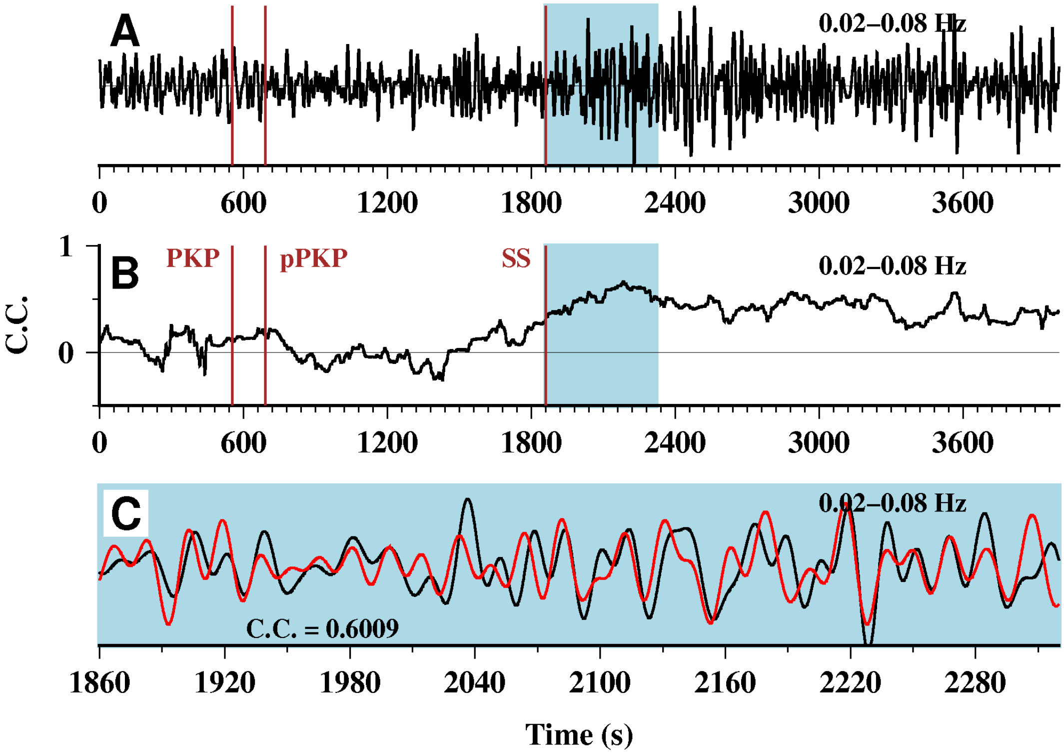

Figure 2.S5: Waveform coherence. F-k filtered waveforms as shown in Figure 9 stacked in a 5-km moving window between 10 and 40 km (plotted at the midpoint of the stacked interval). (A) Bandpassed 0.5-1 Hz, showing the arrival of the PKP and pPKP phases, and (B) bandpassed 0.02-0.08 Hz, showing the arrival of the S-wave train. Note that the filtering procedure applied is non-causal, so some coherent PKP energy can be observed before the true PKP arrival, especially between 12-20 km. A similarly effective causal filter could be designed for more accurate travel-time picking.

complete S-wave train (Fig. 2.S4).

Teleseism amplitude comparison

The 2018-08-19 M_w8.2 Fiji deep earthquake is an atypical event to consider when testing the seismic monitoring capabilities of an instrument, so we include some comparative analysis here. With an epicentral depth around 600 km, the Fiji earthquake did not produce a significant surface wave train. The BDASA was also recording at an epicentral distance of 146^o, in the "shadow zone," meaning that the primary body phases observed were PKP and SS, the former of which can be strongly attenuated. Comparing the velocity spectrum of the Fiji earthquake recorded at BOST with mean velocity spectra of regional and teleseismic earthquakes (Clinton and Heaton, 2002), we observe an expected correspondence between the Fiji event and

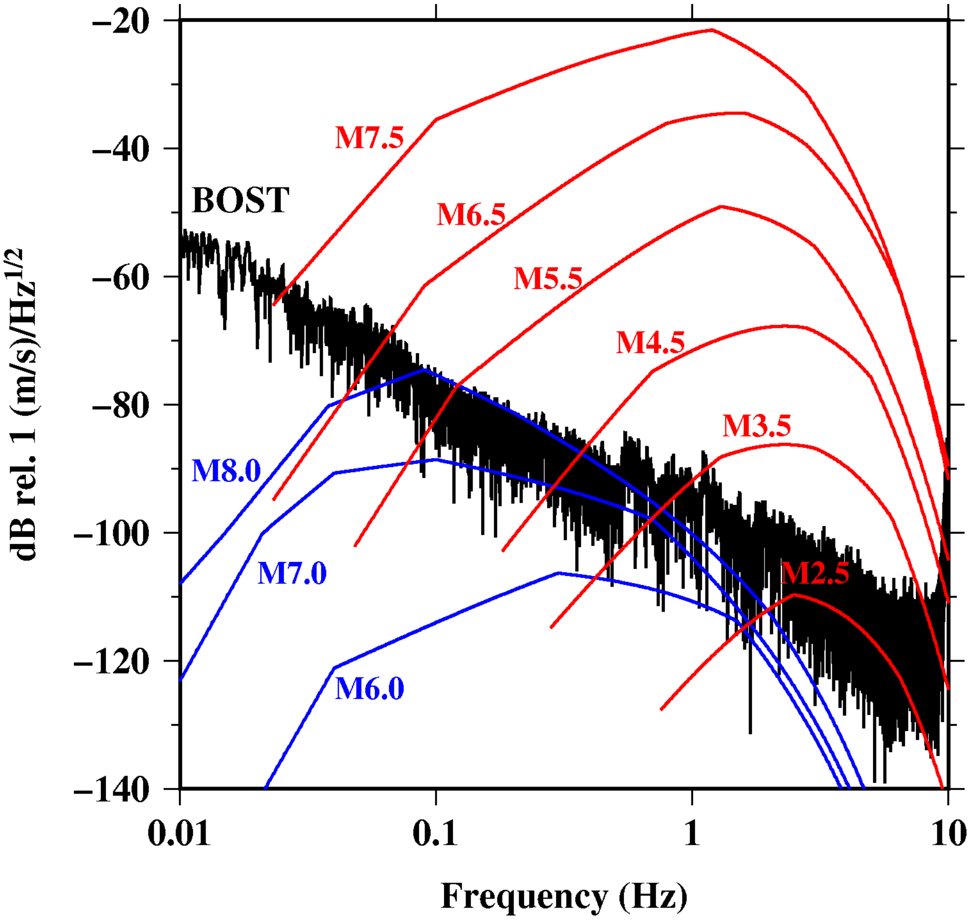

Figure 2.S6: Earthquake scaling. BOST.BHE spectrum of the 2018-08-19 M 8.2 Fiji deep earthquake (black) compared with average spectra of teleseismic (blue, ~3000 km) and regional (red, ~100 km) earthquakes from Clinton and Heaton (2002) (converted from acceleration into velocity units).

mean M8.0 event over a broad band, with stronger S-wave energy at low frequencies than in the mean M 8.0 event (Fig. 2.6). Because we have recovered the principal phases of the Fiji earthquake between 0.01-1 Hz on the BDASA, even in a high-noise shallow-water environment, we can assume that the spectrum observed on nearby broadband BOST exceeds the instrumental noise floor of the BDASA across this band. Hence, we can compare the mean spectra of other event sizes and distances from Clinton and Heaton (2002) indirectly with our demonstrated detection capabilities. As shown in Figure 2.S6, the Fiji earthquake observed at BOST and BDASA is a relatively weak signal, with regional earthquakes (~100-km epicentral distance) above M3.5 exceeding this threshold across most of their band.

References

Ajo-Franklin, J.B. et al. (2019). “Using Dark Fiber and Distributed Acoustic Sensing for Near-Surface Characterization and Broadband Seismic Event Detection”. In: *Scientific Reports* 9.1, p. 1328.

Berger, J. et al. (2016). “An ocean bottom seismic observatory with near real-time telemetry”. In: *Earth and Space Science* 3, pp. 66–77.

Bradner, H., J.G. Doods, and R.E. Foulks (1965). “Investigation of microseism sources with ocean-bottom seismometers”. In: *Geophysics* 30.4.

Bromirski, P.D. (2001). “Vibrations from the "Perfect Storm"”. In: *Geochemistry, Geophysics, Geosystems* 2.7.

Bromirski, P.D., F.K. Duennebier, and R.A. Stephen (2005). “Mid-ocean microseisms”. In: *Geochemistry, Geophysics, Geosystems* 6.4.

Cessaro, R.K. (1994). “Sources of primary and secondary microseisms”. In: *Bull. Seis. Soc. Am.* 84.1, pp. 142–148.

Chapron, B., F. Collard, and F. Ardhuin (2005). “Direct measurements of ocean surface velocity from space: Interpretation and validation”. In: *J. Geophys. Res.: Oceans* 110.C7, p. C07008.

Chen, D., Q. Lui, and Z. He (2017). “Phase-detection distributed fiber-optic vibration sensor without fading-noise based on time-gated digital OFDR”. In: *Optics Express* 25.7, pp. 8315–8325.

Clinton, J. and T. H. Heaton (2002). “Potential advantages of a strong-motion velocity meter over a strong-motion accelerometer”. In: *Seis. Res. Lett.* 73, pp. 332–342.

Costa, L. et al. (2018). “Reaching pε/Hz sensitivity in a distributed optical fiber strain sensor”. In: *Optical Fiber Sensors Conference*. Lausanne, Switzerland, TuD3.

Dolenc, D. et al. (2005). “Observations of infragravity waves at the Monterey ocean bottom broadband station (MOBB)”. In: *Geochemistry, Geophysics, Geosystems* 6.9.

Dorman, L.M. et al. (1993). “Deep-water seafloor array observations of seismo-acoustic noise in the eastern Pacific and comparisons with wind and swell”. In: *Natural Physical Sources of Underwater Sound*. Springer, New York, pp. 165–174.

Fernandez-Ruiz, M. R., H. F. Martins, L. Costa, et al. (2018). “Steady-sensitivity distributed acoustic sensors”. In: *Journal of Lightwave Technology* 36.23, pp. 5690–5696.

Fernandez-Ruiz, M. R., H. F. Martins, J. Pastor-Graells, et al. (2016). “Phase-sensitive OTDR probe pulse shapes robust against modulation-instability fading”. In: *Optics Letters* 41.24, pp. 5756–5759.

Fernandez-Ruiz, M. R., J. Pastor-Graells, et al. (2018). “Laser phase-noise cancellation in chirped-pulse distributed acoustic sensing”. In: *Journal of Lightwave Technology* 36.4, pp. 979–985.

Forsyth, D.W. et al. (1998). “Phase velocities of Rayleigh waves in the MELT experiment on the East Pacific Rise”. In: *Science* 280, pp. 1235–1238.

Friedrich, A., F. Krueger, and K. Klinge (1998). “Ocean-generated microseismic noise located with the Gräfenberg array”. In: *Journal of Seismology* 2.1.

Frye, D. et al. (2005). “An acoustically-linked deep-ocean observatory”. In: *Oceans 2005–Europe, vol. 2*. Brest, France, pp. 969–974.

Gabai, H. and E. Avishay (2016). “On the sensitivyt of distributed acoustic sensing”. In: *Opt. Lett.* 41, pp. 5648–5651.

Goertz, A. and A. Wuestefeld (2018). “Real-time passive monitoring with a fibre-optic ocean bottom array”. In: *First Break* 36, pp. 55–61.

Goodman, D. et al. (1989). “Directional spectra observations of seafloor microseisms from an ocean-bottom seismometer array”. In: *Journal of the Acoustical Society of America* 86.2309.

Goodman, J.W. (1994). *Introduction to Fourier Optics*. McGraw-Hill.

Gyger, F. et al. (2014). “Extending the sensing range of Brillouin optical time-domain analysis up to 325 km combining four optical repeaters”. In: *Proceedings of SPIE*, 9157Q.

Hasselmann, K. (1963). “A statistical analysis of the generation of microseisms”. In: *Reviews of Geophysics* 1.2, pp. 177–210.

Haubrich, R.A. and K. McCamy (1969). “Microseisms: coastal and pelagic sources”. In: *Reviews of Geophysics* 7, pp. 539–571.

Hello, Y. et al. (2011). “Modern mermaids: New floats image the deep Earth”. In: *Eos Trans. AGU* 92.40, pp. 337–338.

Holthuijsen, L.H. (2007). *Waves in Oceanic and Coastal Waters*. Cambridge University Press.

Hornman, K. et al. (2013). “Field trial of a broadside-sensitive distributed acoustic sensing cable for surface seismic”. In: *75th EAGE Conference and Exhibition Extended Abstracts*. London, U.K.

Huang, N.E. et al. (1972). “Interactions between steady non-uniform currents and gravity waves with applications for current measurements”. In: *Journal of Physical Oceanography* 2, pp. 420–431.

Ito, A. et al. (2012). “Detection of small earthquakes along the Pacific-Antarctic Ridge from T-waves recorded by abyssal ocean-bottom observatories”. In: *Mar. Geophys. Res.* 33, pp. 229–238.

Jousset, P., T. Reinsch, J. Henninges, et al. (2017). “Crustal Exploration and Monitoring Seismic Events with a Fibre-optic Cable Deployed at the Ground Surface in Iceland”. In: *EAGE/DGG Workshop on Fibre Optic Technology in Geophysics*. Potsdam, Germany.

Jousset, P., T. Reinsch, T. Ryberg, et al. (2018). “Dynamic strain determination using fiber-optic cables allows imaging of seismological and structural features”. In: *Nat. Comm.* 9.1, p. 2509.

Kaplan, D.M. et al. (2003). “Large diurnal temperature fluctuations in the nearshore water column”. In: *Estuarine and Coastal Shelf Science* 57, pp. 385–398.

Kedar, S. et al. (2008). “The origin of deep ocean microseisms in the North Atlantic Ocean”. In: *Proceedings of the Royal Society A* 464, pp. 777–793.

Kibblewhite, A.C. and C.Y. Wu (1993). “A description of the ULF acoustic noise field in the ocean”. In: *Natural Physical Sources of Underwater Sound*. Springer, New York, pp. 189–202.

Kim, P. et al. (2001). “Novel in-service supervisory system using OTDR for long-haul WDM transmission link including cascaded in-line EDFAs”. In: *IEEE Photonics Technology Letters* 13.10, pp. 1136–1138.

Lay ed., T. (2009). “Seismological Grand Challenges in Understanding Earth’s Dynamic Systems”. In: *Report to the National Science Foundation*. IRIS Consortium.

Li, Z. and Z. Zhan (2018). “Pushing the limit of earthquake detection with distributed acoustic sensing and template matching: a case study at the Brady geothermal field”. In: *Geophys. J. Int* 215.3, pp. 1583–1593.

Lindsey, N.J., E.R. Martin, et al. (2017). “Fiber-optic network observations of earthquake wavefields”. In: *Geophys. Res. Lett.* 44.23, pp. 11792–11799.

Lindsey, N.J., H. Rademacher, et al. (2019). “How Broadband is DAS? Two Empirical Evaluations of Instrument Response”. In: *Seismological Society of America Annual Meeting 2019 Technical Sessions*.

Longuet-Higgins, M.S. (1950). “A theory of the origin of microseisms”. In: *Phil. Trans. Roy. Soc. A* 243.857, pp. 1–35.

Lumpkin, R. and M. Pezos (2007). “Measuring surface currents with Surface Velocity Program drifters: the instrument, its data, and some recent results”. In: *Lagrangian analysis and prediction of coastal and ocean dynamics*, pp. 39–67.

MacDonald, I.R. et al. (2005). “Thermal and visual time-series at a seafloor gas hydrate deposit on the Gulf of Mexico slope”. In: *Earth and Planet. Sci. Lett.* 233, pp. 45–59.

Marra, G. et al. (2018). “Ultrastable laser interferometry for earthquake detection with terrestrial and submarine cables”. In: *Science* 361, pp. 486–490.

Martin, E.R. (2018). *Passive imaging and characterization of the subsurface with distributed acoustic sensing*. Ph.D. Thesis, Dept. of Geophysics, Stanford University, Stanford, CA.

Martin, E.R. et al. (2017). “Continuous Subsurface Monitoring by Passive Seismic with Distributed Acoustic Sensors - The "Stanford Array" Experiment”. In: *79th EAGE Conference and Exhibition Extended Abstracts*. Paris, France.

Martins, H. F. et al. (2015). “Distributed vibration sensing over 125 km with enhanced SNR using phi-OTDR over a URFL cavity”. In: *Journal of Lightwave Technology* 33.12, pp. 2628–2632.

Mateeva, A. et al. (2012). “Advances in distributed acoustic sensing (DAS) for VSP”. In: *SEG Technical Program Expanded Abstracts 2012*, pp. 1–5.

McGuire, J.J., T. Plank, and et al. (2017). “The SZ4D Initiative: Understanding the Processes that Underlie Subduction Zone Hazards in 4D”. In: *Vision Document Submitted to the National Science Foundation*. The Iris Consortium.

Mellors, R.J. et al. (2018). “Understanding distributed fiber optic sensing response for modeling of signals”. In: *SEG Technical Program Expanded Abstracts 2018*, pp. 4679–4682.

Mestayer, J. et al. (2011). “Field trials of distributed acoustic sensing for geophysical monitoring”. In: *SEG Technical Program Expanded Abstracts 2011*, pp. 4253–4257.

MODE Group (1978). “The Mid-Ocean Dynamics Experiment”. In: *Deep Sea Research* 25, pp. 859–910.

Nakata, N. et al. (2015). “Body wave extraction and tomography at Long Beach, California, with ambient-noise interferometry”. In: *J. Geophys. Res.: Solid Earth* 120.2, pp. 1159–1173.

Nye, T. and T. Yamamoto (1994). “Field Test of Buried Ocean-Wave Directional Spectrometer System”. In: *Journal of Waterway, Port, Coastal, and Ocean Engineering* 120.5.

Paduan, J.D. and L. Washburn (2013). “High-frequency radar observations of ocean surface currents”. In: *Ann. Rev. Marine Sci.* 5, pp. 115–136.

Parker, T., S. Shatalin, and M. Farhadiroushan (2014). “Distributed Acoustic Sensing - A new tool for seismic applications”. In: *First Break* 32, pp. 61–69.

Pastor-Graells, J., H. F. Martins, et al. (2016). “Single-shot distributed temperature and strain tracking using direct detection phase-sensitive OTDR with chirped pulses”. In: *Optics Express* 24.12, pp. 13121–13133.

Pastor-Graells, J., J. Nuño, et al. (2017). “Chirped-pulse phase-sensitive reflectometer assisted by first-order Raman amplification”. In: *Journal of Lightwave Technology* 35.21, pp. 4677–4683.

Rauch, D. (1980). “Seismic interface waves in coastal waters: a review”. In: *SACLANT-CEN Report SR 42*.

Rost, S. and C. Thomas (2002). “Array seismology: methods and applications”. In: *Reviews of Geophysics* 40.3, pp. 2-1–2-27.

Shinohara, M. et al. (2011). “Aftershock observation of the 2011 off the Pacific coast of Tohoku Earthquake by using ocean bottom seismometer network”. In: *Earth Planets Space* 63, pp. 835–840.

Suetsugu, D., M. Shinohara, et al. (2005). “Mantle discontinuity depths beneath the west Philippine basin from receiver function analysis of deep-sea borehole and seafloor broadband waveforms”. In: *Bull. Seismol. Soc. Am.* 95, pp. 1947–1956.

Suetsugu, D. and H. Shiobara (2014). “Broadband ocean-bottom seismology”. In: *Annu. Rev. Earth Planet. Sci.* 42, pp. 27–43.

Sugioka, H. et al. (2012). “Tsunamogenic potential of the shallow subduction plate boundary inferred from slow seismic slip”. In: *Nat. Geosci.* 5, pp. 414–418.

Tan, Y.J. et al. (2016). “Dynamics of a sea-floor spreading episode at the East Pacific Rise”. In: *Nature* 540, pp. 261–265.

Toomey, D.R. et al. (1998). “Mantle seismic structure beneath the MELT region of the East Pacific Rise from P and S wave tomography”. In: *Science* 280, pp. 1224–1227.

Traer, J. et al. (2012). “Microseisms and hum from ocean surface gravity waves”. In: *Journal of Geophysical Research: Solid Earth* 117.B11307.

Wang, H.F. et al. (2018). “Ground motion response to an ML 4.3 earthquake using co-located distributed acoustic sensing and seismometer arrays”. In: *Geophys. J. Int.* 213.3, pp. 2020–2036.

Wang, Z. N. et al. (2014). “Ultra-long phase-sensitive OTDR with hybrid distributed amplification”. In: *Optics Letters* 39.20, pp. 5866–5868.

Webb, S.C. (1998). “Broadband seismology and noise under the ocean”. In: *Reviews of Geophysics* 36.1, pp. 105–142.

Webb, S.C. and W.C. Crawford (2010). “Shallow-water broadband OBS seismology”. In: *Bull. Seis. Soc. Am.* 100.4, pp. 1770–1778.

Webb, S.C., T.K. Deaton, and J.C. Lemire (2001). “A broadband ocean-bottom seismometer system based on a 1-Hz natural period geophone”. In: *Bull. Seismol. Soc. Am.* 91, pp. 304–312.

Williams, E.F. et al. (2018). “Dense mapping of shallow velocity structure in the Raymond Basin using the Pasadena Distributed Acoustic Sensing Array”. In: *Southern California Earthquake Center Annual Meeting, Proceedings Vol. XXVIII*. Contribution No. 8543, Palm Springs, California.

Wunsch, C. (2015). *Modern observational physical oceanography*. Princeton University Press.

Yu, C. et al. (2019). “The potential of DAS in teleseismic studies: Insights from the Goldstone Experiment”. In: *Geophys. Res. Lett.* 46.

Chapter 3

SCHOLTE WAVE INVERSION AND PASSIVE SOURCE IMAGING WITH OCEAN-BOTTOM DAS

Williams, E. F. et al. (2021). “Scholte wave inversion and passive source imaging with ocean-bottom DAS”. In: *The Leading Edge* 40.8, pp. 576–583.

Abstract

Geotechnical characterization of marine sediments remains an outstanding challenge for offshore energy development, including foundation design and site selection of wind turbines and offshore platforms. We demonstrate that passive distributed acoustic sensing (DAS) surveys offer a new solution for shallow offshore geotechnical investigation where seafloor power or communications cables with fiber-optic links are available. We analyze Scholte waves recorded by DAS on a 42-km power cable offshore Belgium in the southern North Sea. Ambient noise cross-correlations converge acceptably with just over one hour of data, permitting multi-modal Scholte wave dispersion measurement and shear-wave velocity inversion along the cable. We identify anomalous off-axis Scholte wave arrivals in noise cross-correlations at high frequencies. Using a simple passive source imaging approach, we associate these arrivals with individual wind turbines, suggesting they are generated by structural vibrations. While many technological barriers must be overcome before ocean-bottom DAS can be applied to global seismic monitoring in the deep oceans, high-frequency passive surveys for high-resolution geotechnical characterization and monitoring in coastal regions are easily achievable today.

3.1 Introduction

With the growth of both conventional and renewable offshore energy production, high-resolution and low-cost methods for geotechnical characterization of submarine sediments are of increasing significance for site selection, design, and monitoring of marine structures, pipelines, and cables. Of particular significance is the shear-wave velocity profile of shallow sediments. Shear-wave velocity parameters such as VS30 and Z1.0 are commonly used in ground motion prediction equations, which are a primary tool in estimating both probabilistic seismic and liquefaction hazard (e.g. Abrahamson and Silva (2008)). Shear modulus or shear-wave velocity is also used as a proxy for site properties such as the small-strain stiffness and large-strain strength of sediments (Seed and Idriss, 1970; Shi and Asimaki, 2017). In combination with measurements of compressional wave velocity or bulk modulus, shear-wave velocities are sensitive to the pore fluid saturation, pore fluid composition, and porosity of sediments (Berryman, Berge, and Bonner, 2002). Time-dependent changes in the shear-wave velocity of shallow sediments may be utilized to monitor compaction and deformation patterns associated with oil and/or gas production (Hatchell, Wills, and Didraga, 2009).

Most conventional approaches to onshore seismic site characterization, however, are challenging or even impossible to apply offshore because the water column is opaque to shear waves. For example, the popular multichannel analysis of surface waves (MASW) method (Park, Miller, and Xia, 1999) can be accomplished on land by a small crew using only a hammer or weight-drop source and standard geophone array; whereas, underwater MASW utilizing converted Scholte waves requires a towed source such as an airgun, along with an array of ocean-bottom hydrophones or seismometers (Bohlen et al., 2004; Park, Miller, Xia, et al., 2005). On land, the advent of ambient noise interferometry for surface wave tomography has revolutionized seismic site characterization by eliminating the need for an active source, permitting non-invasive passive investigations using surface waves generated by distant ocean-solid Earth interactions (microseism) or local human activities such as vehicle traffic (Shapiro et al., 2005). Offshore studies with ambient noise Scholte waves have shown significant potential in creating highly repeatable maps of near-surface velocity structure (de Ridder and Dellinger, 2011; de Ridder and Biondi, 2013; Mordret et al., 2013). However, the trade-off between cost and resolution in ocean-bottom seismometry limits the potential of conventional instrumentation for high-resolution, shallow studies. Where pre-existing seafloor fiber optic cables are available, such as at offshore wind farms, distributed acoustic sensing (DAS) offers a viable alternative to ocean-bottom seismometers because deployment cost does not scale with the number of sensors.

DAS arrays leveraging pre-existing fiber-optic cables have shown tremendous potential for near-surface geophysics and infrastructure monitoring onshore (Z. Zhan, 2020). The particular sensitivity of DAS to longitudinal waves renders it well-suited to surface wave studies, which have been widely employed in seismic site characterization and shear-wave velocity inversion (Dou et al., 2017; Spica, Perton, et al., 2020). Further, the ability of DAS to record strain signals across a broad frequency band has permitted such diverse applications as pipeline integrity monitoring (Tanimola and Hill, 2009), urban traffic monitoring (X. Wang et al., 2020), active-source seismic imaging (Mateeva et al., 2013), and earthquake detection (Jousset et al., 2017; Lindsey, Martin, et al., 2017; Li and Z. Zhan, 2018). Recently, three concurrent studies by Lindsey, Dawe, and Ajo-Franklin (2019), Sladen et al. (2019), and Williams et al. (2019) demonstrated that DAS can have similar value when deployed on seafloor fiber-optic cables, recording local, regional, and teleseismic earthquakes along with ambient noise Scholte waves generated by ocean-solid Earth interaction. Subsequently, Spica, Nishida, et al. (2020) and Cheng et al. (2021) demonstrated that Scholte waves in ocean-bottom DAS data can be utilized for structural investigations, and G. Zhan, van Gestel, and Johnston (2020) and Karrenbach et al. (2020) showed that ocean-bottom DAS can record active source shots with similar fidelity to ocean-bottom seismometers.

In this article, we demonstrate the utility of DAS for offshore engineering applications by analyzing one hour of passive DAS data from an ocean-bottom cable offshore Belgium. Between 0.3 and 5 Hz the dataset is dominated by Scholte waves propagating along the sediment-water interface. We measure multimode Scholte wave dispersion from ambient noise correlations, and invert for a shallow shear-wave velocity model along the cable. We then investigate anomalous Scholte wave phases present in the noise correlations that interfere with the direct wave between virtual source and receiver. By migrating these off-axis Scholte waves, we find they originate from individual wind turbines operating near the cable.

3.2 Data overview

We analyze a 1-hr passive DAS recording from an optical fiber within a 42-km power cable servicing wind farms in the southern North Sea, offshore Zeebrugge, Belgium. Figure 3.1 shows the path of the cable relative to local bathymetry and offshore wind farms. The water depth is less than 40 m along the entire cable, and crosses several sand ridges. Most notable is Thornton Bank, which has hosted the 54-turbine C-Power wind farm since 2009. The depth of burial of the cable varies between 0.5 and 3.5 m below the seafloor. While nine separate wind farm projects are active or under construction today on both sides of the Belgium-Netherlands maritime boundary, only three of these wind farms were fully commissioned (C-Power, Northwind, and Belwind/Nobelwind) and one was partially commissioned (Rentel) at the time of data acquisition on 19 August 2018 (Figure 3.1).

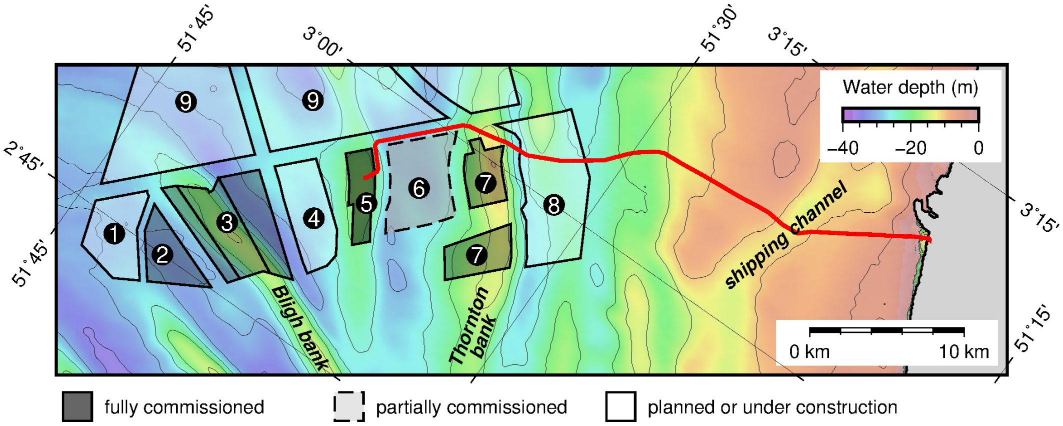

Figure 3.1: Map of seafloor power cable (red line) and wind farms (boxes) offshore Belgium. Labeled wind farms are color coded by degree of completion at the time of data acquisition in August 2018, and are as follows: (1) Mermaid, (2) Northwester, (3) Belwind/Nobelwind, (4) Seastar, (5) Northwind, (6) Rentel, (7) C-Power, (8) Norther, and (9) Borssele.

The fiber was interrogated using a chirped-pulse DAS system built by the University of Alcala (Pastor-Graells et al., 2016). A major advantage of chirped-pulse DAS is its use of direct detection, as opposed to coherent detection used in conventional DAS systems, which eliminates fading sensitivity along the fiber (Fernandez-Ruiz, Martins, et al., 2018), permitting array processing directly from the raw data. . For the interested reader, extended reviews of this technique outlining the instrumental details are available (Fernandez-Ruiz, Costa, and Martins, 2019). The channel spacing was set at 10 m, with 10-m gauge length and 10 Hz sampling rate (down-sampled from a 1 kHz original sampling rate), yielding 4192 channels of continuous data over the full 42-km range of the cable. The DAS recorded ambient noise Scholte waves generated by ocean-solid Earth interactions and anthropogenic sources. This dataset also includes a teleseismic earthquake. While some Scholte wave conversions from teleseismic P- and S-phases may be present, we were unable to identify earthquake-related Scholte waves and assume they do not contribute to the results presented here. For more details about the dataset, choice of interrogator, and cable design we refer the reader to Williams et al. (2019).

3.3 Phase velocity measurement and inversion

To compute ambient noise correlation functions, the one hour DAS record was divided into 3.4 minute windows (2048 samples at 10 Hz) overlapping by 50 percent. The first 1000 channels near shore and in the surf zone were discarded. Spectral

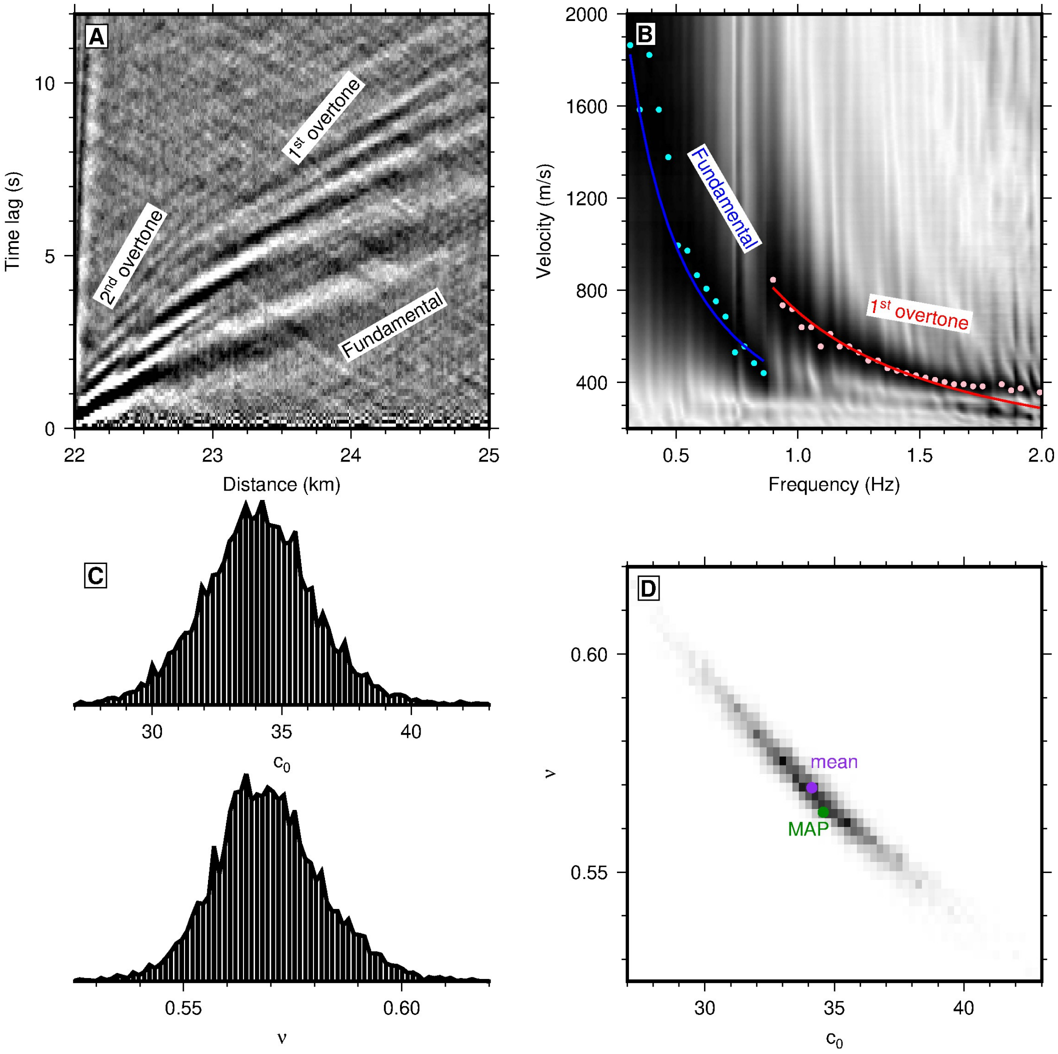

Figure 3.2: Scholte wave dispersion measurement and inversion. (A) Common-source gather with virtual source at 22 km, showing three Scholte wave modes and a weak ocean surface gravity wave mode (near-vertical, along the y-axis) propagating along the array. (B) Normalized dispersion image computed with the $\tau - p$ transform. Dispersion picks for the fundamental mode (blue) and first overtone (red) are shown with the mean posterior fit. (C) Marginal posterior probability density functions (PDFs) for the two parameters c_0 and ν. (D) Joint posterior PDF of c_0 and ν, with the mean point and maximum a posteriori (MAP) point labeled.

whitening was applied to each window, followed by cross-correlation, normalization, and stacking in the frequency domain. Scholte wave dispersion images were computed by applying the $\tau - p$ transform on a 100-channel (1 km) virtual source gather every 10 channels (100 m) along the array, yielding 309 dispersion images (Figure 3.2A,B). Initial phase velocity picks were automatically chosen as the maximum value of the dispersion image in each frequency bin, and then reviewed manually in order to assign mode numbers and remove spurious picks.

Scholte wave phase velocity picks for the fundamental mode and first overtone were jointly inverted for a 1D local shear-wave velocity profile, fixing density at 1.6 g/cc (Figure 3.2C,D). For simplicity, we use a power-law parameterization ($c(z) = c_0 z^{\nu}$) for which an approximate analytical Scholte wave dispersion solution is given by Godin and Chapman (Godin and Chapman, 2001; Chapman and Godin, 2001). A power-law velocity model is convenient because it permits straightforward calculation of common geotechnical quantities such as V_{S30} (the time-averaged shear-wave velocity of the top 30 m; $c_0(1-\nu)30^{\nu}$) and $Z_{1.0}$ (the depth to 1 km/s shear-wave velocity; $\left(\frac{1000}{c_0}\right)^{\frac{1}{\nu}}$) without having to consider the shallow resolution of a layered model or apply non-physical regularization to the inversion. Theoretical and experimental studies have demonstrated that unconsolidated marine sediments typically exhibit power-law shear-wave velocity in the top 10s of meters due to the steep gradient in confining pressure below the seafloor (Hamilton, 1976; Bryan and Stoll, 1988; Godin and Chapman, 1999; Buckingham, 2005). While this assumption may not apply for regions of the cable where unconsolidated Quaternary sediments are thin, consolidated/cemented sediments also exhibit non-linear dependence of shear-wave velocity on confining pressure (e.g. Cristensen and H. F. Wang (1985)), and power-law or piecewise power-law models are frequently used to represent shallow consolidated sediments in ground-motion studies (Boore and Joyner, 1997; Brocher, 2008). Further, choice of a power-law velocity model is supported by the data, as phase velocity is observed to scale as a power of frequency (Figure 3.2B) (Godin and Chapman, 2001; Tsai and Atiganyanun, 2014). The inversion was carried out with the Metropolis-Hastings algorithm, with convergence determined by the effective sample size. The marginal posterior probability density functions for c_0 and ν are approximately Gaussian, but exhibit multiple local maxima due to the high scatter among dispersion picks at low frequencies (Figure 3.2C). Consequently, we consider the mean of the posterior as the solution, instead of the maximum a posteriori (MAP) point (Figure 3.2D).

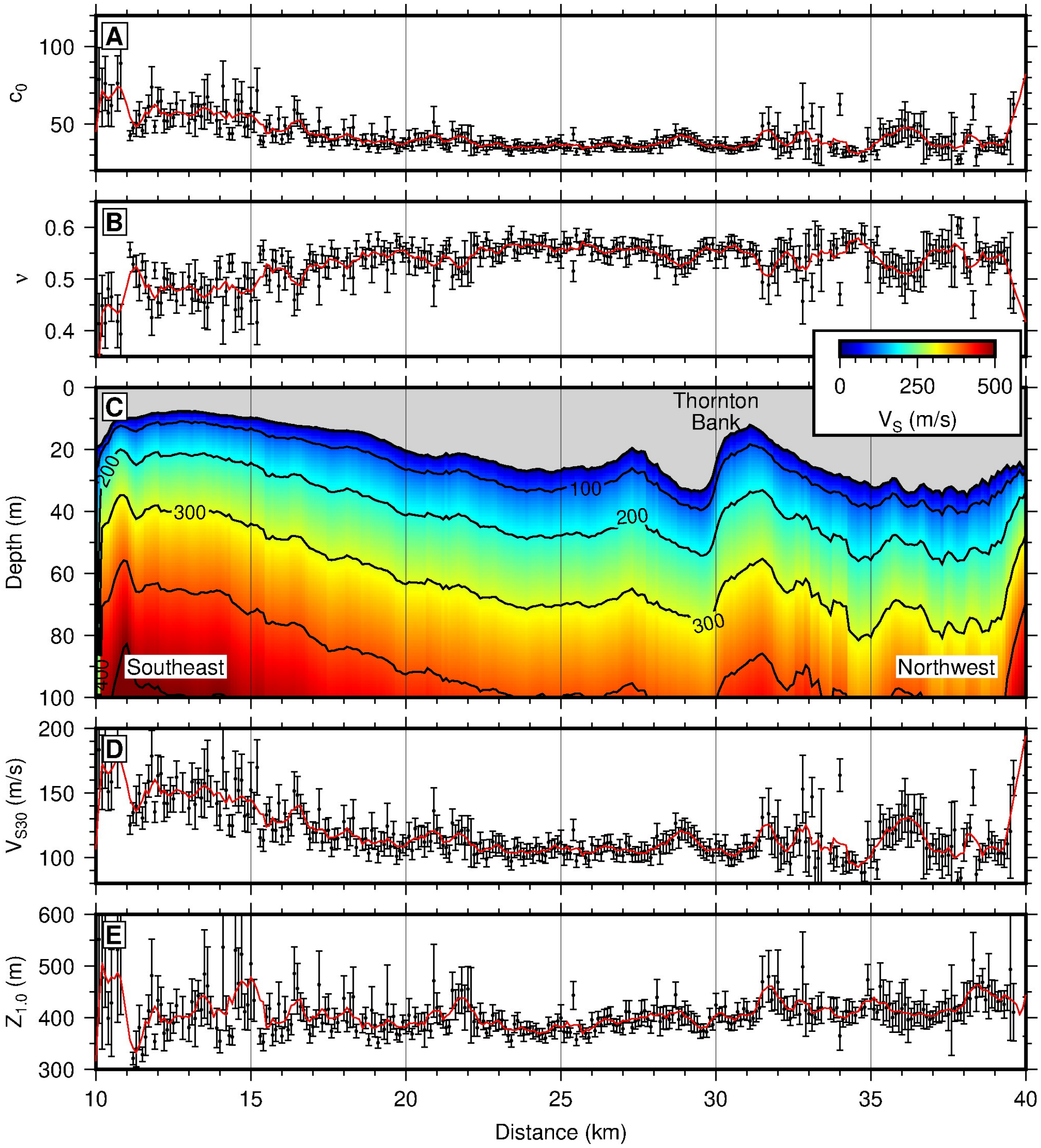

Figure 3.3: Velocity model. (A, B) Inversion results for c_0 and ν along the 30-km array segment from SE to NW, showing the mean posterior solution (black dot), one standard deviation (black bar), and a the mean solution smoothed with a 500-m spatial window (red line). (C) Smoothed velocity model (same as smoothed red line in (A) and (B)) offset by bathymetry. (D, E) Same as (A, B) but for geotechnical parameters V_{S30} and $Z_{1.0}$.

The inverted velocity profile and associated geotechnical parameters are shown in Figure 3.3. All along the cable, uncertainty decreases with water depth. Because only 1 hour of data is available, the signal-to-noise ratio of Scholte waves is a limiting factor in dispersion measurement, and in shallow water ocean surface gravity wave signals dominate the data, inhibiting convergence of noise correlation functions and resulting in more scattered dispersion picks. High uncertainty between 32–34 km may also result from the rough bathymetry of numerous short-wavelength sand dunes on the crest of Thornton Bank. Localized extreme (>50% V_{S30}) high velocity anomalies at 10-11 km and 39-40 km are likely a result of bends in the cable (Figure 3.1).

The resulting shear-wave velocity model is generally consistent with known geologic information, despite the inability of a power-law model to capture discrete interfaces. The shallow stratigraphy of the Belgian Continental Shelf is characterized by Eocene shelf deposits unconformably overlain by Quaternary sands, which form a series of tidal sand banks. Between 10 and 20 km cable distance, the thickness of Quaternary deposits decreases from ~15 m to <5 m, while the composition of Eocene strata (clay to clayey sandstone) remains similar (Le Bot et al., 2005; Mathys, 2009). The thinning of unconsolidated Quaternary sands is consistent with the observed decreasing trend in V_{S30} over this interval (Figure 3D). Several strong anomalies in V_{S30} and $Z_{1.0}$ between 10–20 km may be associated with early Quaternary channels incising the top-Paleoene unconformity, such as have been mapped by Mathys (2009) in multi-channel seismic profiles near the cable path. A small anomaly in both V_{S30} and $Z_{1.0}$ at 22 km is likely associated with a local increase in the thickness of the Quaternary sand. Minimal velocity change is evident at Thornton Bank; rather, significant (20–40%) high-V_{S30} anomalies are observed in the swales on either side of the bank, correlated with the deepest bathymetry at 29 and 36 km (Figure 3.3D,E). Here, the Quaternary deposits are thinnest (<5 m) and in places erosion from tidal currents may expose the Eocene at the seafloor (Le Bot et al., 2005; Mathys, 2009). The velocity model also reveals an increase in $Z_{1.0}$ across the last 15 km of the cable, from ~400 to 450 m, with a step around 32 km under the western flank of Thornton Bank (Figure 3.3E). An increase in $Z_{1.0}$ while the background trend in V_{S30} remains constant indicates a decrease in the gradient of shear-wave velocity with depth. While this could be explained by the changes in sand thickness at Thornton Bank, the cable also crosses several boundaries in the Eocene section grading from clay to sandstone in the last 15 km (Le Bot et al., 2005), so interpretation of this trend is complex.

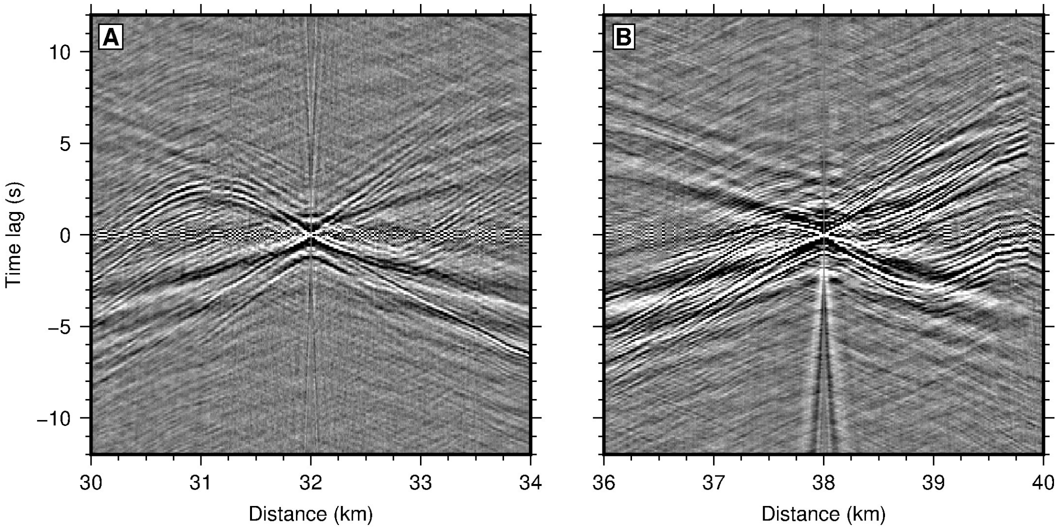

Figure 3.4: Common-source gathers with virtual sources at 32 km (A) and 38 km (B) showing interference between the direct Scholte wave arrivals and strong secondary sources along the cable. Compare with Figure 3.2A where no off-axis arrivals are present.

3.4 Interferometric imaging of noise sources

In addition to the expected direct Scholte wave modes propagating between virtual source and receiver (Figure 3.2A), noise correlation virtual source gathers also exhibit hyperbolae indicative of obliquely incident Scholte waves generated by a strong secondary source or scatterer (Figure 3.4). These off-axis arrivals interfere with the second and third overtones of the direct wave in dispersion images, requiring us to exclude all picks above 2 Hz from the shear-wave velocity inversion above. Similar arrivals were observed by Mordret et al. (2013) in noise correlations across a dense ocean-bottom node array at Valhall, where the source was localized to the drilling platform by beamforming and travel-time fitting. Precursory and coda phases from secondary sources and scatterers are relatively common features of continental-scale noise correlations (e.g. Z. Zhan et al. (2010) and Ma et al. (2013)) and have also been observed in high-frequency noise correlations on terrestrial DAS arrays (Zeng et al., 2017). Given these off-axis arrivals only appear between 30 and 42 km distance where the cable runs along the northern edge of the C-Power, Rentel, and Northwind wind farms, we infer that off-axis arrivals in noise correlation functions represent Scholte waves generated by the structural vibrations of wind turbines. This interpretation is validated by passive source imaging.

In order to visualize the secondary noise sources and prepare for migration, we

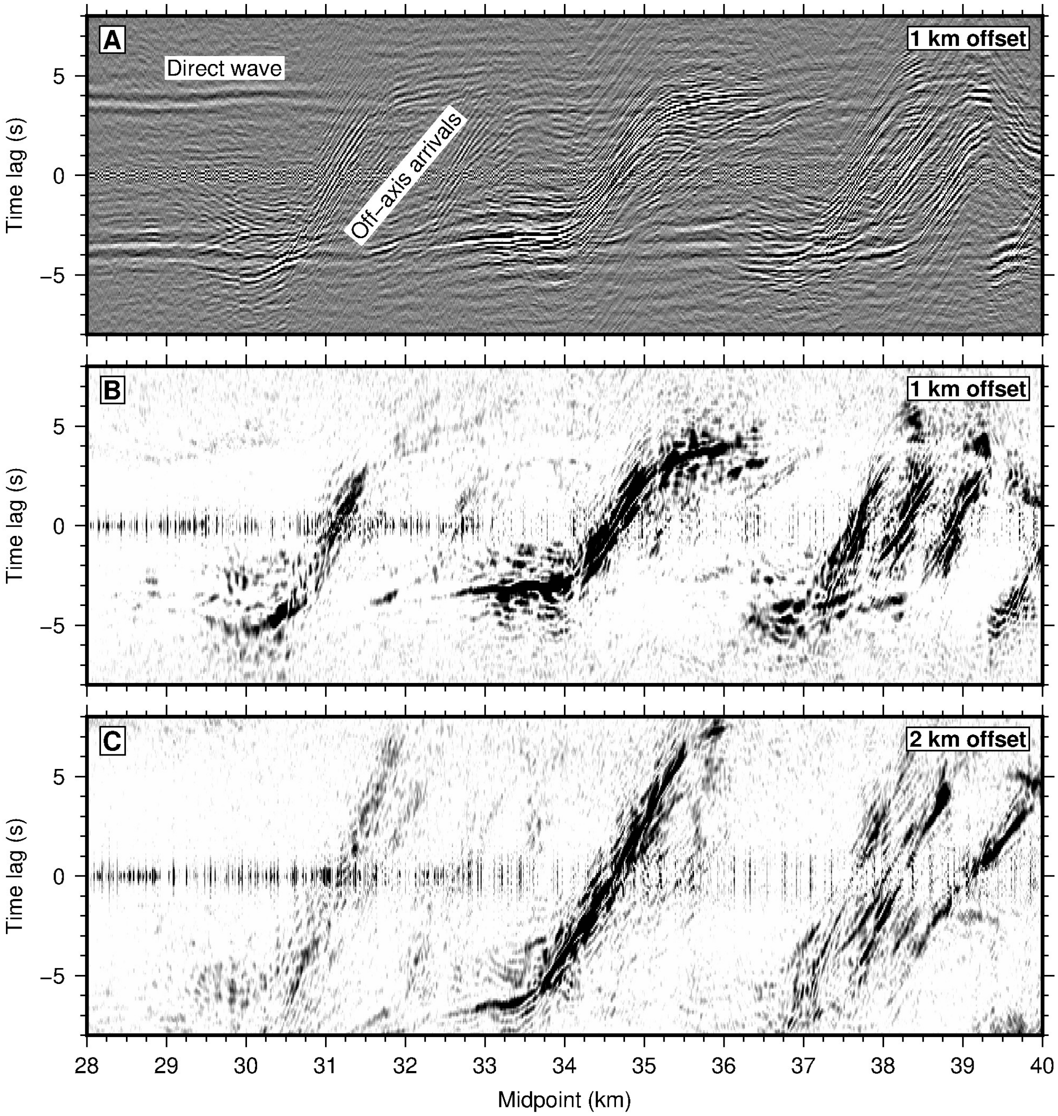

Figure 3.5: (A) Common-offset gather (h = 500 m) showing three areas of strong off-axis Scholte wave arrivals around 31, 35, and 38 km. (B) Common-offset gather from (A) after filtering 1–4 Hz, calculating the envelope, and removing the mean. (C) same as (B) but with h = 1 km.

sort the noise correlations into common-offset gathers (Figure 3.5). In common-offset gathers, the travel-time curve for an off-axis point source or scatterer appears similar to an arc-tangent curve, with zero-crossing at the point where the source is an equal distance from both virtual source and virtual receiver (i.e. located along a line perpendicular to the array), permitting straight-forward visual identification of source locations and minimizing the overlap between each source. Conveniently, the travel-time of the direct wave between virtual source and virtual receiver is approximately constant in common-offset gathers (Figure 3.5A), so the direct wave is effectively removed by subtracting the mean trace from all midpoints (Figure 3.5B). Residual common-mode noise (generated by temperature or vibrations of the DAS interrogator unit) that was not completely removed before cross-correlation concentrates at zero time-lag in the cross-correlation functions and is also mitigated by removing the mean at this stage.

Scholte waves from at least five secondary noise sources are clearly present in the data: one centered around 31 km, a second at 35 km, and at least three more around 38 km. These arrivals are only visible between 1 and 4 Hz, and have a strong spectral peak around 1.1 Hz which varies slightly among sources. The narrow-band source signature combined with the dispersive nature of Scholte waves results in ringy waveforms almost 4 seconds long. By using the envelope, the effect of dispersion can be neglected during migration.

To compute the source image, we migrated individual common-offset gathers using the cross-correlation migration of Schuster et al. (2004), which is simply Kirchhoff migration re-formulated for interferometric travel-times. Because the amplitude of observed Scholte waves varies by an order of magnitude among sources, we divided the data into three continuous segments and migrate each independently: 29.5–32.5 km, 32.5–36.5 km, and 36.5–41.5 km. Because we are migrating the envelope and because we have no information about velocity away from the cable, we used a constant velocity, taken as the average group velocity for the fundamental mode between 1 and 4 Hz, which is between 100 and 120 m/s along the array.

Resulting source images are shown in Figure 3.6. For the first two cable segments, the off-axis arrivals migrate clearly to a single turbine source: turbine I3 in the C-Power wind farm (Figure 3.6B) and turbine E4 in the Rentel wind farm (Figure 3.6C). The smearing of energy along the direction perpendicular to the cable is caused by the linear and one-sided array configuration. For the third cable segment (Figure 3.6D), interpretation of the source image is more ambiguous. Two strong

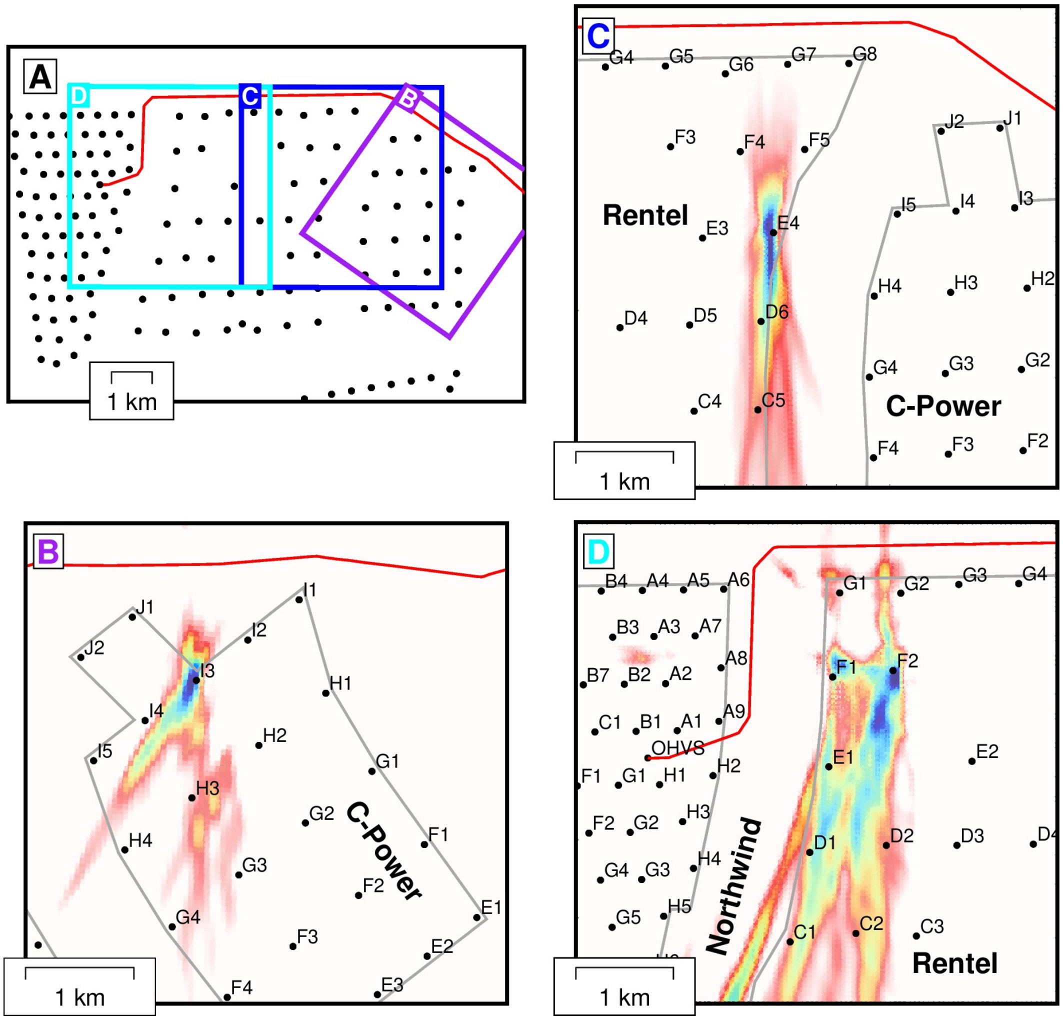

Figure 3.6: Scholte wave source images. (A) Overview map with locations three images. The cable location is shown in red and individual wind turbines are black dots. (B) Source image from common-offset data with midpoints between 29–32.5 km showing a single turbine source in the C-Power wind farm. (C) Source image from midpoints 32.5–36.5 km showing a single turbine source in the Rentel wind farm. (D) Source image from midpoints 36.5–41.5 km showing multiple turbine sources in the Rentel wind farm. Each panel has been rotated relative to the local cable orientation, and the color scale is normalized between 0–1 in each image.

peaks appear at turbines F1 and F2 with two weaker peaks at turbines G1 and G2, due to crossing of travel-time curves around the bend in the DAS array. There is also broad smearing of energy across turbine rows C through E further from the array, which is caused by the overlap of the Scholte waves from each of the sources at longer time lags. Though operational ground-truth is not available from the wind farm operators, at the time of acquisition the Rentel wind farm was still under construction and not fully commissioned until November 2018, which likely explains why only a subset of turbines are observed. No turbines in the Northwind wind farm are clearly identified, though this does not necessarily require that the Northwind turbines were inactive at the time of recording. Turbines in the Northwind complex are smaller 3 MW Vesta turbines, compared with the larger 7 MW Siemens turbines in the adjacent Rentel wind farm, and therefore they likely generate weaker, higher frequency vibrations. Similarly, the majority of C-Power wind turbines were not observed, and the one turbine identified (I3) was the weakest observed source. The C-Power Phase-2 6 MW Senvion turbines nearest the cable are installed on steel jacket foundations, while the Rentel turbines are installed with monopile foundations, so some difference in soil-structure interaction is expected.

3.5 Discussion and conclusions

The results of this study demonstrate that ambient noise interferometry applied to passive ocean-bottom DAS recordings is a powerful tool for subsurface structural investigation and has the capability of detecting and localizing vibrations from offshore structures. The inverted shear-wave velocity model is generally consistent with the known geologic information. Further, source images calculated using the measured Scholte wave velocities migrated individual arrivals to within 100 m of known turbine locations. These results were obtained from only about 1 hour of passive data within the 0.3–4 Hz frequency band. With a longer recording window, the degree of convergence of noise correlation functions (and consequently the signal-to-noise ratio in dispersion images) would likely improve. Similarly, recording at a higher sampling rate would permit utilization of a broader spectrum of environmental noise, such as from short-period microseism and regional shipping traffic, thereby increasing the sensitivity of Scholte wave dispersion spectra to shallow structure and permitting more flexible shear-wave velocity parameterization. However, as in this study, previous passive Scholte wave tomography by Mordret et al. (2013) and de Ridder and Biondi (2013) has been limited to below 2 Hz due to interference from strong, local sources of high frequency noise. Further work on deblending filters or joint source-structure inversion is needed. The first proof-of-concept work exploring ocean-bottom DAS deployments was largely motivated by the potential for seismic monitoring in the deep oceans, for global tomography or hazard early-warning (Lindsey, Dawe, and Ajo-Franklin, 2019; Sladen et al., 2019; Williams et al., 2019). Today, this vision is not yet practical: (1) subsea cable links are relatively sparse and have not been made widely available to the geoscientific community; (2) without two-way optical repeaters, commercial DAS systems are limited to less than 100 km operating range. By contrast, application of ocean-bottom DAS for offshore engineering is feasible today: (1) optical fibers are available in power cable networks at existing wind farms, monitoring arrays at subsea oil and gas fields, or along seafloor pipelines; (2) energy production and development sites are generally within 100 km of the coast or have an associated platform/substation. Further, due to shipping and fishing hazards, ocean-bottom cables in the near-shore environment can include dense armor cladding and are more often buried than deep-sea cables, which is likely to both enhance elastic coupling to the seafloor and reduce temperature-noise in DAS.

Particularly for global wind energy development, deploying DAS on pre-existing optical fibers in power cable links has the potential to become a mainstay of offshore engineering practice. For example, shallow gas presents a hazard to drilling operations and foundation integrity. Near the study area on the Belgian Continental Shelf, gas has been identified in Holocene sediments using high-resolution seismic reflection profiles (Missiaen et al., 2002). Because gas concentration has a large impact on bulk modulus but a small impact on shear modulus and density, shear-wave velocity profiling with Scholte waves complementing conventional seismic investigations permits calculation of V_P/V_S for improved constraints on porosity and pore fluid composition. Similarly, soil-structure interaction models, which are increasingly used in the design of wind turbine foundations, require accurate estimates of the stiffness and strength of shallow sediments (e.g. Lombardi, Bhattacharya, and Wood (2013)). Shear-wave velocity measured in-situ with ocean-bottom DAS can be incorporated in geologic site classification to choose reference strength parameters, or it can be used directly as a proxy in physics-based soil models (e.g. Shi and Asimaki (2017)). Hydrodynamic loading of wind turbines and other offshore structures is another key parameter in foundation design which is difficult to measure in-situ. In addition to seismic signals, ocean-bottom DAS also records the seafloor pressure perturbation from ocean surface gravity waves, which can not only be related to wave intensity (Lindsey, Dawe, and Ajo-Franklin, 2019) but also current speed

(Williams et al., 2019). Ocean-bottom DAS thereby offers diverse value for site selection and foundation design in a geologically and hydrodynamically complex environment such as offshore Belgium.

One major engineering challenge for offshore wind turbines is scouring at the base of the structure, which can jeopardize the integrity of the foundation (Whitehouse et al., 2011). Integration of sediment and water column properties measured with ocean-bottom DAS provides the necessary parameters for scour modeling. Further, our demonstration that ocean-bottom DAS can detect seismic waves radiated from individual wind turbines nearby suggests potential for remote operational and structural health monitoring. Structural vibrations are efficient at generating Scholte waves (or equivalently Rayleigh waves on land) by rocking or shearing of the foundation and Love waves by torsion of the foundation, especially at the natural frequencies of the structure (Favela, 2004). The natural frequencies of wind turbines are highly sensitive to modifications of the sediment-foundation system, such as can be caused by scour (Prendergast, Gavin, and Doherty, 2015). The relative contributions of Scholte and Love waves can also be an indicator of sediment properties and foundation integrity (Favela, 2004). We reserve the development of such methods for future studies where more comprehensive operational ground truth is available.

Presently, the primary limitation of ocean-bottom DAS for engineering applications is the location and timing of cable installation relative to the need for geotechnical information. Pre-existing cables will never be installed at the exact site of planned turbines, so ocean-bottom DAS is unlikely to replace in-situ geotechnical coring or cone penetration tests unless dedicated fibers are laid at the design stage. This challenge is partly mitigated offshore Belgium by the long history of wind energy development: the first power cable was laid in 2007 with the installation of the C-Power Phase-1 turbines at Thornton Bank, and the cable routes for early installations run through planned development sites (Figure 3.1). Given the diverse applications of ocean-bottom DAS demonstrated here, offshore wind developers should consider routes that optimize the site selection, design, and monitoring value of seafloor cables for future projects.

References

Abrahamson, N. and W. Silva (2008). “Summary of the Abrahamson Silva NGA ground-motion relations”. In: *Earthquake Spectra* 24.1, pp. 67–97.

Berryman, J. G., P. A. Berge, and B. P. Bonner (2002). “Estimating rock porosity and fluid saturation using only seismic velocities”. In: *Geophysics* 67.2, pp. 391–404.

Bohlen, T. et al. (2004). “1.5D inversion of lateral variation of Scholte-wave dispersion”. In: *Geophysics* 69.2, pp. 330–344.

Boore, D. M. and W. B. Joyner (1997). “Site amplifications for generic rock sites”. In: *Bull. Seis. Soc. Am.* 87.2, pp. 327–341.

Brocher, T. M. (2008). “Compressional and shear-wave velocity versus depth relations for common rock types in northern California”. In: *Bull. Seis. Soc. Am.* 98.2, pp. 950–968.

Bryan, G. M. and R. D. Stoll (1988). “The dynamic shear modulus of marine sediments”. In: *J. Acoust. Soc. Am.* 83, pp. 2159–2164.

Buckingham, M. J. (2005). “Compressional and shear wave properties of marine sediments”. In: *J. Acoust. Soc. Am.* 117.1, pp. 137–152.

Chapman, D. M. F. and O. A. Godin (2001). “Dispersion of interface waves in sediments with power-law shear speed profiles: II. Experimental observations and seismo-acoustic inversions”. In: *J. Acoust. Soc. Am.* 110.4, pp. 1908–1916.

Cheng, F. et al. (2021). “Utilizing distributed acoustic sensing and ocean bottom fiber optic cables for submarine structural characterization”. In: *Sci. Rep.* 11.1, pp. 1–14.

Cristensen, N. I. and H. F. Wang (1985). “The influence of pore pressure and confining pressure on dynamic elastic properties of Berea sandstone”. In: *Geophysics* 50.2, pp. 207–213.

de Ridder, S. A. L. and B. L. Biondi (2013). “Daily reservoir-scale subsurface monitoring using ambient seismic noise”. In: *Geophys. Res. Lett.* 40, pp. 2969–2974.

de Ridder, S. A. L. and J. Dellinger (2011). “Ambient seismic noise eikonal tomography for near-surface imaging at Valhall”. In: *The Leading Edge* 30.5, pp. 506–512.

Dou, S. et al. (2017). “Distributed acoustic sensing for seismic monitoring of the near surface: A traffic-noise interferometry case study”. In: *Sci. Rep.* 7, p. 11620.

Favela, J. (2004). “Energy radiation from a multi-story building”. PhD thesis. California Institute of Technology.

Fernandez-Ruiz, M. R., L. Costa, and H. F. Martins (2019). “Distributed acoustic sensing using chirped-pulse phase-sensitive OTDR technology”. In: *Sensors* 19, p. 4368.

Fernandez-Ruiz, M. R., H. F. Martins, et al. (2018). “Steady-sensitivity distributed acoustic sensors”. In: *J. Light. Technol.* 36, pp. 5690–5696.

Godin, O. A. and D. M. F. Chapman (1999). “Shear-speed gradients and ocean seismo-acoustic noise resonances”. In: *J. Acoust. Soc. Am.* 106.5, pp. 2367–2382.

– (2001). “Dispersion of interface waves in sediments with power-law shear speed profiles: I. Exact and approximate analytical results”. In: *J. Acoust. Soc. Am.* 110.4, pp. 1890–1907.

Hamilton, E. L. (1976). “Shear-wave velocity versus depth in marine sediments: A review”. In: *Geophysics* 41.5, pp. 985–996.

Hatchell, P. J., P. B. Wills, and C. Didraga (2009). “Production induced effects on near-surface wave velocities at Valhall”. In: *71st Meeting, European Association of Geoscientists and Engineers, Expanded Abstracts* T016.

Jousset, P. et al. (2017). “Crustal exploration and monitoring seismic events with a fibre-optic cable deployed at the ground surface in Iceland”. In: *EAGE/DGG Workshop on Fibre Optic Technology in Geophysics, EAGE/DGG*.

Karrenbach, M. et al. (2020). “Long-range DAS data acquisition on a submarine fiber-optic cable”. In: *EAGE Workshop on Fiber Optic Sensing for Energy Applications in Asia Pacific, European Association of Geoscientists and Engineers*.

Le Bot, S. et al. (2005). “Geological characteristics and geotechnical properties of Eocene and Quaternary deposits on the Belgian continental shelf: synthesis in the context of offshore wind farming”. In: *Neth. J. Geosci.* 84.2, pp. 147–160.

Li, Z. and Z. Zhan (2018). “Pushing the limit of earthquake detection with distributed acoustic sensing and template matching: A case study at Brady geothermal field”. In: *Geophys. J. Int.* 215, pp. 1583–1593.

Lindsey, N. J., T. C. Dawe, and J. B. Ajo-Franklin (2019). “Illuminating seafloor faults and ocean dynamics with dark fiber distributed acoustic sensing”. In: *Science* 366.6469, pp. 1103–1107.

Lindsey, N. J., E. R. Martin, et al. (2017). “Fiber-optic network observations of earthquake wavefields”. In: *Geophys. Res. Lett.* 44.23, pp. 11792–11799.

Lombardi, D., S. Bhattacharya, and D. M. Wood (2013). “Dynamics soil-structure interaction of monopile supported wind turbines in cohesive soil”. In: *Soil Dyn. Earthq. Eng.* 49, pp. 165–180.

Ma, Y. et al. (2013). “Locating a scatterer in the active volcanic area of Southern Peru from ambient noise cross-correlation”. In: *Geophys. J. Int.* 129.3, pp. 1332–1341.

Mateeva, A. et al. (2013). “Distributed acoustic sensing for reservoir monitoring with VSP”. In: *The Leading Edge* 32.10, pp. 1278–1283.

Mathys, M. (2009). “The quaternary geological evolution of the Belgian Continental Shelf, southern North Sea”. PhD thesis. Universiteit Gent.

Missiaen, T. et al. (2002). “Very high-resolution seismic mapping of shallow gas in the Belgian coastal zone”. In: *Cont. Shelf Res.* 22, pp. 2291–2301.

Mordret, A. et al. (2013). “Near-surface study at the Valhall oil field from ambient noise surface wave tomography”. In: *Geophys. J. Int.* 193, pp. 1627–1643.

Park, C. B., R. D. Miller, and J. Xia (1999). “Multichannel analysis of surface waves”. In: *Geophysics* 64.3, pp. 800–808.

Park, C. B., R. D. Miller, J. Xia, et al. (2005). “Underwater MASW to evaluate stiffness of water-bottom sediments”. In: *The Leading Edge* 24.7, pp. 724–728.

Pastor-Graells, J. et al. (2016). “Single-shot distributed temperature and strain tracking using direct detection phase-sensitive OTDR with chirped pulse”. In: *Optics Express* 24, pp. 13121–13133.

Prendergast, L. J., K. Gavin, and P. Doherty (2015). “An investigation into the effect of scour on the natural frequency of an offshore wind turbine”. In: *Ocean Engineering* 101, pp. 1–11.

Schuster, G. T. et al. (2004). “Interferometric/daylight seismic imaging”. In: *Geophys. J. Int.* 157.2, pp. 838–852.

Seed, H. B. and I. M. Idriss (1970). “Soil moduli and damping factors for dynamic response analyses”. In: *UCB/EERC-70/10, Earthquake Engineering Research Center, University of California at Berkeley*.

Shapiro, N. M. et al. (2005). “High-resolution surface-wave tomography from ambient seismic noise”. In: *Science* 307.5715, pp. 1615–1618.

Shi, J. and D. Asimaki (2017). “From stiffness to strength: Formulation and validation of a hybrid hyperbolic nonlinear soil model for site-response analyses”. In: *Bull. Seis. Soc. Am.* 107.3, pp. 1336–1355.

Sladen, A. et al. (2019). “Distributed sensing of earthquakes and ocean-solid Earth interactions on seafloor telecom cables”. In: *Nature Communications* 10.1, p. 5777.

Spica, Z. J., K. Nishida, et al. (2020). “Marine sediment characterized by ocean-bottom fiber-optic seismology”. In: *Geophys. Res. Lett.* 47.16.

Spica, Z. J., M. Perton, et al. (2020). “Urban seismic site characterization with fiber-optic seismology”. In: *J. Geophys. Res.: Solid Earth* 125.3.

Tanimola, F. and D. Hill (2009). “Distributed fibre optic sensors for pipeline protection”. In: *J. Nat. Gas Sci. Eng.* 1.4–5, pp. 134–143.

Tsai, V. C. and S. Atiganyanun (2014). “Green’s functions for surface waves in a generic velocity structure”. In: *Bull. Seis. Soc. Am.* 104.5, pp. 2573–2578.

Wang, X. et al. (2020). “Rose parade seismology: Signatures of floats and bands on optical fiber”. In: *Seis. Res. Lett.* 91.4, pp. 2395–2398.

Whitehouse, R. J. S. et al. (2011). “The nature of scour development and scour protection at offshore windfarm foundations”. In: *Mar. Pollut. Bull.* 62, pp. 73–88.

Williams, E. F. et al. (2019). “Distributed sensing of microseisms and teleseisms with submarine dark fibers”. In: *Nature Communications* 10.1, p. 5778.

Zeng, X. et al. (2017). “Properties of noise cross-correlation functions obtained from a distributed acoustic sensing array at Garner Valley, California”. In: *Bull. Seis. Soc. Am.* 107.2, pp. 603–610.

Zhan, G., J. P. van Gestel, and R. Johnston (2020). “DAS data recorded by a subsea ubilical cable at Atlantis field”. In: *SEG Technical Program Expanded Abstracts 2020, SEG*.

Zhan, Z. (2020). “Distributed acoustic sensing turns fiber-optic cables into sensitive seismic antennas”. In: *Seis. Res. Lett.* 91.1, pp. 1–15.

Zhan, Z. et al. (2010). “Retrieval of Moho-reflected shear wave arrivals from ambient seismic noise”. In: *Geophys. J. Int.* 182.1, pp. 408–420.

Chapter 4

SURFACE GRAVITY WAVE INTERFEROMETRY AND OCEAN CURRENT MONITORING WITH OCEAN-BOTTOM DAS

Williams, E. F., Z. Zhan, H. F. Martins, M. R. Fernandez-Ruiz, S. Martin-Lopez, M. Gonzalez-Herraez, and J. Callies (2022). "Surface Gravity Wave Interferometry and Ocean Current Monitoring With Ocean-Bottom DAS". In: *Journal of Geophysical Research: Oceans* 127.e2021JC018375.

Abstract

The cross-correlation of a diffuse or random wavefield at two points has been demonstrated to recover an empirical estimate of the Green's function under a wide variety of source conditions. Over the past two decades, the practical development of this principle, termed ambient noise interferometry, has revolutionized the fields of seismology and acoustics. Yet, because of the spatial sparsity of conventional water column and seafloor instrumentation, such array-based processing approaches have not been widely utilized in oceanography. Ocean-bottom distributed acoustic sensing (OBDAS) repurposes pre-existing optical fibers laid in seafloor cables as dense arrays of broadband strain sensors, which observe both seismic waves and ocean waves. The thousands of sensors in an OBDAS array make ambient noise interferometry of ocean waves straightforward for the first time. Here, we demonstrate the application of ambient noise interferometry to surface gravity waves observed on an OBDAS array near the Strait of Gibraltar. We focus particularly on a 3-km segment of the array on the continental shelf, containing 300 channels at 10-m spacing. By cross-correlating the raw strain records, we compute empirical ocean surface gravity wave Green's functions for each pair of stations. We first apply beamforming to measure the time-averaged dispersion relation along the cable. Then, we exploit the non-reciprocity of waves propagating in a flow to recover the depth-averaged current velocity as a function of time using a waveform stretching method. The result is a spatially-continuous matrix of current velocity measurements with resolution <100 m and <1 hr.

4.1 Introduction

Flow occurs across a broad spectrum of space and time scales in the global oceans, from oceanic gyres ($> 10^6$ m and $> 10^6$ s) to small-scale turbulent mixing ($< 10^{-2}$ m and $< 10^1$ s). Instrumental observation of complex oceanic flows is therefore challenging. Contemporary methods are generally divided into two categories: Lagrangian and Eulerian. Lagrangian methods, including floats and drifters, are inherently multi-scale because they follow the motion of a fluid parcel. However, the spatial distribution of drifters is biased by the flow and measurements are not temporally repeatable. Eulerian methods, including moored current meters, acoustic Doppler current profilers (ADCP), and high-frequency (HF) radar, measure flow velocity relative to a fixed point. Bottom-installed ADCP and moored instruments can resolve time-dependent flow at a single location; however, deploying extensive instrument networks is often prohibitively expensive. Conversely, while radar-based methods can capture the spatial complexity of flow, they only measure the flow at the surface.

One innovative approach to ocean current measurement came in the form of ocean acoustic tomography. By comparing the acoustic travel time measured from reciprocal experiments along the same ray path, Worchester (1977) demonstrated that the path-averaged flow speed can be recovered. Repeating the experiment at regular intervals and utilizing an array of sources and receivers, along-path time delays can then be tomographically inverted for spatio-temporal variations in current speed. Ocean acoustic tomography has been employed in diverse environments across spatial scales of $10^2 - 10^6$ m and temporal scales of $10^2 - 10^7$ s (Dushaw et al., 1994; Howe, Worchester, and Spindel, 1987; Lin et al., 2005). But, in spite of these successes, ocean acoustic tomography has not been deployed on a large scale owing to concern about the impact of repeating, active acoustic sources on marine mammals.

More recently, Lobkis and Weaver (2001) demonstrated that cross-correlations of passive recordings of a diffusive wavefield converge to the acoustic Green's function after sufficient temporal stacking, providing a non-invasive alternative to active sources. This method, termed ambient noise interferometry, was quickly adapted from the laboratory scale to global seismology in order to probe the solid Earth without the need to wait for earthquakes (Campillo and Paul, 2003; Shapiro et al., 2005). Ambient noise interferometry was subsequently applied to ocean acoustics (Roux, Kuperman, and the NPAL Group, 2004; Godin, Zabotin, and Goncharov, 2010; Brown, Godin, et al., 2014). And, in an experiment in the Straits of Florida, Godin, Brown, et al. (2014) demonstrated that flow velocities could be recovered from passive hydrophone recordings using travel-time differences in reciprocal measurements. However, passive ocean acoustic tomography has not proven widely successful due to several unique challenges: the strongly time-dependent nature of the ocean environment can inhibit convergence through stacking; autonomous hydrophones can experience significant clock drift; and the relative location of hydrophones can be perturbed by local flow conditions (Brown, Godin, et al., 2014; Godin, 2018).

The theory of ambient noise interferometry has also been extended to ocean surface gravity waves (OSGW) (Godin, Zabotin, Sheehan, et al., 2014; Brown and Lu, 2016). High-frequency OSGW in the 0.03 to 1 Hz band, termed wind waves, are generated by wind stresses at the sea surface throughout the oceans. Wind waves from distant storms can be observed at intermediate frequencies (< 0.1 Hz) as swell. Interaction of wind waves and swell with coastal bathymetry and resonance of wave groups generate lower frequency OSGW termed infragravity waves in the 0.001-0.03 Hz band, which can propagate across ocean basins (Herbers, Elgar, and Guza, 1995). Pressure perturbations from surface gravity and infragravity waves can be observed by seafloor pressure gauges, such as those often deployed with ocean-bottom seismometers (OBS), with the bandwidth determined by water depth (Webb, 1998). Harmon et al. (2012) first cross-correlated pressure gauge data from 5 OBS deployed offshore Sumatra and back-projected the envelope of the noise correlation functions (NCF) to determine infragravity wave source regions. Similar studies have been done by Neale, Harmon, and Srokosz (2015) and Tonegawa et al. (2018) on OBS arrays offshore Cascadia and Japan. Godin, Zabotin, Sheehan, et al. (2014) cross-correlated a year of pressure gauge data from an array of 28 OBS deployed offshore the South Island of New Zealand and used a coherence-based transformation to measure the frequency-dependent directional spectrum of infragravity waves. Focusing instead on higher frequency waves in shallow water, Brown and Lu (2016) proved that cross-correlations of wave height time-series converged to the OSGW Green's function in a controlled wave-tank experiment, but were unable to extract coherent NCF from surface buoy data collected offshore New Jersey. No study has yet attempted to utilize OSGW interferometry to measure ocean currents, but the theory has been demonstrated by Godin (2006) whose general framework for interferometry of acoustic-gravity waves in a moving medium includes the specific case of OSGW propagating in a current.

Here, we build upon this work and propose a novel method for high-resolution measurement of ocean currents by cross-correlation of OSGWs recorded on an ocean-bottom fiber optic cable using distributed acoustic sensing (DAS). Despite the promise of passive current monitoring by acoustic or OSGW interferometry, deployment costs and logistics for autonomous hydrophones, OBS, and pressure gauges are too high for the large-N arrays that would be needed to capture multi-scale variations in flow across oceanic environments. DAS offers a competitive alternative to conventional instrumentation through re-purposing pre-existing submarine telecommunications fibers as networks of ocean-bottom sensors. A DAS system works by transmitting short laser pulses through an optical fiber and recording the backscattered light from micro-scale imperfections in the fiber. When the optical path length between scatterers is modified by deformation (such as from seismic waves, pressure transients, or acoustic vibrations), the recorded backscatter trace exhibits a coherent phase shift from one pulse to the next. The phase shifts measured from each pulse (or pair of pulses) are integrated over consecutive fiber segments and converted to units of physical strain based on a linear scaling. A DAS system thereby transforms an ordinary optical fiber into a dense array of broadband strainmeters with thousands of channels, 1-10 m channel spacing, 0.1-10 kHz sampling rates, and up to $\sim$ 100 km sensing range. Such spatial density is impossible with conventional ocean-bottom or water-column instrumentation.

Over the past decade, DAS has fueled a revolution in large-N geophysical sensing, with broad applications, from vertical seismic profiling and borehole flow monitoring with vertical arrays to receiver functions and surface wave tomography with horizontal arrays (Zhan, 2020; Lindsey and Martin, 2021). Recently, concurrent studies by Lindsey, Dawe, and Ajo-Franklin (2019), Sladen et al. (2019), and Williams et al. (2019) demonstrated that DAS applied to optical fibers in submarine cables (ocean-bottom DAS or OBDAS) could record both seismological and oceanographic phenomena, observing earthquakes from local to teleseismic distances as well as local OSGW, swell, and infragravity waves. In particular, Williams et al. (2019) showed that OSGW directional spectra observed with OBDAS exhibited a clear Doppler shift indicating the presence of a current. Lindsey, Dawe, and Ajo-Franklin (2019) also speculated about possible signatures of internal gravity waves and tidal bores, and later Ide, Araki, and Matsumoto (2021) reported tidal signals in deep water. Yet, the oceanographic applications of OBDAS remain largely unexplored.

In this paper, we utilize the non-reciprocity of OSGW ambient noise cross-correlation functions (NCFs) computed from passive OBDAS data to measure spatio-temporal variations in ocean current velocity. In Section 2, we introduce our data set, a 4.5 day DAS recording from a sea floor power cable in the Strait of Gibraltar. OSGWs are the dominant signal observed in shallow water ($<$ 150 m), consisting of both wind waves and swell, which are strongly modulated by the tides. We demonstrate that the DAS is sensitive to sea floor pressure perturbations, though the mechanism of strain transfer to the fiber remains ambiguous. In Section 3, we describe our processing workflow. After computing OSGW NCFs, we first invert for the water depth and current velocity that describe the time-averaged OSGW dispersion relation measured along the cable. Then, we use a waveform stretching method to measure differential changes in current velocity between each pair of channels as a function of time. In Section 4, we present the result: a spatially-continuous matrix of current velocity time-series across a 3-km cable segment over a period of 4.5 days. In Section 5, we compare these results to a tidal current model, and also verify that the measurements are consistent with the primitive approach of Williams et al. (2019). Then, we discuss potential sources of bias and sensitivity to depth-dependent flow, which are demonstrated with synthetic data sets. Finally, we review our findings and discuss the generalizability of the method.

4.2 Data

4.2.1 Strait of Gibraltar DAS acquisition

We analyze OSGW in DAS data recorded on an optical fiber within a 30-km seafloor power cable running from Spain to Morocco across the Strait of Gibraltar (Fig. 4.1). The fiber was interrogated by a chirped-pulse DAS system built by Aragon Photonics and operated by the University of Alcala (Pastor-Graells et al., 2016; Fernandez-Ruiz, Martins, et al., 2018) for 22 days during October 2019, of which we use 4.5 days' continuous data between 2019-10-21 18:38:00 UTC and 2019-10-26 06:38:00 UTC. A review of the chirped-pulse DAS method is given by Fernandez-Ruiz, Costa, and Martins (2019). The DAS system recorded the finite strain over a 10 m gauge length every 10 m along the fiber, for a total of 2976 channels. Throughout this paper we adopt the notational convention that strain is expressed as $1\varepsilon \equiv 1m/m$, such that $1n\varepsilon \equiv 10^{-9}m/m$. The original data was recorded at 1 kHz and later down-sampled to 1 Hz for this study.

The fiber path runs in a north-south arc immediately east of Camarinal Sill, with the northern landing site about 5 km west of Tarifa and the southern landing site due south of Tarifa on the Morocco coast near Ksar es-Seghir. The maximum water

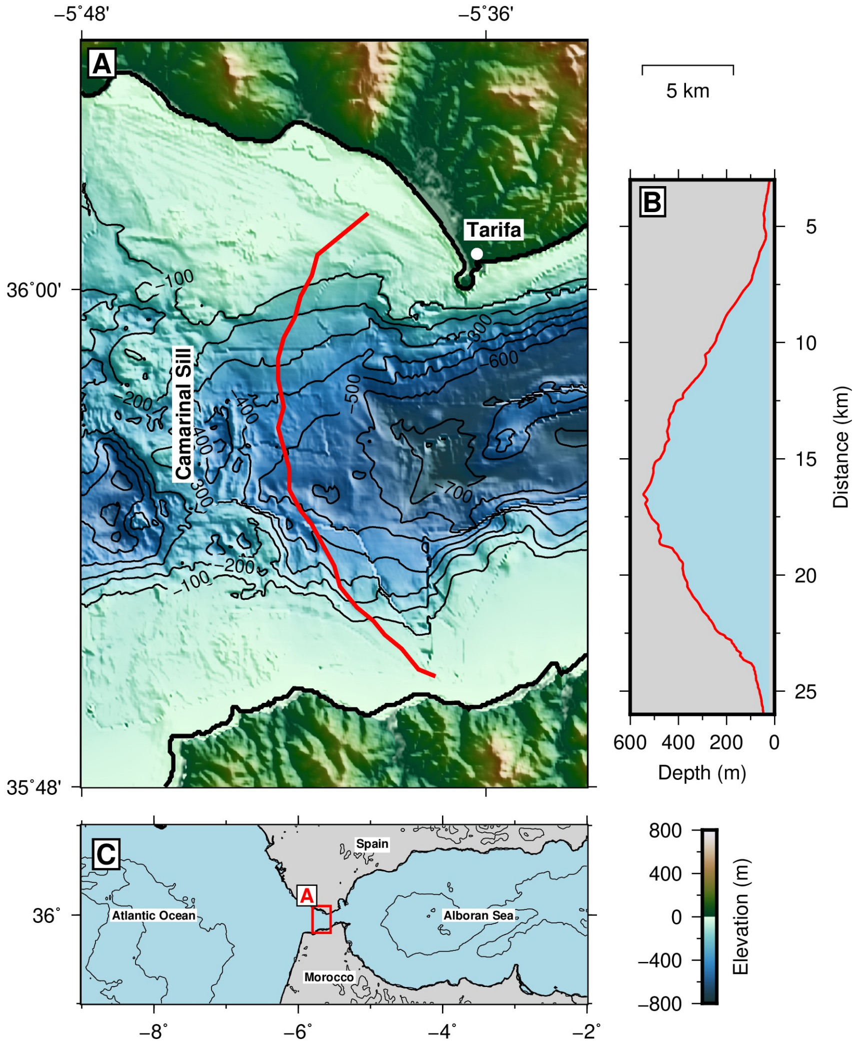

Figure 4.1: (A) Map of cable path across the Strait of Gibraltar, crossing between the Camarinal Sill and Tarifa Narrows. (B) Cable depth profile interpolated from the local EMODnet bathymetry grid (EMODnet Bathymetry Consortium, 2020). (C) Regional setting of (A).

depth along the cable is ~ 550 m. Over the first 8.5 km near Spain, the cable is generally buried, beyond which it is exposed at the seafloor. However, the depth of burial is poorly constrained, and several free spans (sections of cable that are hanging freely in the water column above the sea floor due to locally rough bathymetry) have been noted by the cable operators in past reconnaissance. Channels on the northern end of the cable near the Spanish coast exhibit clearer ocean wave signals than channels on the southern end of the cable, and we focus only on the northern end of the cable in this study. Due to security concerns, the cable landing locations have been omitted from Figure 4.1.

4.2.2 OSGW signals in DAS data

From the Spanish shoreline to about 9-km along the cable, OSGWs are the main signal observed in the Strait of Gibraltar DAS dataset, dominating the unfiltered data between 0.03-0.3 Hz. Waves propagating towards the shore (northeast along the cable) are significantly stronger than waves propagating away from shore (southwest along the cable). Yet, waves in both directions can be discerned by eye in the raw data (Fig. 4.2A). The apparent phase speed is about 10 m/s, and the phase speed appears to increase with distance along the cable as the water depth increases (Fig. 4.2A). A frequency-wavenumber (FK) transform separates the wavefield components by direction of propagation and phase speed. Fig. 4.2B shows a FK spectrum calculated for 1 hr and 300 channels of DAS data, which demonstrates that the waves observed here generally follow the theoretical dispersion relation for OSGWs:

$$\omega^2 = gk \tanh(kh) \tag{4.1}$$

where ω is angular frequency, k is angular wavenumber, h is the water depth, and g is gravitational acceleration. The FK spectrum appears broader than the curve defined by Eq. 4.1 because waves crossing the linear array at oblique angles exhibit higher apparent velocity and smaller apparent wavenumber. To be consistent between time-domain, FK-domain, and cross-correlation representations, throughout this paper we will generally follow the convention that distance increases away from the interrogator unit (southward along the fiber from the Spanish coast) and that distances/wavenumbers are positive. Consequently, waves travelling northeast towards shore (landward) have negative time, negative frequency, and negative speed; whereas, waves travelling in the opposite direction (seaward) have positive quantities.

The median hourly power spectral densities (PSD) for the 800 channels between 2 and 10 km optical distance are plotted in Fig. 4.2C. The cable is subaerial until the landing point at 2.7 km. Beyond 2.7 km, the OSGW spectrum is the strongest feature, consisting of two overlapping peaks between 0.05 and 0.4 Hz. The higher frequency peak represents locally generated wind waves, with a central period that decreases systematically from 6 s to 8s over the first 4-5 km, beyond which it merges with the lower frequency peak. The lower frequency peak represents swell and has a central period of about 14 s, which is invariant with water depth. While the double relationship between these two peaks mimics the double-frequency shape of the global microseism spectrum, the two peaks are unlikely to be related here. The 6-8 s peak obeys the dispersion relation for free OSGW (Fig. 4.2B), which is

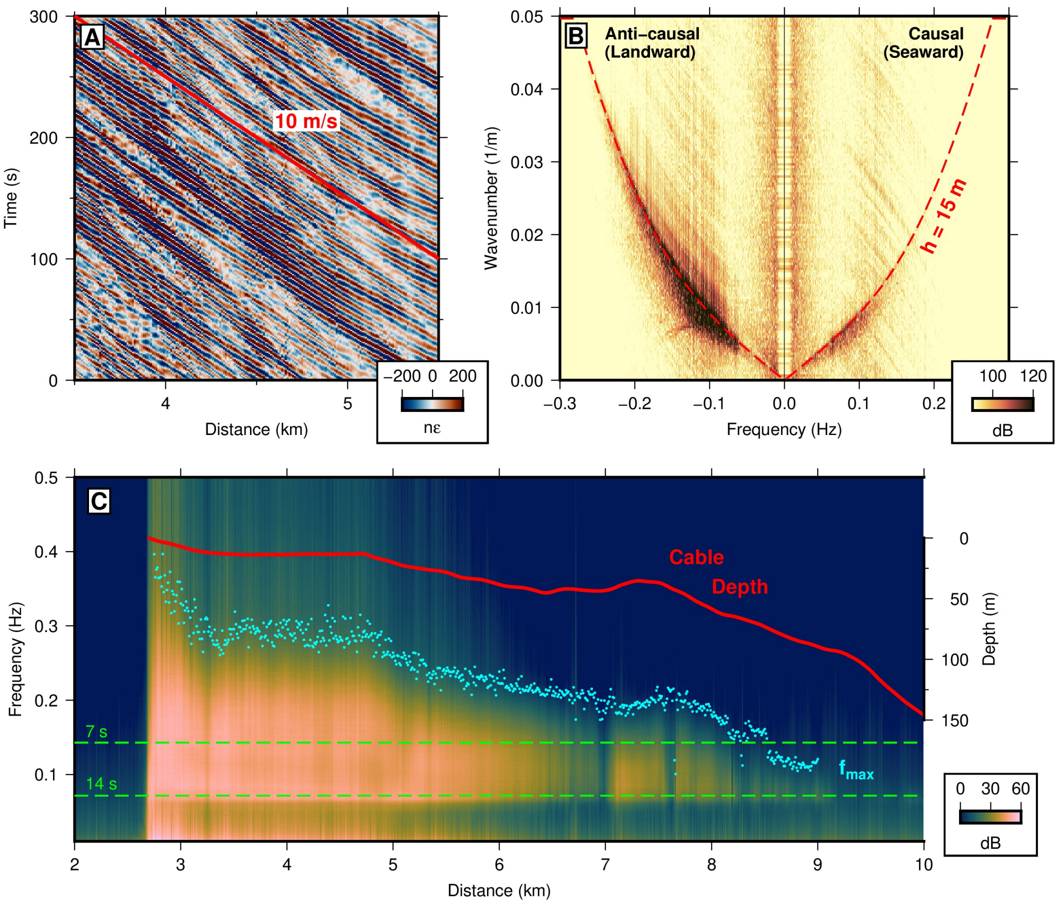

Figure 4.2: (A) Raw data gather showing strong ocean surface gravity waves (OSGW) propagating NE along the cable towards Tarifa, and weak OSGW propagating in the opposite direction. (B) Frequency-wavenumber (FK) spectrum of 1 hr and 300 channels of raw data, with theoretical dispersion relations for 15 m (red) water depth from Eq. 4.1 (units are dB relative to 1 $n\varepsilon^2 \times s \times m$). (C) Median power spectral density (PSD) for each channel in the first 10 km of the cable, plotted with cable depth (red) and the calculated maximum frequency (blue) (units are dB relative to 1 $n\varepsilon^2/Hz$).

incompatible with the non-linear term that the Longuet-Higgins (1950) theory of secondary microseism generation predicts at 7 s for a 14-s primary swell. Rather, the 6-8 s peak is representative of a sea state determined by local meteorological conditions. A weather station near Tarifa reported an average wind speed around 8 m/s during the experiment (Fig. 4.3B), which corresponds to a modal period of about 6 s according to the Pierson-Moskowitz wave spectral formulation (Pierson and Moskowitz, 1964; Ochi, 1998).

The spectral amplitude of both OSGW peaks decreases with water depth, and the signal disappears shortly after 9 km distance, where the water depth is about 100 m (Fig. 4.2C). Previous OBDAS studies have also observed decreasing depth-dependent OSGW amplitude, consistent with pressure in the linear theory of free surface gravity waves (Lindsey, Dawe, and Ajo-Franklin, 2019; Sladen et al., 2019; Williams et al., 2019). The pressure perturbation p_d beneath an OSGW of height ζ decays exponentially with water depth as

$$p_d(z) = \rho g \zeta \frac{\cosh(k(h+z))}{\cosh(kh)} \tag{4.2}$$

such that $p_d(z=-h) = \rho g \zeta / \cosh(kh)$ at the seafloor. Several localized decreases in ocean wave SNR, seen as vertical stripes in Fig. 4.2C, are present along the cable, most notably at 3.2, 7, and 7.7 km. These could correspond to sharp bathymetric features such as channels, sections of increased cable burial depth, or free spans where the cable coupling (and thereby the nature of the measurement) differs. The OSGW bandwidth is also strongly modulated by water depth. The maximum frequency in the first 0.5 km after the landing point decreases rapidly from 0.4 to 0.28 Hz as the water depth increases to about 10 m. This rapid transformation of high-frequency wave energy in shallow water is likely enhanced by non-linear wave-wave interactions and surf-zone breaking, which have been widely observed to broaden the wave spectrum (e.g. (Elgar and Guza, 1985; Herbers, Orzech, et al., 2003)). Along the next 6 km, the maximum frequency of the higher OSGW peak follows the bathymetry closely, including a flat segment from 3.2 to 4.7 km where the shelf is level and an increase from 7 to 8 km where there is a local bathymetric high. To aid in visualizing this trend, the inflection point in the spectrum where the OSGW signal drops below the instrumental noise floor (f_{max}) was measured from the second derivative of the smoothed spectrum and plotted in Fig. 4.2C (blue dots). The minimum swell frequency of ~ 0.05 Hz does not change with water depth. Eq. 4.2 implies that when the wavelength is close to the water depth ($kh \sim 2\pi$), the OSGW pressure at the seafloor vanishes. Following W. C. Crawford, Webb, and

Hildebrand (1991), we can then predict the maximum frequency at which OSGW are observable from Eq. 4.1, as

$$f_{max} = \sqrt{\frac{g}{2\pi hn}} \tag{4.3}$$

where $n = 2\pi/kh \sim 1$. We revisit these relationships in the following section.

Spectrograms for three individual channels (at 3, 6, and 9 km) are shown in Fig. 4.3, along with weather and tide data from a station in Tarifa. The high-frequency wind waves are strongly tidally modulated, with both the spectral amplitude and the maximum frequency at their highest during low tide. One simple mechanism for this modulation is purely observational—an ocean-bottom instrument is closer to the surface at low tide and experiences a stronger pressure perturbation. This effect is described by Eq. 4.3, which we evaluate with the tide gauge data from Fig. 4.3A and plot as blue lines on Fig. 4.3C,E,G. While the phase of the predicted modulation is consistent with the spectrogram observation and the effect diminishes similarly with depth (the tidal change in sea level is a smaller fraction of total water depth), the variation in f_{max} is underestimated by at least a factor of two. Additionally, both the bandwidth and minimum frequency of the swell are tidally modulated over the last three days of the experiment, which can not be described by the change in water depth alone. The phase of the modulated swell is also ahead of the wind waves by at least 45 degrees. These features are illustrated schematically by the dashed black lines on Fig. 4.3C. Together, these effects suggest that non-linear wave-current interaction mechanisms are necessary to describe the spatio-temporal variation of the OSGW spectrum recorded here.

Another clear time-dependent feature is the enhancement of wind wave energy between 0.1-0.3 Hz on days 2-3 of the dataset (Fig. 4.3). The high frequency band suggests that local excitation, and not a passing storm or other distant event, is responsible. One possible explanation is that the dominant wave direction rotates into the azimuth of the cable for these two days. DAS measures longitudinal strain, and therefore is more sensitive to slow waves and particle motion parallel to the fiber (Martin et al., 2018). The dominant wind direction is approximately parallel to the cable for the entire experiment: for hours 0-12 and 72-108 the wind is from the northeast along the cable, and for hours 12-72 the wind is from the southwest 180 degrees opposing (Fig. 4.3B). Throughout all 4.5 days, the stronger component of OSGW is observed to be propagating to the northeast towards shore (Fig. 4.2B), and the amplitude ratio of the two directional components remains approximately

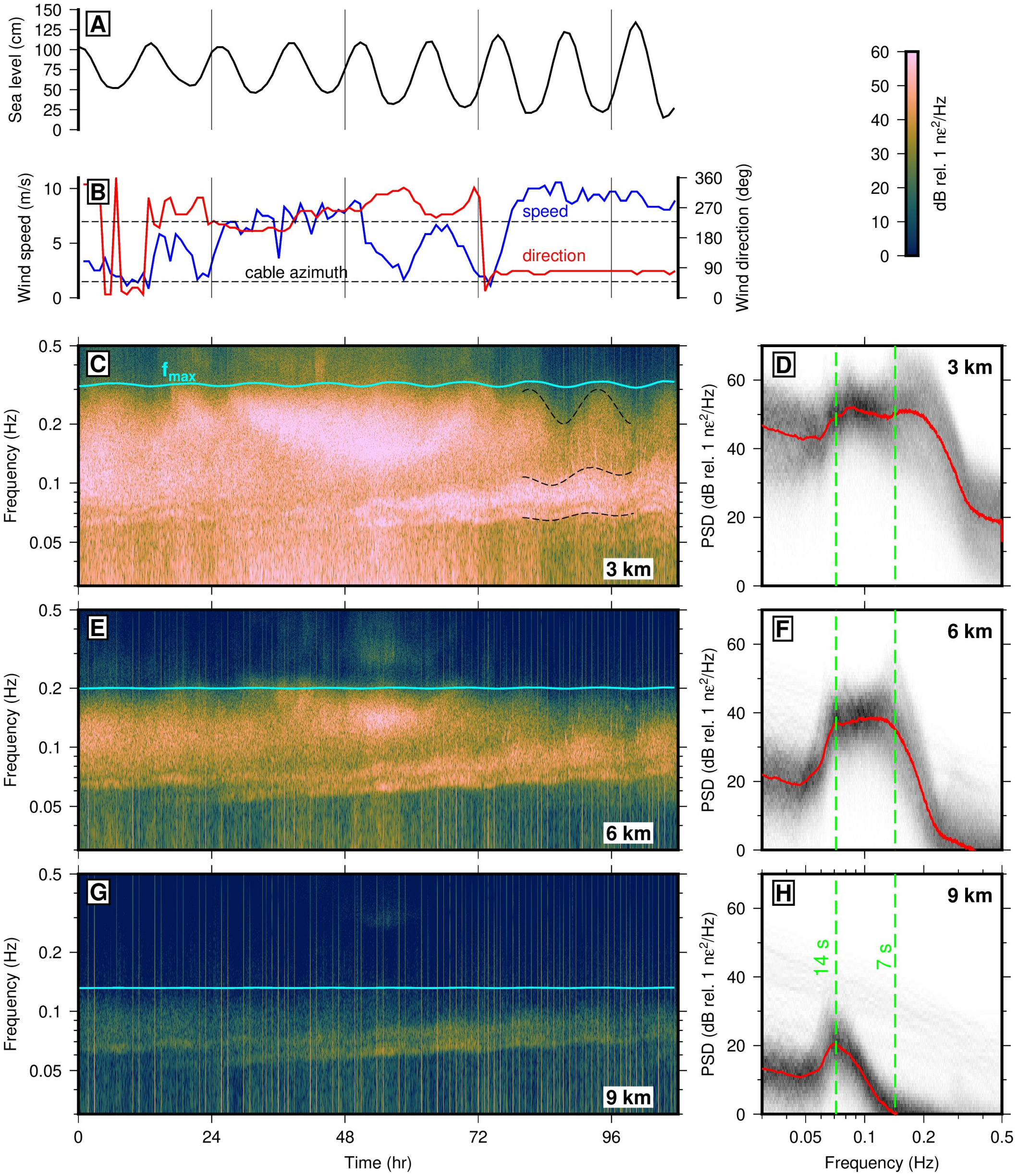

Figure 4.3: (A) Data from a tide gauge in Tarifa during the experiment. (B) Data from a weather station in Tarifa showing wind speed (blue), wind direction (red), and the azimuth of the cable (black). (C,E,G) Spectrograms for individual channels at 3, 6, and 9-km cable distance showing the temporal evolution of ocean wave signals. Blacked dash lines illustrate the tidal modulation of wind wave and swell energy. (D,F,H) Noise probability density functions (PDFs, normalized histograms of (C,E,G)) for the same channels with the median power spectral density (PSD) plotted in red.

constant. Because the shallow cable segment is close to the coast on the northeast side (Fig. 4.1), this suggests that waves propagating southwest away from shore are primarily the result of coastal reflection, and, as the coastal reflection coefficient does not vary in time, changes in the point spectrum (e.g. Fig. 4.3C) must result from varying wave conditions in the Strait to the south. The 3-6 km cable segment will observe waves generated south of this segment by the southwesterly wind on days 2-3, whereas waves generated in the same location by the northeasterly wind on other days will propagate away from the array. However, the wind speed is significantly higher on days 4-5 when the wind wave signal is weakest. Quantitative modeling would be necessary to definitively identify the cause of this high-frequency wave event.

4.2.3 The nature of the measurement

The measurement principle of DAS when applied as a seismometer relies on the assumption that changes in optical path length in the fiber are dominated by deformations of the physical fiber length, i.e. elastic strains. However, DAS is sensitive to temperature as well—the combined effects of temperature on the index of refraction and thermal expansion equate to an equivalent elastic strain of 1 nε per 10 mK. At seismic frequencies, thermal signals can be neglected (Lindsey, Rademacher, and Ajo-Franklin, 2020), but at tidal frequencies and in submarine environments with significant temperature gradients, temperature effects may dominate the DAS measurement (Ide, Araki, and Matsumoto, 2021). Throughout the experiment, observed OSGW amplitudes are on the order of 100 nε between 3-6 km where the average water depth is about 40 m. This equates to a temperature signal of order 1 K, which is unreasonable given typical stratification and OSGW displacement near the seafloor. The effect of temperature can therefore be neglected here.

Having established that OSGW observations in OBDAS data from the Strait of Gibraltar represent elastic strain of the fiber element within the cable, we must consider how the DAS measurement is related to OSGW physical quantities. As described above, Eq. 4.3 describes the maximum frequency at which seafloor observation of OSGW pressure is possible. Plotting the observations of f_{max}^2 for each channel from Fig. 4.2C against the bathymetric prediction $\frac{g}{2\pi h}$, Fig. 4.4A shows that $n \approx 1$ over the 3.2-9 km cable segment, meaning that frequency band of OBDAS strain scales consistently with pressure. The only exception is in the 0.5 km closest to shore in $<$ 10 m water depth, where $n > 2$, meaning that the observed f_{max} is lower than predicted by the water depth. This is likely a result of the instrumental noise floor being higher for the individual channels in the surf zone which are saturated with strong wave energy, so the observed f_{max} corner appears lower even though the wave energy is higher.

On conventional OBS, surface gravity waves are observed on both the pressure gauge and seismometers, indicating that the hydrodynamic pressure from gravity waves is large enough to deflect the seafloor—a likely mechanism by which OSGW pressure is related to OBDAS strain. The measure of this deflection is termed seafloor compliance (the ratio of displacement to applied stress, $\xi = u/\tau_{zz}$), and has been used for both OSGW in shallow water (Yamamoto and Torii, 1986) and infragravity waves in deep water (W. C. Crawford, Webb, and Hildebrand, 1991) to constrain the elastic structure of oceanic lithosphere. OBDAS measures the average horizontal strain over a gauge length ($\varepsilon_{xx}^{L} \approx \frac{1}{L}\int_{-L/2}^{L/2} \varepsilon_{xx} dx$), which is close to the horizontal strain at a point when the wavelength is much longer than the gauge length ($\varepsilon_{xx}^{L} \approx \varepsilon_{xx} = \partial_x u_x = k u_x$). Consequently, the relationship between the applied pressure at the seafloor from OSGW and the horizontal strain observed by OBDAS is the normalized horizontal compliance

$$\eta_x = k\frac{u_x}{\tau_{zz}} = \frac{\varepsilon_{xx}}{p_d} = \frac{\lambda + 2\mu}{2\mu(\lambda + \mu)} \tag{4.4}$$

where (λ, μ) are the Lamé parameters in the linearized solution for a uniform elastic half-space (W. C. Crawford, 2004). Normalized horizontal compliance at the high frequencies of wind waves considered here has not yet been studied and is strongly dependent on the V_P/V_S ratio of shallow sediments, which can vary by an order of magnitude. At 0.01 Hz, $\eta_x \sim 10^{-10}$ to 10^{-9} Pa^{-1} (Doran and Laske, 2016). At 0.1 Hz, plausible values of normalized horizontal compliance could range from 10^{-9} at $V_P/V_S = 2$ to 10^{-7} Pa^{-1} at $V_P/V_S = 20$, using the method of W. C. Crawford, Webb, and Hildebrand (1991) with a generic crustal velocity model and varying V_S in the top 20 m.

We compare the OBDAS strain amplitude spectrum ($E_{xx} = |\mathcal{F}[\varepsilon_{xx}]|$, where $\mathcal{F}$ denotes the Fourier transform) with the expected scaling of seafloor pressure at three frequencies in Fig. 4.4B,C,D for each channel between the landing point and 9 km. Combining the pressure-depth scaling of OSGW (Eq. 4.2) with the definition of compliance (Eq. 4.4), we obtain

$$E_{xx}(\omega) = \eta_x \left(\frac{\rho g S(\omega)}{\cosh(kh)}\right) \tag{4.5}$$

where $S = |\mathcal{F}[\zeta]|$ is the Pierson and Moskowitz (1964) spectrum for wave height (evaluated for a modal period of 6 s and converted into units of m/Hz$^{1/2}$). While

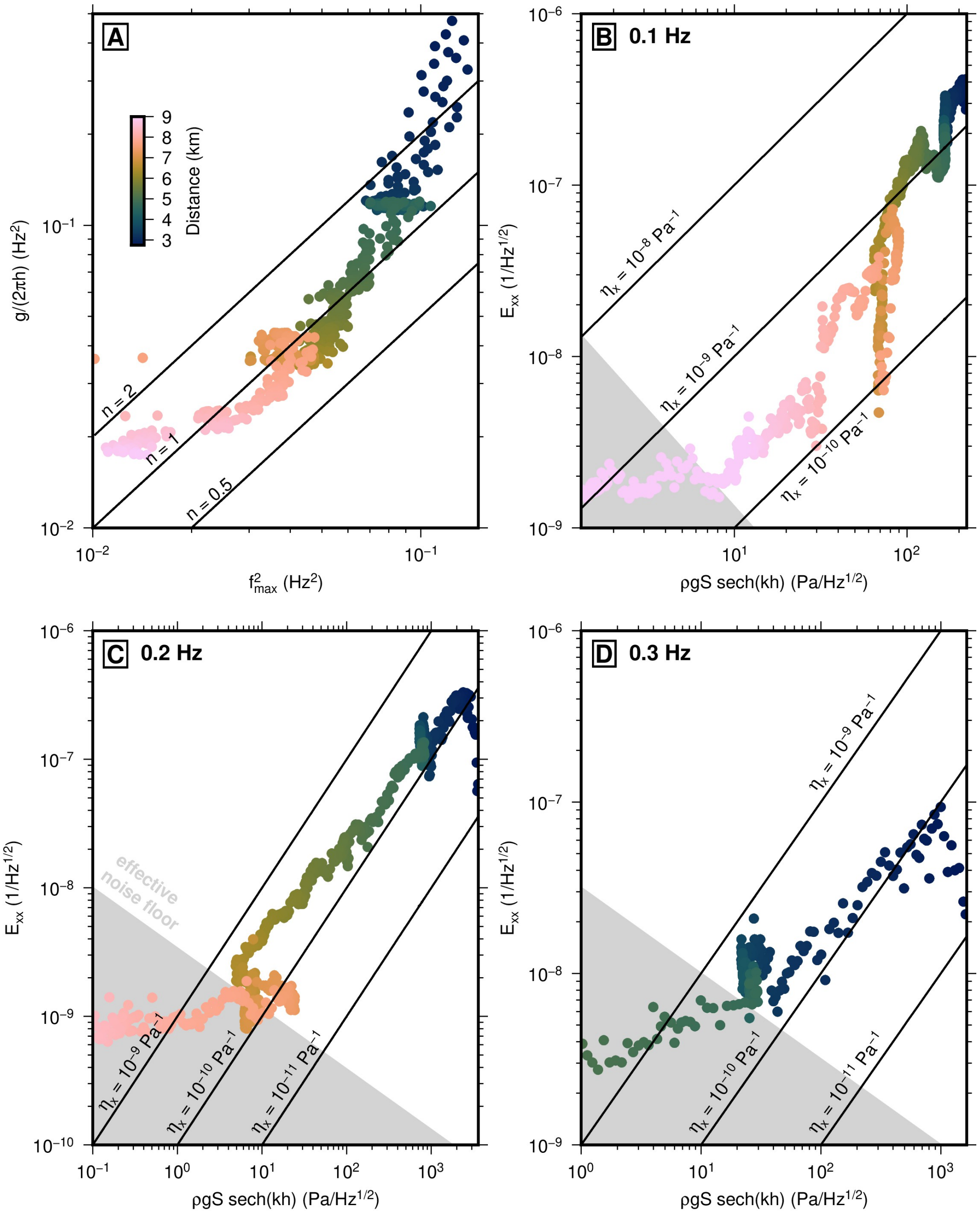

Figure 4.4: (A) Scaling between water depth and the maximum frequency of OSGW (f_{max}) according to Eq. 4.3. Each point represents an individual channel, colored by distance along the cable. (B) Scaling between observed strain amplitude spectrum (E_{xx}) and modeled seafloor pressure spectrum ($\rho g S/\cosh(kh)$) according to Eq. 4.5. (C,D) Same as (B) but for 0.2 Hz and 0.3 Hz respectively. The point where OSGW signals fall below the instrumental noise floor is indicated with gray shading.

Eq. 4.2 is derived under the assumption of a rigid seafloor, the relative contribution of seafloor deformation to the ocean-bottom pressure field is small and can be neglected for reasonable values of compliance (Yamamoto and Torii, 1986; Latychev and Edwards, 2003). Note that the pressure-depth scaling in each panel of Fig. 4.4B,C,D differs because $k = k(\omega, h)$ following Eq. 4.1. The near-horizontal tail in the bottom-left corner of each panel represents instrument noise at channels where the OSGW signal is too weak to be observed, as delineated by f_{max} in Fig. 4.2C.

At 0.2 and 0.3 Hz (Fig. 4.4C,D), the observed strain generally follows the linear functional form predicted by compliance theory (Eq. 4.5), which offers further evidence that OBDAS is observing a quantity proportional to OSGW dynamic pressure. The value of normalized horizontal compliance is approximately 10^{-10} Pa^{-1} at both 0.2 and 0.3 Hz, which is 10 to 1000 times too small to be physically plausible. Laboratory experiments have demonstrated that the amplitude response of DAS (the difference between observed and applied strain) is flat across the range of frequencies examined here, though field experiments have shown that the design or installation properties of the cable may affect the apparent amplitude response by mediating strain transfer to the fiber (Lindsey, Rademacher, and Ajo-Franklin, 2020; Paitz et al., 2021). Submarine cables often include a gel layer designed specifically to protect the interior components from strain during deployment, so the strain experienced by the fiber may be much smaller than the exterior deformation of the seafloor. A second possible explanation for the amplitude discrepancy relates to the use of a point spectrum for sea surface height. Realistic wind-driven ocean wave fields exhibit a non-isotropic directional spectrum, meaning that the horizontal displacement spectrum of the seafloor from OSGW compliance is azimuthally dependent. In previous analysis of OBS horizontal compliance data, Doran and Laske (2016) rotated the horizontal seismometer components into the direction that maximized coherence with the pressure gauge. Because DAS only measures one wavefield component, such a correction is impossible, and the probability that the cable is oriented away from the principal wave direction is high. Consequently the observed horizontal strain is only a fraction of the total seafloor deformation that would be predicted from a point spectrum of sea surface height. Finally, cable burial could explain the low strain amplitude, because compliant deformation under OSGW loading decays exponentially with depth below the seafloor (W. C. Crawford, Webb, and Hildebrand, 1991; W. C. Crawford, 2004). The depth of burial has not been mapped for this cable, so the effect of burial cannot be evaluated. Notably, Lior et al. (2021) found that earthquake strain amplitudes observed on an unburied, light weight seafloor cable were consistent with nearby seismometer records after accounting for the direction of wave propagation.

At 0.1 Hz (Fig. 4.4B), the observed strain is not consistent with the expected pressure-depth scaling from Eq. 4.5. The values of compliance shown in Fig. 4.4B are less realistic because the wave energy at 0.1 Hz is dominated by swell, which is not adequately described by the Pierson and Moskowitz (1964) spectrum. However, we still expect to observe the same linear scaling. Instead, the necessary value of η_x increases by a factor of 10 from deep water at 9 km to the landing point at 2.7 km, indicating that, after accounting for the difference in water depth, the amplitude systematically increases towards the coast. This increase in apparent amplitude may represent a change in the cable-seafloor elastic coupling or burial depth beyond $\sim$ 6 km cable distance. Because the wavelength at 0.1 Hz is long compared to the water depth ($\lambda \approx 100$ m), growth of swell amplitude due to shoaling on the sloping bathymetry may also contribute.

Alternatively, if the cable is unburied or poorly coupled to seafloor sediments, the observed relationship between OSGW dynamic pressure and OBDAS strain may result from direct pressure loading of the cable and not compliant deformation of the seafloor. In this case, a local change in pressure exerts an isotropic radial stress on the cable, resulting in longitudinal strain according to the Poisson's ratio of the cable itself. Mecozzi et al. (2021) considered the effect of direct pressure loading to account for ocean swell observations on Google's transoceanic Curie cable and estimated a sensitivity of $\frac{\varepsilon}{\Delta p} \approx 3 \times 10^{-9}$ Pa^{-1}. The result of Mecozzi et al. (2021) is also consistent with the transfer function between OBDAS and a collocated pressure gauge reported by Matsumotu et al. (2021) for high-frequency hydroacoustic waves. This value is about 10 times too large to account for the observed strain here and is of similar magnitude to the normalized horizontal compliance discussed above. Because the deep sea Curie cable is a telecommunications cable (centimeter-scale diameter and light-weight construction), whereas the data analyzed here is from a power cable (decimeter-scale diameter with three insulated metal conductors), differences in construction could account for a reduction in Poisson's ratio and account for our observation of $\frac{\varepsilon_{xx}}{p_d} \approx 10^{-10}$ Pa^{-1}.

In summary, OBDAS is sensitive to the hydrodynamic pressure from OSGW, but the mechanism by which seafloor pressure is transferred to the cable remains ambiguous. Further calibration experiments are needed to constrain the sensitivity of OBDAS, ideally including in-situ measurements of ocean-bottom pressure and directional wave spectra. Importantly, both mechanisms of pressure-to-strain conversion considered above have a flat phase response. Therefore OBDAS data can be treated as ocean-bottom pressure data for the purposes of ambient noise interferometry in the analysis that follows.

4.3 Methods

4.3.1 OSGW interferometry

The OSGW field measured at any point in time and space represents the superposition of waves generated by a distribution of diverse sources. Such measurements are not repeatable, but OSGW observations appear coherent across a broad range of space and time scales (Webb, 1986; Webb, Zhang, and W. Crawford, 1991) both because the individual wavefield components propagate deterministically in a shared continuum and because the sources tend to obey quantifiable statistics (Ochi, 1998). These same properties are observed for ambient seismic and ocean acoustic noise. Provided the wavefield is sufficiently diffuse, cross-correlation (interferometry) of ambient noise time-series recorded at two points yields an empirical approximation of the Green's function for waves propagating between those points (e.g. Godin, Zabotin, Sheehan, et al. (2014), Brown and Lu (2016)):

$$x_{AB}(t) = \int_{-\infty}^{\infty} u_A(\tau) u_B(t+\tau) d\tau \propto d(t) * [g(B|A,t) + g(A|B,-t)] \tag{4.6}$$

Here, x_{AB} is the noise cross-correlation function (NCF) between the wavefield u recorded at points A and B, and d collapses the source terms of the ambient wavefield and should approximate a delta function. The Green's function terms $g(B|A,t)$ and $g(A|B,-t)$ represent wave propagation along reciprocal ray paths between A and B. When applied to seismic waves in the solid earth, the reciprocity relation dictates that $g(B|A,t) = g(A|B,t)$, and the NCF is symmetric. However, for waves in a moving medium, such as OSGW propagating in a current, $g(B|A,t) \neq g(A|B,t)$; rather, $g(B|A,t) = \tilde{g}(A|B,t)$, where $\tilde{g}$ denotes the Green's function in a medium where the flow is reversed (Godin, 2006). The flow velocity directly dictates the degree of non-reciprocity, and thereby the asymmetry of the NCF (Eq. 4.6). This property was used by Godin, Brown, et al. (2014) with acoustic interferometry to measure flow between hydrophones, and we can exploit it again here to map the spatio-temporal variation of current speed along the Strait of Gibraltar OBDAS array.

To compute cross-correlations, we select only channels 300–600 where the OSGW energy is strong, broadband, and spatially smooth (no sharp changes in cable prop-

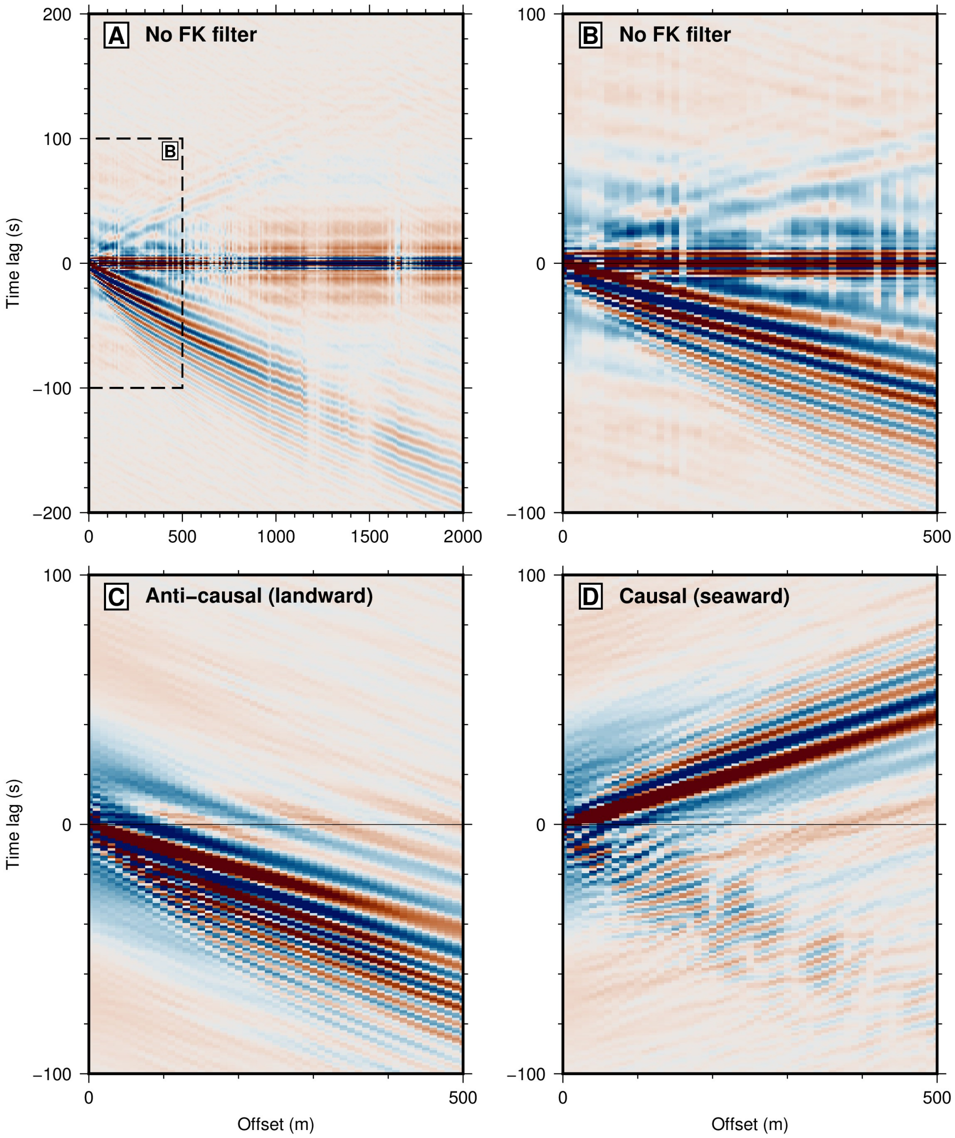

Figure 4.5: Example virtual source gather formed by cross-correlating channel 350 (at 3.5 km) with all channels between 350 and 550 (5.5 km). (A) Virtual source gather computed without FK filtering, and (B) same as (A) but zoomed in to the first 500 m offset. (C,D) Same as (B) but with FK filtering selecting negative (landward propagating) speeds and positive (seaward propagating) speeds, respectively. Amplitude is normalized to arbitrary units during spectral whitening (0.01-0.5 Hz).

erties), and divide the 108-hr dataset into 215 1-hr subsets overlapping by 50%. For each hour, we apply FK filters with a pass-band of $c = f/k \in [2, 50]$ m/s and $c \in [-50, -2]$ m/s to separate the data into separate workflows for positive and negative wavespeeds (causal and anti-causal time lags) and eliminate all non-OSGW signals. The rest of the processing closely follows the standard workflow proposed by Bensen et al. (2007): the filtered, hourly data subsets are divided further into 8.5-minute (512 sample) windows, spectral normalization is applied to each channel over $f \in [0.01, 0.5]$ Hz, each pair of channels is cross-correlated in the frequency domain for a total of $N(N+1)/2 = 45150$ pairs, and the 8.5-minute windows are normalized and stacked to form hourly NCFs. The result is 215×45150 hourly NCFs for each of the causal and anti-causal wavefield components.

An example virtual source gather (the cross-correlation of one channel with each adjacent channel in a subarray) stacked over the complete 4.5 day dataset is shown in Fig. 4.5, illustrating how the interferometric processing transforms a random wavefield (as in Fig. 4.2A) into an organized wavefield, with a single OSGW packet propagating away from a point source. Fig. 4.5A,B show the result of processing if the FK filtering step is omitted, while Fig. 4.5C,D show the separated results. Without FK filtering, NCFs are imbalanced between causal and anti-causal time lags, with much stronger wave energy propagating towards the shore as observed in the raw data. Spectral whitening is applied before cross-correlation in order to boost the contribution from weaker frequencies that still have coherent phase information, which has an unbalanced effect if the raw data is dominated by a single directional component. By separating the causal and anti-causal components into the separate workflows, the high frequency energy propagating away from the shore is enhanced. Instrumental noise that concentrates at zero lag in cross-correlations can also be mitigated by FK filtering the raw data. However, FK filtering does introduce some spatial smoothing, which may result in loss of resolution, and sharp features in the data such as poorly-coupled channels can introduce ringing artifacts if not treated carefully.

4.3.2 Current measurement

In order to measure current velocity, we compare NCFs for the two directional wave components and fit the non-reciprocity with a dispersion relation that describes OSGW propagating in a current. In the absence of a current, the OSGW problem reduces to the 2D Helmholtz equation, which can be expressed either in terms of wave height or ocean-bottom pressure (see Godin, Zabotin, Sheehan, et al. (2014)

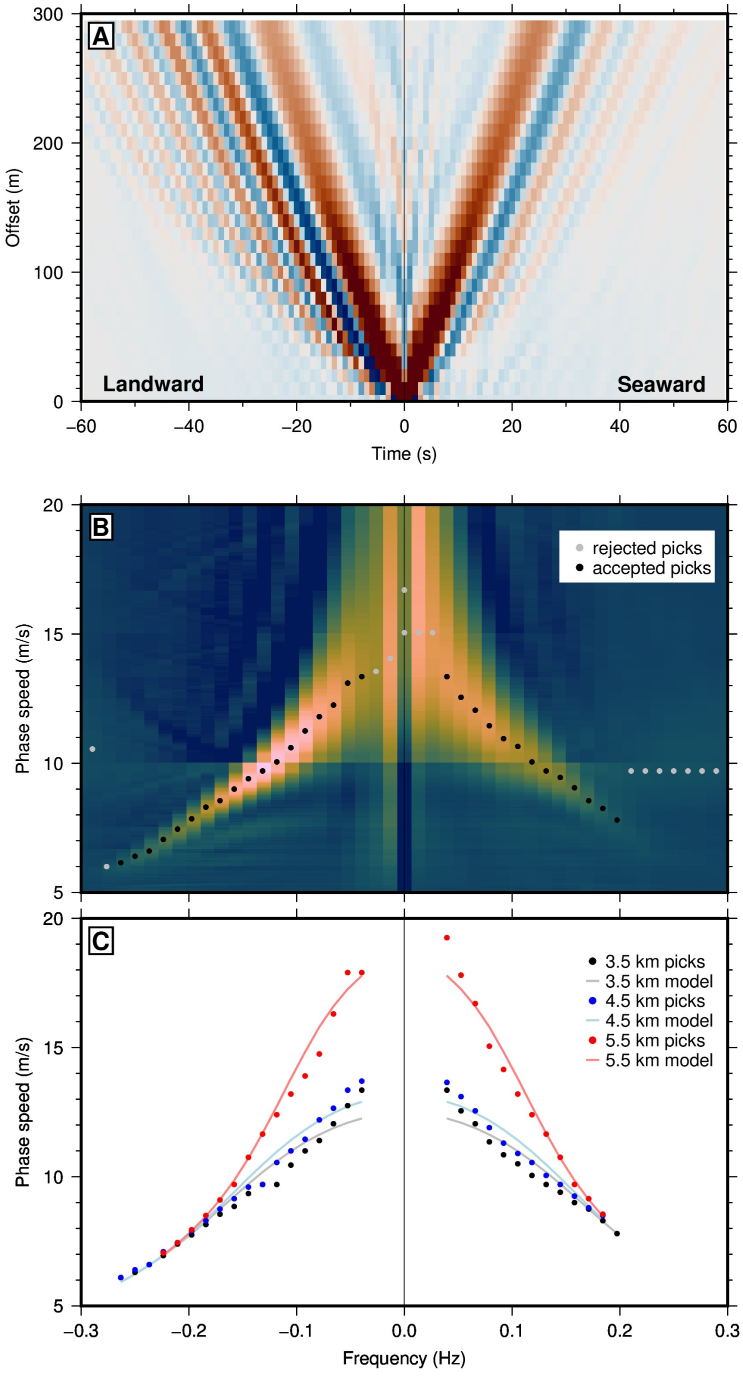

Figure 4.6: Composite images combining FK-separated cross-correlations showing: (A) example 300-m virtual source gather used in dispersion analysis; (B) dispersion images computed from (A) by slant stacking with picks in each frequency bin; and (C) example dispersion picks and best-fitting dispersion curve at three locations along the cable. Although spectral whitening was applied over 0.01-0.5 Hz, reliable dispersion picks are only made between 0.03-0.27 Hz (anti-causal) and 0.03-0.2 Hz (causal).

and Brown and Lu (2016) for a detailed derivation). For $k(\omega)r \gg 1$, the Green's function solution for pressure ($G(r,\omega) = \mathcal{F}[g(r,t)]$) is then

$$G(r,\omega) \propto H_0^{(1)}(k(\omega)r) \approx \sqrt{\frac{2}{\pi k(\omega)r}} e^{i(k(\omega)r-\pi/4)}. \tag{4.7}$$

The term above is $k(\omega)r = \frac{\omega r}{c_0(\omega)}$, with the phase speed $c_0(\omega) = \frac{\omega}{k} = \pm\sqrt{\frac{g}{k}\tanh kh}$ defined by Eq. 4.1. For small currents, we can modify this solution by perturbing the dispersion relation. In the case of a uniform current $U(z) = U_m$, the dispersion relation is simply $c(\omega, U_m) = c_0(\omega) + U_m$. Note that c_0 is negative for one directional component, so the addition of U_m is non-reciprocal—a Doppler shift.

Although the signal-to-noise ratio (SNR) of computed OSGW NCFs is high when stacked over the complete 4.5 day experiment (Fig. 4.5), the SNR of hourly NCFs is much lower, especially for the causal (seaward) directional component. In order to exploit the coherent phase information over a broad frequency band in the 4.5-day stack, we propose a two-step approach to current measurement. First, we measure phase speed dispersion for the complete stack and solve for the best-fitting dispersion relation, which includes the water depth and mean current as a function of distance along the cable. Second, we measure the difference in current velocity at each hour relative to the mean using a modified form of the popular stretching method from seismology.

4.3.2.1 Mean state inversion

We divide the array into overlapping 300 m (30 channel) subarrays and form virtual source gathers for each of the two directional components (Fig. 4.6A). The subarray aperture is chosen to maximize the bandwidth of dispersion picks while minimizing the effect of smoothing the recovered bathymetry profile. Due to attenuation, the highest-frequency OSGW energy (above 0.2 Hz) is only evident in NCFs with offset less than about 100 m, so the subarray must begin close to the virtual source. Conversely, the dispersion relation for OSGWs results in fast move-out of low-frequency energy, so the beamforming resolution is poor for offsets shorter than about 100 m. For the case of the Gibraltar dataset, bathymetric features along the cable path such as the sharp shelf break at 4.7 km and two bumps around 5.5 km cannot be recovered if the subarray is larger than 300 m.

We then apply beamforming and a Fourier transform to measure phase speed dispersion as a function of frequency for each of the two directional components:

$$B_i(\omega, c') = \sum_{j=i}^{i+N} X_{ij}(\omega) e^{\frac{-i\omega r_{ij}}{c'}}, \tag{4.8}$$

where $c' \in [5, 20]$ m/s, $X_{ij}(\omega) = \mathcal{F}\left[x_{ij}(t)\right]$, and i, j are channel numbers. The resulting dispersion images $B_i(\omega, c')$ for each subarray can be interpreted as a likelihood map for the phase speed in each frequency bin. We take the phase speed as $\underset{c'}{\operatorname{argmax}} B_i(\omega, c')$ for each frequency ≥ 0.03 Hz, and manually set a threshold value of B to exclude spurious picks at high frequencies, as illustrated in Fig. 4.6B. Combining the set of dispersion measurements for the two independent directional components, we use a non-linear least squares (Levenberg-Marquardt) solver to find the values of (h, U_m) that minimize the misfit with the dispersion relation for uniform flow across both positive and negative frequencies (Fig. 4.6C):

$$c(\omega, U_m) = \pm\sqrt{\frac{g}{k}\tanh{(kh)}} + U_m. \tag{4.9}$$

Across the complete 3-km cable segment (Fig, 4.7A), the maximum frequency of dispersion picks is about 0.2 Hz for the causal component, whereas the anti-causal component includes picks up to 0.3 Hz in shallow water, decreasing with depth following the same trend as f_{max} in Fig. 4.2C. Even though the phase speed is more sensitive to water depth than current velocity (a typical value of U_m is < 0.5 m/s), incorporating picks on both positive and negative frequency sides of the dispersion relation into the inversion mitigates the covariance between current speed and water depth, as a change in current speed is an asymmetric shift. In principle, the same procedure can be applied for any wave-current model parameterization, such as for depth-dependent flow.

4.3.2.2 Stretching

The stretching method is a common approach to measuring time-dependent changes in the velocity of coda waves from earthquakes or ambient noise cross-correlations (Sens-Schönfelder and Wegler, 2006). Because perturbations from environmental processes are small relative to the absolute speed of seismic waves ($\ll 1\%$), the associated change in travel-time is difficult to measure. The stretching method solves for differential changes in velocity by warping the waveform measured at one time until it matches a reference waveform, thereby incorporating all the phase information from a complete trace into the search for a single parameter. For the case

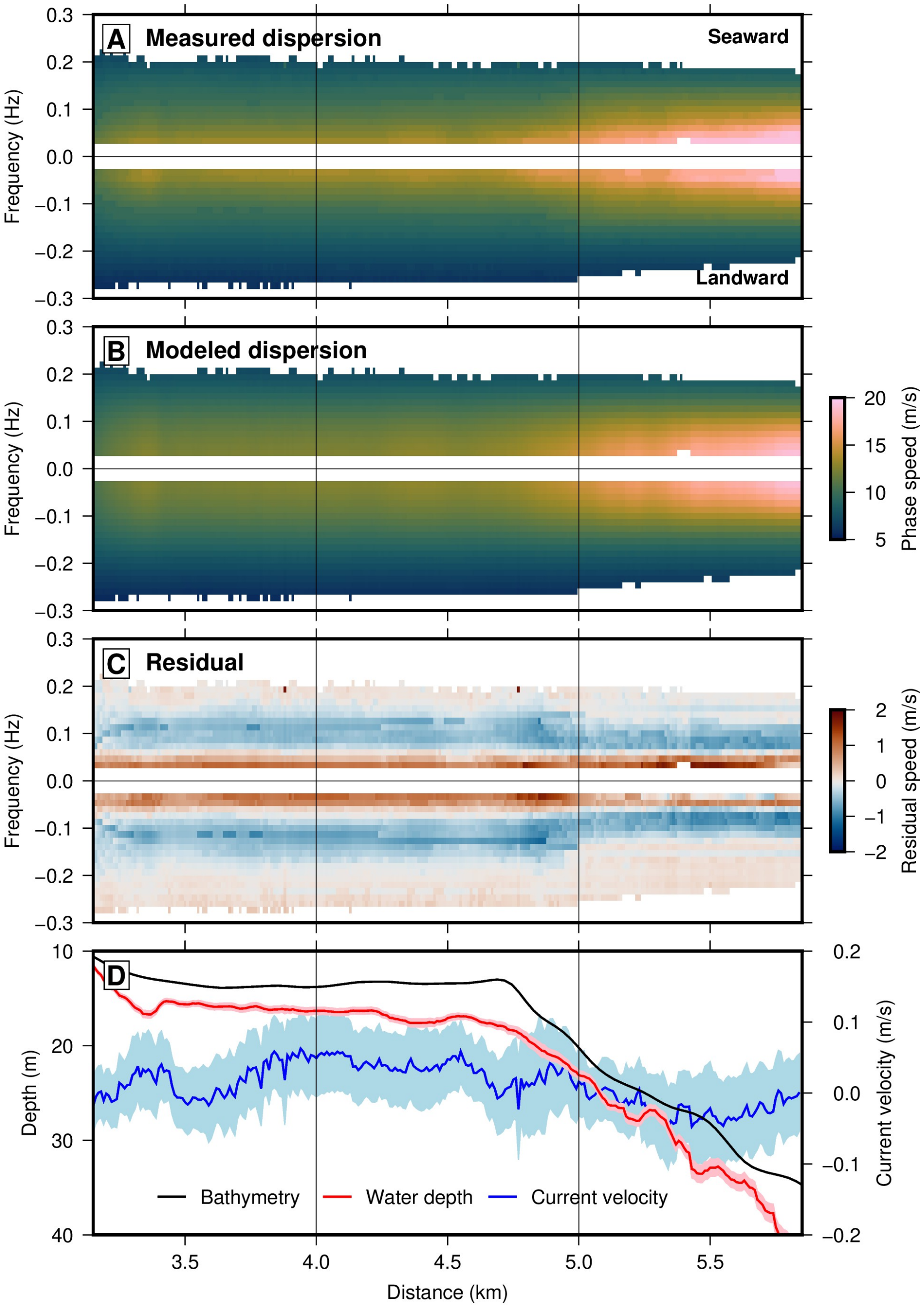

Figure 4.7: Mean-state inversion results: (A) dispersion picks for all subarrays along the cable; (B) modeled (best-fitting) dispersion curves; (C) difference between (A) and (B); and (C) inverted model parameters water depth (h) and flow velocity (U) plotted with 1σ error bars.

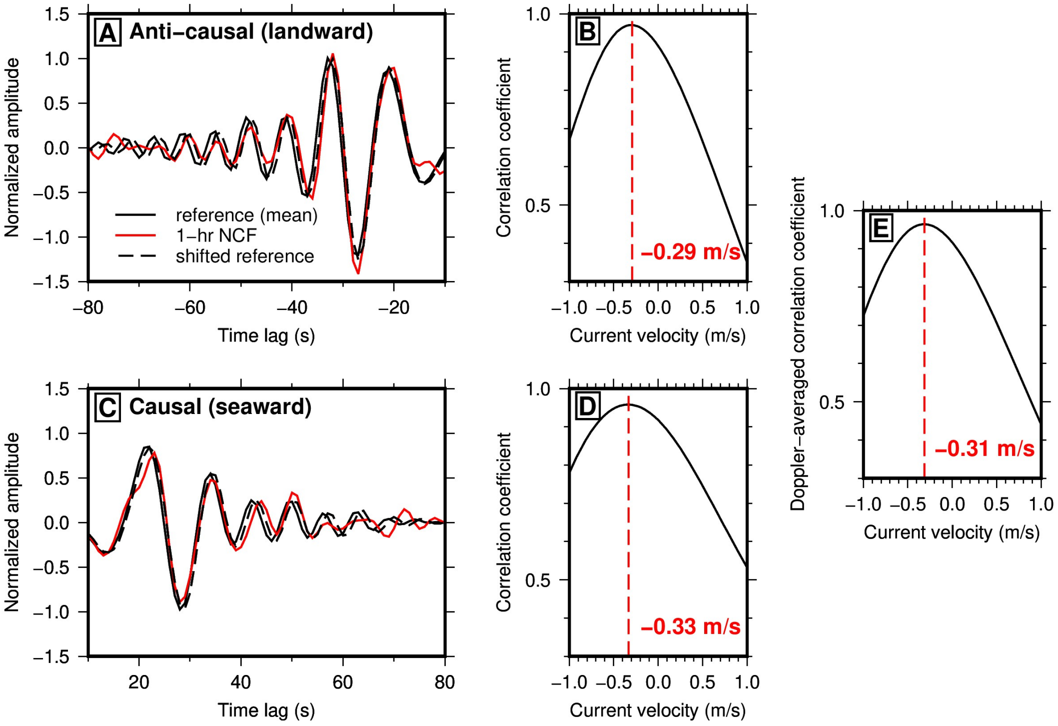

Figure 4.8: Example of the modified stretching method for the NCF of a single pair of channels at one point in time, showing: (A,C) the 1-hr stacked NCF, the reference NCF, and the shifted reference NCF that maximizes the correlation coefficient with the 1-hr NCF for the anti-causal and causal sides respectively; (B,D) the correlation coefficient as a function of current velocity for the NCFs in (A,C); (E) the doppler-averaged correlation coefficient (DACC) from (B,D).

of OSGW interferometry, the relative velocity perturbations from ocean currents can be quite large (up to 10% at high frequencies), but the ocean environment evolves rapidly relative to the time scale of convergence of NCFs. Consequently the SNR for a single hourly NCF may be too low to make independent phase speed measurements at a sufficiently broad range of frequencies to constrain the dispersion relation, as done above. The stretching method leverages the higher SNR of the reference trace to extract the coherent phase information contained in individual traces even when SNR is low. The original method uses a linear stretching factor to model the response of scattered, non-dispersive waves to a homogeneous velocity change; the modified stretching method proposed here uses a frequency-dependent stretching factor to model the response of ballistic, dispersive waves to a non-reciprocal velocity change.

For each NCF pair, we define the reference trace as the stack of all hourly NCFs across the complete 4.5 day dataset because this maximizes the SNR and we already know the dispersion relation for the mean state. Following from Eq. 4.6 and 4.7, the reference trace can be expressed as $X_{ij}^0(\omega) = A^0(\omega)e^{\frac{i\omega r_{ij}}{c_m(\omega)}}$, where $c_m = c_0 + U_m$ as above. Similarly, any given hourly NCF is $X_{ij}^n(\omega) = A^n(\omega)e^{\frac{i\omega r_{ij}}{c(\omega,U)}}$, where $c = c_0 + U$. Assuming that $A^0(\omega)$ and $A^n(\omega)$ are similar, we can write the hourly NCF in terms of the reference trace:

$$X_{ij}^n(\omega) \approx X_{ij}^0(\omega)e^{i\omega r_{ij}\delta s} = X_{ij}^{\delta s}(\omega, U), \quad \text{where } \delta s(\omega, U) = \frac{1}{c(\omega, U)} - \frac{1}{c_m(\omega)} \tag{4.10}$$

This defines a frequency-dependent stretching factor $\delta s(\omega, U)$, which can transform the phase spectrum of the reference trace X_{ij}^0 into any given hourly NCF X_{ij}^n (Fig. 4.8A,C).

Because there is only one unknown parameter, U, we can directly invert for the flow velocity, and a simple grid search is sufficiently computationally efficient. We pre-compute a dictionary of stretched reference traces $x_{ij}^{\delta s}(t, U) = \mathcal{F}^{-1}\left[X_{ij}^0(\omega)e^{i\omega r_{ij}\delta s(\omega,U)}\right]$, $U \in [-1, 1]$, then compute the correlation coefficient for each hourly NCF with each stretched reference trace:

$$CC_{ij}^n(U) = \frac{\int_{t_1}^{t_2} x_{ij}^n(t)x_{ij}^{\delta s}(t, U)dt}{\sqrt{\int_{t_1}^{t_2} x_{ij}^{n\,2}(t)dt \int_{t_1}^{t_2} x_{ij}^{\delta s 2}(t)dt}} \tag{4.11}$$

where $t_1 = r_{ij}/c_g(\omega_2)$ and $t_2 = r_{ij}/c_g(\omega_1)$ define the travel-time window containing the ballistic wave. Here, $c_g(\omega) = \frac{c_0(\omega)}{2}\left(1 + \frac{2kh}{\sinh(2kh)}\right)$ is the OSGW group velocity, which is evaluated at the minimum and maximum frequencies of interest (ω_1, ω_2). The values $(\omega_1, \omega_2) = 2\pi(0.03, 0.3)$ are chosen to ensure that the full available bandwidth is included in the computation of $CC_{ij}^n(U)$ for all water depths. For this data set, although we start with spectral normalization over the band 0.01-0.5 Hz, the resulting NCFs only exhibit coherent OSGW signals over 0.03-0.3 Hz (e.g. Fig. 4.7). In a data set with greater variations in bathymetry along the cable path, the window could be set adaptively based on the coherence between traces instead, or using the theoretical maximum observable frequency $f_{max}(h)$ (Eq. 4.3). The result is an array of $CC(U)$ for each of the causal and anti-causal components (Fig. 4.8B,D,E), which can be interpreted as a likelihood function for U. This formulation neglects the effect of temporal variations in water depth on OSGW dispersion, which may be significant in shallow water. A change in h results in a reciprocal (symmetric) change in the phase speed (Eq. 4.9), which can be removed by combining the causal and anti-causal sides into a joint inversion (see Section

5.1.). So, we average the two $CC_{ij}^{n}(U)$ into a single Doppler-averaged correlation coefficient (DACC) and take the maximum value as the solution. Generally, the peak values of the DACC are > 0.95 for all traces and all time windows.

The time-lapse evolution of a single representative NCF pair separated by 300 m is shown in Fig. 4.9A,B, exhibiting clear periodicity in travel-times at the M2 tidal period. Applying the modified stretching method to each 1-hr window in the 4.5-day time-series produces a matrix of correlation coefficients for each candidate U at each hour. The selected U values for the anti-causal side (red) show a clear tidal signal with a reasonable amplitude of about 0.5 m/s (Fig. 4.9C). The selected values for the causal side (blue) appear much noisier, owing to the lesser SNR of the NCFs for this wavefield component, but still show a tidal signal (Fig. 4.9D). When superimposed it is clear that even though the causal side measurement (Fig. 4.9D) appears much noisier, it is actually broadly consistent with the anti-causal side measurement. This is significant because the FK pre-processing and parallel workflows ensure that these measurements are independent. Combining Fig. 4.9C,D into the DACC and making a joint estimate of U (black), results in a current velocity time-series in between the two one-sided estimates (Fig. 4.9E).

4.4 Results

4.4.1 Depth profile

The results of subarray beamforming to invert for the mean state are shown in Fig. 4.7. Dispersion picks (Fig. 4.7A) are symmetric for both causal and anti-causal wavefield components, which suggests that the mean current is small. Picks converge to a constant phase speed around 0.2 Hz all along the cable segment, consistent with the deep water limit of the OSGW dispersion relation which is insensitive to water depth. At low frequencies (< 0.15 Hz), the measured phase speed is approximately constant between 3–5 km distance, and then increases gradually over the last kilometer, indicating an increase in water depth. The modeled dispersion picks from Eq. 4.8 (Fig. 4.7B) reproduce these trends. The residual (Fig. 4.7C) between measured and modeled dispersion is everywhere less than 10% of the measured phase speed, approaching zero at high frequencies. The modeled dispersion systematically under-predicts the highest phase speeds measured at low frequencies and over-predicts the phase speeds measured at intermediate frequencies, because the measured dispersion curves are more linear than the theoretical OSGW dispersion relation can produce for any set of parameters. In spite of the $\sim$ 1 m/s misfit at lower frequencies, the inverted depth profile (Fig. 4.7D) accurately reproduces the

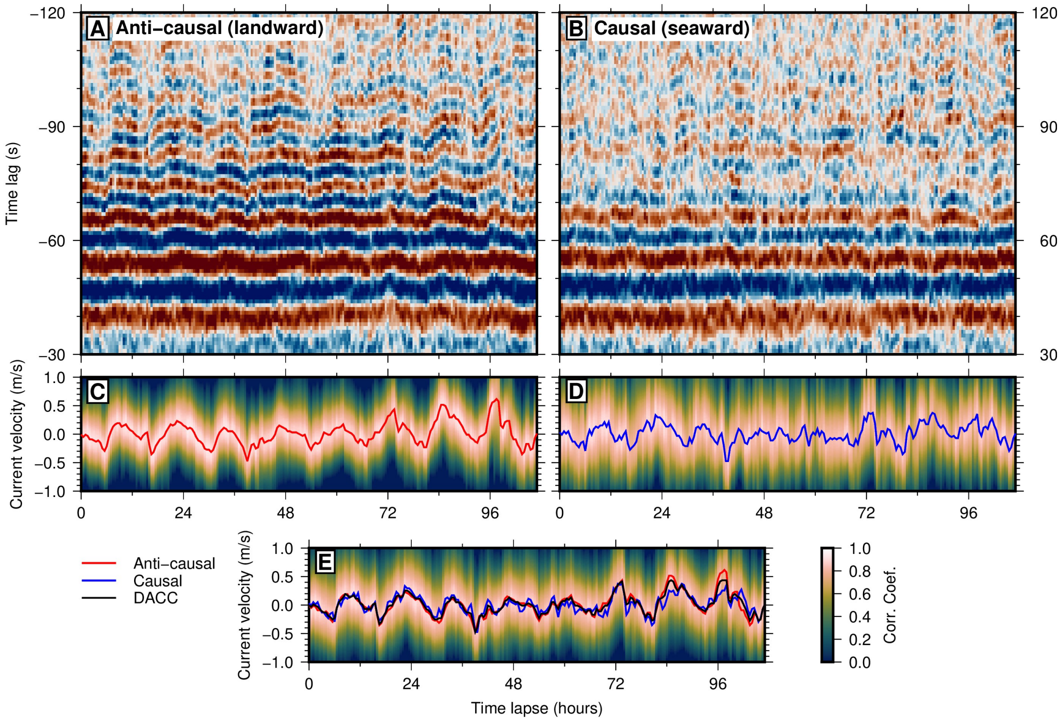

Figure 4.9: Results of applying the modified stretching method to an example NCF for a single pair of channels across all 1-hr windows. (A,B) Time-lapse gathers for the anti-causal and causal sides respectively showing time-dependent changes in the arrival time of OSGW. Note that the relative amplitude of NCFs is not preserved between the causal and anti-causal sides due to the separate processing workflows (Fig. 4.5). (C,D) Correlation coefficients computed from stretching (A,B) over a range of velocities, with the velocity that maximizes the correlation coefficient with the reference NCF indicated in red and blue. (E) The Doppler-averaged correlation coefficient (DACC) computed from (C,D) superimposed with the optimal velocities from (C,D) and the DACC pick in black.

bathymetric profile along the cable path interpolated from EMODnet Bathymetry Consortium (2020), with a maximum difference < 5 m. The inverted profile captures the flat shelf up to 4.7 km, as well as the slope angle from 4.7–6 km, but is systematically too deep. This systematic difference may result from a mismatch in tidal datum between the measurements and the bathymetry model, poor interpolation of the bathymetry model in shallow water, or uncertainty in cable location, which is on the order of 100 m. The directional spectrum of ocean swell at low frequencies could also contribute to this difference, since waves arriving from an oblique azimuth appear with faster apparent phase speed along the cable direction. If the swell is highly anisotropic, such oblique incidence can yield a biased Green's function estimate, which could explain why the measured dispersion picks

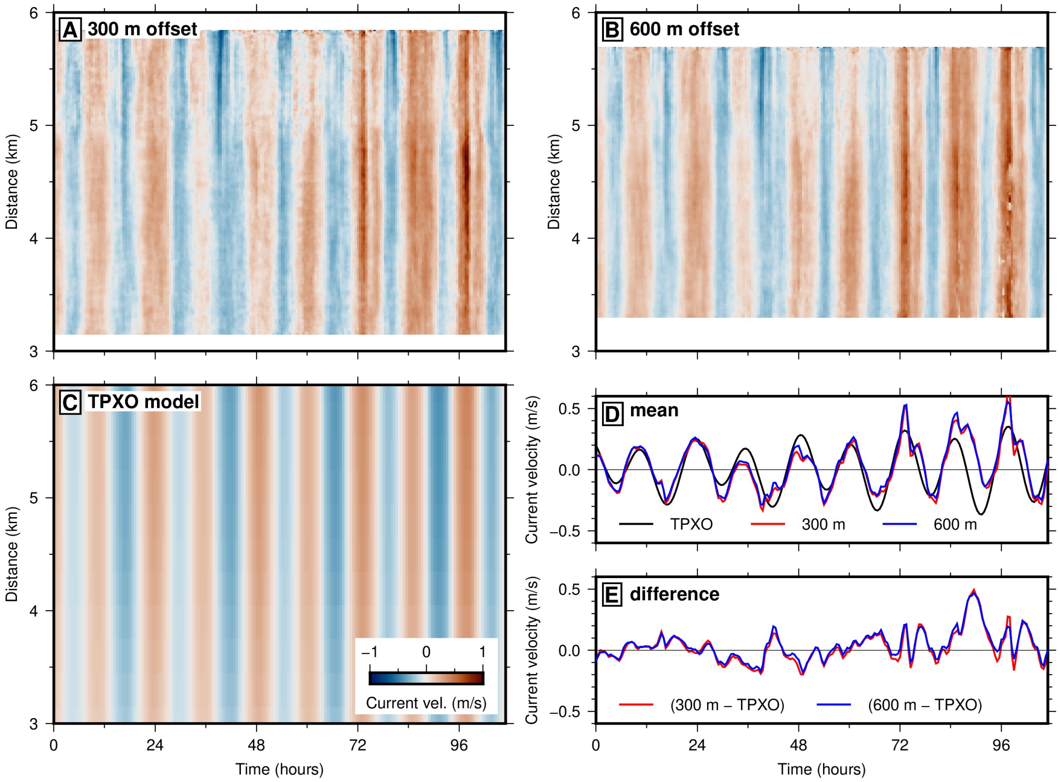

Figure 4.10: (A) Measured current velocity as a function of time and distance for all NCF pairs with 300 m offset. (B) Same as (A) but for 600-m offset pairs. (C) Current velocity TPXO tidal model computed at each channel location for the time of the experiment and rotated into the azimuth of the cable. (D) Comparison of the mean TPXO-predicted tidal current velocity along the cable with the mean measured current velocity for all channel pairs with 300-m or 600-m offset. (E) Difference between results and TPXO model.

are under-predicted around 0.03-0.05 Hz (Fig. 4.6C, 4.7C) and why the inverted profile is deeper (faster) than the bathymetry model (Fig. 4.7D). Because the phase speed is highly sensitive to water depth at low frequencies ($\frac{\partial c}{\partial h} = \frac{g}{2}(gh)^{-1/2}$), the 1σ uncertainty is always ≤ 1 m.

4.4.2 Tidal current

The inverted mean current is within 1σ of 0 m/s across the entire cable segment (Fig. 4.7D). This is expected since tidal currents dominate the flow in many shallow water settings. The M2 tide (12.4 hr) is the largest constituent, and divides about evenly into the 108-hr dataset, so the mean flow should be negligible.

Combining the mean and differential current measurements results in a matrix of current velocity in space and time, shown in Fig. 4.10A for all channel pairs with

300 m offset. The most prominent feature is sinusoidally time-dependent flow at the M2 tidal period, with an amplitude that begins around ±0.2 m/s on the first day of the experiment and gradually increases to $+0.5/-0.4$ m/s on the last day. The current is locked in phase across the 3-km cable segment, and the only feature correlated to water depth is a small decrease in the current velocity from 5–6 km where the bathymetry is steeper and deeper. Over the first three days, the measured current is centered around zero mean, but starts to drift away from the reference towards positive values in the last 36 hrs. This drift reflects the limitation of using a single reference state for differential current measurement over an extended time-lapse. Notably neither the high-frequency wave event nor the swell dispersion trend observed OSGW spectrograms in Fig. 4.3 are evident in the final current results. The measured current time-series also include a pattern of jumps (up to 0.3 m/s difference in one hour) at the maximum positive current (flow towards the southwest along the cable), which is discussed in the following section.

Each pixel in Fig. 4.10A represents the measurement from an independent pair of channels, so even considering the overlap of adjacent pairs, the map is remarkably smooth. In principle, a current velocity can be measured from all 45150 NCFs and incorporated into a tomographic inversion to increase the spatial resolution and decrease uncertainties. In practice, this is a highly over-determined problem which requires strong regularization and considerable computational time for very little improvement. The difference between current measurements from 300-m (Fig. 4.10A) and 600-m (Fig. 4.10B) offset pairs is < 0.05 m/s (Fig. 4.10D,E), so the information is redundant. However, not all NCFs yield useful information. The path-integrated travel-time shifts (e.g. Fig. 4.9) induced by currents were too small to measure reliably for channel pairs with offset < 150 m. At offsets > 1 km, attenuation of high frequency waves restricted the analysis to < 0.1 Hz, resulting in high uncertainties.

Because no in-situ observations of current velocity are available, we compare our measured current velocity with a model of tidal flow generated by the OSU Tidal Prediction Software from the TPXO9 tidal solutions, which are a shallow-water model fit to global altimetry observations of sea-surface height (Egbert and Erofeeva, 2002). The TPXO9 prediction for the barotropic current is evaluated at each point along the 3-km cable segment for the dates of the experiment and projected onto the direction of the cable (Fig. 4.10C). The measured current velocity accurately reproduces the principal properties of the model (Fig. 4.10D). The amplitude

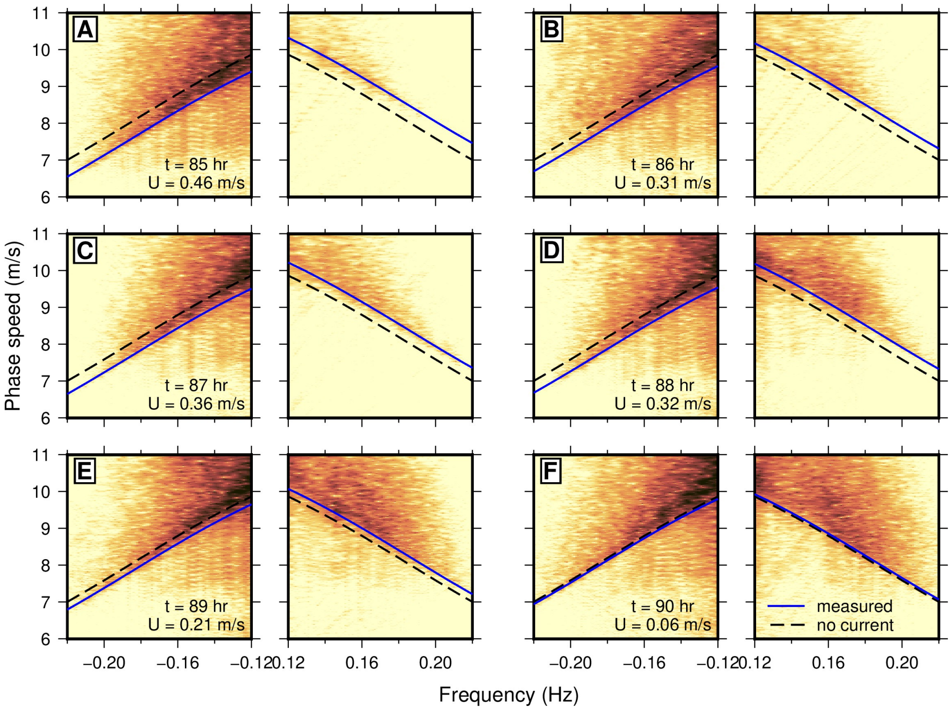

Figure 4.11: Comparison of current velocities measured with OSGW interferometry and the modified stretching method to hourly frequency-wavenumber (FK) spectra computed from the raw data. Each FK spectrum has been transformed to coordinates of phase speed vs. frequency and only a small area of the spectrum is shown. Panels (A)-(F) are computed for consecutive hours, with the landward-propagating (anti-causal) component on the left and the seaward-propagating (causal) component on the right. The same theoretical dispersion relation for OSGW in the absence of a current (Eq. 4.1) is plotted on all panels in black, and the measured wave-current dispersion relation for each time window is plotted in blue.

matches both the long-term increasing trend over the 4.5-day time-lapse and the beating pattern of the M1 and M2 tides such that every other 12-hr cycle has a smaller amplitude over the first three days. The TPXO9 model and measured current agree that the phase is constant along the 3-km cable segment. The sharp jumps during the last 36 hours cannot be accounted for by ordinary tidal harmonic constituents.

4.5 Discussion

While the results of ocean current measurement by interferometry of the ambient OSGW field compare favorably to the TPXO9 solution for the barotropic tide, several outstanding features deserve further discussion. Significantly, the last 36 hours exhibit several sharp jumps in current velocity at non-tidal frequencies and a systematic discrepancy in phase relative to the tidal model. In order to verify that the observed jumps in current velocity are features of the raw data and not artifacts of our particular processing methodology, we first compare our results with FK spectra following the simple approach of Williams et al. (2019). The complete 3-km cable segment is divided into hourly windows, two Fourier transforms are applied to obtain the FK spectrum for each time window, the FK spectrum is transformed into coordinates of phase speed vs. frequency using the coordinate transform $c = f/k$, and the mean current velocity measured along the cable is super-imposed. Six consecutive hours are plotted in Fig. 4.11 as an example, zoomed in to a small part of the spectrum where the dispersion relation is approximately linear. In these coordinates, the OSGW energy is concentrated in a packet that sits above the dispersion relation for a wave propagating along the cable direction, so the lower-velocity edge, which is quite sharp, is the target of visual comparison. As expected, the FK spectra exhibit a non-reciprocal shift in the dispersion relation (Doppler shift) that evolves over time, and generally corresponds to the OSGW interferometry solution, including the sharp jumps in current velocity during the last 36 hours. These jumps are thus present in the raw data and likely a signature of real flow patterns.

One possible origin for the sharp variations in measured current velocity is by interaction of surface and internal gravity waves. Internal solitary waves generated every 12-24 hrs by tidal flow over the Camarinal Sill (Fig. 4.2) have been observed frequently by satellites and moorings, propagating east through the Strait of Gibraltar across the cable path (Ziegenbein, 1970). Their typical propagation speed is 0.5–2 m/s, with a wavelength (inter-soliton distance) of 0.5–2 km and a period of 10-15 mins, though these parameters vary considerably among observations and their shallow-water shoaling behavior on the shelf has not been studied (Ziegenbein, 1970; Watson and Robsinson, 1990; Brandt, Alpers, and Backhaus, 1996). Because the wavelength is much longer and the speed is much slower than OSGWs, the interaction of internal waves with short surface waves is comparable to advection by a surface current (Alpers, 1985; Lenain and Pizzo, 2021). The propagation time of an internal wave from the Camarinal Sill to the 3-6 km cable segment is about 2–4 hours at these speeds, so the timing of the sharp jumps in our current velocity time-series is consistent with this interpretation, as is the sole occurrence of these features immediately following the maximum southwestward (Mediterranean outflow) current (Vazquez et al., 2008). Because the finest temporal resolution of the current measurements is 0.5 hr, such an internal solitary wave would appear as a near-instantaneous jump in flow velocity along the cable segment, which is also consistent with our measurements. However, the pattern of the jumps (gradual increase in flow to the southwest followed by a sharp decrease) is opposite to the polarity that would be predicted for an internal wave of depression (Alpers, 1985; Lamb, 1997). Internal wave interaction is also predicted to modulate the directional spectrum and height of surface waves, and while we noted evidence of wave-current interaction at tidal periods, no sharp modulations in wave spectra are apparent at the time of the jumps in current velocity during the last 36 hours (Fig. 4.3).

4.5.1 Sources of bias

We proposed that these features could relate to internal solitary waves, which have been observed in the Strait of Gibraltar, but, with no complementary data to support a physical interpretation and considering the generalizability of this method to other ocean environments, it is necessary to constrain sources of observational bias as well as the sensitivity of OSGW interferometry. One major source of potential bias in ambient noise interferometry is the heterogeneous distribution of sources in real earth environments. This problem has been recognized in seismology, but is largely ignored despite potentially introducing significant errors into tomographic velocity models (Yao and Van Der Hilst, 2009). The anisotropic nature of the ocean wave directional spectrum makes this a particular challenge for OSGW interferometry. The ambient OSGW field is frequently modeled using a point specrum $S(\omega)$ and a directional spreading function $D(\omega, \theta)$, such that the wave directional spectrum is a function of both azimuth and frequency ($S(\omega, \theta) = S(\omega)D(\omega, \theta)$) (Ochi, 1998). Commonly, the spreading term D is expressed as a power of $\cos(\theta)$, resulting in a very narrow directional spectrum. In the limiting case of a single stationary source, cross-correlation of the wave records at two points yields a distorted representation of the Green's function according to the azimuth of the source ($k' = k/\cos(\theta)$). For a diffuse and isotropic source distribution, the same cross-correlation yields an exact representation of the Green's function, as in Eq. 4.6. For realistic OSGW source distributions, the scenario is likely somewhere between the two. As discussed previously, the overestimated OSGW phase speed at low frequencies in Fig. 4.7C and the misfit between observed and predicted bathymetry in Fig. 4.7D are possibly a result of bias from an anisotropic OSGW directional spectrum. Because the OSGW energy around 0.1 Hz is dominated by swell from a distant source, the low-frequency component of the wave spectrum is likely to be more anisotropic. Because the apparent speed of a wave measured between two stations can only increase with obliquity and OSGW phase speed increases with water depth, if the dominant direction of OSGW propagating across the array is at an angle to the cable direction, OSGW interferometry will yield a water depth too deep. This effect can be corrected if the dominant wave azimuth is known.

We follow after Lu (2015) in constructing synthetic datasets to test the effect of anisotropic, time-dependent source distributions. A 12-hr synthetic recording of random waves is generated by convolving a Ricker wavelet with the OSGW Green's function for seafloor pressure at 120,000 randomly distributed source locations and two receivers. Then, cross-correlation and stretching are applied to the synthetic dataset to extract the apparent time-lapse of current velocity. This is illustrated in Fig. 4.12A where the random wavefield from a spatially uniform distribution of far-field sources is recorded in the presence of a current with a period of 12 hrs and amplitude of 0.5 m/s oriented at 45 degrees to the cable direction. The result (Fig. 4.12B), is that the component of flow along the direction of the cable is successfully recovered, as predicted by theory. Next, we consider no current but an azimuthally bimodal normal distribution of sources, which rotates by 20 degrees in the same direction as a function of time (Fig. 4.12C). Stretching only the causal or anti-causal side of the cross-correlation results in a spurious apparent current (Fig. 4.12D); however, incorporating both components into the DACC, these terms cancel out so that the observed current (none) is correct. If instead the two peaks of the source distribution rotate symmetrically in opposite directions over time (Fig. 4.12E), the resulting spurious current measurements add together to simulate a tidal current (Fig. 4.13). Yet, the spurious current is small—a rotation of 20 degrees for both source clusters results in a 0.2 m/s current. These scenarios mimic, for example, a coastal OBDAS array where wind waves reflect from shallow water to generate a bimodal directional spectrum. Therefore, in many but not all cases, the incorporation of non-reciprocal paths directly into the stretching workflow mitigates the bias introduced by an anisotropic and time-dependent distribution of sources.

The strong local modulation of waves by tides, as observed in Fig. 4.3, must also be excluded as a source of bias. In particular, conventional time-domain application of the stretching method in coda wave interferometry is known to introduce spurious velocity changes due to variations in the source amplitude spectrum (Zhan, Tsai, and Clayton, 2013). We chose to apply stretching in the frequency domain in order to mitigate this effect. We repeated our synthetic analysis with the same uniform source distribution as Fig. 4.12A above but varied the center frequency of the source wavelet between 0.15 ± 0.02 Hz continuously at 12-hr period (which is comparable to the observation in Fig. 4.3C). The result (Fig. 4.13A) shows that changing the amplitude spectrum does not introduce a spurious current here. Similarly, the effect of tides on water column depth modulates OSGW dispersion. We also repeated our synthetic analysis varying the water depth between 15 ± 1 m at 12-hr period (Fig. 4.13B). The changing water depth can introduce a small spurious current in the stretching results for each individual directional component; however, the effect is reciprocal and eliminated by Doppler-averaging. The spurious current measured for each directional component is also in-phase with the sea surface height, which is typically 90 degrees out of phase with the flow for tidal currents. Note that for both Fig. 4.13A and B the maximum correlation coefficient is much lower and the width of the correlation coefficient peak (which is implicitly tied to uncertainty) is much broader than in Fig. 4.12. This is because changing the frequency content or dispersion relation results in low waveform coherence. Other conditions not considered here that could contribute to a non-reciprocal bias include measurement bias from recording the horizontal component of strain or pressure on a sloping bottom, non-linear energy transfer between waves and the current or breaking of waves, and retardation of waves by shoaling (e.g. the mild-slope equation). Overall, no single source of bias is evident that easily describes the sharp deviations from the TPXO tidal current model in Fig. 4.10, suggesting these are physical signals of complex flow.

4.5.2 Depth sensitivity

In this study we have so far only considered the simple case of OSGW propagating in a uniform current (Eq. 4.9), but depth-dependent flow is common, especially in coastal environments. Not only is the assumption of uniform flow then a potential source of bias, but constraining the vertical structure of currents can be significant for understanding processes like sediment transport and mixing. Consider, for example, the case of a linear shear current: $\frac{\partial U}{\partial z} = U_s s'$, where U_s is the surface current and $s' \in [0, h^{-1}]$ a constant such that $s' = h^{-1}$ represents no flow at the bottom. Linearization of the relevant dispersion relation (Kirby and Chen, 1989) yields

$$c(\omega, U_0, s') = c_0(\omega) + \left(1 - \frac{s' c_0(\omega)^2}{2g}\right) U_s. \tag{4.12}$$

Generating synthetic data for OSGW propagating in a shear current as above and inverting for the uniform current speed using the incorrect dispersion relation (Eq. 4.9), Fig. 4.14A-C demonstrates how the shape and amplitude of the current

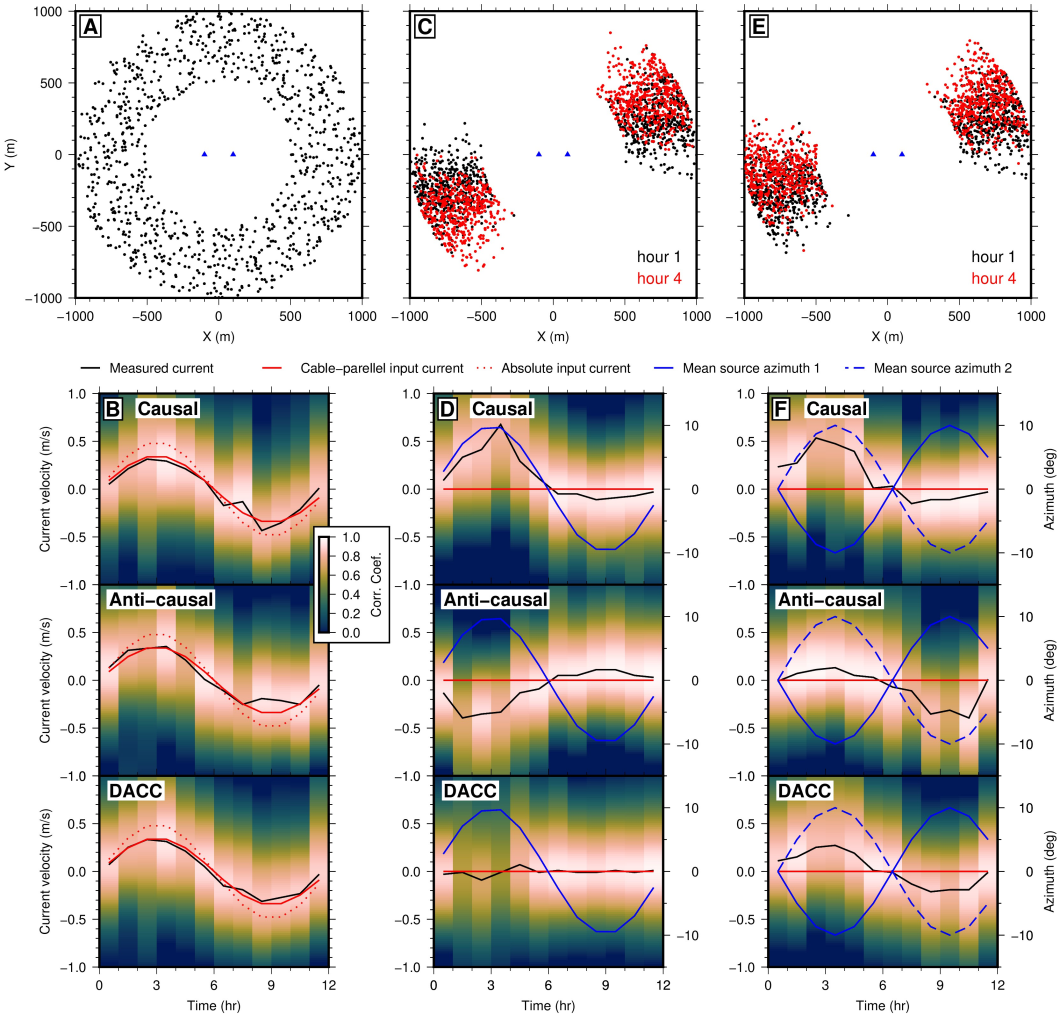

Figure 4.12: Synthetic OSGW interferometry and stretching. (A) A uniform, far-field OSGW source distribution (black dots) recorded at two channels (black triangles) in the presence of a current oriented at 45 degrees from the x-axis. (B) Results of cross-correlating and stretching the synthetic data from (A), showing that the component of the current along the x-axis is recovered, not the absolute current. (C) A bimodal OSGW source distribution that rotates symmetrically by 20 degrees at 12-hr period. (D) Results of the synthetic data from (C) showing that Doppler-averaging cancels out spurious current measurements. (E) A bimodal OSGW source distribution that rotates asymmetrically by 20 degrees over 12-hr period. (F) Results of the synthetic data from (E) showing that a small spurious current is measured in this unique case.

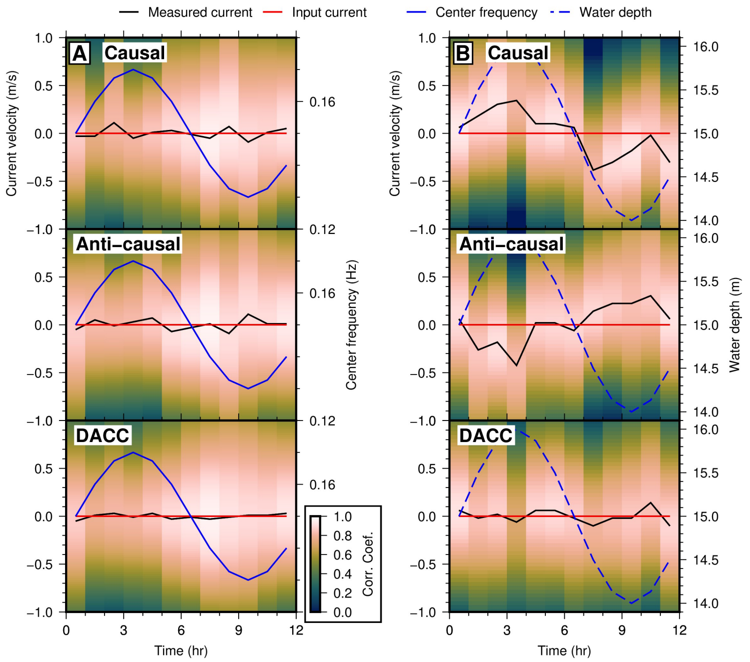

Figure 4.13: Synthetic OSGW interferometry and stretching results with the same source distribution as Fig. 4.12A. (A) The center frequency of the source wavelet varies at 12-hr period, and no spurious current is measured but the correlation coefficient is lower. (B) The water depth varies at 12-hr period, resulting in a spurious current that cancels out through Doppler-averaging.

measurement can be biased. In particular, if the vertical structure s' is out of phase with the tidal surface current U_s, such as may result from bottom friction, the apparent phase of the measured current can change significantly (Fig. 4.14B).

Parameterizing differential current measurement by stretching with Eq. 4.12 and solving for an additional parameter, however, is challenging because s' and U_s co-vary. We re-calculated the stretching results for the Strait of Gibraltar DAS array with a shear model but were unable to recover a coherent map of s'. This is illustrated in Fig. 4.14D, which shows an example grid-search of the DACC for a single NCF pair for the two-parameter case in Eq. 4.12. Whether measuring depth-varying flow is possible depends on the bandwidth over which NCFs are obtained, which is modulated by water depth (Fig. 4.14E). For the limiting case where $s' = h^{-1}$, the mean current is simply $U_m = U_s/2$. Therefore, at low frequencies (in the shallow water limit), $\Delta c = (1 - \frac{c_0^2}{2gh})U_s - U_m \approx \frac{1}{2}U_s - U_m = 0$, so the correct depth-averaged current velocity can be recovered but no depth-dependent information can be discerned. Similarly, at high frequencies (in the deep water limit) $\Delta c \approx U_s - U_m = \frac{1}{2}U_s$, so OSGW are only sensitive to the surface flow,

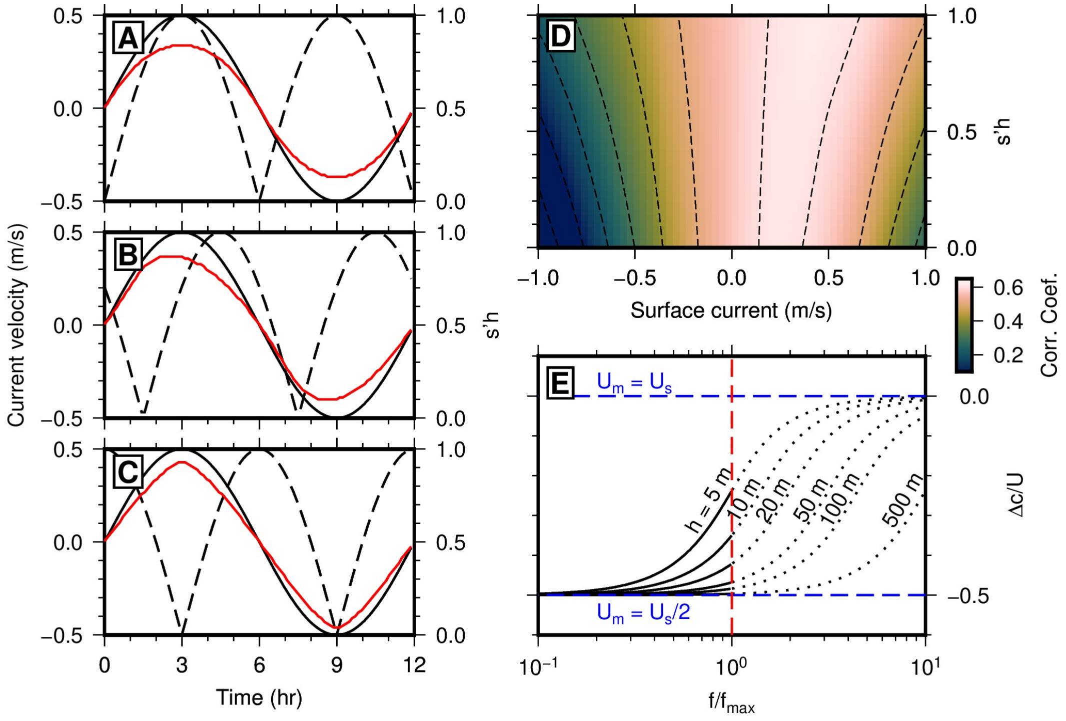

Figure 4.14: (A-C) Synthetic example demonstrating how a shear current can bias the results of the modified stretching method if a uniform current model is used. The input velocity gradient ($s' = (1/U)\partial U/\partial z$, black dashed line) is advanced in phase by (A) 0, (B) 45, and (C) 90 degrees relative to the input surface current (black solid line) in each panel. The measured current (red line), can become rounded, sharpened, or asymmetrical. (D) Example DACC matrix from stretching an example NCF using the dispersion relation for a linear shear current and searching over two parameters (U,s'). (E) Difference in current velocity between a linear shear current and a uniform current for different water depths. The solid black lines represent the range that can be observed from ocean-bottom pressure measurements ($f < f_{max}$).

resulting in both an overestimated current velocity (by a factor of two) and no depth-dependent information. Such deep-water waves, however, cannot be observed at the bottom. Constraining vertical structure thereby requires observation of intermediate frequencies. Recalling the observational constraint that $f < f_{max}$ (Eq. 4.3), Fig. 4.14E demonstrates that intermediate frequencies can only be recorded by OBDAS in very shallow water ($h \lesssim 10$ m), which further helps explain why the sensitivity is so low here (Fig. 4.14D). OSGW interferometry with OBDAS may therefore be well suited for vertically sheared flows in rivers or estuaries, whereas surface measurements (such as attempted by Brown and Lu (2016)) may be needed to constrain depth-dependent structure in oceanic settings.

4.6 Conclusions

We have demonstrated that ocean current velocity can be measured along pre-existing submarine fiber-optic cables using distributed acoustic sensing and ambient noise interferometry. Raw OBDAS records from the Strait of Gibraltar contain OSGW signals between $< 0.03 - 0.3$ Hz, including both wind waves and swell. Applying a directional (FK) filter, we split the OSGW field into two directional components and calculated cross-correlations for each, resulting in an empirical approximation of the OSGW Green's function for reciprocal paths between each pair of channels along the OBDAS array. Then, introducing a two-step workflow, we measured the OSGW dispersion relation along the cable and extracted a 1D profile of water depth and 2D map (distance vs. time) of current speed. Our results correlate well with a tidal current model, though some sharp, anomalous changes in current speed over the last 36 hours of the dataset may relate to internal waves. Numerical experiments demonstrate that by exploiting reciprocal measurements we mitigate potential bias from a non-uniform source distribution and time-varying wave spectrum in most but not all cases. Such capabilities for bathymetric profiling and flow monitoring indicate the broad scope of applications for OBDAS in observational physical oceanography.

References

Alpers, W. (1985). "Theory of radar imaging of internal waves". In: *Nature* 314.21, pp. 245–247.

Bensen, G. D. et al. (2007). "Processing seismic ambient noise data to obtain reliable broad-band surface wave dispersion measurements". In: *Geophys. J. Int.* 169.3, pp. 1239–1260.

Brandt, P., W. Alpers, and J. O. Backhaus (1996). "Study of the generation and propagation of internal waves in the Strait of Gibraltar using a numerical model and synthetic aperture radar images of the European ERS1 satellite". In: *J. Geophys. Res.* 101.C6, pp. 14237–14252.

Brown, M. G., O. A. Godin, et al. (2014). "Acoustic Green's function extraction from ambient noise in a coastal ocean environment". In: *Geophys. Res. Lett.* 41, pp. 5555–5562.

Brown, M. G. and C. Lu (2016). "Green's function retrieval in a field of random water waves". In: *Wave Motion* 60, pp. 8–19.

Campillo, M. and A. Paul (2003). "Long-range correlations in the diffuse seismic coda". In: *Science* 299, pp. 547–549.

Crawford, W. C. (2004). “The sensitivity of seafloor compliance measurements to sub-basalt sediments”. In: *Geophys. J. Int.* 157, pp. 1130–1145.

Crawford, W. C., S. C. Webb, and J. A. Hildebrand (1991). “Seafloor compliance observed by long-period pressure and displacement measurements”. In: *J. Geophys. Res.* 96.B10, pp. 16151–16160.

Doran, A. K. and G. Laske (2016). “Infragravity waves and horizontal seafloor compliance”. In: *J. Geophys. Res.: Solid Earth* 121, pp. 260–278.

Dushaw, B. D. et al. (1994). “Barotropic currents and vorticity in the central North Pacific in summer 1987 determined from long-range acoustic transmissions”. In: *J. Geophys. Res.* 99, pp. 3262–3272.

Egbert, G. D. and S. Y. Erofeeva (2002). “Efficient inverse modeling of barotropic ocean tides”. In: *J. Atmos. Ocean. Technol.* 19.2, pp. 183–204.

Elgar, S. and R. T. Guza (1985). “Observations of bispectra of shoaling surface gravity waves”. In: *J. Fluid Mech.* 161, pp. 425–448.

EMODnet Bathymetry Consortium (2020). “EMODnet Digital Bathymetry (DTM)”. In.

Fernandez-Ruiz, M. R., L. Costa, and H. F. Martins (2019). “Distributed acoustic sensing using chirped-pulse phase-sensitive OTDR technology”. In: *Sensors* 19, p. 4368.

Fernandez-Ruiz, M. R., H. F. Martins, et al. (2018). “Steady-sensitivity distributed acoustic sensors”. In: *J. Light. Technol.* 36, pp. 5690–5696.

Godin, O. A. (2006). “Recovering the Acoustic Green’s Function from Ambient Noise Cross Correlation in an Inhomogeneous Moving Medium”. In: *Phys. Rev. Lett.* 97.054301.

– (2018). “Acoustic noise interferometry in a time-dependent coastal ocean”. In: *J. Acoust. Soc. Am.* 143, pp. 595–604.

Godin, O. A., M. G. Brown, et al. (2014). “Passive acoustic measurement of flow velocity in the Straits of Florida”. In: *Geosci. Lett.* 1.16.

Godin, O. A., N. A. Zabotin, and V. V. Goncharov (2010). “Ocean tomography with acoustic daylight”. In: *Geophys. Res. Lett.* 37, p. L13605.

Godin, O. A., N. A. Zabotin, A. F. Sheehan, et al. (2014). “Interferometry of infragravity waves off New Zealand”. In: *J. Geophys. Res.: Oceans* 119, pp. 1103–1122.

Harmon, N. et al. (2012). “Infragravity wave source regions determined from ambient noise correlation”. In: *Geophys. Res. Lett.* 39, p. L04604.

Herbers, T. H. C., S. Elgar, and R. T. Guza (1995). “Generation and propagation of infragravity waves”. In: *J. Geophys. Res.* 100.C12, pp. 24863–24872.

Herbers, T. H. C., M. Orzech, et al. (2003). “Shoaling transformation of wave frequency-directional spectra”. In: *J. Geophys. Res.* 108.C1, p. 3013.

Howe, B. M., P. F. Worchester, and R. C. Spindel (1987). “Ocean acoustic tomography: mesoscale velocity”. In: *J. Geophys. Res.* 92, pp. 3785–3805.

Ide, S., E. Araki, and H. Matsumoto (2021). “Very broadband strain-rate measurements along a submarine fiber-optic cable off Cape Muroto, Nankai subduction zone, Japan”. In: *Earth, Planets, Space* 73.63.

Kirby, J. T. and T. Chen (1989). “Surface waves on vertically sheared flows: approximate dispersion relations”. In: *J. Geophys. Res.: Oceans* 94.C1, pp. 1013–1027.

Lamb, K. G. (1997). “Particle transport by non-breaking, solitary internal waves”. In: *J. Geophys. Res.* 102.C8, pp. 18641–18, 660.

Latychev, K. and R. N. Edwards (2003). “On the compliance method and the assessment of three-dimensional seafloor gas hydrate deposits”. In: *Geophys. J. Int.* 155, pp. 9223–952.

Lenain, L. and N. Pizzo (2021). “Modulation of surface gravity waves by internal waves”. In: *J. Phys. Oceanogr.* 51, pp. 2735–2748.

Lin, J. et al. (2005). “Accurate imaging and prediction of Kanmon Strait tidal current structures by the coastal acoustic tomography data”. In: *Geophys. Res. Lett.* 32.14, p. L14607.

Lindsey, N. J., T. C. Dawe, and J. B. Ajo-Franklin (2019). “Illuminating seafloor faults and ocean dynamics with dark fiber distributed acoustic sensing”. In: *Science* 366.6469, pp. 1103–1107.

Lindsey, N. J. and E. R. Martin (2021). “Fiber-optic seismology”. In: *Ann. Rev. Earth Planet. Sci.* 49, pp. 309–336.

Lindsey, N. J., H. Rademacher, and J. B. Ajo-Franklin (2020). “On the broadband instrument response of fiber-optic DAS arrays”. In: *J. Geophys. Res.: Solid Earth* 125, e2019JB018145.

Lior, I. et al. (2021). “On the detection capabilities of underwater distributed acoustic sensing”. In: *J. Geophys. Res.: Solid Earth* 126.3, e2020JB020925.

Lobkis, O. I. and R. L. Weaver (2001). “On the emergence of the Green’s function in the correlations of a diffuse field”. In: *J. Acoust. Soc. Am.* 110.6, pp. 3011–3017.

Longuet-Higgins, M. S. (1950). “A theory of the origin of microseisms”. In: *Philos. Trans. R. Soc. A* 243.857, pp. 1–35.

Lu, C. (2015). “Water wave Green’s function retrieval from a random wave field”. PhD thesis. University of Miami.

Martin, E. R. et al. (2018). “Introduction to interferometry of fiber optic strain measurements”. In: *EarthArXiv*, pp. 1–33.

Matsumotu, H. et al. (2021). “Detection of hydroacoustic signals on a fiber-optic submarine cable”. In: *Scientific Reports* 11.2797.

Mecozzi, A. et al. (2021). “Polarization sensing using submarine optical cables”. In: *Optica* 8.6, pp. 788–795.

Neale, J., N. Harmon, and M. Srokosz (2015). “Source regions and reflection of infragravity waves offshore the U.S. Pacific Northwest”. In: *J. Geophys. Res.: Oceans* 120, pp. 6474–6491.

Ochi, M. K. (1998). “Ocean waves: the stochastic approach”. In.

Paitz, P. et al. (2021). “Empirical investigations of the instrument response of distributed acoustic sensing (DAS) across 17 octaves”. In: *Bull. Seis. Soc. Am.* 111.1, pp. 1–10.

Pastor-Graells, J. et al. (2016). “Single-shot distributed temperature and strain tracking using direct detection phase-sensitive OTDR with chirped pulse”. In: *Optics Express* 24, pp. 13121–13133.

Pierson, W. J. and L. Moskowitz (1964). “A proposed spectral form for fully developed wind seas based on the similarity theory of S.A. Kitaigorodskii”. In: *J. Geophys. Res.* 69.24, pp. 5181–5190.

Roux, P. A., W. A. Kuperman, and the NPAL Group (2004). “Extracting coherent wave fronts from acoustic ambient noise in the ocean”. In: *J. Acoust. Soc. Am.* 116, pp. 1995–2003.

Sens-Schönfelder, C. and U. Wegler (2006). “Passive image interferometry and seasonal variations of seismic velocities at Merapi volcano (Indonesia)”. In: *Geophys. Res. Lett.* 33.L21302.

Shapiro, N. M. et al. (2005). “High-resolution surface-wave tomography from ambient seismic noise”. In: *Science* 307.5715, pp. 1615–1618.

Sladen, A. et al. (2019). “Distributed sensing of earthquakes and ocean-solid Earth interactions on seafloor telecom cables”. In: *Nature Communications* 10.1, p. 5777.

Tonegawa, T. et al. (2018). “Excitation location and seasonal variation of transoceanic infragravity waves observed at an absolute pressure gauge array”. In: *J. Geophys. Res.: Oceans* 120, pp. 40–52.

Vazquez, A. et al. (2008). “Meteorologically forced subinertial flows and internal wave generation at the main sill of the Strait of Gibraltar”. In: *Deep Sea Res. I* 55.10, pp. 1277–1283.

Watson, G. and I.S. Robsinson (1990). “A Study of Internal Wave Propagation in the Strait of Gibraltar Using Shore-Based Marine Radar Images”. In: *J. Phys. Oceanogr.* 20, pp. 374–395.

Webb, S. C. (1986). “Coherent pressure fluctuations observed at two sites on the deep sea floor”. In: *Geophys. Res. Lett.* 13.2, pp. 141–144.

Webb, S. C. (1998). “Broadband seismology and noise under the ocean”. In: *Reviews of Geophysics* 36.1, pp. 105–142.

Webb, S. C., X. Zhang, and W. Crawford (1991). “Infragravity waves in the deep ocean”. In: *J. Geophys. Res.* 96.C2, pp. 2723–2736.

Williams, E. F. et al. (2019). “Distributed sensing of microseisms and teleseisms with submarine dark fibers”. In: *Nature Communications* 10.1, p. 5778.

Worchester, P. F. (1977). “Reciprocal acoustic transmission in a midocean environment”. In: *J. Acoust. Soc. Am.* 62, pp. 895–905.

Yamamoto, T. and T. Torii (1986). “Seabed shear modulus profile inversion using surface gravity (water) wave-induced bottom motion”. In: *Geophys. J. R. Astron. Soc.* 85, pp. 413–431.

Yao, H. and R. D. Van Der Hilst (2009). “Analysis of ambient noise energy distribution and phase velocity bias in ambient noise tomography with application to SE Tibet”. In: *Geophys. J. Int.* 179.2, pp. 1113–1132.

Zhan, Z. (2020). “Distributed acoustic sensing turns fiber-optic cables into sensitive seismic antennas”. In: *Seis. Res. Lett.* 91.1, pp. 1–15.

Zhan, Z., V. C. Tsai, and R. W. Clayton (2013). “Spurious velocity changes caused by temporal variations in ambient noise frequency content”. In: *Geophys. J. Int.* 194.3, pp. 1574–1581.

Ziegenbein, J. (1970). “Spatial observations of short internal waves in the Strait of Gibraltar”. In: *Deep Sea Res.* 17.5, pp. 867–875.

Chapter 5

FIBER-OPTIC OBSERVATIONS OF INTERNAL WAVES AND TIDES

Williams, E. F., A. Ugalde, H. F. Martins, C. E. Becerril, J. Callies, M. Claret, M. R. Fernandez-Ruiz, M. Gonzalez-Herraez, S. Martin-Lopez, J. Pellegri, K. B. Winters, and Z. Zhan (in preparation). "Fiber-optic observations of internal waves and tides". In:

Abstract

Although typically used to measure dynamic strain from seismic and acoustic waves, Rayleigh-based distributed acoustic sensing (DAS) is also sensitive to temperature, offering longer range and higher sensitivity to small temperature perturbations than conventional Raman-based distributed temperature sensing. Here, we demonstrate that ocean-bottom DAS on pre-existing fiber-optic cables can be employed to study internal wave and tide dynamics in the bottom boundary layer, a region of enhanced ocean mixing but scarce observations. First, we show temperature transients up to 4 K from a power cable in the Strait of Gibraltar south of Spain, associated with passing groups of internal solitary waves in water depth <200 m. Second, we show the bore-like propagation of the nonlinear internal tide on the supercritical slope of the island of Gran Canaria, off the coast of west Africa, with perturbations up to 2 K at 1-km depth and 0.2 K at 2.5-km depth. With spatial averaging, we also recover a signal proportional to the barotropic tidal pressure, which resolves the lunar fortnightly tide but is an order of magnitude smaller than temperature signals at the same location. Oceanographic temperature transients therefore pose a significant challenge for seafloor geodesy and tsunami monitoring with ocean-bottom DAS.

5.1 Introduction

Internal gravity waves generated by tides, currents, and atmospheric forcing mediate the intensity of ocean mixing, with broad implications for circulation, climate, and biogeochemistry. Early work by W. H. Munk (1966), Garrett and W. Munk (1972), and others proposed that mixing is primarily accomplished through nonlinear interactions and breaking of topographically generated internal waves distributed throughout the ocean interior. However, over the past three decades, observational campaigns have found that the most vigorous mixing occurs near the bottom in regions of rough bathymetry, and that rates of turbulent dissipation vary by at least three orders of magnitude (Toole, Schmitt, and K. L. Polzin, 1994; Kunze and Sanford, 1996; K. Polzin et al., 1997; Ledwell et al., 2000; Rudnick et al., 2003; Waterhouse et al., 2014). Yet, observations of internal wave-driven ocean mixing remain exceedingly sparse, especially in the bottom boundary layer. Moored and towed thermistor arrays, current meters, and microstructure profilers can provide high-resolution, local estimates of diapycnal diffusivity and turbulent dissipation rates (e.g. Toole, Schmitt, and K. L. Polzin, 1994; van Haren, 2006), whereas satellite altimetry provides a coarse global budget of internal wave generation and dissipation (Egbert and R. Ray, 2000; Egbert and R. D. Ray, 2001). Reconciling internal wave and boundary layer dynamics across the vast gulf in scales from astronomical forcing to turbulent dissipation and understanding the physical processes governing the generation and distribution of turbulence are outstanding theoretical and observational challenges, especially for the parameterization of mixing in ocean circulation models.

Distributed fiber-optic sensing offers a promising new approach to observe internal wave dynamics at the seafloor by converting a fiber-optic cable into a dense array of high-resolution temperature sensors. Recently, Connolly and Kirincich (2019), Davis et al. (2020), and others have demonstrated the value of distributed temperature sensing (DTS) for studying shoaling internal waves. Most DTS systems use the intensity of Raman scattering from a repeated laser pulse to estimate temperature along a fiber and are insensitive to other variables like fiber strain. With proper calibration (e.g. Sinnett et al. (2020)), DTS offers absolute temperature measurements with a sensitivity of about 0.01 K and sub-meter sampling up to a range of 10–30 km (Li and Zhang, 2022). However, DTS suffers from a trade-off between distance and sensitivity, which limits its application to shallow water environments insomuch as the DTS laser interrogator must remain onshore. Further, DTS is best suited for multi-mode fiber, which means that pre-existing ocean-bottom telecommunications "dark" fiber cannot be easily repurposed as temperature sensing arrays because it is mostly single-mode. Another fiber-optic sensing technology, distributed acoustic sensing (DAS) uses the phase of Rayleigh-scattered laser light to estimate changes in the optical path length, which can be caused by both temperature and elastic deformation with an equivalence of $1K = 10\mu\varepsilon$ (or $10^{-5}m/m$) (Fernandez-Ruiz, Soto, et al., 2020; Lindsey and Martin, 2021). At short periods (<50-100 s) or in shallow water (<100-200 m), mechanical strain from ocean surface gravity, acoustic, and seismic waves always dominates over temperature effects, permitting diverse applications of ocean-bottom DAS from earthquake detection and structural characterization of the seafloor (Sladen et al., 2019; Cheng et al., 2021; Williams, Fernandez-Ruiz, Magalhaes, Vanthillo, Zhan, Gonzalez-Herraez, and Martins, 2021) to monitoring sea state and tracking coastal currents (Lindsey, Dawe, and Ajo-Franklin, 2019; Williams, Fernandez-Ruiz, Magalhaes, Vanthillo, Zhan, and Gonzalez-Herraez, 2019; Williams, Zhan, et al., 2022). However, at long periods or in deep water, temperature transients associated with internal waves and tides may rise to the fore. Ide, Araki, and Matsumoto (2021) first reported complex temperature signals at tidal periods in ocean-bottom DAS measurements offshore Cape Muroto in southern Japan. With a field sensitivity of about $1 - 10n\varepsilon = 0.0001 - 0.001K$, DAS is actually more sensitive to small temperature signals than DTS and can operate up to 100 km without significant reduction in sensitivity, permitting oceanographic investigations at abyssal depths where temperature anomalies are small. However, DAS faces several challenges of its own: temperature and mechanical strain effects cannot be definitively separated in a single measurement, temperature calibrations for DAS have not yet been standardized, and the instrumental noise increases with period on most DAS systems.

Here, we present two novel observations of internal wave dynamics from ocean-bottom DAS arrays. In Section 3, we show temperature perturbations up to 4 K associated with internal solitary waves crossing a power-cable in the Strait of Gibraltar, south of Spain. In Section 4, we show temperature perturbations up to 2 K associated with nonlinear, bore-like propagation of the internal tide on the supercritical slope of Gran Canaria, in the Canary Islands offshore west Africa. Throughout, we assume that these long-period signals solely represent temperature, an assumption which we then discuss and justify in Section 5.

5.2 Data

We analyze and compare observations from two DAS datasets acquired on seafloor cables containing optical fibers. The first was recorded in October 2019 on a 30-km power cable running from Spain to Morocco across the Strait of Gibraltar, with depths up to about 550 m (Figure 5.1A). The cable is generally buried on the Spanish shelf, and emerges at the seafloor at 8.6 km optical distance. The second was recorded in August and September 2020 on a 176-km telecommunications cable connecting Gran Canaria to Tenerife in the Canary Islands, with depths up to about 4 km (Figure 5.1B). The cable is entirely unburied beyond the surf zone. Fibers

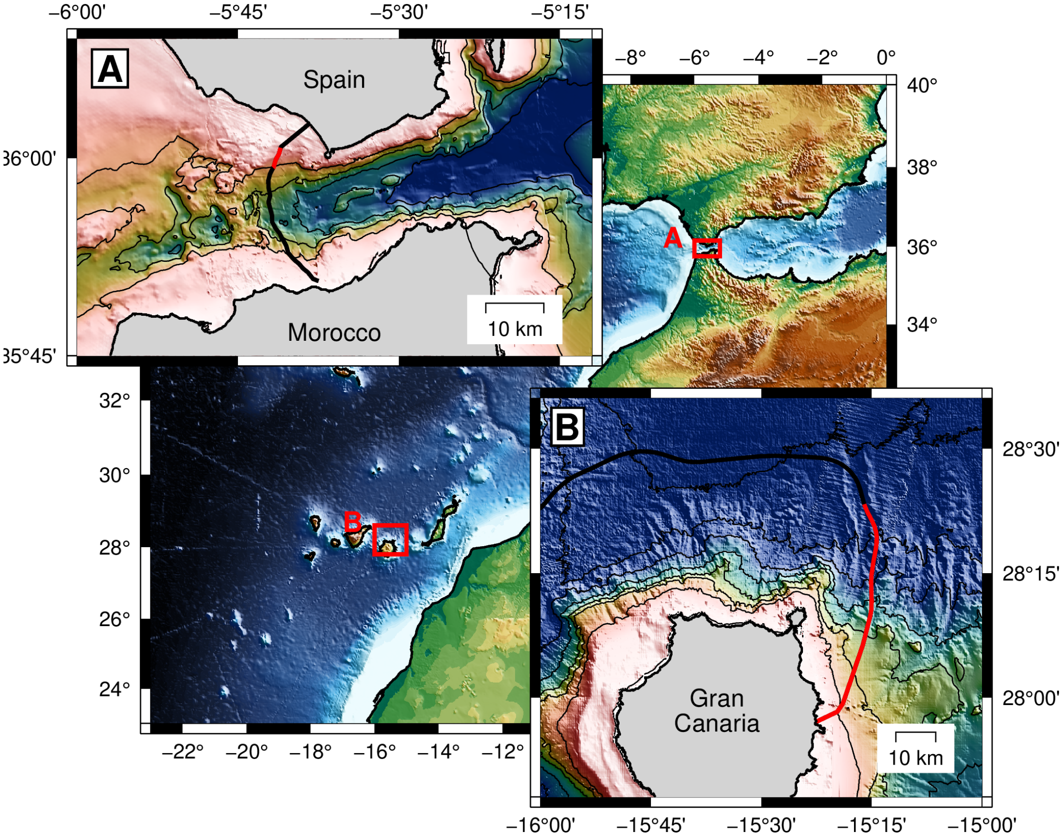

Figure 5.1: Map of cable locations. (A) Power cable from Spain to Morocco across the Strait of Gibraltar (black) with section shown in Figure 5.2 in red; 200-m bathymetry contours (B) Telecommunications cable from Gran Canaria to Tenerife (black) with section shown in Figure 5.3 in red; 1000-m bathymetry contours.

in both cables were interrogated with a chirped-pulse DAS system built by Aragon Photonics and operated by the University of Alcala (Pastor-Graells et al., 2016; Fernandez-Ruiz, Martins, et al., 2018; Fernandez-Ruiz, Costa, and Martins, 2019), using a 10-m gauge length and 10-m channel spacing. The raw DAS data were first decimated from 1 kHz to 1 Hz by averaging. A five-point median filter was applied to the 1-Hz data to prevent instrumental noise like spikes and steps from biasing long period results, and then the data were further decimated to 100-s sampling period. For more information, see Williams, Zhan, et al. (2022) and Ugalde et al. (2022).

5.3 Internal solitary waves in the Strait of Gibraltar

5.3.1 Observations

Four days from the Strait of Gibraltar DAS dataset are plotted in Figure 5.2. Across the buried section of the cable, there is no evident temperature signal at any period.

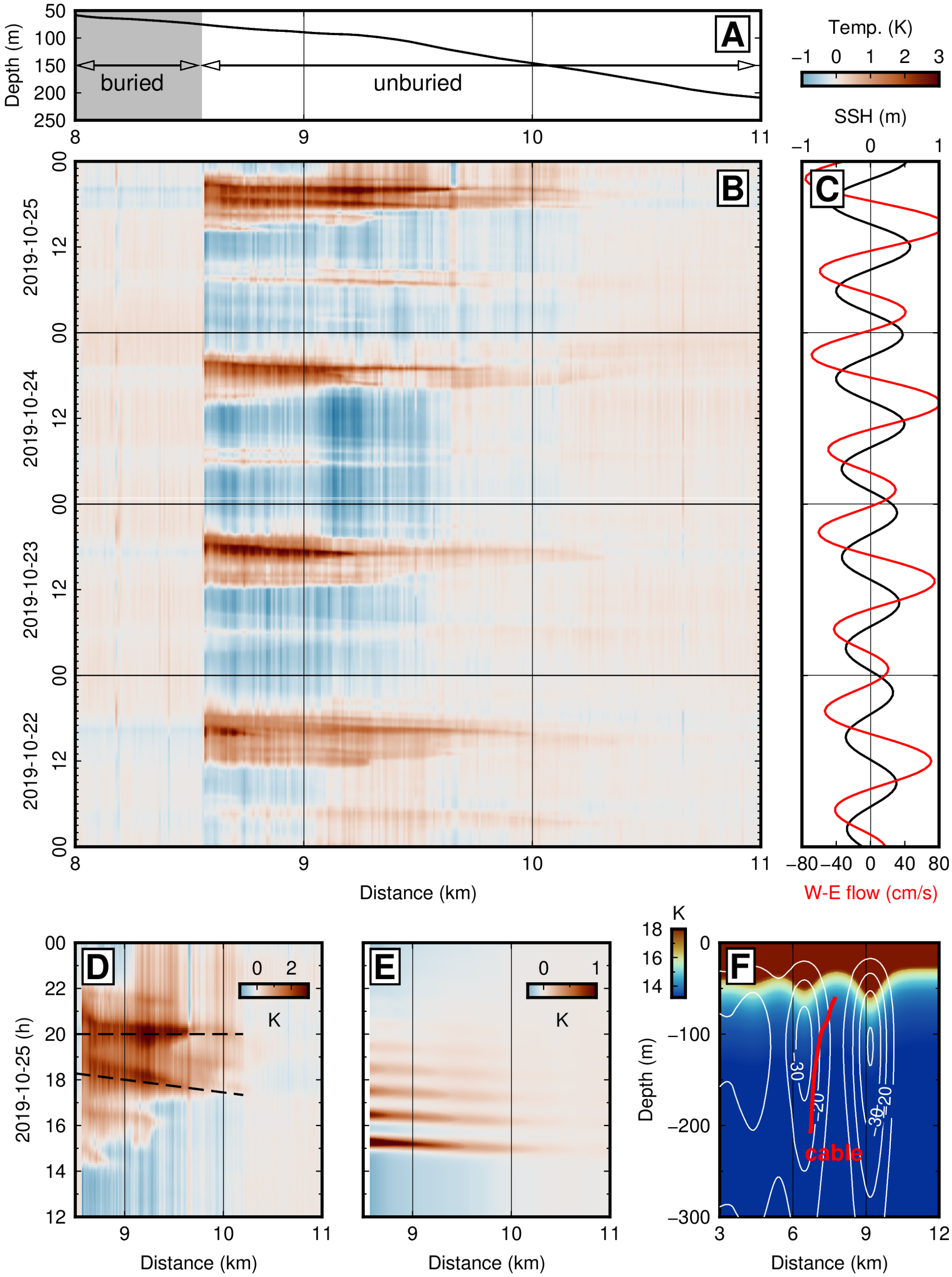

Figure 5.2: Internal solitary wave groups on the Gibraltar cable. (A) Cable bathymetry profile with shading to indicate burial. (B) DAS data from 2019-10-22 to 2019-10-25 for the 8–11-km cable section. (C) Tidal predictions for sea surface height (SSH, black) and meridional flow (red) from TPXO. (D) Zoom-in to Figure 2B showing a group of internal solitons, with dashed black lines schematically indicating the difference in apparent speed between individual solitons. (E) Synthetic data generated using the "dnoidal" model of Apel (2003) for the 8–11-km cable with a source at the north end of Camarinal Sill on the Spanish shelf. (F) Cross-section of the model after Apel (2003) at $T = 4$ h with absolute temperature, contours of constant isopycnal displacement (white lines), and depth vs. distance from source for the 8–11-km cable segment (red).

Emerging abruptly at 8.6 km where the cable is exposed at the seafloor, a constant background temperature is periodically broken by positive excursions up to 4 K, indicative of internal waves of depression. Each internal wave group lasts 2-8 h and is composed of 2–6 subsidiary solitary waves, each with a period of 1–2 h (Figure 5.2B,D). These excursions occur twice daily immediately following the maximum eastward tidal flow and exhibit a daily oscillation in amplitude, which correlates with the daily inequality of the diurnal and semidiurnal tides as expressed in the TPXO9 shallow-water solution for the local barotropic current (Figure 5.2C) (Egbert and Erofeeva, 2002). The amplitude is strongest where the cable emerges at 8.6 km distance (75 m depth) and decays monotonically with distance, disappearing before the 11-km mark (200 m depth).

5.3.2 Interpretation

Hydrodynamics in the Strait of Gibraltar are characterized by a two-layer exchange flow between salty Mediterranean water at the bottom and less-salty Atlantic water at the surface, with a strong pycnocline typically measured at 50-100 m depth near the cable location east of the Camarinal Sill. Modulation of the exchange by tidal currents results in partial blocking of the Mediterranean outflow over the Camarinal Sill and the generation of weakly-dispersive internal solitary waves, which propagate eastward into the Alboran Sea and have been widely observed by moorings and in synthetic aperture radar (SAR) imagery (Brandt, Alpers, and Backhaus, 1996; Wesson and Gregg, 1994; Vazquez et al., 2008; Ziegenbein, 1969; Ziegenbein, 1970; Watson and Robsinson, 1990). Although no clear SAR images of internal waves were acquired during the four-day data window, the Sentinel-1A satellite captured an internal wave group propagating past Gibraltar at 2019-10-26 06:27:44 UTC, shortly after the end of DAS acquisition (Figure 5.S1A). This likely corresponds to the wave group shown in Figure 5.2D and confirms that this well-studied phenomenon occurred during our experiment.

In order to understand the relationship between internal wave parameters and the temperature signals recorded in DAS data, we compare our observations with synthetic data generated from the "dnoidal" model of Apel (2003) (Figure 5.2E,F), which combines an analytical solution of the Korteweg-de Vries equation for weakly-nonlinear solitary wave propagation with a vertical structure function obtained by numerical solution of the Taylor-Goldstein equation (see Supplementary Information). While the observed inter-soliton period and group shape are poorly reproduced by this simplistic model, the synthetic data match the amplitude of the temperature anomaly within a factor of two and mimic its quasi-triangular shape with depth and distance (Figure 5.2D,E). The DAS temperature observations can consequently be understood as an oblique cross-sectional slice of the internal wave group along the cable trajectory, where the shape is governed by a combination of the isotherm displacement with the thermal stratification and the moveout is determined by the source azimuth and propagation speed (Figure 5.2F). Though the travel-time curve along the cable varies slightly from one solitary wave to the next, suggesting a complex source distribution (Figure 5.2D), the apparent speed of propagation along the fiber direction is almost instantaneous, which requires broad-side incidence of the internal wave group and a source at the northern end of the Camarinal Sill or on the Spanish shelf (Figure 5.S2). The ESE-ward propagation perpendicular to the cable azimuth that would result from a dominant source at the northern end of the Camarinal Sill is supported by SAR imagery (Figure 5.S1B, see also Brandt, Alpers, and Backhaus (1996) Figure 16B). However, given trade-offs between speed, source time, and source location as well as refraction across the steep bathymetry, it is impossible to uniquely identify the source without more elaborate modeling.

5.4 Nonlinear internal tides at Gran Canaria

5.4.1 Observations

Three days from the Gran Canaria DAS dataset are plotted in Figure 5.3, showing semidiurnal temperature oscillations up to 2 K in amplitude which persist along the entire slope spanning a depth range >3 km. The observations can generally be divided into three domains. On the main slope of Gran Canaria (12–30 km distance, 500–1500 m depth) three to five sharp, bore-like cold fronts form every 12 hrs and propagate up slope during the southward phase of barotropic tidal flow (Figure 5.3C, 5.4B; Supplementary Movie S1). Here, the slope is slightly supercritical, with $1 \leq \tan(\alpha_s)/\tan(\alpha_w) \leq 3$, where the α_s is the absolute slope angle and α_w is the angle of internal wave energy propagation (Figure 5.3B). As these fronts form and accelerate up to an apparent velocity of 0.5 m/s along the cable, they intensify to a contrast in excess of 1 K over a distance of only a few hundred meters. Then, as the tidal flow reverses direction, the cold fronts slow, dissipate, and reform into a series of weaker warm fronts that recede down the slope. In shallow water (7–12 km distance, <500 m depth, $\tan(\alpha_s)/\tan(\alpha_w) > 3$), the shoaling cold fronts slow to an apparent velocity of 0.1 m/s and divide into 5-10 weaker fronts across each semidiurnal cycle (Figure 5.4A; Supplementary Movie S2). Beyond a sharp ridge at 30-km distance, the seafloor fabric is much rougher and the flow pattern more

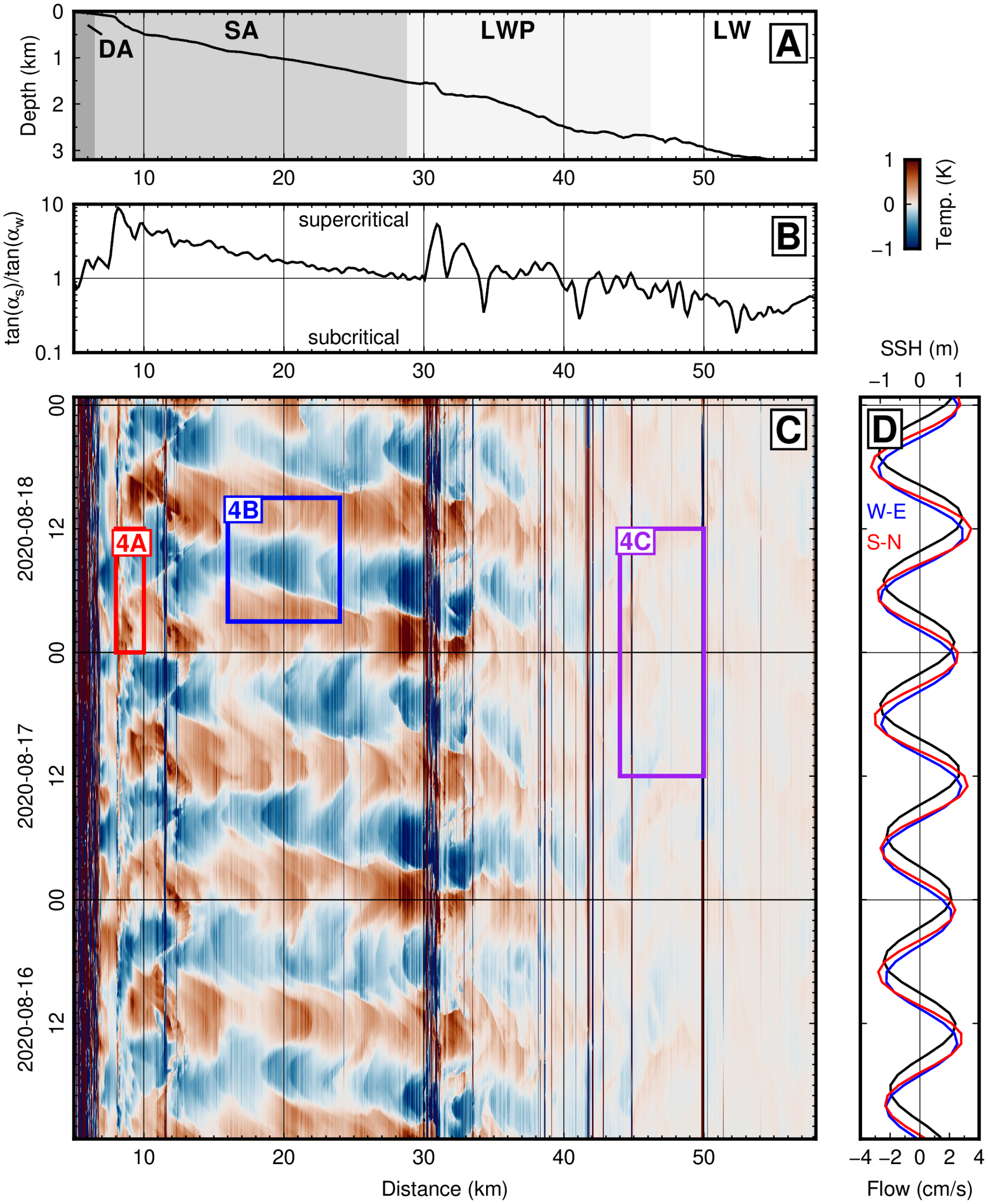

Figure 5.3: Nonlinear internal tide on the slope of Gran Canaria. (A) Cable bathymetry profile with shading to indicate cable type: double armored (DA), single armored (SA), light-weight protected (LWP), and light-weight (LW). (B) Slope criticality along the cable profile, defined as the ratio of the absolute slope angle to the angle of internal wave energy propagation. (C) DAS data from 2020-08-16 to 2020-08-18 for the 5–58-km cable section. (D) Tidal predictions for sea surface height (black), meridional flow (blue), and zonal flow (red) from TPXO.

complex, but sharp temperature fronts up to about 0.2 K still persist and are advected horizontally by the tidal current (Figure 5.4C).

5.4.2 Interpretation

Steep submarine topography acts as both a source for the conversion of barotropic tidal motions into internal waves and a sink where the internal tide reflects and breaks, thus mediating the cascade of energy in the ocean from large to small scales where mixing occurs (Klymak et al., 2011; St. Laurent and Garrett, 2002; Rudnick et al., 2003). High-resolution thermister observations and modeling of steep, near-critical slopes have shown that the generation and shoaling of the internal tide drives the formation and propagation of nonlinear bore-like fronts in the bottom boundary layer (van Haren, 2006; Winters, 2015) associated with intensified turbulent mixing and shear instability (van Haren and Gostiaux, 2012; van Haren, Cimatoribus, and Gostiaux, 2015; van Haren and Gostiaux, 2010). These observations are broadly consistent with the temperature oscillations in DAS data from Gran Canaria, including frontal velocities in the range 0.1-0.5 m/s and temperature perturbations up to 3 K at 500-m depth (van Haren and Gostiaux, 2012), 2 K at 1400-m depth (van Haren, 2006), and 0.2 K at 2500-m depth. (van Haren, Cimatoribus, and Gostiaux, 2015). The observed pattern of the shoaling, weakening, and reversal of bore-like fronts is similar to signals observed in very shallow water with DTS at Dongsha Atoll, which Davis et al. (2020) termed "relaxation" and may relate to breaking or overturning in the boundary layer (van Haren and Gostiaux, 2012; van Haren and Gostiaux, 2010).

The temperature spectra from DAS data exhibit dominant peaks at semidiurnal (M_2) and diurnal (O_1, K_1) frequencies (Figure 5.4D,E). At the latitude of Gran Canaria, the inertial frequency is very close to O_1, so the prominence of the diurnal peak could relate to both forcing of the diurnal tide and local generation of near-inertial waves on the slope, such as by flow. Also evident are several tidal overtones (MK_3, M_4, etc.), which persist in relative amplitude across the full range of observations, indicating nonlinear interactions on the slope associated with local conversion of the barotropic tide or steepening of the internal tide (van Haren, Maas, and van Aken, 2002). For the deepest cable segment beyond 40-km distance, the spectrum approximately scales as f^{-2} (Figure 5.4D), similar to the canonical Garrett-Munk spectrum for internal waves in the ocean interior, away from generation sites. For the 7–30-km cable segment, the spectrum is flatter from about 1 up to 10 cpd, indicative of stronger nonlinearity, approximately scaling as f^{-1}. At higher frequencies, the spectrum

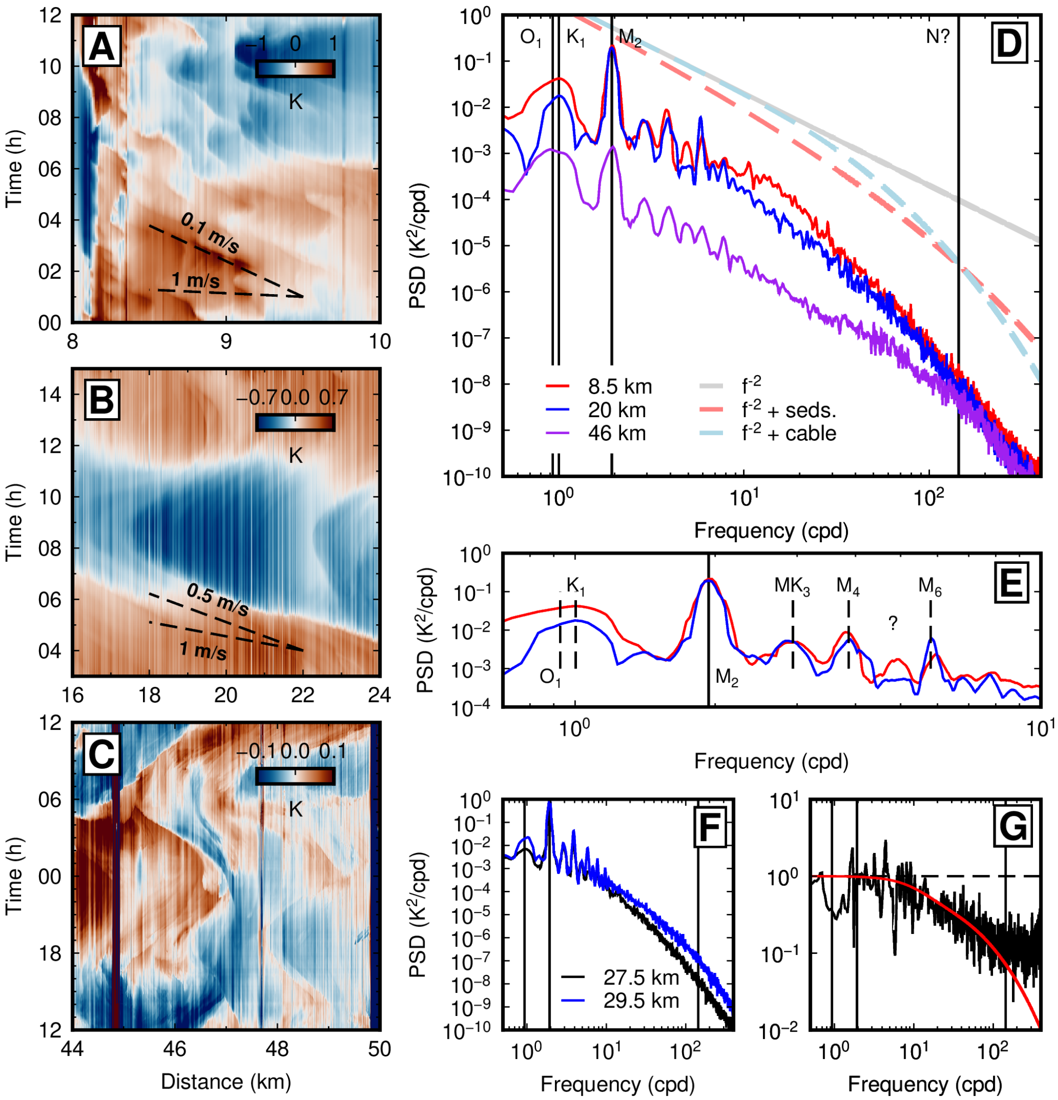

Figure 5.4: (A) Zoom-in to the 8–10–km cable segment of the Gran Canaria dataset showing many small cold fronts shoaling on the shallow shelf. (B) Zoom-in to the 16–24-km cable segment showing a sharp cold front propagating up slope, slowing around 18-km, and reversing or breaking. (C) Zoom-in to the 44–50-km cable segment showing complex, sharp temperature fronts oscillating at tidal periods. (D) Thirty-day power spectral density (PSD) for a represenentative channel from each panel of (A,B,C), compared with a reference slope of f^{-2} and dashed lines illustrating the effect of burial (light red) or cable thickness (light blue) on the frequency-dependent temperature response. (E) Zoom-in to (D) showing the ordinary tidal harmonics (O_1, K_1, M_2) and nonlinear overtones (MK_3, M_4, M_6) present at all water depths. (F) Spectra for two channels on either side of the single-armored to light-weight protected cable transition, showing a frequency-dependent difference in response. (G) Transfer function between the two channels in (F) (black line) and simple thermal model based on the actual difference in cable diameter (red line).

steepens beyond f^{-3}, which may reflect diminished temperature sensitivity due to the finite thickness of the cable construction or even a few millimeters of sediment drape (Figure 5.4D). Comparing adjacent cable segments across the transition from single-armored (SA, 26-mm diameter) to light-weight protected (LWP, 19.6-mm diameter) cable type, there is a clear frequency-dependent difference in response, which can be adequately described with a simple thermal transfer-function model (Figure 5.4F,G). Consequently, the spectral slope at high frequencies should probably not be interpreted. For such a model, the phase response of the cable to external thermal forcing is also frequency-dependent and non-negligible, which implies that the sharp temperature fronts observed here may truly be sharper still if observed by a thermister at the same location (see Supplementary Information, Figure 5.S3).

5.4.3 Pressure signature of the barotropic tide

During acquisition of the Gran Canaria dataset, the DAS interrogator implemented a laser denoising workflow, which subtracted the median of each sample between the 15–30-km cable segment from the entire dataset (Fernandez-Ruiz, Pastor-Graells, et al., 2018). While this default choice of a reference fiber segment was effective at removing laser drift, which affects all channels simultaneously, it also had the unintended effect of isolating a long-wavelength semidiurnal signal, which was added back in to the onshore channels, including equally channels both buried and hanging freely in slack loops and therefore not possibly related to solid-Earth tides. This signal, here arbitrarily taken from a quiet buried segment near the beach at 4-km distance, is plotted in Figure 5.5 and compared with the seafloor pressure for the barotropic tide, estimated from TPXO (Egbert and Erofeeva, 2002). The recovered signal matches the predicted phase of the barotropic tide as well as the fortnightly variation (M_f), which strongly suggests that this signal represents mechanical strain in the cable due to pressure. The observed amplitude is of order 1 $\mu\varepsilon$ and scales to pressure as $\frac{\varepsilon}{\Delta p} \sim 3 \times 10^{-10}$ Pa^{-1}, which is a plausible value of normalized horizontal seafloor compliance (Crawford, Webb, and Hildebrand, 1991) at semidiurnal period—that is, the ratio of horizontal strain to applied pressure, which is a function of lithospheric shear modulus—and about ten times smaller than the predicted strain induced in a cable from hydrostatic pressure perturbations (Mecozzi et al., 2021). While we note that this accidental filtering procedure does not guarantee the full recovery of the tidally-induced mechanical strain signal, the demonstrated sensitivity is promising for application of ocean-bottom DAS in seafloor geodetic studies.

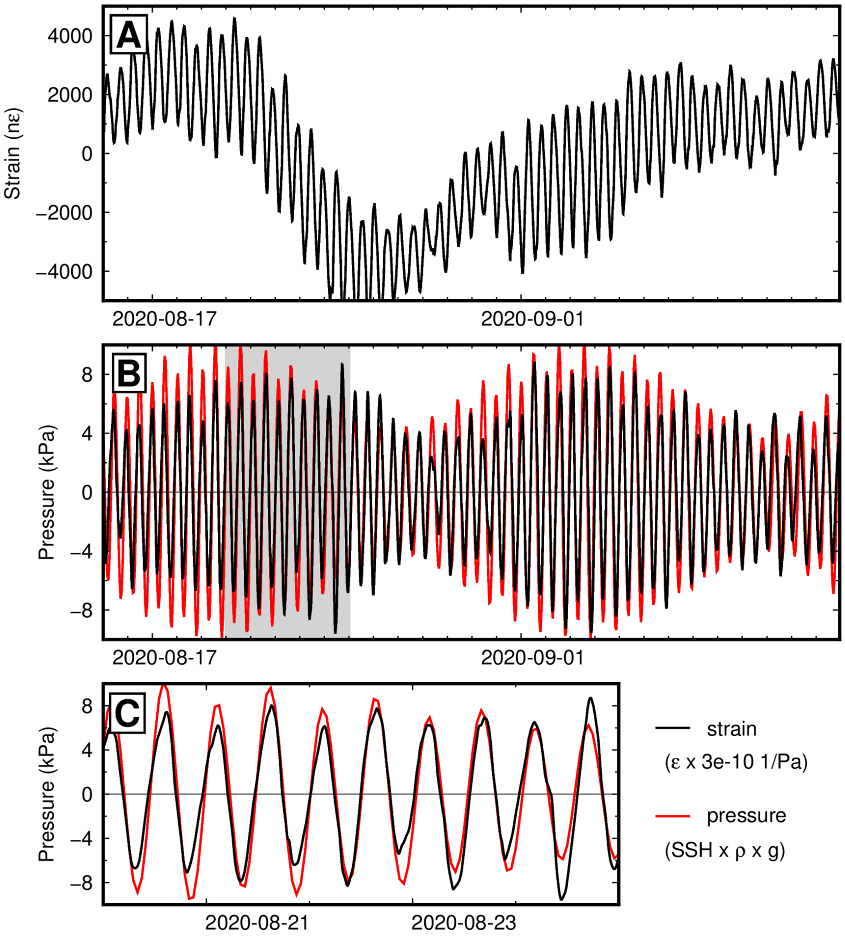

Figure 5.5: (A) Long-period DAS signal removed by the default laser denoising parameters in units of nanostrain. (B) Same as (A) with low-pass filter with a corner frequency of 48 h scaled to units of pressure as $p = \varepsilon/(3 \times 10^{-10})$ (black), and barotropic tidal pressure from TPXO (red). (C) Zoom-in to the gray shaded window in (B).

5.5 Discussion and conclusions

Thus far we have assumed that the long-period transients observed in DAS data from the Strait of Gibraltar and Gran Canaria are dominated by temperature. Conventional applications of DAS are, however, as a dynamic strain sensor, and the extraction of a signal proportional to barotropic tidal pressure indicates that mechanical strain is non-negligible. For a finite fiber segment of length L, the differential phase is given by:

$$\Delta\phi = \frac{4\pi nL}{\lambda}\left(\frac{\delta L}{L} + \frac{\delta n}{n}\right)$$

where n is the index of refraction and λ is the laser wavelength. Changes in the optical path length measured by DAS can therefore result from mechanical strain or a change in temperature. Both mechanisms include a physical strain $\frac{\delta L}{L}$ and a change in refractive index $\frac{\delta n}{n}$. Letting $\phi = \frac{4\pi nL}{\lambda}$, for mechanical strain ε, $\frac{\Delta\phi}{\phi} = (1 + \psi)\varepsilon$, where $\psi \approx -0.22$ accounts for the effect of photoelasticity at $\lambda = 1550$ nm. For a change in temperature ΔT, $\frac{\Delta\phi}{\phi} = (\alpha_T + \xi)\Delta T$, where the thermal expansion coefficient is $\alpha_T \approx 5 \times 10^{-7}$ K^{-1} and the thermo-optic coefficient is $\xi \approx 6.8 \times 10^{-6}$ K^{-1}. Therefore the equivalence between temperature and strain is $\frac{\Delta T}{\varepsilon} \approx 10^5$ K (e.g. Koyamada et al. (2009)). The uncertainty in these parameters is challenging to quantify, since no calibration has been performed in situ, but a factor of two deviation in the strain-to-temperature relation is conceivable, considering only the range of published values. Cable construction and burial can only thermally insulate the fiber, so the conversion used here should otherwise represent a minimum value of relative temperature (Sidenko et al., 2022).

Based on four key points of observation, we assert that the long-period transients described above are predominately if not entirely changes in the temperature of the fiber:

1. A 40 $\mu\varepsilon$ strain, equivalent to the 4 K observed in Gibraltar, is simply too large to be physically plausible, being comparable to the near-field (<1-km epicentral distance) peak strain recorded during the 2019 M7.1 Ridgecrest earthquake (Farghal, Baltay, and Langbein, 2020) and order 10% of the yield strain of common Earth materials. Further, the 2 K transient observed at Gran Canaria is coherent over a >10-km distance, which would imply an integrated displacement of at least 20-cm every 12-hr across the cable.

2. The sudden disappearance of a 4 K signal at the point of burial of the Gibraltar cable over a distance of one channel (10 m) (Figure 5.2) can only be attributed to temperature. Any pressure forcing sufficient to deform a cable at the seafloor 40 $\mu\varepsilon$ must be transmitted at a measurable level to a shallowly buried cable, as evidenced by much smaller surface gravity wave pressure signals observed on the buried 3–6-km section of this same cable (Williams, Zhan, et al., 2022). Conversely, thermal signals may be retarded by as little as a few centimeters of sediment, owing to the small thermal diffusivity of geological materials.

3. The observed signature of the nonlinear internal tide at Gran Canaria (Figure 5.3) is about 40 times larger than the recovered pressure signature of the barotropic tide (Figure 5.5), which is inconsistent with mechanical strain. The

ocean-bottom pressure due to the barotropic tide (order 1-10 kPa) is larger than that due to internal waves and tides (order 10-100 Pa), because the density difference at the sea surface is about 1000 times larger than the density difference across the pycnocline, even though internal wave displacement may be up to about 100 times larger (e.g. Moum and Smyth (2006)). Conversely, the ocean-bottom temperature perturbation from the barotropic tide is negligible, whereas internal waves and tides can induce >1 K changes even at depths >1 km (e.g. van Haren (2006)).

4. The change in cable type between single-armored and light-weight protected around 29-km on the Gran Canaria cable (Figure 5.3A) manifests a frequency-dependent change in sensitivity which can be adequately described using a simple thermal model (Figure 5.4F,G).

We conclude that the observed long-period transients in both datasets are dominated by temperature effects. However, the relative contributions of strain and temperature may not be so simple to separate in most ocean-bottom DAS datasets. In particular, DAS has potential as a seafloor geodetic method for monitoring offshore fault zones, but the solid-Earth strains associated with processes like fault creep and slow earthquakes will likely be smaller than or comparable to oceanic temperature signals from internal tide and boundary layer dynamics along the slopes of active margins. Concurrent measurement with both DAS and DTS may provide one solution, but is limited by the short range of DTS. Another possibility is to utilize bespoke cables with fibers of differing thermal properties so that the temperature signal can be subtracted (Zumberge, Hatfield, and Wyatt, 2018), but this excludes pre-existing submarine telecommunications cables. Here, we recovered mechanical strain associated from pressure by naive spatial averaging, which was successful owing to the difference in wavelength between the internal and barotropic tides. This suggests that a more general multi-scale approach like principal component analysis might be capable of separating mechanical and thermal signals, as is commonly performed to remove secular and seasonal trends from geodetic time-series.

Our study highlights several other outstanding challenges for fiber-optic oceanography. DAS sensitivity to temperature has not been calibrated in a field environment, and the thermal amplitude and phase response of submarine cables is generally not known. In both the Strait of Gibraltar and Gran Canaria DAS datasets, we observed "striping," indicative of differences in long-period response between even

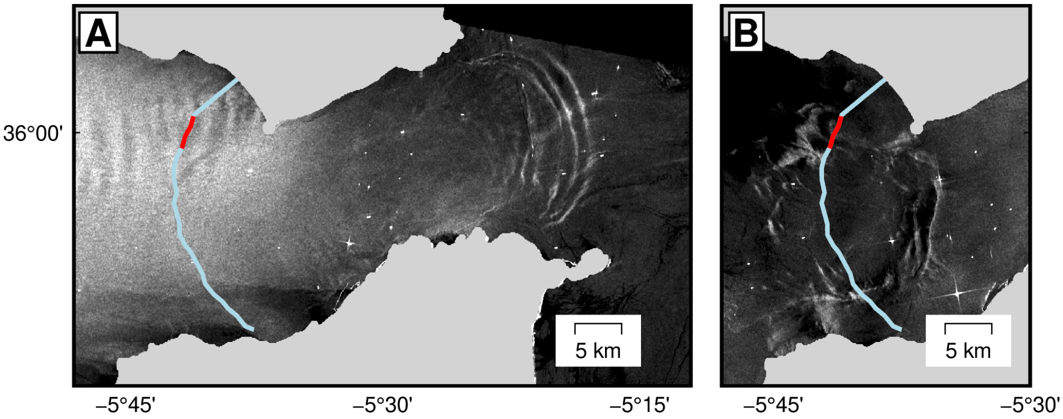

Figure 5.S1: (A) Synthetic aperture radar (SAR) image of the Strait of Gibraltar from Sentinel-1A acquired at 2019-10-26 06:27:44 UTC, showing an internal wave group propagating eastward into the Alboran Sea (normalized color scale). (B) SAR image from Sentinel-1B acquired at 2019-10-02 18:17:43 UTC showing a nascent internal wave group near the cable location propagating ESE, suggestive of a source towards the north of the Strait.

adjacent channels, which could not be accounted for with a simple thermal model for partial burial or variations in sediment drape. Beyond the instrument itself, the novel observation of a continuous horizontal profile of seafloor temperature needs to be reconciled with conventional oceanographic measurements. For example, in-situ comparison with data from current meters and moored thermisters could help explain whether the dissipation and reversal of temperature fronts on the slope of Gran Canaria is associated with internal wave breaking, and whether the internal tide is being generated locally or remotely. Importantly, without complementary measurements it is not possible to directly calculate the diapycnal diffusivity or other key parameters necessary to quantify the intensity of mixing and tidal dissipation observed here. Until such calibrations and validations are available, the ability of ocean-bottom DAS to leverage widespread, pre-existing submarine telecommunications infrastructure at relatively low cost for monitoring near-bottom dynamics from the abyssal ocean to the shallow shelf may prove most useful for targeted site selection of conventional oceanographic surveys and generalization of local measurements to larger scales.

Supplementary Material

A schematic internal wave model after Apel (2003)

In order to understand the relationship between the temperature excursions observed with DAS and internal solitary wave parameters, we constructed synthetic data

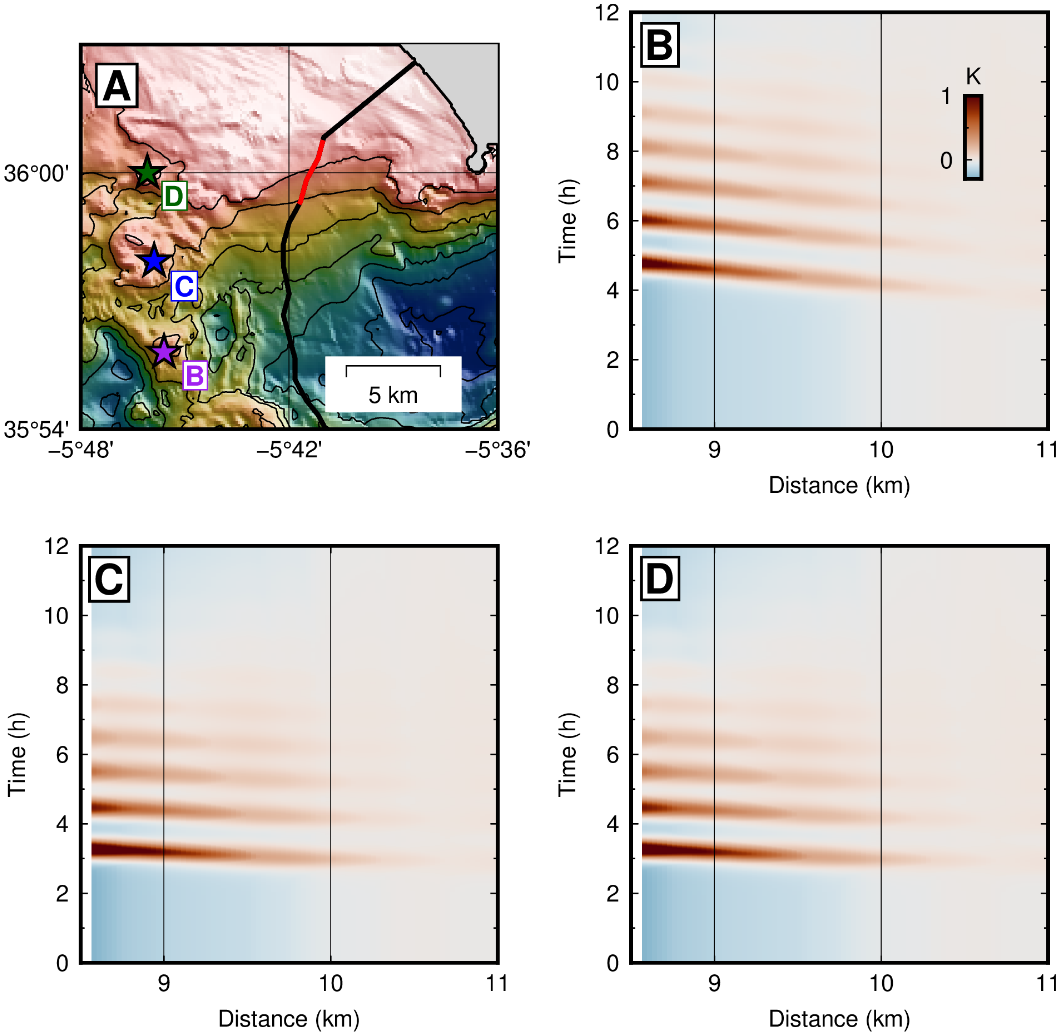

Figure 5.S2: (A) Map of the Camarinal Sill and Strait of Gibraltar cable location, with the segment from Figure 2 shown in red. (B,C,D) Synthetic data generated using the schematic model of Apel (2003) for different point sources shown in (A), assuming straight-ray propagation. Panel (D) is the same as Figure 2E.

using the "dnoidal" model of Apel (2003). We first picked a relatively arbitrary source location at the northern end of the Camarinal Sill towards the Spanish shelf (green star in Figure 5.S2A) and calculated the propagation distance for each point along the cable path. Then, we evaluated the Apel's model to obtain the isopycnal displacement at each point along the cable as a function of time:

$$\eta(x,z,t;k) = \eta_0 W_k(z) I(x,t) \left[2\mathrm{dn}^2_{s(x)} \left(\frac{1}{2} k_0 (x - Vt) \right) - \left(1 - s^2(x) \right) \right]$$

Here, $W_k(z)$ is the vertical structure function determined by numerical solution of the Taylor-Goldstein equation given realistic stratification for the Strait of Gibraltar. The duration and decay of the wave group is given by $I(x,t)$, which is an envelope function. The term $\mathrm{dn}_{s(x)}$ is a Jacobian elliptic function and a solution to the Korteweg-de Vries equation for weakly nonlinear wave propagation. The term $s(x)$ is a shape parameter for the Jacobian elliptic function which determines the dispersion. Apel (2003) provides expressions to evaluate each of these terms along with hyperparameters used by Apel to model SAR images of internal solitary wave propagation in the Strait of Gibraltar. We set the leading-soliton wavelength k at 2-km to match SAR scenes acquired around the time of our experiment (Figure 5.S1) and modified one parameter in I to make the group duration 6-h for comparison with the data. Otherwise, all parameters are as provided by Apel (2003).

Given the model time-series of isopycnal displacement along the cable, we then multiplied the isopycnal displacement by the local temperature gradient $\frac{\partial T}{\partial z}$ using a CTD profile from the 1986 Gibraltar Experiment nearest the cable location (Kinder and Bryden, 1987) in order to obtain the relative temperature at each point. This assumes negligible diapycnal transformation during wave propagation. Previous authors have noted a persistent change in stratification following the passage of internal solitary wave groups in the Strait of Gibraltar (Ziegenbein, 1969), which implies this may be a poor assumption, although the background temperature observed in DAS data is unchanged between passing wave groups (Figure 5.2). The validity of this assumption is relatively minor, however, compared to other simplifying assumptions made by this model: any background current is neglected, propagation is assumed along a straight raypath, and the effect of bathymetry on propagation speed is neglected. Consequently, the synthetic data in Figure 5.2E and 5.S3 should only be considered a schematic representation.

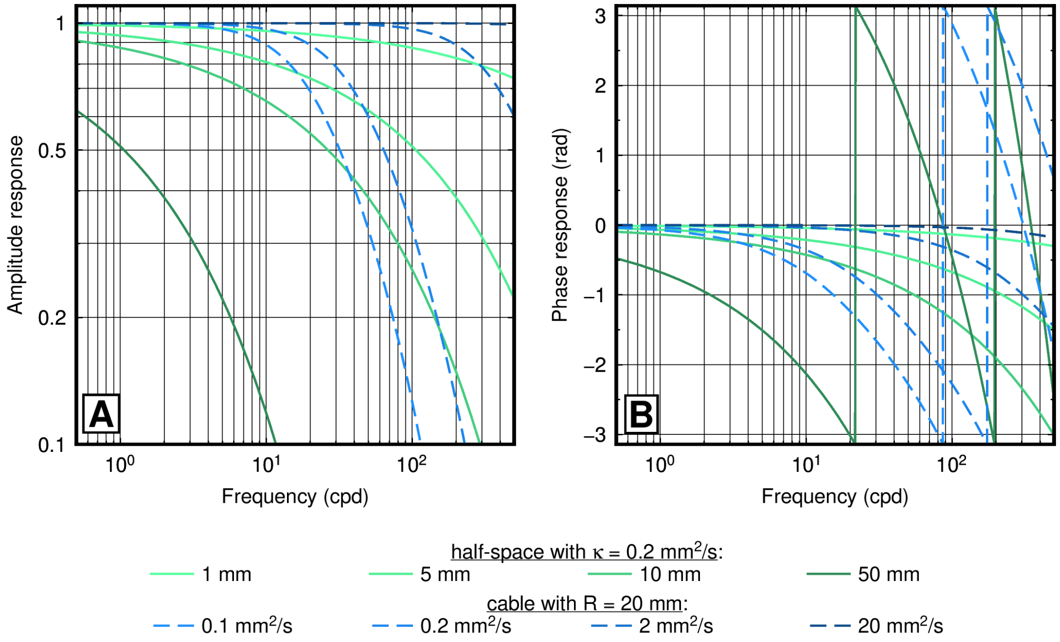

Figure 5.S3: Amplitude (A) and phase (B) response to harmonic temperature forcing at the free surface for a point in a half-space (green) and at the center of a disk (blue) with uniform thermal diffusivity, which are simple models of sediment burial and cable thickness.

Simple thermal models for the attenuation of temperature by cable construction and burial

To represent the effect of sediment cover or burial on the temperature measured within a cable by DAS, consider heat conduction in a semi-infinite solid $u_t = \kappa u_{zz}$ with uniform thermal diffusivity κ and time-harmonic temperature forcing at the free surface $u(z = 0, t) = Ae^{i\omega t}$. This has solution $u(z, t) = Ae^{-z\sqrt{i\omega/\kappa}}e^{i\omega t}$, which is well-known. Treating this as a filter, the temperature response of a point at depth $z = z_0$ relative to the free surface is simply:

$$H(z = z_0, \omega) = \frac{u(z = z_0, \omega)}{u(z = 0, \omega)} = e^{-z_0\sqrt{i\omega/\kappa}}.$$

Similarly, to represent the effect of finite cable thickness on the temperature measured internally by DAS, consider heat conduction in a uniform disk $\frac{1}{\kappa}u_t = \frac{1}{r}u_r + u_{rr}$ with time-harmonic temperature forcing at the surface $u(r = R, t) = Ae^{i\omega t}$. This has solution

$$u(r, t) = A\frac{J_0(r\sqrt{-i\omega/\kappa})}{J_0(R\sqrt{-i\omega/\kappa})}e^{i\omega t}$$

for $r \in [0, R]$, where J_0 is a Bessel function of the first kind. The temperature response of a fiber at the center of the cable relative to the exterior is then:

$$H(r = 0, \omega) = \frac{u(r = 0, \omega)}{u(r = R, \omega)} = \frac{1}{J_0(R\sqrt{-i\omega/\kappa})}.$$

These two models are plotted in Figure 5.S3 for various parameters. Burial beyond a few centimeters strongly attenuates temperature across the internal wave continuum band and tidal periods, using a typical value of thermal diffusivity for marine sediments of 0.2 mm^2/s. For a 20-mm radius cable, a thermal diffusivity similar to common polymers used in cable construction (e.g. rubber, polypropylene, nylon) around 0.1 mm^2/s strongly attenuates temperature across the internal wave continuum band, whereas a value similar to steel or aluminum commonly used for cable armoring around 20 mm^2/s has no effect. Consequently, the exact construction will greatly influence the thermal sensitivity of any cable, though the reduction in sensitivity between armored and unarmored cable is mostly a result of differing thickness.

The difference in response between two cables of identical thermal diffusivity but different diameter to the same forcing is:

$$H(R_1, R_2, \omega) = \frac{J_0(R_1\sqrt{-i\omega/\kappa})}{J_0(R_2\sqrt{-i\omega/\kappa})}$$

as plotted in Figure 5.4G, comparing the difference in response between single-armored and light-weight protected cable.

References

Apel, J. R. (2003). “A new analytical model for internal solitons in the ocean”. In: *J. Phys. Oceanogr.* 33.11, pp. 2247–2269.

Brandt, P., W. Alpers, and J. O. Backhaus (1996). “Study of the generation and propagation of internal waves in the Strait of Gibraltar using a numerical model and synthetic aperture radar images of the European ERS1 satellite”. In: *J. Geophys. Res.* 101.C6, pp. 14237–14252.

Cheng, F. et al. (2021). “Utilizing distributed acoustic sensing and ocean bottom fiber optic cables for submarine structural characterization”. In: *Sci. Rep.* 11.1, pp. 1–14.

Connolly, T. P. and A. R. Kirincich (2019). “High-Resolution Observations of Subsurface Fronts and Alongshore Bottom Temperature Variability Over the Inner Shelf”. In: *J. Geophys. Res.: Oceans* 124, pp. 593–614.

Crawford, W. C., S. C. Webb, and J. A. Hildebrand (1991). “Seafloor compliance observed by long-period pressure and displacement measurements”. In: *J. Geophys. Res.* 96.B10, pp. 16151–16160.

Davis, K. A. et al. (2020). “Fate of internal waves on a shallow shelf”. In: *J. Geophys. Res.: Oceans* 125, e2019JC015377.

Egbert, G. D. and S. Y. Erofeeva (2002). “Efficient inverse modeling of barotropic ocean tides”. In: *J. Atmos. Ocean. Technol.* 19.2, pp. 183–204.

Egbert, G. D. and R. Ray (2000). “Significant dissipation of tidal energy in the deep ocean inferred from satellite altimeter data”. In: *Nature* 405, pp. 775–778.

Egbert, G. D. and R. D. Ray (2001). “Estimates of M2 tidal energy dissipation from TOPEX/Poseidon altimeter data”. In: *J. Geophys. Res.* 106.C10, pp. 22475–22502.

Farghal, N., A. Baltay, and J. Langbein (2020). “Strain-Estimated Ground Motions Associated with Recent Earthquakes in California”. In: *Bull. Seis. Soc. Am.* 110.6, pp. 2766–2776.

Fernandez-Ruiz, M. R., L. Costa, and H. F. Martins (2019). “Distributed acoustic sensing using chirped-pulse phase-sensitive OTDR technology”. In: *Sensors* 19, p. 4368.

Fernandez-Ruiz, M. R., H. F. Martins, et al. (2018). “Steady-sensitivity distributed acoustic sensors”. In: *J. Light. Technol.* 36, pp. 5690–5696.

Fernandez-Ruiz, M. R., J. Pastor-Graells, et al. (2018). “Laser Phase-Noise Cancellation in Chirped-Pulse Distributed Acoustic Sensors”. In: *J. Lightwave Technol.* 36.4, pp. 979–985.

Fernandez-Ruiz, M. R., M. A. Soto, et al. (2020). “Distributed acoustic sensing for seismic activity monitoring”. In: *APL Photonics* 5.3, p. 030901.

Garrett, C. and W. Munk (1972). “Oceanic mixing by breaking internal waves”. In: *Deep Sea Research and Oceanographic Abstracts* 19, pp. 823–832.

Ide, S., E. Araki, and H. Matsumoto (2021). “Very broadband strain-rate measurements along a submarine fiber-optic cable off Cape Muroto, Nankai subduction zone, Japan”. In: *Earth, Planets, Space* 73.63.

Kinder, T. H. and H. L. Bryden (1987). “The 1985–1986 Gibraltar Experiment: Data collection and preliminary results”. In: *Eos, Trans. Am. Geophys. Union* 68, pp. 786–795.

Klymak, J. M. et al. (2011). “The breaking and scattering of the internal tide on a continental slope”. In: *J. Phys. Oceanogr.* 41, pp. 926–945.

Koyamada, Y. et al. (2009). “Fiber-optic distributed strain and temperature sensing with very high measurand resolution over long range using coherent OTDR”. In: *J. Lightwave Technol.* 27, pp. 1142–1146.

Kunze, E. and T. B. Sanford (1996). “Abyssal mixing: where it is not”. In: *J. Phys. Oceanogr.* 26, pp. 2286–2296.

Ledwell, J. R. et al. (2000). “Evidence for enhanced mixing over rough topography in the abyssal ocean”. In: *Nature* 403, pp. 179–182.

Li, J. and M. Zhang (2022). “Physics and applications of Raman distributed optical fiber sensing”. In: *Light Sci. Appl.* 11.128.

Lindsey, N. J., T. C. Dawe, and J. B. Ajo-Franklin (2019). “Illuminating seafloor faults and ocean dynamics with dark fiber distributed acoustic sensing”. In: *Science* 366.6469, pp. 1103–1107.

Lindsey, N. J. and E. R. Martin (2021). “Fiber-optic seismology”. In: *Ann. Rev. Earth Planet. Sci.* 49, pp. 309–336.

Mecozzi, A. et al. (2021). “Polarization sensing using submarine optical cables”. In: *Optica* 8.6, pp. 788–795.

Moum, J. N. and W. D. Smyth (2006). “The pressure disturbance of a nonlinear internal wave train”. In: *J. Fluid Mech.* 558, pp. 153–177.

Munk, W. H. (1966). “Abyssal recipes”. In: *Deep-Sea Research* 13, pp. 707–730.

Pastor-Graells, J. et al. (2016). “Single-shot distributed temperature and strain tracking using direct detection phase-sensitive OTDR with chirped pulse”. In: *Optics Express* 24, pp. 13121–13133.

Polzin, K. et al. (1997). “Spatial variability of turbulent mixing in the abyssal ocean”. In: *Science* 276, pp. 93–96.

Rudnick, D. L. et al. (2003). “From tides to mixing along the Hawaiian ridge”. In: *Science* 301, pp. 355–357.

Sidenko, E. et al. (2022). “Experimental study of temperature change effect on distributed acoustic sensing continuous measurements”. In: *Geophysics* 87.3, pp. D111–D122.

Sinnett, G. et al. (2020). “Distributed temperature sensing for oceanographic applications”. In: *J. Atmos. Ocean. Tech.* 37, pp. 1987–1997.

Sladen, A. et al. (2019). “Distributed sensing of earthquakes and ocean-solid Earth interactions on seafloor telecom cables”. In: *Nature Communications* 10.1, p. 5777.

St. Laurent, L. and C. Garrett (2002). “The role of internal tides in mixing the deep ocean”. In: *J. Phys. Oceangr.* 32, pp. 2882–2899.

Toole, John M., Raymond W. Schmitt, and Kurt L. Polzin (1994). “Estimates of Diapycnal Mixing in the Abyssal Ocean”. In: *Science* 264.5162, pp. 1120–1123.

Ugalde, Arantza et al. (2022). “Noise Levels and Signals Observed on Submarine Fibers in the Canary Islands Using DAS”. In: *Seismol. Res. Lett.* 93.1, pp. 351–363.

van Haren, H. (2006). “Nonlinear motions at the internal tide source”. In: *Geophys. Res. Lett.* 33, p. L11605.

van Haren, H., A. Cimatoribus, and L. Gostiaux (2015). “Where large deep-ocean waves break”. In: *Geophys. Res. Lett.* 42, pp. 2351–2357.

van Haren, H. and L. Gostiaux (2010). “A deep-ocean Kelvin-Helmholtz billow train”. In: *Geophys. Res. Lett.* 37, p. L03605.

– (2012). “Detailed internal wave mixing above a deep-ocean slope”. In: *J. Mar. Res.* 70, pp. 173–197.

van Haren, H., L. Maas, and H. van Aken (2002). “On the nature of internal wave spectra near a continental slope”. In: *Geophys. Res. Lett.* 29.12, p. 1615.

Vazquez, A. et al. (2008). “Meteorologically forced subinertial flows and internal wave generation at the main sill of the Strait of Gibraltar”. In: *Deep Sea Res. I* 55.10, pp. 1277–1283.

Waterhouse, A. F. et al. (2014). “Global Patterns of Diapycnal Mixing from Measurements of the Turbulent Dissipation Rate”. In: *J. Phys. Oceanogr.* 44.7, pp. 1854–1872.

Watson, G. and I.S. Robsinson (1990). “A Study of Internal Wave Propagation in the Strait of Gibraltar Using Shore-Based Marine Radar Images”. In: *J. Phys. Oceanogr.* 20, pp. 374–395.

Wesson, J. C. and M. C. Gregg (1994). “Mixing at Camarinal Sill in the Strait of Gibraltar”. In: *J. Geophys. Res.* 99.C5, pp. 9847–9878.

Williams, E. F., M. R. Fernandez-Ruiz, R. Magalhaes, R. Vanthillo, Z. Zhan, and M. Gonzalez-Herraez (2019). “Distributed sensing of microseisms and teleseisms with submarine dark fibers”. In: *Nature Communications* 10.1, p. 5778.

Williams, E. F., M. R. Fernandez-Ruiz, R. Magalhaes, R. Vanthillo, Z. Zhan, M. Gonzalez-Herraez, and H. F. Martins (2021). “Scholte wave inversion and passive source imaging with ocean-bottom DAS”. In: *The Leading Edge* 40.8, pp. 576–583.

Williams, E. F., Z. Zhan, et al. (2022). “Surface gravity wave interferometry and ocean current monitoring with ocean-bottom DAS”. In: *J. Geophys. Res.: Oceans* 127, e2021JC018375.

Winters, K. B. (2015). “Tidally driven mixing and dissipation in the stratified boundary layer above steep submarine topography”. In: *Geophys. Res. Lett.* 42, pp. 7123–7130.

Ziegenbein, J. (1969). “Short internal waves in the Strait of Gibraltar”. In: *Deep Sea Res.* 16, pp. 479–487.

– (1970). “Spatial observations of short internal waves in the Strait of Gibraltar”. In: *Deep Sea Res.* 17.5, pp. 867–875.

Zumberge, M. A., W. Hatfield, and F. K. Wyatt (2018). “Measuring Seafloor Strain With an Optical Fiber Interferometer”. In: *Earth and Space Science* 5, pp. 371–379.

Chapter 6

VARIABILITY IN THE NATURAL FREQUENCIES OF A NINE-STORY CONCRETE BUILDING FROM SECONDS TO DECADES

Williams, E. F., T. H. Heaton, Z. Zhan, and V. R. Lambert (2022). "Variability in the natural frequencies of a nine-story concrete building from seconds to decades". In: *The Seismic Record* in press.

Abstract

Since 2001, the Southern California Seismic Network has archived continuous waveform data from strong-motion station CI.MIK in Caltech Hall (formerly Millikan Library), a nine-story reinforced concrete building. Simple spectral analysis of this 20-year record reveals that the building's fundamental frequencies have increased gradually by 5.1% (E-W) and 2.3% (N-S), with larger long-term variability up to 9.7% (E-W) and 4.4% (N-S). This finding is unexpected, as previous analysis of forced vibration tests and strong-motion records has shown that between 1968 and 2003 the fundamental frequencies decreased by 22% (E-W) and 12% (N-S), largely attributed to minor structural damage and soil-structure system changes from major earthquakes. Today, the building's apparent structural stiffness is comparable to what it was in 1986, before the Whittier Narrows earthquake. Using data from earthquakes and forced vibrations, we also document the building's nonlinear dynamic elasticity, which is characterized by a rapid softening (decrease in apparent frequencies) at the onset of strong motion, followed by a slower, log-linear recovery trend over the scale of minutes. This nonlinear behavior does not appear to have changed with time.

6.1 Introduction

Reliable estimation of the natural frequencies of a building is essential for earthquake and structural engineering practice, from design-stage fragility analysis to post-earthquake damage assessment. Current engineering approaches rely on the assumptions that the natural frequencies, serving as a proxy for stiffness, are time-invariant and follow linear elasticity up to the yield point. For example, widely-employed intensity measures like spectral acceleration filter design ground motions through a linear, time-invariant harmonic oscillator (e.g. Baker, Bradley, and Stafford (2021)). Even so-called nonlinear methods, such as nonlinear response-history analysis, typically assume linear elasticity and only consider large-strain and material inelasticity or elasto-plasticity (e.g. Haselton et al. (2017) and Zimmerman et al. (2017)). However, the exponential proliferation of digital seismographs over the past several decades has shown that these assumptions poorly describe the behavior of many classes of structures. Numerous examples have been reported of non-damaging earthquakes causing temporary softening of the soil-structure system that recovers rapidly after shaking (Astorga, Gueguen, and Kashima, 2018; Trifunac, Ivanovic, and Todorovska, 2001; Udwadia and Trifunac, 1974), as well as small permanent changes (Clinton et al., 2006). Non-earthquake loading by wind or anthropogenic vibrations has been observed to have a similar effect (Clinton et al., 2006; Gueguen, Johnson, and Roux, 2016; Kohler, Davis, and Safak, 2005). These effects have been variously interpreted as the result of small-strain nonlinear elasticity of construction materials, reactivation of fractures in previously damaged structural elements, nonlinear elasticity or elasto-plasticity of foundation soils, or some combination thereof. Passive environmental changes also have a marked impact on apparent structural stiffness, including positive correlations with temperature and rainfall (Clinton et al., 2006; Todorovska and Al Rjoub, 2006).

To date, studies of anomalous changes in the natural frequencies of civil structures have largely focused on relatively short time scales due to the paucity of long, continuous waveform records. Consequently, the long-term stability of these frequencies over the lifetime of a structure is not generally understood. In this article, we quantify the variability and long-term changes in the first six natural frequencies of Caltech Hall, a nine-story reinforced concrete building, over a span of twenty years from 2001 to 2021. Formerly known as the Robert A. Millikan Memorial Library (or Millikan Library), Caltech Hall has been the subject of extensive study since its construction in 1967. Initially subject to minor damage in the 1971 San Fernando earthquake and repeatedly shaken by subsequent Southern California earthquakes, the fundamental frequencies of Caltech Hall in the east-west and north-south directions decreased by 22% and 12% respectively from 1967 to 2002 (Clinton et al., 2006). What changes occurred between these major events are only illuminated by a temporally scattered record of forced and ambient vibration tests. In 2001, the Southern California Seismic Network (SCSN) installed a triaxial accelerometer (station CI.MIK) on the ninth floor of the building and began archiving continuous waveform data. Clinton et al. (2006) examined the initial 1.5 years of data from

CI.MIK, documenting the response of the building to environmental forcing on the scale of hours to weeks and three small earthquakes. The twenty-year continuous record up to the present provides the opportunity not only to examine frequency variations over much longer time-scales, but also construct a continuous spectrum of nonlinear elasticity with almost seven-hundred regional and local earthquakes.

6.2 Background and data

Caltech Hall is a nine-story reinforced concrete building on the campus of the California Institute of Technology (Caltech) in Pasadena, CA (Figure 6.S1). The 44-m superstructure consists of a reinforced concrete moment frame, two N-S-oriented reinforced concrete shear walls on the east and west faces of the building, and a reinforced concrete central core. Below a 4-m basement level, the structure is supported by a concrete pad foundation that runs E-W across the center of the building joining the shear walls. For a detailed description of the structure, see Kuriowa (1967), Favela (2004), Clinton et al. (2006), and references therein. As a result of this construction, the responses of the building in the E-W and N-S directions differ dramatically. The apparent system frequencies of Caltech Hall—that is, the frequencies measured from peaks in the ambient vibration spectrum of a station in the building—include the coupled effects of the fixed-base stiffness of the superstructure and the shearing and rocking stiffness of the soil-foundation system (Luco, Trifunac, and Wong, 1987). In particular, as a result of the shear-wall geometry, the N-S deformations are dominated by rigid-body rocking, whereas E-W deformations more closely approximate fixed-base shearing (Luco, Trifunac, and Wong, 1988). Whether earthquake-related changes in the natural frequencies of Caltech Hall should be attributed to changes in structural stiffness (Luco, Trifunac, and Wong, 1987) or soil-structure interaction (Todorovska, 2009b) has been a subject of considerable historical debate.

We utilize recordings from strong-motion station CI.MIK, located on the ninth floor of Caltech Hall, over a twenty-year period from May 2001 to May 2021. Since 2001, CI.MIK has been instrumented with a Kinemetrics Episensor ES-T triaxial accelerometer, and continuous waveform and event data have been archived by the Southern California Earthquake Data Center (SCEDC). There is a gap in continuous waveform data from the SCEDC archive in 2008-2009, but event data from this period are available.

6.3 Long-term changes

In order to track the time-dependent variation of the natural frequencies of Caltech Hall, we apply a simple frequency-time analysis to the continuous waveform data. For ambient vibrations, we use the Fast Fourier Transform to calculate the power spectral density (PSD) for each hour of data, compute the weekly median PSD, and pick the maximum value in a 0.2-Hz band around each modal frequency. We refer to Bradford et al. (2004) for modal identification (see Supplementary Information, Figure 6.S2). Because the frequencies generally vary smoothly with time on the scale of weeks to months and do not overlap, automatic tracking of the modal peak is therefore possible, and computing a weekly median effectively removes strong diurnal trends from temperature and building use. Weekly median spectrograms are plotted in Figure 6.1 for the first six natural frequencies of Caltech Hall, exhibiting a complex superposition of seasonal and interannual trends. A complete summary of changes and variability for each frequency is given in Table 6.S1.

6.3.1 Interannual trends

Comparing the median frequencies from the months of May 2001 and May 2021, the fundamental frequency in the east-west direction (hereafter EW1) increased by 5.1%, from 1.18 to 1.24 Hz (Figure 6.1A), which is equivalent to a 10.4% increase in the apparent stiffness of the combined soil-structure system ($f \propto \sqrt{\frac{k}{m}}$ where k is stiffness and m is mass). The fundamental frequency in the north-south direction (NS1) increased by 2.3% over this time period, from 1.71 to 1.75 Hz (Figure 6.1C), or a 4.7% increase in apparent stiffness. The 20-year net change in EW1 and NS1 can be further divided into a combination of discrete events and gradual trends. The first major increase in the apparent stiffness of Caltech Hall occurred during two stages of non-structural renovations converting library floors into office space during spring 2003 and fall 2004. The first of these projects had the greatest impact on the fundamental frequencies EW1 and NS1, whereas the second had a larger impact on the torsional fundamental frequency (T1) and the first east-west overtone (EW2) (Figure 6.1). Following each sharp increase in 2003-2004, all affected frequencies decreased gradually at varying rates until around 2008. As discussed by Clinton et al. (2006), who also examined the first of these renovation projects, the fractional magnitude of the increase in apparent structural stiffness is surprisingly large: EW1 increased ~3% over three months in 2003 and ~2% over one month in 2004. Further, it is unclear why such work could have initiated a softening trend, as construction materials like adhesives tend to stiffen with time after application (e.g. Moussa et al.

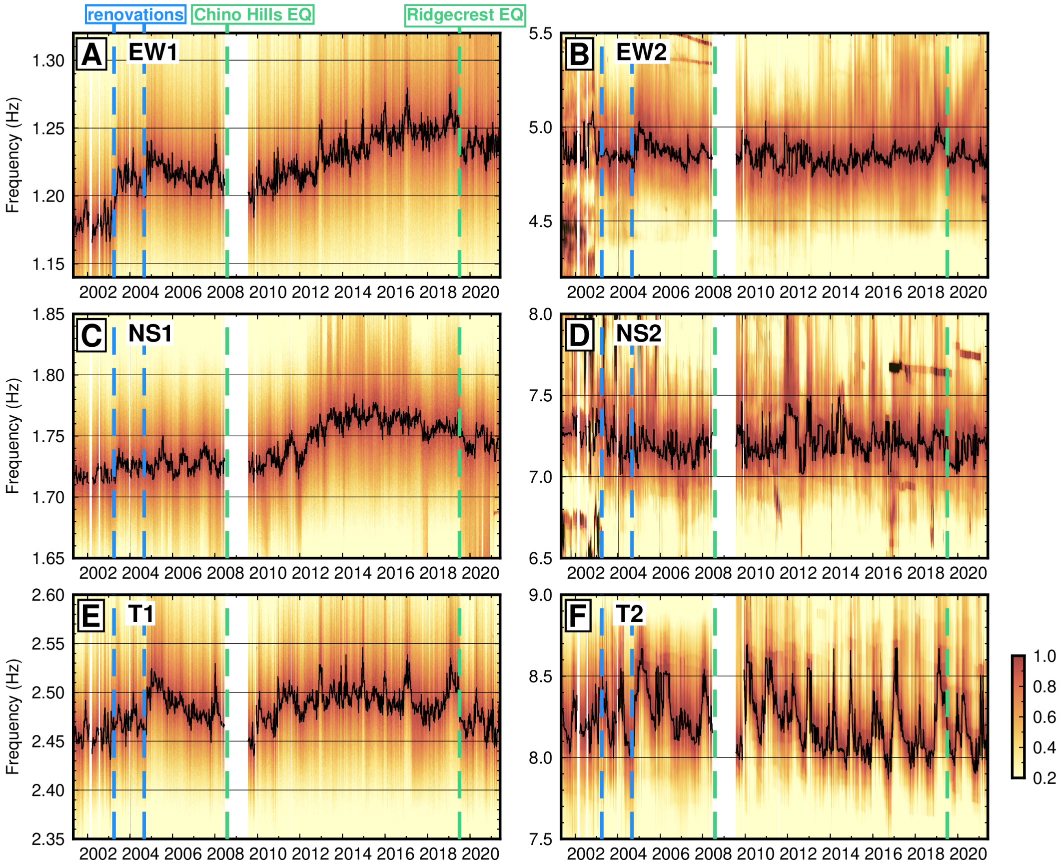

Figure 6.1: Long-term changes in the first six frequencies of Caltech hall from ambient vibrations. (A,B) Spectrograms of CI.MIK.BLE and CI.MIK.BNE from May 2001 to May 2021, enlarged to show the (A) first and (B) second natural frequencies of the E-W system. The color scale has been normalized in each frequency bin from decibels relative to 1 count. A median filter was applied to (B) along the frequency axis in order to reduce artifacts from motors in the building with similar vibrational frequencies (see spikes on Figure 6.S2). (C,D) Same as (A,B) but for CI.MIK.BLN and CI.MIK.BNN showing the first two frequencies of the N-S system. (E,F) Same as (A,B) but for the torsional frequencies measured on the E-W seismometer component. Black lines indicate the weekly median frequency.

(2013)).

From late 2009 (following a data gap), the fundamental frequencies EW1 and NS1 began a period of gradual increase, indicating apparent healing of the soil-structure system. EW1 increased at a rate of ~1%/yr until around 2017, when the trend slowed. At its maximum in January 2017, EW1 was up 8.5% from May 2001, or +17.7% apparent stiffness. Although NS1 also increased during this time period, the timing of changes in the two frequencies are not clearly correlated. NS1 increased rapidly from 2012 to 2014, and peaked in mid-2014 at a 4.1% increase relative to May 2001. Starting in 2016, NS1 began to decrease again, whereas EW1 remained approximately constant. We are not aware of any environmental trends or construction work that correlate with the observed interannual trends in apparent stiffness.

Over this period, Caltech Hall was subject to only two moderate regional earthquakes. The 2008 M5.4 Chino Hills earthquake coincides with the change in interannual behavior of both EW1 and NS1, though it is unclear why strong motion would induce a decade-long healing trend when there was no apparent permanent coseismic decrease in stiffness. The M6.4 and M7.1 Ridgecrest earthquakes in 2019, however, did result in a 2.5% permanent decrease in EW1 and 1.6% decrease in T1 despite peak east-west accelerations at CI.MIK of only 0.77 and 0.75 m/s^2 for the two events. This permanent softening is comparable in magnitude to the inferred historical changes in EW1 from the 1988 M6.1 Whittier Narrows and 1994 M6.7 Northridge earthquakes, when the peak east-west accelerations at the upper floors of Caltech Hall were observed to be much higher at 2.62 and 1.43 m/s^2, respectively (Figure 6.5) (Clinton et al., 2006). Despite this recent softening, the apparent fundamental frequencies of the combined soil-structure system from ambient vibrations are comparable today to their values before the Whittier Narrows, Sierra Madre, and Northridge earthquakes, indicating a significant net increase in stiffness.

6.3.2 Seasonal variability

The natural frequencies of Caltech Hall also exhibit seasonal variability (Figure 6.2). Clinton et al. (2006) previously observed a rapid increase in the fundamental frequencies over the scale of 1-2 days during periods of rain, followed by recovery over the scale of a week with NS1 least affected. The twenty-year record of weekly median measurements of EW1 and T1 shows a sharp increase of up to ~3% in winter months coincident with periods of rainfall, consistent with the short-term

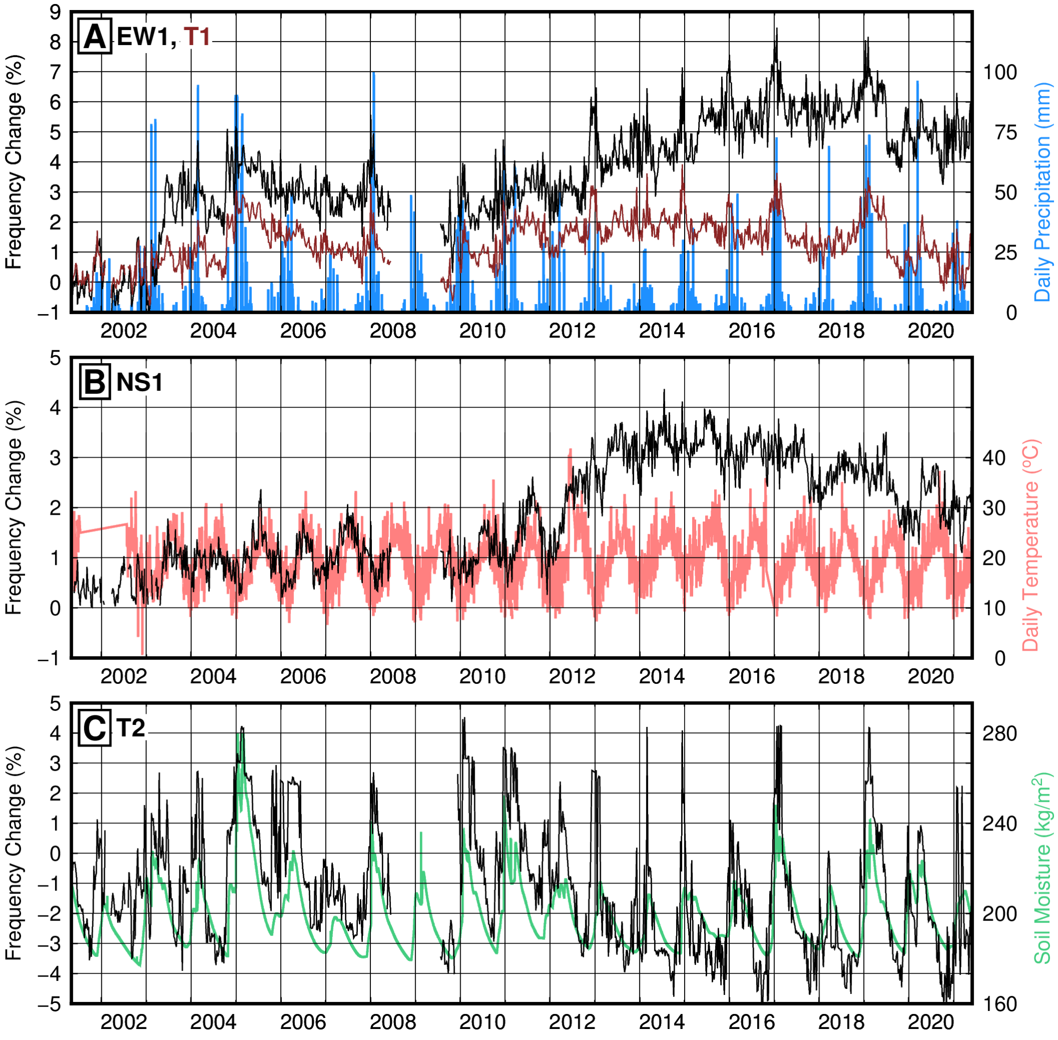

Figure 6.2: Seasonal and interannual changes in the natural frequencies of Caltech Hall from ambient vibrations compared with environmental data. (A) Fractional changes in the fundamental E-W and torsional frequencies relative to May 2001 compared with daily precipitation from the Climate Hazards Group InfraRed Precipitation with Station data (CHIRPS) rainfall database (Funk et al., 2014). (B) The fundamental N-S frequency compared with daily mean temperature measurements at nearby Santa Fe Dam from the Global Historical Climatology Network daily (GHCNd) database (Menne et al., 2012). (C) The second torsional frequency compared with soil moisture at 100-200 cm depth extracted from the Global Land Data Assimilation System (GLDAS-2.1) model (Rodell et al., 2004).

observations (Figure 6.2A). In years with longer separation between storms, such as 2013 and 2017, the seasonal effect of rainfall is negligible; however, in years with a concentrated period of rainfall over 1-2 months, such as 2012, the cumulative increase in stiffness is greater. Poroelastic effects in saturated soil increase the horizontal stiffness of an embedded foundation (Todorovska and Al Rjoub, 2006), which suggests that the time-scale of the precipitation-induced increases in EW1 and T1 is related to the drainage time-scale of shallow soil. However, the first torsional overtone (T2) surprisingly exhibits a much larger increase, up to $\sim$9%, during periods of heavy rainfall, and unlike EW1 and T1, the change in T2 decays slowly over the scale of a year (Figure 6.2C). Ghahari et al. (2015) found that the flexible-base mode shape for T2 includes significant vertical displacement, which suggests a higher dependence on the vertical stiffness of the soil-foundation system relative to EW1 and T1. The variability of T2 correlates well with modeled soil moisture (Rodell et al., 2004), which serves as a proxy for the depth to fully saturated soil. Changes in EW1 and T1 after rainfall may thereby diminish quickly as the <4-m shallow soil buttressing the foundation drains, decreasing the horizontal foundation stiffness; whereas changes in T2 may diminish slowly as the water table draws down and the integrated vertical stiffness of sub-foundation soil decreases.

On a seasonal scale, NS1 is largely unaffected by precipitation, but shows the greatest sensitivity to temperature, with an approximate increase of 1% per 10^{o}C (Figure 6.2B). This is inconsistent with the short-term observations of Clinton et al. (2006), who showed that diurnal variations in temperature have a similar influence on all fundamental frequencies. The shear walls on the east and west faces of Caltech Hall are 30.5-cm thick, whereas the thermal skin depth for diurnal forcing is around 5-10 cm ($\sqrt{2\kappa/\omega}$, for $\kappa \sim 0.1 - 0.5$ mm^2/s), suggesting that seasonal temperature changes will have a greater thermal expansion effect on the shear walls than diurnal variations.

6.4 Short-term changes

In order to document the response of Caltech Hall to earthquake loading, we downloaded 684 regional earthquakes, representing all SCEDC cataloged events with M>4 and peak acceleration at CI.MIK >0.001 m/s^2 between May 2001 and May 2021. For each event we define the apparent event frequency in the E-W and N-S directions as the peak in the PSD of a 60-s record beginning at the P-wave arrival. For a subset of 54 events with peak acceleration >0.01 m/s^2 and excluding closely spaced aftershocks, we compute the spectrogram of a five-minute record and pick the apparent frequencies in each time window in order to track the post-earthquake recovery of the building. The apparent event frequency is generally proportional to and slightly higher than the minimum frequency derived from time-frequency analysis because the minimum frequency is always coincident with the peak acceleration, but is more stable for small events. We also supplement earthquake data with new and historical forced vibration tests (Supplementary Information; Table 6.S2).

6.4.1 Nonlinear response

The apparent event frequency for all 684 earthquakes is plotted in Figure 6.3 against time and peak acceleration. For both EW1 and NS1, earthquakes clearly follow the same seasonal and interannual trends as measured from ambient vibrations, though the variability is higher due to the combination of a nonlinear reduction in frequency with strong motion and the rapid wander of the building's frequencies on sub-weekly time-scales not captured by the ambient vibration curve (Figure 6.3A,C). A decrease in the apparent frequencies of Caltech Hall with increased shaking intensity was first noted by Kuriowa (1967) during forced vibration tests. Clinton et al. (2006) compiled available earthquake records through 2004, mostly exceeding 0.1 m/s^2 peak acceleration, and noted a power-law scaling between the apparent event frequency and peak acceleration. Extending this analysis with all events 2001-2021, we observe that the nonlinear relationship between apparent frequency and acceleration persists continuously down to at least 0.001 m/s^2, close to the intensity of ambient vibrations (Figure 6.3B,D). Importantly, there is no linear elastic regime for any level of excitation. We also repeated the experiment of Kuriowa (1967) in November 2019 and conducted forced vibration tests to measure EW1 at six different levels of forcing. These results are plotted as black crosses on Figure 6.3B and follow the same relationship between frequency and acceleration as exhibited by earthquakes, suggesting that peak acceleration is an adequate single intensity measure and the influence of other factors like shaking duration is comparatively small.

A single power-law relationship, however, poorly describes the complete spectrum of nonlinear behavior from 0.001 to >1 m/s^2. Rather, we identify a weakly nonlinear regime and a strongly nonlinear regime separated by a transition acceleration around 0.02-0.04 m/s^2, which is higher for NS1 than EW1. A factor of 10 increase in acceleration for EW1 results in a ~3% reduction in apparent frequency in the weakly nonlinear regime and a ~9% reduction in the strongly nonlinear regime

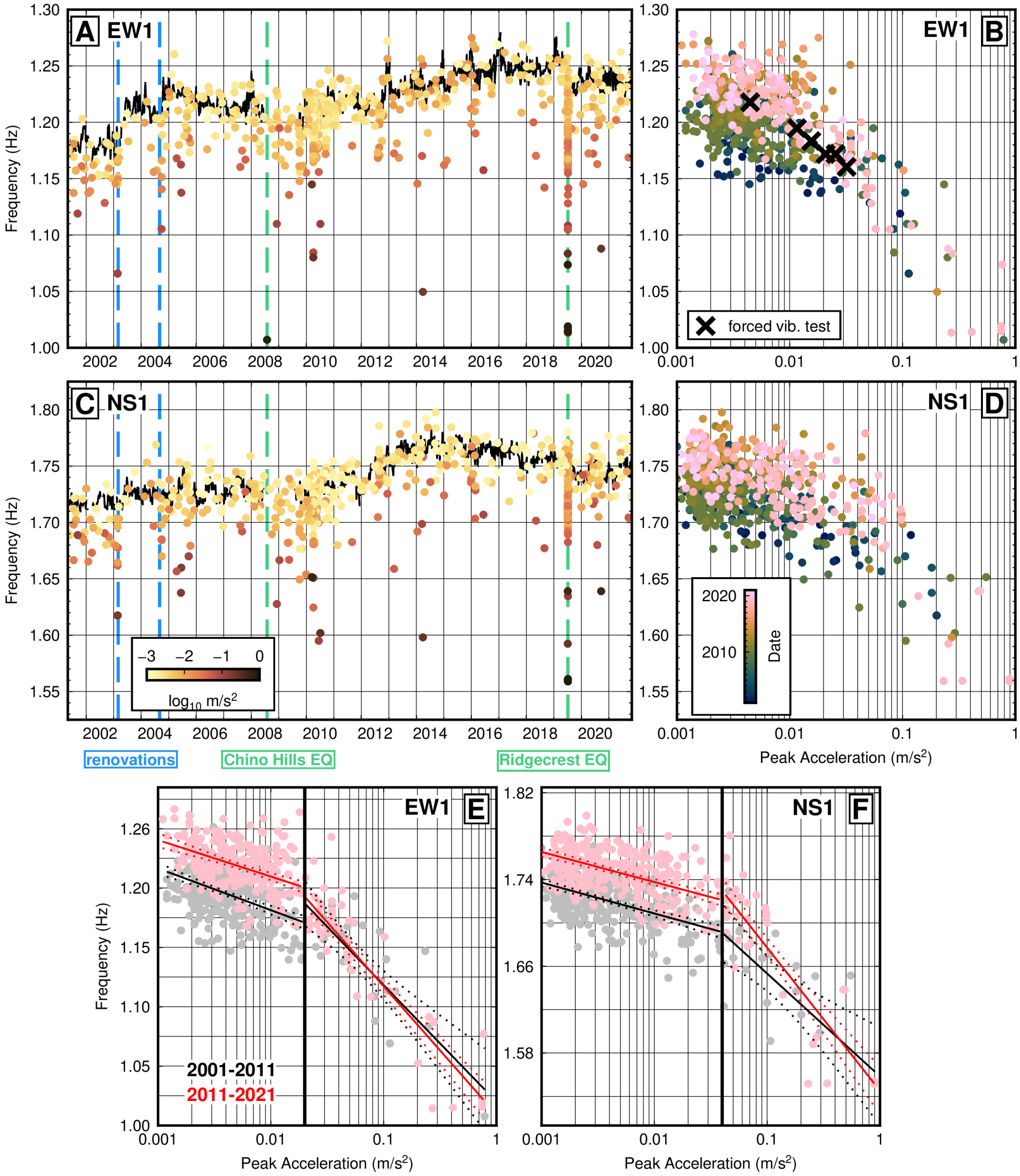

Figure 6.3: Response of Caltech Hall to 684 local and regional earthquakes >M4 between 2001 and 2021. (A) Apparent E-W fundamental frequency for each earthquake plotted against the ambient vibration curve (black line) and colored by peak acceleration at CI.MIK. (B) Same data as in (A) but plotted against peak acceleration and colored by date, compared with forced vibration tests (black crosses, see Figure 6.S4). (C,D) Same as (A,B) but for the apparent fundamental frequency in the N-S direction. (E,F) Same as (B,D) on a log-log scale with earthquakes divided between the periods 2001-2011 (black) and 2011-2021 (red). The trends in nonlinear response are illustrated with a linear regression (solid lines) and 95% confidence interval (dashed lines) above and below a transition frequency. Note that a few of the largest events are truncated from these plots.

(1.5% and 6% respectively for NS1). In addition to the difference in scaling, these two regimes exhibit distinct time-dependent behavior. Separating all events into two bins from 2001-2011 and 2011-2021, for both EW1 and NS1 the long-term increasing trend in apparent stiffness manifests as a uniform upward shift in the event frequencies across the weakly nonlinear regime, with no difference in slope (Figure 6.3E,F). Conversely, there is no statistically significant change in either the slope or the mean event frequency across the strongly nonlinear regime for either EW1 or NS1, though the relatively small number of strong events contributes to large uncertainty bounds at high accelerations. Todorovska (2009b) found that the rocking stiffness in the north-south direction of Caltech Hall decreases dramatically during strong motion, whereas the reduction in the stiffness of the superstructure is less. If the reduction in the rocking stiffness can be attributed to nonlinear elastic or elastoplastic soil-structure interaction above a small-strain threshold, then the weakly and strongly nonlinear regimes may be distinguished by the relative contributions of the superstructure and soil-foundation system to the apparent dynamic softening of the combined system. Such effects cannot be separated, however, using a single station analysis.

6.4.2 Log-linear recovery

Although a small permanent reduction in the natural frequencies of Caltech Hall has been observed for non-damaging historical earthquakes, the frequencies recover rapidly to their pre-event levels for the majority of events (Clinton et al., 2006). Such rapid dynamic softening (often termed anomalous nonlinear fast dynamics or ANFD) followed by slow recovery (often termed slow dynamics) has been widely documented in laboratory rock mechanics (TenCate, Smith, and Guyer, 2000; Johnson and Sutin, 2005), and recently reported for several structures (Astorga, Gueguen, and Kashima, 2018; Astorga and Gueguen, 2020; Gueguen, Johnson, and Roux, 2016; Kohler, Davis, and Safak, 2005). Example spectrograms with a resolution of 12.8 s are plotted in Figure 6.4 for two earthquakes, showing that the apparent system frequencies of Caltech Hall drop suddenly at the onset of strong motion and then recover slowly following an approximately log-linear curve over the scale of minutes. For these two events, the 2007 M4.7 Trabuco Canyon (Figure 6.4A-D) and 2008 M5.4 Chino Hills (Figure 6.4E-H) earthquakes, the peak acceleration at CI.MIK differs by a factor of 10, but the recovery curves follow a similar trend. The relative recovery of the apparent frequency in each time window, $(f - f_{min})/(f_0 - f_{min})$, is reasonably well described by a log-linear function of time (Figure 6.4I,J) and is

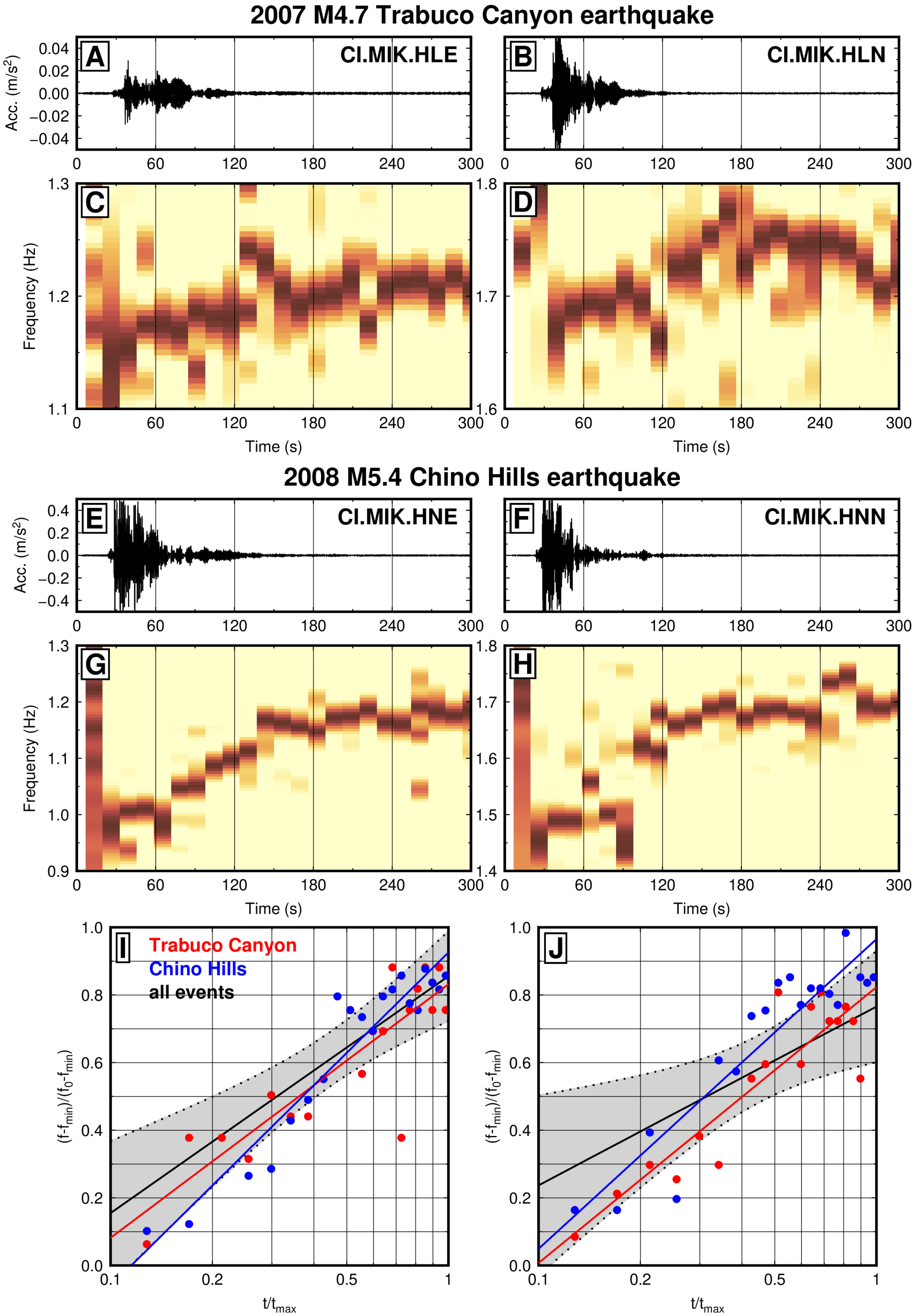

Figure 6.4: (Caption next page)

Figure 6.4: Nonlinear response and log-linear recovery for earthquakes with similar shaking duration but an order of magnitude difference in peak acceleration. (A,B) Acceleration recorded at CI.MIK in the E-W and N-S directions from the 2007-09-02 M4.7 Trabuco Canyon earthquake (75 km epicentral distance). (C,D) Spectrograms of (A,B) showing near-instantaneous decrease in apparent fundamental frequencies at the onset of strong motion, followed by log-linear recovery over the scale of minutes. (E-H) Same as (A-D) but for the 2008-07-29 M5.4 Chino Hills earthquake (39 km epicentral distance). (I) Peak frequencies in the E-W direction in each spectrogram time window (12.8 s) plotted as the fractional increase from the observed minimum frequency relative to the total coseismic drop, where f_0 is the median frequency measured over an hour before each event. The scaled time has $t = 0$ at 30 seconds before the S-wave arrival and $t_{max} = 300$ s.(J) Same as (I) but for the N-S component. Red points and red linear regression represent the Trabuco Canyon earthquake from (C,D), blue points and blue linear regression represent the Chino Hills earthquake from (G,H), and black represents the average across 54 earthquakes, the subset of all events in Figure 6.3 with peak acceleration >0.01 m/s^2 and excluding most aftershocks. Black dashed lines and shading represent one standard deviation of fitted slopes for all events.

85-95% recovered after five minutes for both earthquakes. We extended this analysis to all 54 events with peak acceleration >0.01 m/s^2, and the mean and standard deviation of regressed recovery-rates are expressed as gray shading in Figure 6.4I,J. Even though the scatter among individual events is large, likely due to order of magnitude variations in shaking duration, the average trend highlights that ~20% recovery typically occurs rapidly after the peak acceleration and ~80% recovery occurs within 5 minutes. There is no significant difference in recovery rate for either EW1 or NS1 and no significant change in recovery rate over the period of study.

6.5 Discussion and conclusions

Since 2001, the natural frequencies of Caltech Hall have increased by 5.1% (EW1) and 2.3% (NS1). While a fraction of the twenty-year change can be attributed to the installation of non-structural office partitions in 2003-2004, the majority of the increase in apparent structural stiffness occurred gradually between 2009 and 2017, and is not clearly correlated with any environmental trends or construction work. In the only other comparable longitudinal study of a building to date, Astorga, Gueguen, and Kashima (2018) showed that the natural frequencies of a steel and reinforced concrete building in Japan gradually decreased over a 12-year period preceding the 2011 Tohoku-Oki earthquake. Such long-term softening is the expected lifetime behavior of reinforced concrete structures, as many well-documented mechanisms can contribute to degradation, such as fracture formation, thermal stressing, carbonation, and corrosion of rebar (Lees, 1992). The anomalous long-term stiffening of Caltech Hall is more difficult to explain. Minor cracking of the concrete slabs and shear walls at the ground floor level of the building were observed following the 1971 San Fernando earthquake, potentially associated with a reduction in foundation stiffness (Foutch and Jennings, 1978). One possible explanation is that migration of groundwater through cracks in the foundation could deposit calcite and heal the foundation concrete over long time scales (e.g. Edvardsen (1999) and Roig-Flores and Serna (2020)). Alternatively, the cumulative effect of small and large building vibrations could act to compact the soil beneath the foundation and increase the stiffness. Incorporation of multi-station records to decompose the superstructure and soil-foundation contributions to the apparent stiffness (e.g. Todorovska (2009a)) and identify temporal changes in the building's mode shapes would be necessary to further probe the cause of the Caltech Hall's increasing stiffness.

Over twenty years, the natural frequencies of Caltech Hall also exhibited an overall variability of 9.7% (EW1) and 4.4% (NS1). This variability should be considered a minimum estimate, as the weekly median frequency analysis discounts short-term effects of diurnal temperature changes, wind, and rainfall, which can be as large as 3% (Clinton et al., 2006) and does not include the effect of amplitude-dependent nonlinear elasticity. Such large variability poses a significant challenge for structural health monitoring and post-earthquake damage assessment. The observed variability exceeds the building's inferred permanent decrease in frequencies from the 1987 Whittier Narrows, 1991 Sierra Madre, and 1994 Northridge earthquakes (Figure 6.5). Further, if the long-term healing of Caltech Hall has been a persistent trend throughout the building's fifty-five year lifetime, then inferences from a scattered record of ambient and forced vibration tests may significantly underestimate the permanent changes from historical earthquakes (Figure 6.5). Establishing a reliable baseline for structural health monitoring thereby requires continuous recording in order to correct for environmental trends and long-term changes that are aliased by sporadic monitoring. Even full-scale forced vibration tests may fail to identify moderate damage or falsely identify damage if conducted in isolation without considering the passive variations of a building's natural frequencies, as evidenced by the comparable variability of forced and ambient vibration tests over the last 30 years (Figure 6.5). The significant dynamic softening of Caltech Hall during strong motion for some non-damaging events such as the 2008 Chino Hills earthquake (Figures 6.4, 6.5) is comparable in magnitude to the temporary softening experienced during the 1971 San Fernando earthquake, which did cause minor damage, and in other buildings experiencing more significant damage (e.g. Trifunac, Ivanovic, and Todorovska (2001)), suggesting that triggered strong motion records may be insufficient to identify damage without a detailed model of a building's nonlinear elastic response. Triggered records are also typically too short to capture enough of the time-dependent recovery process to make an asymptotic inference of the final post-event frequencies (Udwadia and Trifunac, 1974) (Figure 6.4). We conclude that continuous recording should be a requirement for urban strong-motion networks, and that linear, time-invariant elasticity is an exceedingly poor assumption in the analysis of concrete structures.

Data and resources

The seismographic data used in this study are available for public download through the Southern California Earthquake Data Center (SCEDC, 2013). Rainfall data from the Climate Hazards Group InfraRed Precipitation with Station data (CHIRPS) rainfall database (Funk et al., 2014) can be acccessed at `chc.ucsb.edu/data/chirps`. Temperature data from the Global Historical Climatology Network daily (GHCNd) database (Menne et al., 2012) can be accessed at `www.ncei.noaa.gov/data/global-historical-climatology-network-daily/`. Soil moisture data from the Global Land Data Assimilation System (GLDAS-2.1) model (Rodell et al., 2004) can be accessed at `disc.gsfc.nasa.gov/datasets/GLDAS_NOAH025_3H_2.1/summary`. The supplemental material includes additional details of modal identification and forced vibration tests.

Supplementary Material

Ambient vibration analysis and mode assignment

We track the temporal evolution of the first six natural frequencies of Caltech Hall based on correlation with modes identified by Bradford et al. (2004) from forced vibration tests conducted in 2002. The median PSDs (i.e. the median of hourly spectra) for the east-west and north-south components of CI.MIK for the months of May 2001 and 2021 are shown in Figure 6.S2 and labeled according to each mode. The first torsional overtone (T2) was initially incorrectly identified as the second east-west overtone (EW3) by Bradford et al. (2004), but this was later corrected by Cheng, Heaton, and Kohler (2014) and Ghahari et al. (2015).

The shape of the ambient vibration spectrum around the fundamental frequencies

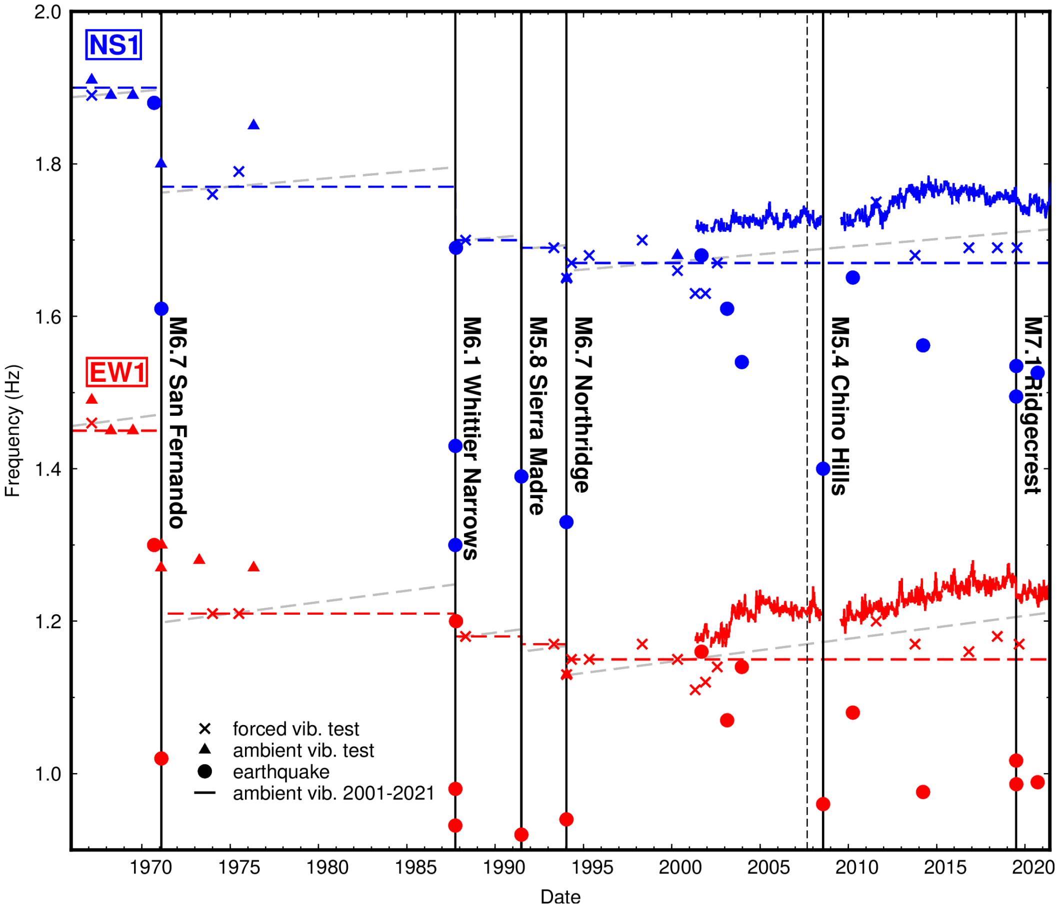

Figure 6.5: Lifetime changes in the EW (red) and NS (blue) fundamental frequencies of Caltech Hall, including ambient vibrations (triangles before 2001, solid lines after 2001), forced vibration tests (crosses), and major earthquakes (circles). Data are compiled from this study and Bradford et al. (2004). From left to right, the unlabeled significant earthquakes are 1970 M5.2 Lytle Creek, 2001 M4.2 Beverly Hills, 2003 M5.4 Big Bear, 2003 M6.6 San Simeon, 2010 M7.2 El Mayor-Cucapah, 2014 M5.1 Brea, and 2020 M4.5 South El Monte. The 2007 M4.7 Trabuco Canyon earthquake from Figure 6.4 is marked with a black dashed line. Colored dashed lines indicate the constant frequency between historical earthquakes speculatively inferred by Clinton et al. (2006) from forced vibration tests. Gray dashed lines schematically indicate the change in frequency that might have occurred between historical earthquakes if the long-term healing trend persisted before continuous instrumentation. Figure expanded from Figure 2 of Clinton et al. (2006).

Table 6.S1: Changes in apparent frequency from ambient vibrations 2001-2021

	East-West		North-South		Torsional	
Hz	Mode 1	Mode 2	Mode 1	Mode 2	Mode 1	Mode 2
May 2001	1.18	4.97	1.71	7.28	2.45	8.32
May 2021	1.24	4.84	1.75	7.24	2.46	8.09
Change	0.06	-0.13	0.05	-0.04	0.01	-0.23
%	[+5.1]	[-2.6]	[+2.3]	[-0.1]	[+0.0]	[-2.8]
Maximum	1.28	5.08	1.78	7.50	2.55	8.70
Minimum	1.17	4.73	1.71	7.01	2.43	7.87
Variability	0.11	0.35	0.07	0.48	0.12	0.83
%	[9.7]	[7.1]	[4.4]	[6.7]	[4.7]	[10.0]

Summary of changes in the apparent frequencies of Caltech Hall from ambient vibrations, 2001-2021. Variability is defined as the maximum minus the minimum weekly median frequency. Percentages are calculated relative to May 2001.

changed dramatically after the upgrade in instrumentation at CI.MIK in September 2008, exhibiting greater cross-talk between horizontal components (Figure 6.S2C,D). There is also a new peak, labeled C1 in Figure 6.S2, which is exactly the harmonic mean of EW1 and NS1. While this new peak could represent a change in the structure or mass distribution resulting in apparent "coupling" between the north-south and east-west vibrational systems of Caltech Hall, the simplest explanation is that the Episensor was not leveled properly during installation and is rocking on a diagonal axis.

Earthquake data analysis

To assess the response of Caltech Hall to earthquake loading, we download all M>4 earthquakes from SCEDC catalog between May 2001 and May 2021, and select all events with a peak acceleration >0.001 m/s^2 in either the E-W or N-S directions, for a total of 684 events (Figure 6.S3). An acceleration of 0.001 m/s^2 is comparable to the amplitude of ambient vibrations during high-occupancy, daytime hours, and thereby represents a minimum threshold of detectability. We select only earthquakes with M>4 so ensure that the shaking duration is long enough for robust analysis. For the earthquake frequencies shown in Figure 6.3, we select a 60-second window starting at the onset of earthquake motion, calculate the amplitude spectrum, and pick the peak frequency within a 0.2 Hz window around the expected fundamental frequencies for the east-west and north-south components. This apparent event

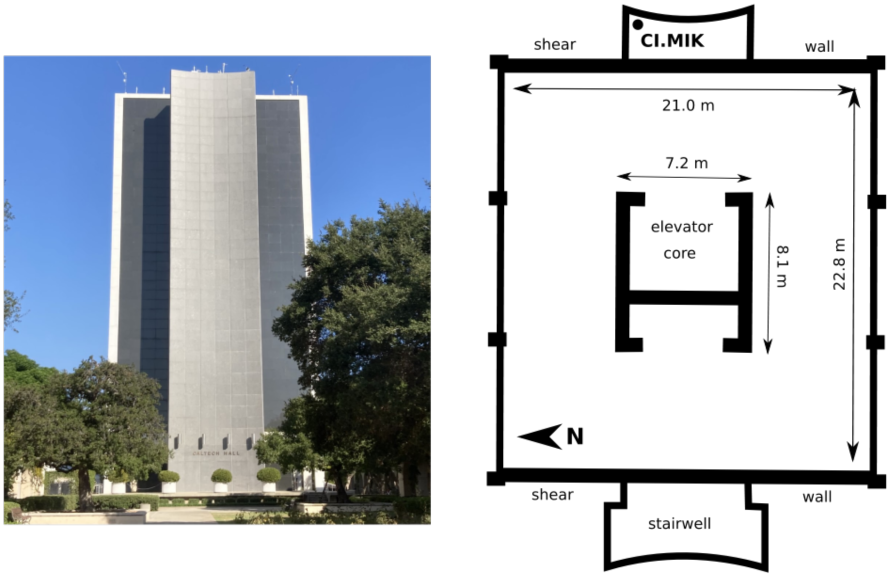

Figure 6.S1: (left) East-facing photograph of Caltech Hall showing the west shear wall and stairwell. (right) Plan-view schematic of Caltech Hall showing the major structural elements of the building and the location of CI.MIK on the ninth floor.

frequency is generally proportional to and slightly higher than the minimum event frequency determined from a frequency-time analysis, since the minimum frequency typically coincides with the strongest acceleration. However, such an apparent event frequency can be calculated robustly down to the ambient vibration noise floor, whereas the frequency determined from frequency-time analysis with a shorter window is not stable at low accelerations. For the earthquake frequencies shown in Figure 6.4, we exclude events with peak acceleration <0.01 m/s2, and instead divide the event records into overlapping 12.8-s windows, apply zero-padding, calculate the amplitude spectrum, and pick the peak frequency in each time window.

Forced vibration tests

In 1972, a Kinemetrics VG-1 Synchronized Vibration Generator (commonly referred to as the Millikan shaker) was permanently installed on the roof of Caltech Hall, and has been employed for numerous forced vibration tests (see Bradford et al. (2004) for a review). The shaker operates over a range of ~0.8-9.7 Hz and consists of two counter-rotating buckets that can be loaded with up to twelve weights of

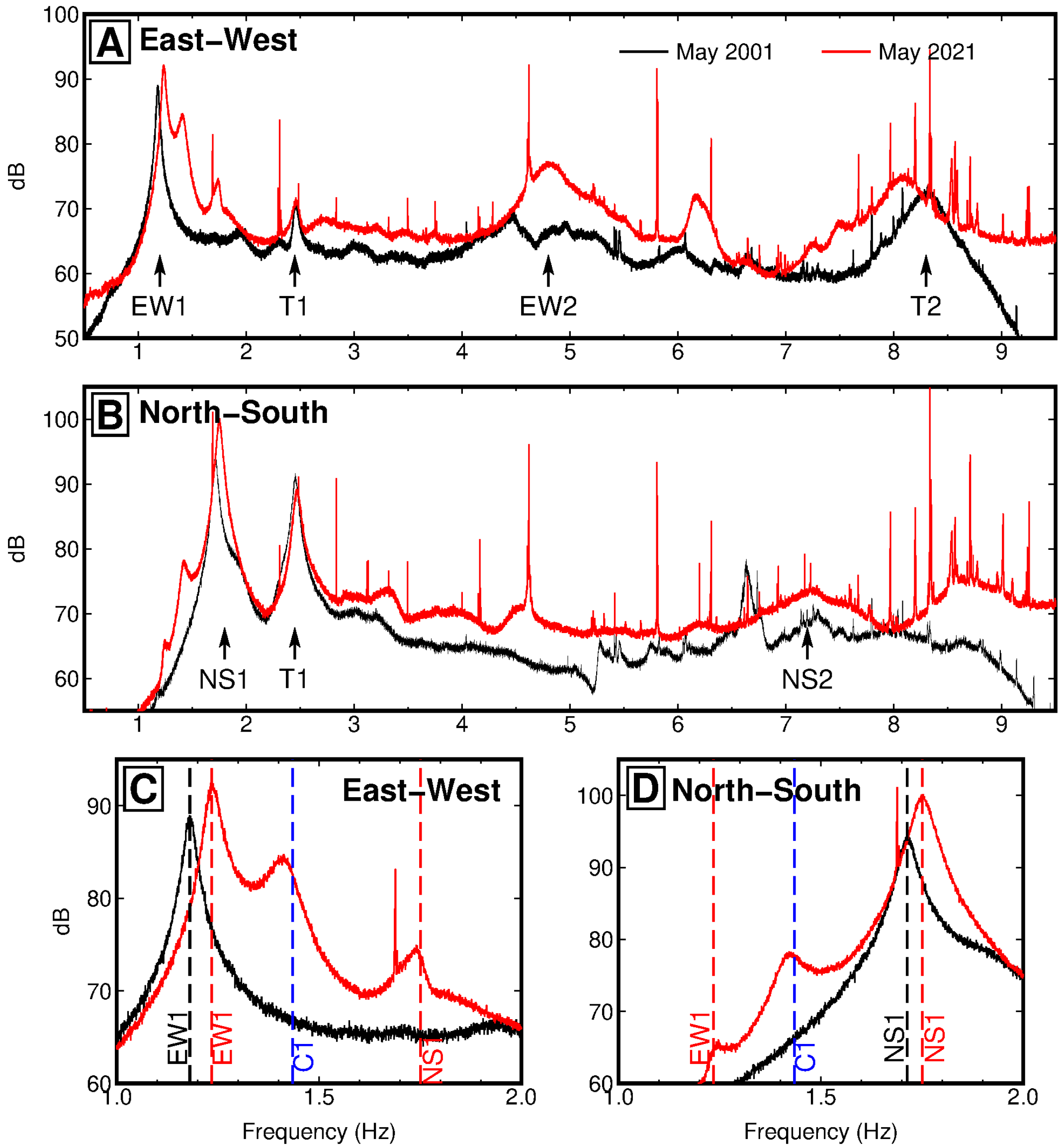

Figure 6.S2: Long-term changes in the ambient vibration spectrum of Caltech Hall to ambient vibrations. (A) Median spectrum of CI.MIK.BLE in May 2001 (black) and CI.MIK.BNE in May 2021 (red) with the peaks corresponding to each modal frequency annotated. (B) Median spectrum of CI.MIK.BLN in May 2001 (black) and CI.MIK.BNN in May 2021 (red). (C) Enlarged view of the E-W spectrum from A showing an increase in EW1, a more prominent peak associated with the NS1, and an entirely new peak. The line C1 represents the average period (beating frequency) between the estimated values of EW1 and NS1 in May 2021. (D) Same as C but for the N-S system. The increased cross-talk between the EW and NS components is possibly a result of seismometer misorientation and/or rocking, or a change in the structure itself.

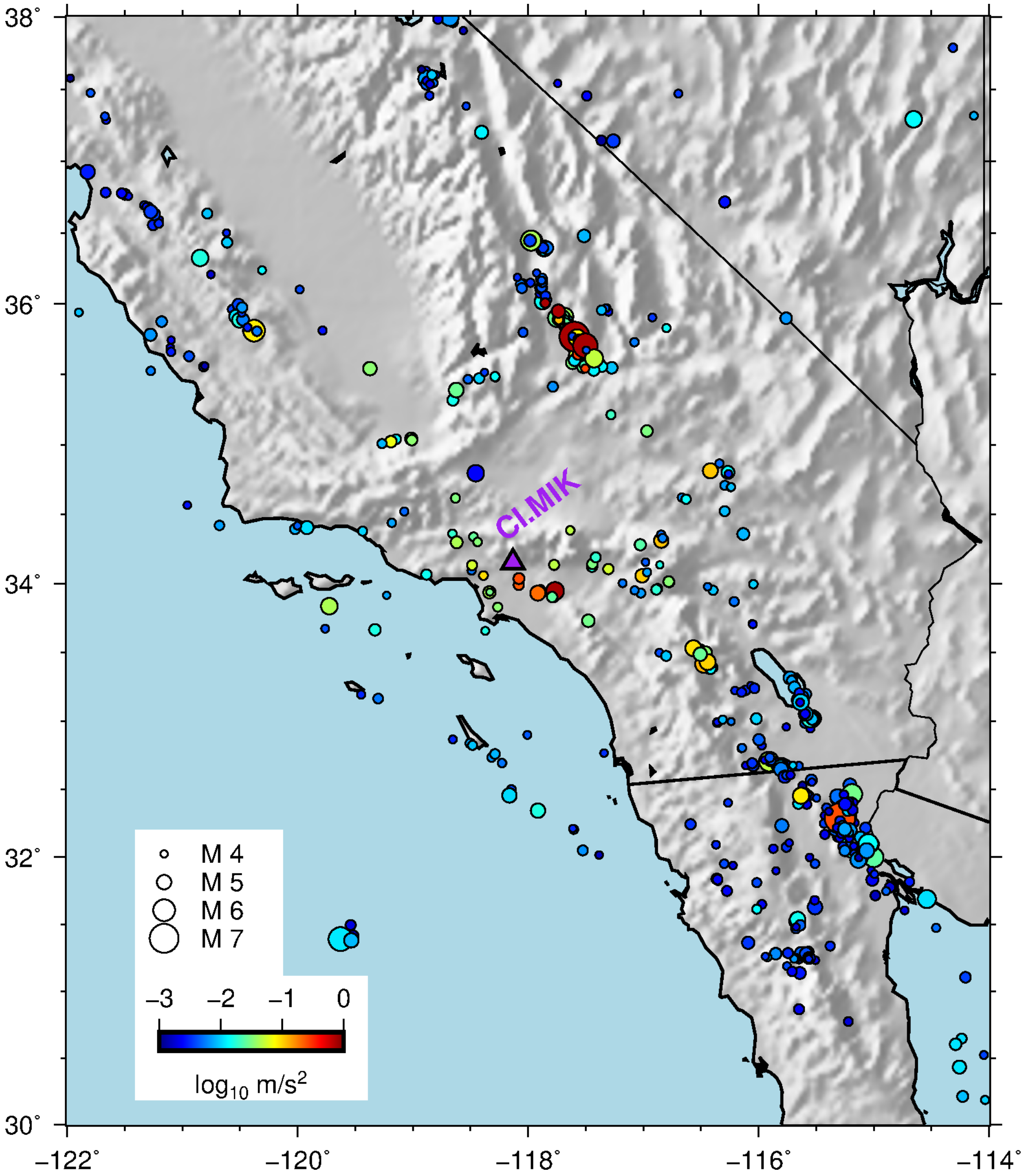

Figure 6.S3: Earthquakes in the Southern California region 2001-2021 with M>4 used in this study, colored by peak E-W acceleration at CI.MIK. The location of Caltech Hall and SCSN station MIK is marked by a purple triangle.

varying mass. Over the past decade, forced vibration tests have been conducted as part of Caltech civil engineering classes, which we reanalyse here using the record of each test on CI.MIK. Most tests constituted a frequency sweep, where the operators manually stepped up/down the forcing frequency by increments of 0.01-0.02 Hz every 60-120 s, though the weight configuration used seems to have varied considerably among tests. For this forced vibration data, information about timing, test plans, and weight configurations from past tests has generally been lost, and so a general approach is required. We first identify the time window of each forced vibration test with an automatic amplitude-thresholding search followed by manual inspection of the data, and discard brief or unusual tests, the results of which are not reported here. For the remaining tests, we divide the data into overlapping 12.8-s windows, zero-pad to increase frequency resolution, and calculate the amplitude spectrum. We select the peak frequency and average acceleration in each window, then manually remove spurious picks. A cubic spline interpolation is applied to the data points within 0.1 Hz of the target frequency, and the point of maximum acceleration is selected as the modal frequency for that test. Results of previously unreported forced vibration tests between 2011 and 2019 are included in Table S2.

An example up-sweep forced vibration test is shown in Figure 6.S4A,B. Repeating this same test for six different weight configurations yields the response curves shown in Figure 6.S4C. The EW1 and T1 modal peaks for all six tests are then plotted against peak acceleration in Figure 6.S4D,E, showing the reduction in apparent frequency with increased shaking.

References

Astorga, A. and P. Gueguen (2020). "Structural health building response induced by earthquakes: Material softening and recovery". In: *Eng. Rep.* 2.e12228.

Astorga, A., P. Gueguen, and T. Kashima (2018). "Nonlinear elasticity observed in buildings during a long sequence of earthquakes". In: *Bull. Seis. Soc. Am.* 108.3A, pp. 1185–1195.

Baker, J. W., B. A. Bradley, and P. J. Stafford (2021). *Seismic hazard and risk analysis*. Cambridge University Press, p. 581.

Bradford, S. C. et al. (2004). "Results of Millikan Library forced vibration testing". In: *Earthquake Enginering Research Laboratory Report* 2004-03.

Cheng, M. H., T. H. Heaton, and M. D. Kohler (2014). "Interpretation of Millikan Library's vibrating modes using a magneto coil to measure phase shifts". In: *Earthquake Engineering Research Laboratory Report* 2014-02.

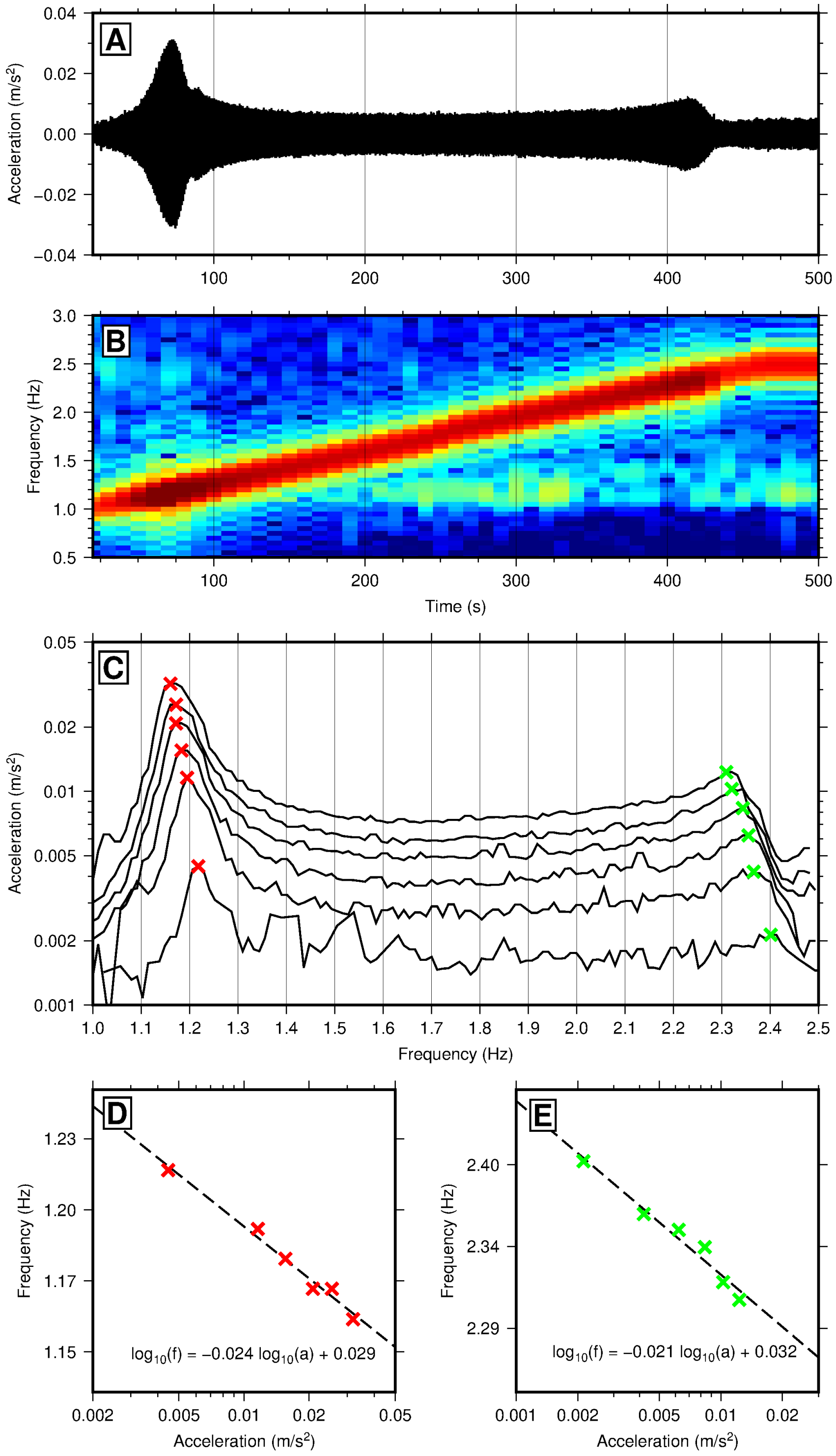

Figure 6.S4: (A) Example of a swept-frequency forced vibration test to identify the fundamental mode in the E-W direction and torsional mode. (B) Spectrogram of A. (C) Results of six forced vibration tests with different weight configurations showing the nonlinear response of each modal frequency to different shaking intensities. (D) Zoom-in to picks for EW1 from C with log-log fit. (E) Same as D but for T1.

Table 6.S2: Results of forced vibration tests 2011-2019

	East-West		North-South		Torsional	
Hz	Mode 1	Mode 2	Mode 1	Mode 2	Mode 1	Mode 2
Jul 31 2011	1.20	4.90	1.75	7.26	2.46	8.15
Oct 12 2013	1.17	4.82	1.68	7.23	2.37*	-
Oct 29 2016	1.16	-	1.69	-	2.45	-
Jun 10 2018	1.18	4.74	1.69	-	2.40	-
Jul 21 2019	-	-	1.69	7.21	2.50	-
Sep 01 2019	1.17	4.76	-	-	2.40*	-

Modal frequencies identified from forced vibration tests between 2011 and 2019. Measurements of T1 marked with an asterisk are taken from excitation of the E-W system, whereas others are from excitation of the N-S system. During forced vibration tests, the torsional mode appears systematically lower by 0.04-0.08 Hz for shaking in the E-W direction. Note also that the weight configuration varies among tests, which can modify the apparent frequency by about 5% percent. In particular, the test on July 31, 2011 was conducted with no weights. For a complete review of historical forced vibration data, see Bradford et al. (2004).

Clinton, J. F. et al. (2006). “The observed wander of the natural frequencies in a structure”. In: *Bull. Seis. Soc. Am.* 96.1, pp. 237–257.

Edvardsen, C. (1999). “Water permeability and autogenous healing of cracks in concrete”. In: *ACI Mater. J.* 96, pp. 448–454.

Favela, J. (2004). “Energy radiation from a multi-story building”. PhD thesis. California Institute of Technology.

Foutch, D. A. and P. C. Jennings (1978). “Foundation response of a nine-story reinforced concrete building”. In: *Bull. Seis. Soc. Am.* 68.1, pp. 219–229.

Funk, C. C. et al. (2014). “A quasi-global precipitation time-series for drought monitoring”. In: *U. S. Geological Survey Data Series* 832, p. 4.

Ghahari, S. F. et al. (2015). “Blind identification of Millikan Library from earthquake data considering soil-structure interaction”. In: *Struct. Control Health Monit.* 23, pp. 684–706.

Gueguen, P., P. Johnson, and P. Roux (2016). “Nonlinear dynamics induced in a structure by seismic and environmental loading”. In: *J. Acoust. Soc. Am.* 140, pp. 582–590.

Haselton, C. B. et al. (2017). “Response history analysis for the design of new buildings in the NEHRP provisions and ASCE/SEI 7 standard: Part II – structural analysis procedures and acceptance criteria”. In: *Earthquake Spectra* 33.2, pp. 397–417.

Johnson, P. and A. Sutin (2005). “Slow dynamics and anomalous nonlinear fast dynamics in diverse solids”. In: *J. Acoust. Soc. Am.* 117.1, pp. 124–130.

Kohler, M. D., P. M. Davis, and E. Safak (2005). “Earthquake and ambient vibration monitoring of the steel-frame UCLA Factor Building”. In: *Earthq. Spectra* 21.3, pp. 1–22.

Kuriowa, J. H. (1967). “Vibration test of a multistory building”. PhD thesis. California Institute of Technology.

Lees, T. P. (1992). “Deterioration mechanisms”. In: *Durability of concrete structures: investigation, repair, protection*. Ed. by G. C. Mays. E. & F. N. Spon Press, pp. 10–36.

Luco, J. E., M. D. Trifunac, and H. L. Wong (1987). “On the apparent change in dynamic behavior of a nine-story reinforced concrete building”. In: *Bull. Seis. Soc. Am.* 77.6, pp. 1961–1983.

– (1988). “Isolation of soil-structure interaction effects by full-scale forced vibration tests”. In: *Earthq. Eng. Struct. Dyn.* 16, pp. 1–21.

Menne, M. J. et al. (2012). “An overview of the Global Historical Glimatology Network-Daily Database”. In: *Journal of Atmospheric and Oceanic Technology* 29, pp. 897–910.

Moussa, M. et al. (2013). “Long-term development of thermophysical and mechanical properties of cold-curing structural adhesives due to post-curing”. In: *J. Appl. Polym. Sci.* 127.4, pp. 2490–2496.

Rodell, M. et al. (2004). “The Global land data assimilation system”. In: *Bull. Amer. Meteor. Soc.* 85.3, pp. 381–394.

Roig-Flores, M. and P. Serna (2020). “Concrete early-age crack closing by autogenous helaing”. In: *Sustainability* 12, p. 4476.

SCEDC (2013). Southern California Earthquake Data Center, Caltech Dataset. doi: `https://doi.org/10.7909/C3WD3xH1`.

TenCate, J. A., E. Smith, and R. A. Guyer (2000). “Universal slow dynamics in granular solids”. In: *Phys. Rev. Lett.* 85.5, pp. 1020–1023.

Todorovska, M. I. (2009a). “Seismic interferometry of a soil-structure interaction model with coupled horizontal and rocking response”. In: *Bull. Seis. Soc. Am.* 99.2A, pp. 611–625.

– (2009b). “Soil-structure system identification of Millikan Library north-south response during four earthquakes (1970–2002): what caused the observed wandering of the system frequencies?” In: *Bull. Seis. Soc. Am.* 99.2A, pp. 626–635.

Todorovska, M. I. and Y. Al Rjoub (2006). “Effects of rainfall on soil-structure system frequency: examples based on poroelasticity and a comparison with full-scale measurements”. In: *Soil Dyn. Earthq. Eng.* 26.6–7, pp. 708–717.

Trifunac, M. D., S. S. Ivanovic, and M. I. Todorovska (2001). “Apparent periods of a building, II: Time-frequency analysis”. In: *J. Struct. Eng.* 127.5, pp. 527–537.

Udwadia, F. E. and M. D. Trifunac (1974). “Time and amplitude dependent response of structures”. In: *Earthq. Eng. Struct. Dyn.* 2, pp. 359–378.

Zimmerman, R. B. et al. (2017). “Response history analysis for the design of new buildings in the NEHRP provisions and ASCE/SEI 7 standard: Part III – example applications illustrating the recommended methodology”. In: *Earthquake Spectra* 33.2, pp. 419–447.

Chapter 7

CONCLUSIONS

In this thesis, we offered several case studies demonstrating multi-scale solutions to sensing problems in seismology, oceanography, and engineering. Chapters 2 and 3 showed that ocean-bottom DAS leveraging pre-existing fiber-optic infrastructure can be employed for earthquake monitoring, subsurface characterization, and noise source localization in a similar manner to dense onshore seismometer deployments like nodal arrays. Chapter 4 demonstrated that ocean-bottom DAS is sensitive to ocean wave pressure in shallow water, permitting insights into sea surface statistics and measuring ocean currents. Chapter 5 explored the potential of DAS as a temperature sensor in the ocean environment, with sufficient long-period sensitivity to resolve tide dynamics across a broad range of depths. Finally, Chapter 6 showed that triggered strong motion records alone are insufficient to monitor the dynamic variability in structural stiffness of concrete buildings over time scales from seconds to decades.

With the rise of machine learning techniques in recent years, big data has become synonymous with automation. Although every dataset in this thesis was big, owing largely to the fine spatio-temporal sampling of DAS, the major discoveries were a result of *looking*, not *learning*: From the subtle Doppler shift in frequency-wavenumber images in Chapter 2, which first indicated to us that DAS observations of ocean waves might resolve ocean current velocity, to the spurious arrivals in ambient noise cross-correlations offshore Belgium in Chapter 3, which we later localized to individual wind turbines sources, to the tidal pressure signal in Chapter 5 which was initially removed by a laser denoising workflow. There is no doubt that machine learning applied to DAS data will uncover many scientific discoveries, like subtle patterns in microseismicity. But as much as this thesis has proven the value of treating DAS like a dense array of conventional seismometers, it has shown how little is known about DAS sensitivity in the field. Fiber-optic seismology and oceanography are still nascent fields, and care should be taken to understand and exploit the potential of DAS as a fundamentally new type of geophysical sensor, which records a combination of strain, pressure, and temperature and can be deployed in previously inaccessible environments.

Throughout this thesis, we attempted to calibrate the sensitivity of DAS in situ by comparing observations with a priori physical predictions for seismic and ocean waves. While often successful, for example in relating ocean wave pressure to DAS strain in the wind-wave band in Chapter 4, such an approach represents a fundamental limitation to data-driven exploration. If fiber-optic sensing is ever to replace conventional point sensors as the backbone of global observing networks for seismology and oceanography, a detailed evaluation of DAS instrument response must take place both in the laboratory and in the field, taking into account the possible effects of cable design and installation conditions. Further, a framework for DAS metadata must be established so that calibrations associated with particular instruments or cables are standardized, reproducible, and usable by the community, as is common practice in contemporary seismometry.

Development of DAS over the last 10-15 years has largely been driven by the oil industry, and consequently most commercial instruments available today are tailored with high-frequency, active-source seismic surveys in mind. As the scope of fiber-optic sensing grows to include applications like earthquake and structural seismology, physical oceanography, and perhaps even geodesy, the DAS technology must also evolve. In order to move beyond the continental shelf, ocean-bottom DAS requires either a reduction in power consumption, so that DAS units can be deployed with battery packs in the abyssal ocean much like ocean-bottom seismometers, or an increase in sensing range beyond 100 km. While numerous unused "dark" fibers exist in urban fiber networks, bandwidth in submarine fiber-optic links is more limited, so standardization and commercialization of DAS multiplexing with ordinary optical communications will be a necessary step in leveraging existing subsea infrastructure for geophysical sensing. The instrumental noise floor generally increases with period for DAS; this is partly a result of optoelectronic hardware choices and can certainly be improved. Also, most commercial DAS systems are comparable to high-gain seismometers in that they saturate at relatively weak ground motions and have a limited dynamic range, which is a major barrier for incorporation in earthquake early warning systems. These challenges can be overcome by clearly defining the sensing needs of the geophysical community and working with photonic engineers to develop the next generation of DAS systems.

Finally, we must acknowledge that fiber-optic sensing is far from a universal solution to the problem of multi-scale sensing. For example, DAS is poorly suited to studying structural dynamics compared to conventional instrumentation because it is a non-inertial sensor. A DAS array embedded in the floors or columns of a building is expected to record the longitudinal strain in each element, which is small; whereas an accelerometer will record the absolute motions of the complete structure, permitting direct calculation of key engineering parameters like interstory drift. Similarly, for ground motion studies, strain is challenging to reconcile with standard intensity measures because it is a wavefield gradient. In most cases where triggered instrumentation already exists, the most effective solution for multi-scale structural health monitoring and strong-motion networks is simply to upgrade the data logging and telemetry to permit continuous waveform recording, or to densify the array by adding low-cost point sensors like MEMS accelerometers.

Appendix A

ADDITIONAL OBSERVATIONS OF WIND TURBINE VIBRATIONS

In Chapter 3, we analyzed approximately one hour of DAS data from a buried subsea power cable in the Belgian North Sea from August 2018, demonstrating that high-frequency Scholte waves observed locally along the cable were associated with structural vibrations of nearby wind turbines. Subsequently, we acquired two additional short datasets, which support this interpretation. Here, we review the major observations of each dataset briefly.

On 2019-12-15, 24-h of DAS data were recorded on a buried subsea power cable running parallel to the cable from Chapter 3. As before, a chirped-pulse DAS instrument was used with 10-m channel spacing and 10-m gauge length. Common-offset gathers and source imaging with the 2018 dataset showed a clear source of Scholte waves near 34-km cable distance, at the southeast end of the Rentel wind farm, and two-to-four additional weaker sources between 37–40-km distance, at the northwest end of Rentel. In the 2019 data (Figure A.1), a cross-correlation common-offset gather along the same segment shows nine distinct and equally spaced sources, which clearly correspond to the row of nine turbines immediately adjacent to the cable. Further, no sources were observed before 30-km distance in the 2018 dataset; whereas in the 2019 data, six equally spaced sources are evident between 25 and 30 km cable distance, which clearly correspond to the closest row of six turbines in the Norther wind farm (Figure A.1). At the time of recording in August 2018, the Rentel project was only partly commissioned and the Norther project was still under construction (Figure 3.1). Over the subsequent year, both wind farms were completed and fully commissioned by the time of the December 2019 DAS recording. This before-and-after comparison confirms our interpretation in Chapter 3 and provides a simple case study of successful remote operational monitoring.

In March 2021, three weeks of DAS data were recorded on an unburied umbilical power cable connecting several turbines in the Norther wind farm to the offshore high-voltage station (OHVS). The cable rests on the seafloor between turbines and enters the turbine superstructure through the J-tube, a curved metal conduit that

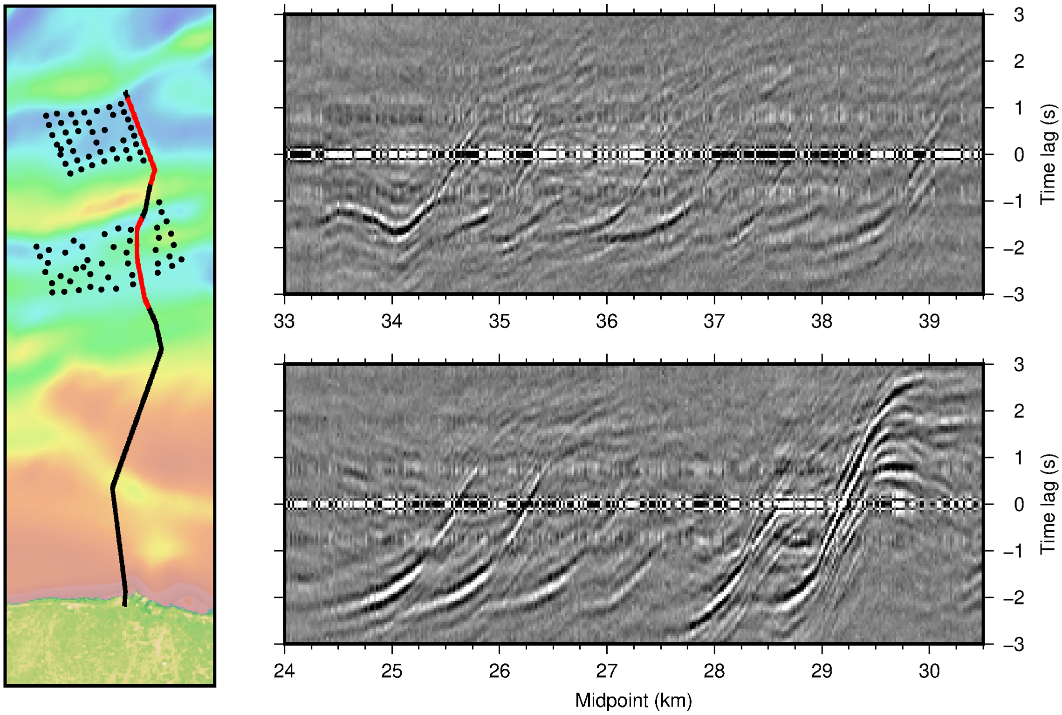

Figure A.1: Common-offset gathers for cross-correlations of ambient seismic noise recorded on a buried cable offshore Belgium, as in Figure 3.5. (Top) Cable segment running through the Rentel wind farm, showing off-axis arrivals from all nine wind turbines in the row closest to the cable. (Bottom) Cable segment running through the Norther wind farm, showing off-axis arrivals from all six wind turbines in the row closest to the cable.

protects the cable from hanging in the water column. Within the turbine itself, the cables may hang freely for a short distance while the optical fiber is spliced into local telecommunications equipment. A short 20-s example of this DAS data is shown in Figure A.2: the cable enters and exits a turbine around 14.7 km, passes close to a second turbine at the seafloor around 15.7 km, and then enters/exits five more turbines, each spaced about 750-m apart. Within each turbine, the high-frequency DAS data (Figure A.2, filtered 2–10 Hz) are incoherent, likely because the fiber is traveling vertically up the superstructure and poorly coupled. As the cable exits through the J-tube, clear structural vibrations emerge which are continuous and coherent out into the sediment. Between turbines, the DAS data are dominated by crossing Scholte waves from multiple sources.

In Chapter 3, we discussed the potential for isolating vibrations from individual turbines in the far field for operational and structural health monitoring applications using the buried power transmission cables that connect each wind development

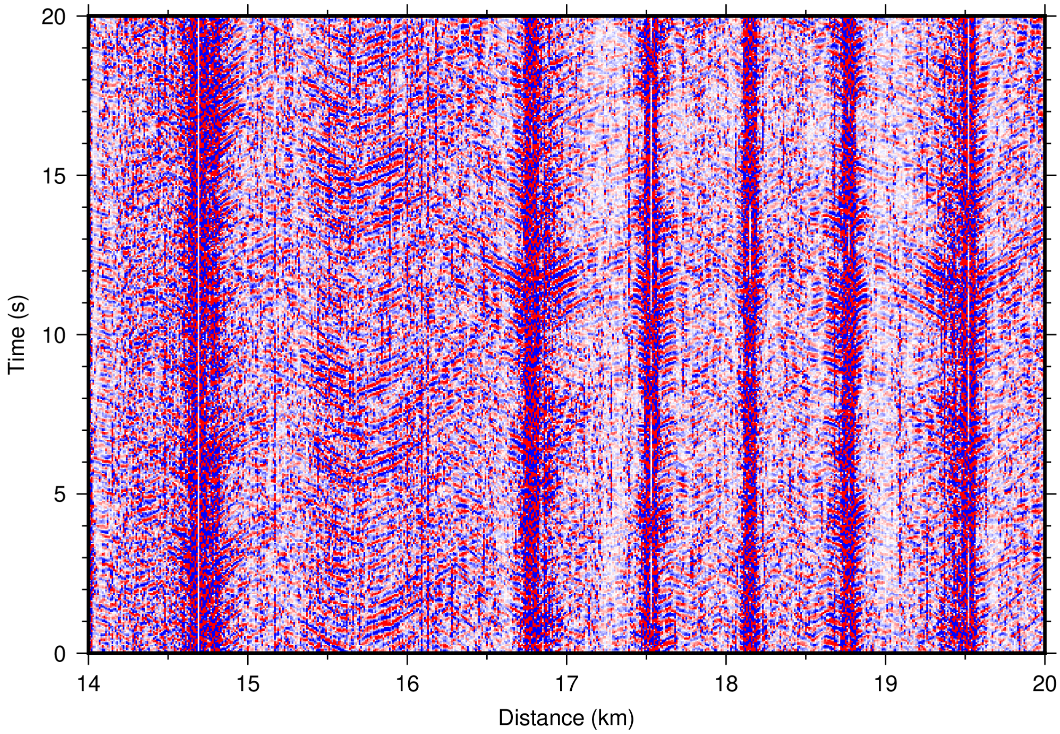

Figure A.2: DAS data filtered 2-10 Hz from an unburied umbilical power cable connecting a row of wind turbines in the Norther development, showing continuity between vibrations recorded within the superstructure of individual turbines and Scholte waves recorded at the seafloor between turbines.

to shore. The signal to noise ratio for data collected on umbilical cables between turbines is significantly poorer, likely because the cables are only resting on the seafloor and therefore prone to disruption by ocean waves and currents. Nonetheless, the umbilical DAS data shows that structural vibrations can be easily discerned in the immediate vicinity of each turbine and in the J-tube, which eliminates the need for backprojection imaging or deblending filters to isolate the signals from individual turbines. Because all umbilical power cables meet at the OHVS, it may be possible to monitor an entire wind development with a single centrally located DAS system.

Appendix B

A SHORT NOTE ON DAS AND HETEROGENEITY

B.1 Introduction

Small-scale inhomogeneities much less than the seismic wavelength have a negligible first-order effect on the particle motions observed by conventional seismometers but can greatly influence wavefield gradients, namely tilt and strain. This problem has long been recognized in the study of solid Earth tides, with deviations from theoretical predictions up to ±50% varying incoherently among early strainmeter observatories (Berger and Beaumont, 1976; Beaumont and Berger, 1975). In addition to three-dimensional elastic heterogeneity, topographic gradients and cavities can modify the local strain field (Harrison, 1976). With many strainmeters installed in vaults or boreholes and thus necessarily subject to bias, various empirical corrections have been developed to compensate for local inhomogeneity, typically calibrated to the theoretical solid-body tide for a spherical, non-rotating, elastic, and isotropic Earth model (Hart et al., 1996; King et al., 1976). However, even with these site corrections, observations of dynamic strains from earthquakes persistently differ from model predictions and estimates with array gradiometry by about 10–30% (Gomberg and Agnew, 1996; Langbein, 2015).

Distributed acoustic sensing (DAS) measures solid-Earth strain from changes in the optical path length in a fiber over a finite gauge length, and is therefore prone to the same biases as any conventional strainmeter or tiltmeter. With the rapid proliferation of DAS arrays for earthquake detection and subsurface characterization, most authors have assumed, implicitly or explicitly, that DAS strain is equivalent to a scaled point measurement of particle motion, an assumption which is only reasonable in a homogeneous medium. Though several authors have noted the potential perils of this assumption in passing (Lindsey, Rademacher, and J. B. Ajo-Franklin, 2020; Paitz et al., 2021), only one effort has so far been made to address it. Building on the recent work of Singh, Capdeville, and Igel (2020), Muir and Zhan (2022) proposed to calibrate the response of DAS channels in an arbitrarily heterogeneous Earth in-situ by application of an empirical coupling tensor. Observations of dynamic strain and particle motion from collocated DAS and seismometer arrays are utilized to invert the tensor, which can then be applied to future events like an instrument response function. While this framework is sufficiently general to correct a complex superposition of biases from three-dimensional heterogeneity and topography, it requires the installation of collocated seismometers, which is impractical for large-scale applications and nullifies the advantages of DAS over conventional point sensors in terms of cost and logistics. Because DAS arrays are spatially coherent across several scales (1-100000 m), it may be possible to identify and correct the effects of sparse or long-wavelength (relative to the DAS resolution) inhomogeneities and topographic slopes using DAS array gradients (the gradient of the wavefield gradient) with the understanding that the distortion of the strain field is spatially coherent. However, such a framework cannot address dense or short-wavelength inhomogeneities, which represent a fundamental limit to the effective DAS resolution.

In this appendix, we show an example DAS dataset where small-scale heterogeneity has a leading order impact and make an initial effort to quantify its effect on distributed strain measurements in a simple theoretical case study.

B.2 Evidence for small-scale heterogeneity in DAS data

For subsurface investigations such as Rayleigh wave tomography with DAS data, phase or group velocity is often estimated by applying a wavefield transformation (such as beamforming) over a finite aperture sub-array, typically some multiple of the anticipated wavelength. At face value, this seems unnecessarily wasteful. If DAS has channel resolution on the order of 1–10 m, why not compute the phase or group moveout between any two channels with arbitrary spacing and resolve the finest possible structure?

Two examples of this approach are shown in Figure B.1 and B.2, looking at a 400-m segment of the Pasadena Array, a fiber-optic loop near Caltech campus. Since 2018, the Pasadena Array has been instrumented with an OptaSense ODH3 DAS interrogator, using a channel spacing of 8 m and a gauge length L of 16 m. In Figure B.1, ambient noise cross-correlations were computed and stacked over several months of data and formed into a common-source gather; then the Rayleigh wave phase velocity between each pair of channels at 8 m ($L/\Delta x = 2$), 16 m ($L/\Delta x = 1$), and 24 m ($L/\Delta x = 0.66$) was estimated by phase tracking. In Figure B.2, time-harmonic Rayleigh waves at 4.9-Hz generated by the forced vibration of Caltech Hall (formerly Millikan Library) at its second E-W mode were narrow-band filtered; then, the phase velocity was estimated between each pair of channels. This

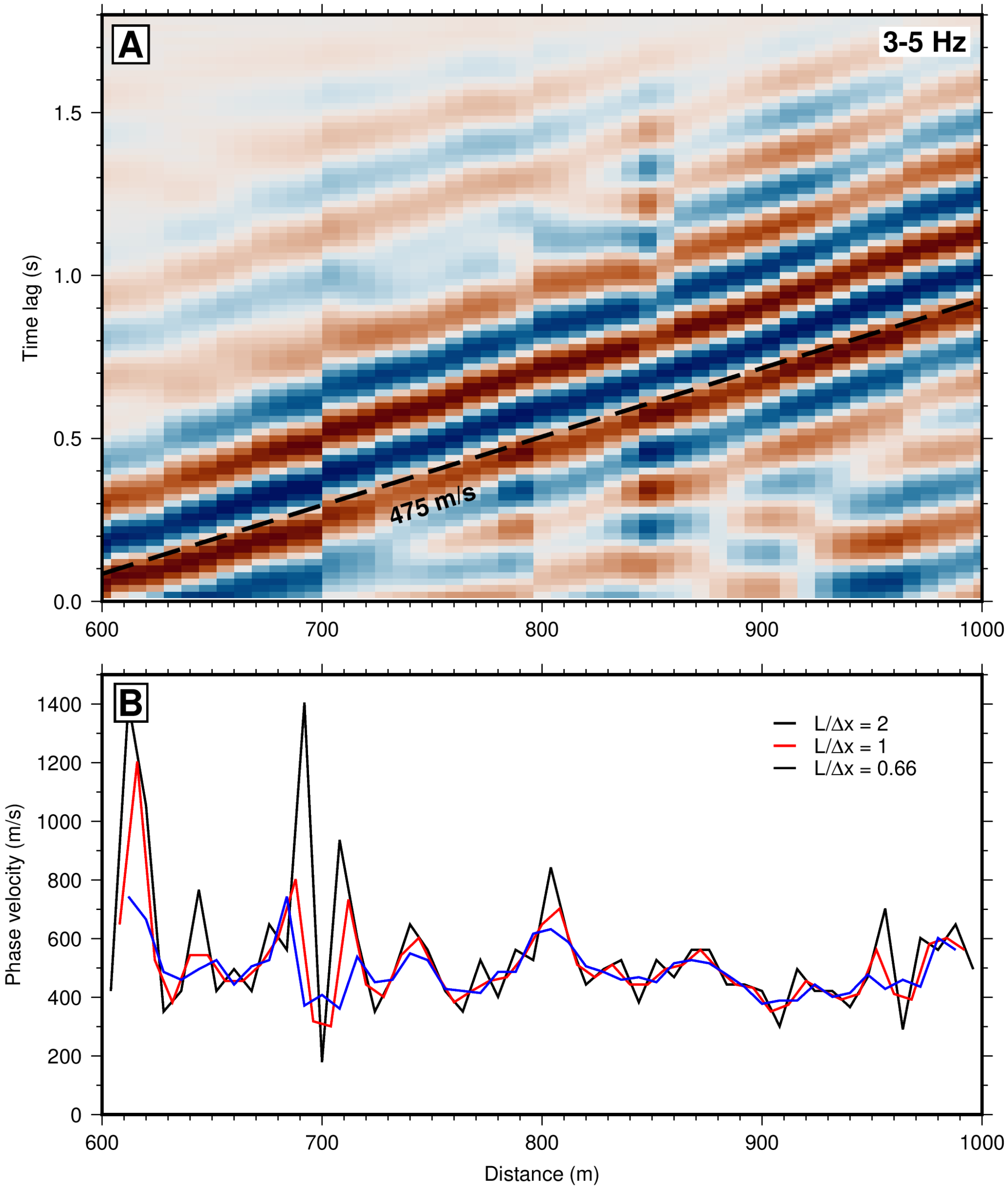

Figure B.1: (A) Ambient noise cross-correlation common-source gather for a virtual source at 560 m, filtered 3–5 Hz. The gauge length is 16 m.(B) Rayleigh wave phase velocity measured from A by calculating the phase lag between channels separated by 8 m (black), 16 m (red), and 24 m (blue). Cross-correlations courtesy of Jiaqi Fang.

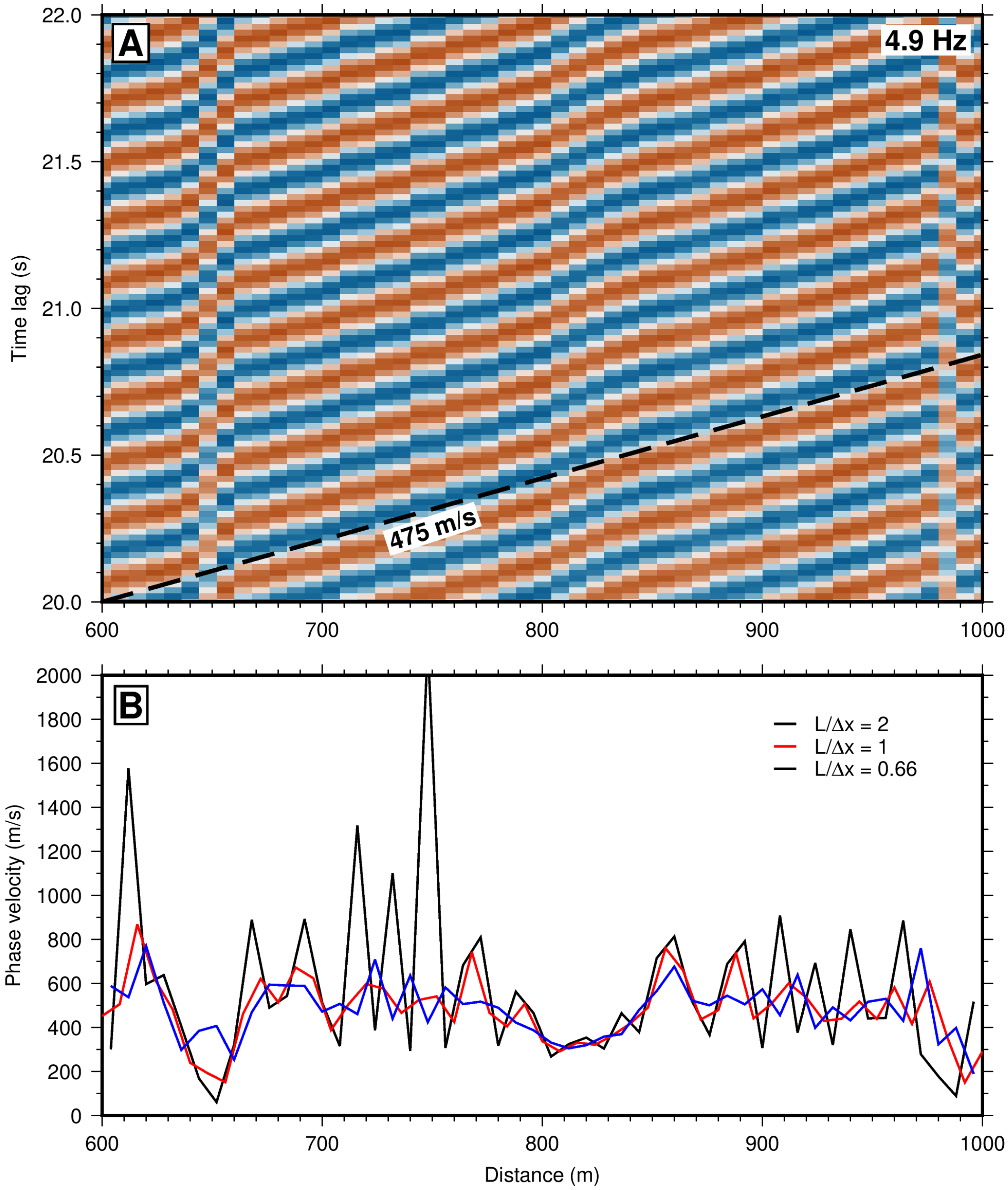

Figure B.2: (A) Snapshot of Rayleigh waves at 4.9 Hz generated by forced vibration of Caltech Hall at its first E-W overtone. The gauge length is 16 m. (B) Rayleigh wave phase velocity measred from A by calculating the phase lag between channels separated by 8 m (black), 16 m (red), and 24 m (blue), averaged over 10 minutes of continuous forced vibrations.

was done by using the Hilbert transform to estimate the instantaneous phase of each channel at each time step, and taking the median over 10 minutes of data, which effectively removes bias from emphemeral signals in the same frequency band, like passing cars. For both these cases, the Rayleigh wave phase velocity around 3-5 Hz is generally a target of interest in seismic microzonation, since the sensitivity is similar to the average shear-wave velocity of the top 100 or so meters.

Both examples in Figure B.1 and B.2 show a consistent background velocity around 475 m/s. However, when the phase velocity is computed between adjacent channels ($L/\Delta x = 2$), small-scale jumps in velocity up to 500% are observed, with a characteristic length scale of 1–2 channels (8–16 m). When the channel spacing is increased by a factor of three to 24 m ($L/\Delta x = 0.66$), the apparent heterogeneity is reduced by about a factor of 10. While the statistics of small-scale velocity perturbations in the crust have not been widely studied, this result is clearly unreasonable. We can draw two immediate conclusions: (1) small-scale inhomogeneities do exist in sedimentary basins like Pasadena and are strong enough to bias distributed strain measurements, and (2) DAS strain exhibits a scale-dependent, nonlinear sensitivity to these inhomogeneities, in which the gauge length seems to play an important role.

B.3 A simple theoretical example

In order to evaluate the effect of small-scale inhomogeneities on DAS strain measurements, we construct a simple theoretical model. Consider a discretely stratified 1D medium governed by a scalar wave equation such that the forward propagator P in any layer and displacement-stress vector f for a monochromatic progressive wave are given by:

$$f(x) = P(x|x_0) f(x_0)$$

$$P(x|x_0) = \begin{bmatrix} \frac{1}{2}e^{i\omega\eta\Delta x} & \frac{i\rho}{2\eta}e^{i\omega\eta\Delta x} \\ -\frac{i\eta}{2\rho}e^{i\omega\eta\Delta x} & \frac{1}{2}e^{i\omega\eta\Delta x} \end{bmatrix}$$

$$f(x_0) = \begin{bmatrix} \sigma \\ \omega u \end{bmatrix} = \begin{bmatrix} \frac{i\rho}{\eta}\omega A e^{-i\omega t} \\ \omega A e^{-i\omega t} \end{bmatrix}$$

with uniform density ρ and slowness η over (x_0, x), initial displacement amplitude A, and ignoring any initial phase. We neglect attenuation and reflection. By neglecting reflection, this is only a reasonable approximation for weak heterogeneity and underestimates the bias induced by large variations in η. A simple two-layer velocity model and its corresponding wavefield is given in Figure B.3. The model is homogeneous at some point x_1 where the slowness is η_1 and has a material discontinuity at x_2, with the slowness in the second layer $\eta_2 = (1+\gamma)\eta_1$. The particle displacement u and point strain ε at any point x are then given by

$$u(x) = \begin{cases} Ae^{-i\omega(t-\eta_1 x)}, & x \leq x_2 \\ Ae^{-i\omega(t-\eta_1 x_2-\eta_2(x-x_2))}, & x > x_2 \end{cases} \tag{B.1}$$

$$\varepsilon(x) = \begin{cases} i\omega\eta_1 Ae^{-i\omega(t-\eta_1 x)}, & x < x_2 \\ i\omega\eta_2 Ae^{-i\omega(t-\eta_1 x_2-\eta_2(x-x_2))}, & x > x_2 \end{cases} \tag{B.2}$$

Here we use the definition of an idealized DAS interrogator which measures the average strain over a gauge length L. The exact sensitivity of real DAS systems is dependent on optical factors such as the pulse length (Dean, Cuny, and Hartog, 2017) and different time-domain or frequency-domain reflectometry schemes (e.g. single-pulse, dual-pulse, chirped-pulse), which may equate to a spatially weighted average of strain or a discrete difference between the optical travel-time of copropagating pulses. If the point strain is not uniform across the gauge length, the response of different DAS systems will likely vary substantially, but such effects are not considered here. The idealized DAS strain ε^L at x_1 then follows as

$$\begin{aligned} \varepsilon^L(x_1) &= \frac{1}{L}\int_{x_1-\frac{L}{2}}^{x_1+\frac{L}{2}} \varepsilon(x)dx \\ &= \frac{A}{L}e^{-i\omega(t-\eta_1 x_1)}\left[e^{i\omega\eta_1\frac{L}{2}} - e^{-i\omega\eta_1\frac{L}{2}}\right] \\ &= \frac{2i}{L}u(x_1)\sin\left(\frac{\omega\eta_1 L}{2}\right) = \varepsilon(x_1)\,\mathrm{sinc}\left(\frac{\omega\eta_1 L}{2}\right) \end{aligned} \tag{B.3}$$

which is a familiar result (Bakku, 2015; Dean, Cuny, and Hartog, 2017). Similarly, the DAS strain at x_2 is

$$\begin{aligned} \varepsilon^L(x_2) &= \frac{1}{L}\int_{x_2-\frac{L}{2}}^{x_2} \varepsilon(x)dx + \frac{1}{L}\int_{x_2}^{x_2+\frac{L}{2}} \varepsilon(x)dx \\ &= \frac{A}{L}e^{-i\omega(t-\eta_1 x_2)}\left[e^{i\omega\eta_2\frac{L}{2}} - e^{-i\omega\eta_1\frac{L}{2}}\right] \\ &= \frac{1}{L}u(x_2)\left[e^{i\omega\eta_2\frac{L}{2}} - e^{-i\omega\eta_1\frac{L}{2}}\right] \end{aligned} \tag{B.4}$$

Unlike the homogeneous case, where $\sin(\omega\eta_1 L/2)$ is purely a constant factor, the last expression has a finite complex argument and cannot be further reduced.

The amplitude and phase response of DAS strain relative to particle displacement for the case at x_2 are plotted in Figure B.4. In a homogeneous medium ($\gamma = 0$, which

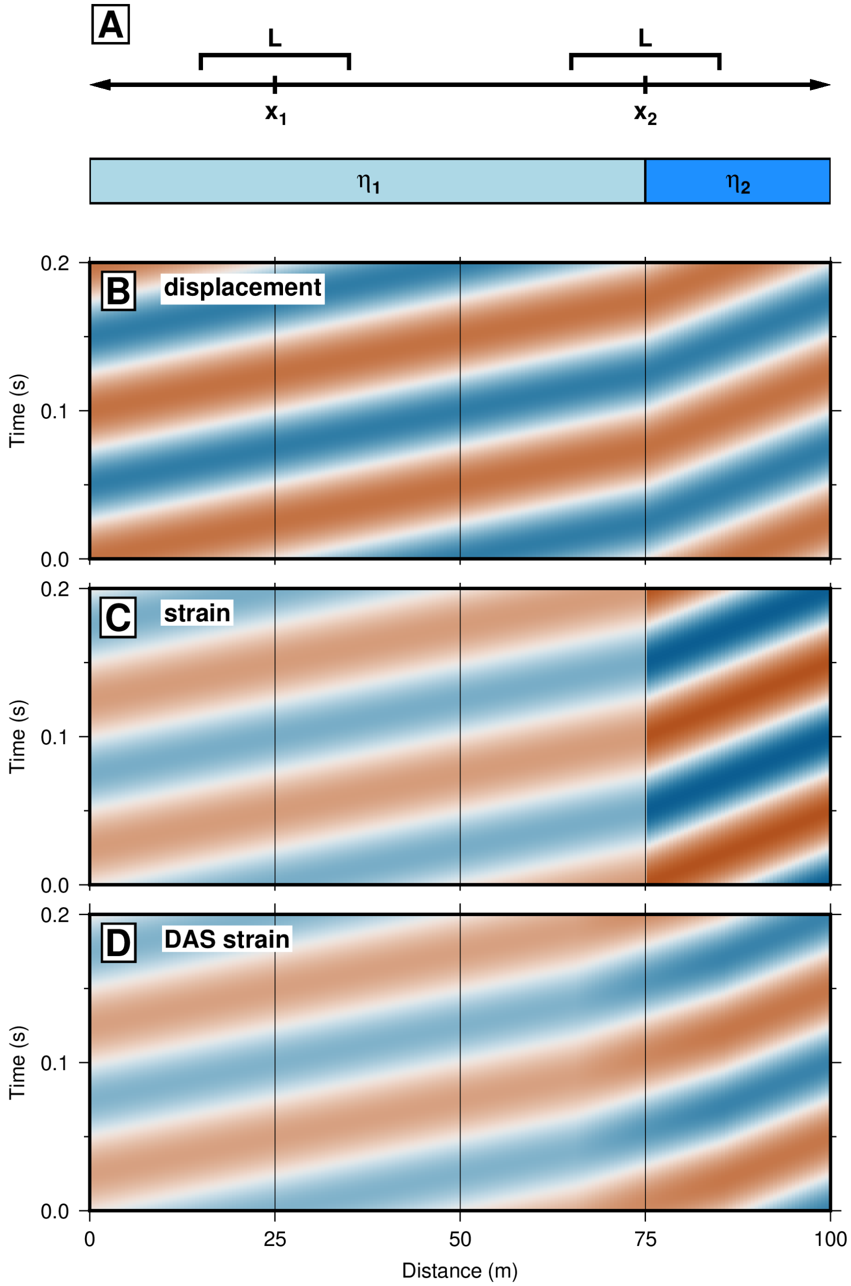

Figure B.3: (A) A simple set-up for a two-layer unbounded medium where the wavefield is recorded at x_1 and x_2, the slowness of each layer is given by η_1 and η_2, and the DAS system measures averaged strain over a gauge length L. (B) Particle displacement (u) for the example of a monochromatic progressive wave with a frequency of 10 Hz where $c_1 = \frac{1}{\eta_1} = 1000$ m/s and $c_2 = \frac{1}{\eta_2} = 500$ m/s. (C) Point strain ($\varepsilon = \partial u / \partial x$) for the same case. (D) DAS strain (ε^L) for the same case where gauge length $L = 20$ m. Color scales are normalized.

is equivalent to x_1), the DAS strain exhibits a flat phase response relative to particle motion, and the sensitivity vanishes at $\frac{\omega\eta_1 L}{2\pi} = n$, where $k = \frac{\omega\eta_1}{2\pi}$ is the wavelength and n is an integer. In an heterogeneous medium, for any $\eta_2 \neq \eta_1$ ($\gamma \neq 0$), the amplitude response is shifted according to the effective wavelength across the gauge from $x_2 - L/2$ to $x_2 + L/2$. Perhaps more importantly, the DAS phase response is no longer flat. With some manipulation, the phase response for $\omega\eta L < 2\pi$ is

$$\arg\left[\frac{\varepsilon^L(x_2)}{u(x_2)}\right] = (\eta_2 - \eta_1)\frac{\omega L}{4} + \frac{\pi}{2} = \frac{\gamma\eta_1\omega L}{4} + \frac{\pi}{2}. \tag{B.5}$$

Even though the point strain is proportional to the particle motion throughout, the phase of a progressive wave is not a linear function of distance in a heterogeneous medium, so averaging over a gauge length results in a spurious phase contribution. The maximum spurious phase occurs at the discontinuity, and so the gauge length centered on x_2 represents the "worst-case" for this simple two-layer model.

The significant differences between DAS strain at x_1 and x_2 relative to particle motion at those same locations indicate that small-scale heterogeneity may introduce a significant bias in common applications. First, consider velocity estimation. DAS is often employed for near-surface site characterization using surface wave inversion (e.g. J. Ajo-Franklin et al. (2019), Jousset et al. (2018), and Williams et al. (2021)). While various wavefield transformations and stacking schemes have been tested, these approaches all measure phase velocity from the difference in phase over some distance along a linear DAS array. Using our example from Figure B.3A again, comparing particle motion at x_1 and x_2 we have the progressive phase

$$\arg\left[\frac{u(x_2)}{u(x_1)}\right] = \omega\eta_1\Delta x \tag{B.6}$$

whereas for DAS strain, we introduce the additional spurious phase:

$$\arg\left[\frac{\varepsilon^L(x_2)}{\varepsilon^L(x_1)}\right] = \omega\eta_1\left(\Delta x + \frac{\gamma L}{4}\right). \tag{B.7}$$

If we assume that the phase response of DAS is constant with respect to particle motion, then we can recover the slowness as $\eta = \Delta\phi/\omega\Delta x$. This yields the apparent slowness:

$$\frac{\eta^{app}}{\eta_1} = 1 + \frac{\gamma L}{4\Delta x} \tag{B.8}$$

which is plotted in Figure B.5A and is notably independent of frequency. The error in estimated phase velocity or slowness is dependent on the ratio of the gauge length to the channel separation $L/\Delta x$, vanishing for $L/\Delta x \ll 1$. While this condition is

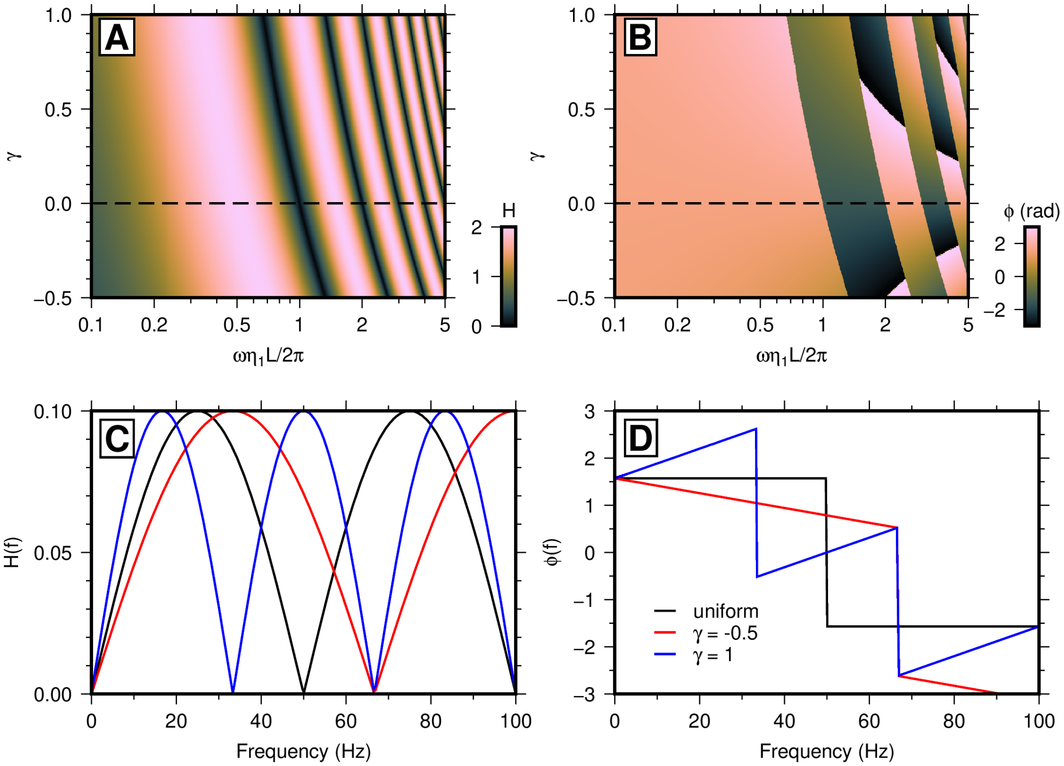

Figure B.4: (A) Dimensionless amplitude response of DAS strain relative to particle displacement for the two-layer case in Figure B.3A, $H = \left|\frac{\varepsilon^L(x)}{u(x)/L}\right|$, plotted by the velocity contrast $\eta_2 = (1+\gamma)\eta_1$ and and ratio of wavelength to gauge length $\frac{\omega\eta_1 L}{2\pi}$. (B) Phase response of the same in units of radians. (C) Dimensional amplitude response $H = \left|\frac{\varepsilon^L(x)}{u(x)}\right|$ evaluated as a function of frequency for the case at x_2 in Figure B.3B-D with $c_1 = \frac{1}{\eta_1} = 1000$ m/s, $\gamma = (-0.5, 0, 1)$, and $L = 20$ m. (D) Phase response corresponding to (C) in units of radians.

reasonable for most surface wave inversion applications, it places a practical limit on DAS array resolution. With contemporary commercial DAS systems that reach 80–120-km sensing distance, it is often necessary to utilize a gauge length up to 50–200 m, and so even though these systems typically record data at 10-m channel spacing, the effective resolution is much lower. For our experiment in Figures B.1 and B.2 with 16-m gauge length and a single 20% step in velocity, the error in estimated slowness using this model is ±10% at 8-m channel spacing and ±2.5% at 24-m channel spacing. While qualitatively similar in that the bias from small-scale heterogeneity only becomes apparent when $L/\Delta x$ is large, this model is insufficient to describe the extreme biases observed with the Pasadena Array, which probably include significant three-dimensional scattering, as evidenced by the strong coda and precursor energy in ambient noise cross-correlation functions (e.g. Figure B.1A).

Another common operation is strain to ground motion conversion of DAS data, which is necessary for H/V site methods, earthquake magnitude determination, and other applications (Spica et al., 2020; Lior et al., 2021; Lindsey, Rademacher, and J. B. Ajo-Franklin, 2020; Wang et al., 2018). Most approaches have used a frequency domain or frequency-wavenumber domain scaling from strain to particle velocity by a factor of the local phase velocity. Given $v(x) = -i\omega u(x)$, it follows from the homogeneous case in Eq. 3 that the particle velocity v is

$$v(x_1) = \frac{-\varepsilon^L(x_1)}{\eta_1 \mathrm{sinc}(\frac{\omega\eta_1 L}{2})}. \tag{B.9}$$

However, this relationship no longer holds at x_2, rather we have

$$v(x_2) = \frac{-i\omega L\varepsilon^L(x_2)}{e^{i\omega\eta_2\frac{L}{2}} - e^{-i\omega\eta_1\frac{L}{2}}} \tag{B.10}$$

As above, we can then quantify the error in particle velocity amplitude introduced by blindly applying Eq. X at x_2 using the locally measured phase slowness η^{app}:

$$\frac{v^{app}(x_2)}{v(x_2)} = \frac{e^{i\omega\eta_2\frac{L}{2}} - e^{-i\omega\eta_1\frac{L}{2}}}{i\omega L\eta^{app}\mathrm{sinc}(\frac{\omega\eta^{app}L}{2})}. \tag{B.11}$$

The amplitude error is plotted in Figure B.5B assuming $\eta^{app} = \eta_1$, which will rarely be true in practice as seen above. While this transformation has most often been applied in the long-wavelength limit so that the term $\mathrm{sinc}(\omega\eta L/2)$ is close to 1, the difference in amplitude response of DAS strain remains non-negligible. In this simple case, for $\omega\eta_1 L < 2\pi$ the fractional error in particle velocity amplitude is exactly half the velocity contrast within a gauge length. However, for wavelengths close to or smaller than a gauge length, the amplitude error can easily be an order of magnitude, even for very weak heterogeneity.

B.4 Conclusions

Elastic heterogeneity can introduce leading-order, scale-dependent bias in DAS strain measurements, effecting both amplitude and phase. For velocity estimation and wavefield gradiometry, this bias can be largely avoided by using channel pairs or sub-arrays with an aperture much greater than the gauge length. For conversion of amplitudes from strain to ground motion, some error is predicted at any wavelength, but especially at short wavelengths the error can exceed 100%. In light of the vast potential of DAS arrays on dark-fiber telecommunications networks for large-scale earthquake early warning applications, further work to quantify and correct for the effect of realistic elastic heterogeneity on DAS strain measurements is needed.

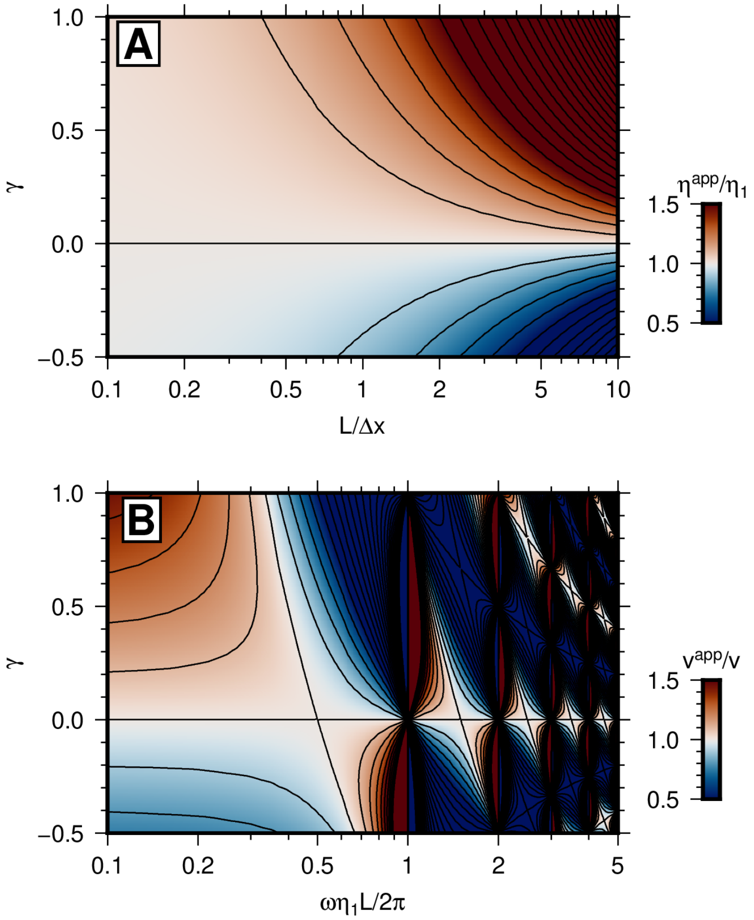

Figure B.5: (A) Error in apparent slowness η^{app} inferred from the difference in phase of DAS strain between x_1 and x_2 in Figure B.3A. (B) Error in particle velocity amplitude v^{app} converted from DAS strain at x_2 using the a priori slowness $\eta^{app} = \eta_1$. For both panels, black lines are contours of 10% error.

References

Ajo-Franklin, J.B. et al. (2019). “Using Dark Fiber and Distributed Acoustic Sensing for Near-Surface Characterization and Broadband Seismic Event Detection”. In: *Scientific Reports* 9.1, p. 1328.

Bakku, S. K. (2015). “Fracture characterization from seismic measurements in a borehole”. PhD thesis. Massachusetts Institute of Technology.

Beaumont, C. and J. Berger (1975). “An analysis of tidal strain observations from the United States of America: I. The laterally homogeneous tide”. In: *Bull. Seis. Soc. Am.* 65.6, pp. 1613–1629.

Berger, J. and C. Beaumont (1976). “An analysis of tidal strain observations from the United States of America: II. The inhomogeneous tide”. In: *Bull. Seis. Soc. Am.* 66.6, pp. 1821–1846.

Dean, T., T. Cuny, and A. H. Hartog (2017). “The effect of gauge length on axially incident P-waves measured using fibre optic distributed vibration sensing”. In: *Geophysical Prospecting* 65.1, pp. 184–193.

Gomberg, J. and D. Agnew (1996). “The accuracy of seismic estimates of dynamic strains: an evaluation of strainmeter and seismometer data from Pinon Flat Observatory, California”. In: *Bull. Seis. Soc. Am.* 86.1A, pp. 212–220.

Harrison, J. C. (1976). “Cavity and topographic effects in tilt and strain measurement”. In: *J. Geophys. Res.* 81.2, pp. 319–328.

Hart, R. H. G. et al. (1996). “Tidal calibration of borehole strainmeters: removing the effects of small-scale heterogeneity”. In: *J. Geophys. Res.* 101.B11, pp. 25553–25571.

Jousset, P. et al. (2018). “Dynamic strain determination using fiber-optic cables allows imaging of seismological and structural features”. In: *Nat. Comm.* 9.1, p. 2509.

King, G. et al. (1976). “Site correction for long period seismometers, tiltmeters and strainmeters”. In: *Geophys. J. R. astr. Soc.* 44, pp. 405–411.

Langbein, J. (2015). “Borehole strainmeter measurements spanning the 2014 Mw6.0 South Napa earthquake, California: The effect of instrument calibration”. In: *J. Geophys. Res.: Solid Earth* 120, pp. 7190–7202.

Lindsey, N. J., H. Rademacher, and J. B. Ajo-Franklin (2020). “On the broadband instrument response of fiber-optic DAS arrays”. In: *J. Geophys. Res.: Solid Earth* 125, e2019JB018145.

Lior, I. et al. (2021). “Strain to ground motion conversion of distributed acoustic sensing data for earthquake magnitude and stress drop determination”. In: *Solid Earth* 12, pp. 1421–1442.

Muir, J. B. and Z. Zhan (2022). “Wavefield-based evaluation of DAS instrument response and array design”. In: *Geophys. J. Int.* 229.1, pp. 21–34.

Paitz, P. et al. (2021). “Empirical investigations of the instrument response of distributed acoustic sensing (DAS) across 17 octaves”. In: *Bull. Seis. Soc. Am.* 111.1, pp. 1–10.

Singh, S., Y. Capdeville, and H. Igel (2020). “Correcting wavefield gradients for the effects of local small-scale heterogeneities”. In: *Geophys. J. Int.* 220, pp. 996–1011.

Spica, Z. J. et al. (2020). “Urban seismic site characterization with fiber-optic seismology”. In: *J. Geophys. Res.: Solid Earth* 125.3.

Wang, H.F. et al. (2018). “Ground motion response to an ML 4.3 earthquake using co-located distributed acoustic sensing and seismometer arrays”. In: *Geophys. J. Int.* 213.3, pp. 2020–2036.

Williams, E. F. et al. (2021). “Scholte wave inversion and passive source imaging with ocean-bottom DAS”. In: *The Leading Edge* 40.8, pp. 576–583.